INFORMATION TO USERS

This manuscript has been reproduced from the microfilm master. UMI films the text directly from the original or copy submitted. Thus, some thesis and dissertation copies are in typewriter face, while others may be from any type of computer printer.

The quality of this reproduction is dependent upon the quality of the copy submitted. Broken or indistinct print, colored or poor quality illustrations and photographs, print bleedthrough, substandard margins, and improper alignment can adversely affect reproduction.

In the unlikely event that the author did not send UMI a complete manuscript and there are missing pages, these will be noted. Also, if unauthorized copyright material had to be removed, a note will indicate the deletion.

Oversize materials (e.g., maps, drawings, charts) are reproduced by sectioning the original, beginning at the upper left-hand corner and continuing from left to right in equal sections with small overlaps.

Photographs included in the original manuscript have been reproduced xerographically in this copy. Higher quality 6" x 9" black and white photographic prints are available for any photographs or illustrations appearing in this copy for an additional charge. Contact UMI directly to order.

NOTE TO USERS

This reproduction is the best copy available.

UMI

VOLCANIC ERUPTIONS AND CLIMATE

A DATA AND MODEL INTERCOMPARISON

A Dissertation Presented

by

CASPAR M. AMMANN

Submitted to the Graduate School of the

University of Massachusetts Amherst in partial fulfillment

of the requirements for the degree of

DOCTOR OF PHILOSOPHY

February 2002

Department of Geosciences

UMI Number: 3039334

Copyright 2002 by
Ammann, Caspar Michael

All rights reserved.

UMI®

VOLCANIC ERUPTIONS AND CLIMATE
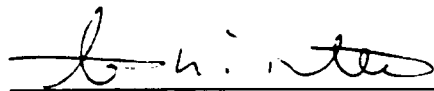# A DATA AND MODEL INTERCOMPARISON
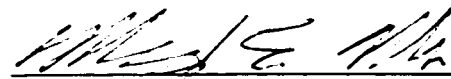
A Dissertation Presented

by

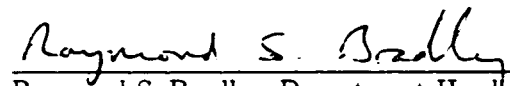CASPAR M. AMMANN

Approved as to style and content by:

Raymond S. Bradley. Chair

Robert M. DeConto. Member

Michael E. Mann. Member

Bette L. Otto-Bliesner. Member

James F. Walker. Member

Raymond S. Bradley. Department Head
Geosciences

Dedication

To my Mother,

who always helped me make my dreams come true.

ACKNOWLEDGMENTS

This dissertation is the result of a long journey, a journey into the unknown, following a path full of ideals, visions, and hope, led by curiosity and, to some extent, the challenge in itself. How wonderful to be able to look back realizing that all these wishes and expectations have been fulfilled, even the most courageous ones. The whole endeavour culminated not only in finalizing of this document, but also in the foundation of a wonderful new family. My wife **Emily** heroically suffered through the occasional absence of my mind, she listened patiently to my crazy ideas, and continuously encouraged me to follow up on thoughts and tasks, even when this meant that our time together was cut short. With this, she significantly contributed to the success of this work, and, most importantly, also a great deal to the fun and inspired life we were able to spend together. Recently, she gave birth to our son Nicolas, who is joining our lives at this moment of 'take-off'. We can only hope that he gets to enjoy the same opportunities we had.

Many other people were directly or indirectly involved in this work:

All my wonderful parents, both in Bern and Zürich, together with the whole family in Switzerland encouraged me from the very beginning for pursuing my ideas and wishes, and supported me in every possible way. Their selfless approach made the realization of my dream possible in the first place. The dedication of this work to my mother, **Susanna Lang,** is only a humble thank for all her support and dedication in her life to make anything possible for her son.

Although my dear friend **Simon** took over the apartment at the Depotstrasse in Bern, he still managed to make the Atlantic appear as a tiny puddle. Despite the separation, we are continuing

to hail the world with thoughts and spontaneous actions. Nothing can keep us from doing so.

Many friends in Switzerland had to suffer from the major cut off. Life developed more in the immediate surroundings and keeping up with the close contacts has not always been my strength. Putting an end to this document is the silver strip at the horizon.

In the United States, my life has been very easy, mostly due to great luck in meeting wonderful people. At the University of Massachusetts, a large number of students and faculty have been helpful and stimulating in many ways. Particularly my friendship with Bomin has been rewarding in personal and scientific ways. An evening with engaged discussions over dumplings and beer is hard to beat and, since the move to Colorado, heavily missed. The whole Climate Lab (including Anne, Mathias, Carsten, Pierre and others) run and entertained by Frank Keimig has been responsible for keeping the fun in life during my stay in Massachusetts.

Ray Bradley, my advisor and sponsor to this adventure had op-pend for me the doors to a thorough apprehension of the field of Paleoclimatology. His enormous background was an outstanding learning field for my broad interests.

Roughly half way through the Ph.D., I got the chance to work at the National Center for Atmospheric Research. **Bette Otto-Bliesner** has been fundamental not only in offering a workplace but in guiding me through the years. Her door was always open for questions and ideas of any sort. Together with her Paleo Group of Esther Brady and Christine Shields, she made the work at NCAR so exciting that the ASP Post-Doc will be a pleasure.

Another person critically involved in making my stay in Boulder possible and by guiding through the scientific world of the CCM3 has been **Jeff Kiehl**. Without his continued and generous support, none of the work would have been possible. With his new model, many very exciting scientific challenges are now lying ahead. I'm looking forward to go after them.

Charlie Zender broke the ice for me to the radiation code and always was ready with good help. His dust implementation has been the direct guide to the volcanic aerosol studies.

The NCAR Library staff, Faith, Gayl, the Judies, and Leslie, have been of particularly great

ABSTRACT

VOLCANIC ERUPTIONS AND CLIMATE

A MODEL AND DATA INTERCOMPARISON

FEBRUARY 2002

CASPAR M. AMMANN,

M.S., UNIVERSITY OF BERN, SWITZERLAND

Ph.D., UNIVERSITY OF MASSACHUSETTS AMHERST

Directed by: Professor Raymond S. Bradley

Explosive volcanism can release large amounts of particles and gases into the atmosphere. Sulfuric acid droplets in the lower stratosphere are the primary substance interacting with the radiative fluxes over many months and possibly years. Because of their sub-micron size, they are more efficient at scattering incoming shortwave radiation from the sun back into space than absorbing and trapping longwave radiation from the earth. This results in a negative impact on the earth energy balance causing a general cooling below the aerosol layer. The magnitude of the cooling depends mostly on the amount of radiatively active aerosol particles as well as the duration of the perturbation. The cooling signal is largest in the upper troposphere through feedbacks with a slowed hydrologic cycle. At the surface, heat release, mostly from the oceans, can buffer some of the cooling.

A combined approach using both observations/proxy data and a state-of-the-art coupled General Circulation Model (GCM) to analyze the volcanic effects on climate can help in our

understanding of the possible range of responses. Here, the most recent large eruption of Mt. Pinatubo (June 1991) was used to verify the implementation of the aerosol parameterization in the radiation code of the GCM. From there, an analysis of the volcanic contribution since 1870 A.D. was performed. A simple way of describing the spatial aerosol distribution is presented. In general, only a handful of eruptions were found large enough to significantly perturb the radiative balance of the earth. These few events caused a global climate signal, which is clearly detectable against the background noise of internal variability of the climate system. Next to the influence of isolated events, model simulations confirm earlier suggestions that temporally closely spaced large events can cause a further cooling in climate before the system can recover. Thus, explosive volcanism must be regarded as an important player in decadal to multi-decadal natural climate variations. In case of the 20th-Century, volcanic cooling in the last decades could have offset any possible warming due to increased solar irradiation. The potential volcanic role in other important time periods in the past must be studied, including the cooling in decades generally solely attributed to the sun. Proxy records, in particular tree rings, point to a potentially large role of explosive volcanism in the past.

Additionally to the radiative effects, increased atmospheric flow at high latitudes, particularly in winter, is the result of dynamical responses to changes in meridional temperature gradients in the lower stratosphere through heating in the aerosol layer. This effect helps to orchestrate the spatial distribution of the climate signal for several years after the eruption. Currently, no clear influence on other internal modes of variability, such as El Niño, could be unanimously confirmed in both observations, proxy reconstructions and the model simulations. But more work is needed, as better proxy climate data for earlier large events get available.

TABLE OF CONTENTS

LIST OF TABLES

LIST OF FIGURES

Chapter 1

INTRODUCTION

1.1 Explosive volcanism - Hazard and Life line

Volcanic eruptions are some of the most spectacular and powerful natural events on our planet. They range in size from the smallest eruption. which produced a little more than one cubic meter of lava (accidently initiated during a hydrothermal drilling attempt *Decker and Decker*, 1991). to volumes of several thousand cubic kilometers of material for some of the largest events known (*Rampino and Self*, 1992). These events are generally concentrated along tectonic plate boundaries (for example the *Ring of Fire* around the Pacific) and at a number of isolated places over mantle plumes, so called *hot spots*, with Hawaii as its most famous example. Eruptions have long captured the interest of man and their enormous power has been honored in many cultures. Dangers and gains from volcanoes have balanced each other to the extent that the presence of volcanoes does not prevent humans from settling. even in closest proximity to continuously active volcanoes.

The spectacular exhibits of earthly power can come with a high price. The impact of big eruptions can be very devastating. depending on the character of the eruption and on the distance of humans and their property to the eruption itself. Pressure waves in the air (and extended in
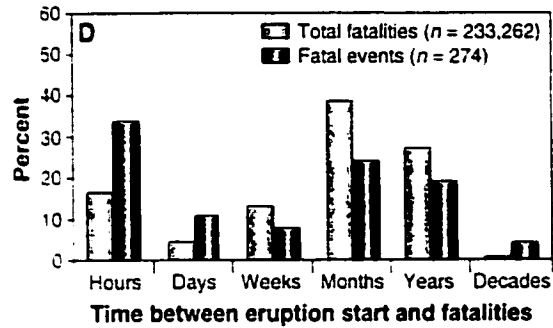
Figure 1.1: Estimates of total number of fatalities directly associated with volcanic eruptions and their distribution over time (lightly shaded bars). The frequency of eruption events with fatalities with their temporal distribution. Source: *Simkin et al.* (2001).

water bodies as tsunamis), pyroclastic flows, volcanic bombs, ash falls (causing roof collapse), mud flows, and even gas emissions can be deadly in the immediate surroundings and, when channeled in valleys, also at great distances. Lava flows usually cause no fatalities, because they move too slowly, but can, on the other hand, cause large property damage and complete loss. While the direct impact of violent volcanic eruptions on humans can be devastating, indirect post-eruptive effects can be at least as damaging and the total number of fatalities long after eruptions actually surpasses the ones suffered from the immediate impact. Figure 1.1 from *Simkin et al.* (2001) shows that only about 15% of total fatalities are caused in the first hours after an eruption. Most deaths occur months and years after a handful of big events. Most fatalities are the result of famines caused by the destruction of fields through ash deposition, starvation though loss of cattle or pollution of drinking water from volcanic deposits.

These numbers demonstrate the potential for volcanic effects to last beyond the eruption itself. If one would also include long distance effects caused by climatic perturbations with its related fatalities, the numbers would rise even higher. One such event occurred with the eruption of Tambora in the year 1815. It caused about 92,000 deaths (*Simkin and Siebert*, 1994) in the vicinity of the eruption, most in the following years through starvation on neighboring

islands where all crops were destroyed by the falling ash. The eruption in 1815 was followed by the so-called *Year without a Summer* (*Stommel and Stommel*, 1983; *Harington*, 1992), whose effects appeared most significantly in eastern North America and Western Europe. The climatic perturbations in the year 1816 caused the western world to suffer its "last great subsistence crisis" (*Post*, 1977), with large economic and political fluctuations lasting for several years. While some links can be implied, a clear cause and effect relationship is difficult to establish. Even farther reaching interpretations are proposed by *Keys* (1999) for a volcanic event in the year 536. Although there are good indications for a large volcanic eruption at that time, evidence for the volcanically caused impacts with subsequent 'domino-effect' like events continuing for several centuries seems questionable. Other natural climate variations, such as strong El Niño events, can also cause contemporal perturbations around the globe (*Philander*, 1990; *Fagan*, 1999). In any case, these examples illustrate both the potential for significant impacts from volcanic eruptions on climate and society and the problems for identifying a volcanic signal against other factors of variability and the climate noise.

Volcanoes are not only destructive forces. They provide ample nutrients to generate very fertile soils which are famous for providing the very best ground to grow coffee or grapes for wine production. The vertical extension of volcanoes also cause a local increase in precipitation, providing a more stable water resource. Volcanoes also play a crucial role in large scale building and recycling of crustal material. Recent suggestions even see volcanoes as a potential source for oxygen in the early atmosphere (*Kump et al.*, 2001), and some suggest life might have originated in hot volcanic vents (*Holm*, 1992). Heat from the earth interior is also used for geothermal energy in a number of volcanically active regions such as Iceland and Italy.

The focus of this study is the relation between large explosive eruptions and their impact on climate. Due to short records, of both volcanic forcing and climate time series, the determination of a cause and effect relationship has been difficult. New reconstructions covering the last millennium increase the number of large events and increase the signal to noise ratio.

3

1.2 Data overview

1.2.1 Volcanologic data

Explosive volcanism releases substantial amounts of ash and gases into the troposphere and stratosphere (*Bluth et al.*, 1993). In order to influence climate, these particles have to remain aloft in large quantities for many months and years (*Wigley*, 1991). To describe these volcanic perturbations, we are primarily concerned with small aerosol particles that were either directly injected into the stratosphere or formed there out of the gas phase. Large particles on the order of several microns (μm) or more generally fall out of the atmosphere very quickly (*Kasten*, 1968), and only a small percentage of the large particles can get transported over long distances. Although this might have been the case in some unusual events (see Chapter 6.3), the general understanding is that such long distance transport and subsequent fall out of large particles long after the eruption is not very common.

Measurements of aerosol by balloon- or airplane-based filtering reveals that small liquid particles represent the highest number concentrations in aerosol clouds (*Junge et al.*, 1961; *Mossop*, 1963, 1964). In fact, this had already been suggested in the last century by the Krakatau Committee *Symons* (1888). They suggested that the main constituents of the stratospheric volcanic dust after Krakatau might have been composed of "condensed gaseous products of the eruption (other than water) such as sulphurous acid or hydrochloric acid" (*Symons*, 1888, p. 445). Although these small droplets also form the majority of particles in the background aerosol, their number and size is strongly increased after large volcanic eruptions (*Castleman et al.*, 1974). They form in the stratosphere from the gaseous volcanic emissions, primarily from SO_2 and H_2S (*Junge et al.*, 1961). This transformation usually takes up to a few months, extending the duration of buildup of the aerosol cloud. The decay of SO_2 gas forming new sulfuric acid aerosol is illustrated in Figure 1.2 for the Pinatubo cloud. The e-folding time (time to decrease the concentration to a value of $1/e$) of SO_2 in the stratosphere is roughly one month (*Bluth et al.*, 1992; *Read et al.*,

4

1993; *Grant et al.*, 1996). The liquid aerosol on the other hand can stay around longer, decaying with an *e*-folding time of about one year. Because these particles often undergo further changes in size and particle concentrations (*Hofmann and Rosen*, 1984c; *Russell et al.*, 1993), the volcanic forcing as the sum of all radiative perturbations is difficult to capture in an exact manner.

Given the various steps from the particle and gas injection to their removal over time, it is the challenge of Chapter 2 and 3 to describe qualitatively and quantitatively the evolution of the climate forcing from explosive volcanic eruptions, at least since the earliest measurements of atmospheric transmission in the early 1880s. Additionally, some inferences about earlier eruptions are presented.

Chapter 2 gives a description of the numerous direct and indirect data sources of volcanic eruptions and introduces their strength and limitations. The goal is to document how well one can reconstruct the volcanic forcing over time, as well as build some understanding on the data sets' limitations.

1.2.2 Forcing Data

Global climate change experiments using various climate models are often run over the instrumental time period, from the middle or late 19th-Century to present. While many of these experiments focus on the increasing greenhouse gas composition of the atmosphere, the external components of solar and volcanic forcing can contribute significantly to the climate variability (*Baldwin et al.*, 1976; *Gilliland and Schneider*, 1984; *Hansen and Lacis*, 1990; *Rind and Overpeck*, 1993; *Lean and Rind*, 1994; *Mann et al.*, 1998; *Lean and Rind*, 1999; *Tett et al.*, 1999; *Crowley*, 2000; *Stott et al.*, 2001). Here, only the volcanic forcing is of concern. Chapter 3 addresses this in two main sections. First, a new volcanic forcing data set that can be used in climate modeling simulations from 1870 to present is developed. Building on the detailed information retrieved from the recent eruption of Pinatubo, this data set includes the temporal and spatial evolution of the volcanic aerosol clouds on monthly time steps using a simple seasonal parameterization

5

TOTAL SO₂ IN MEGATONS

TIME AFTER ERUPTION, IN DAYS

SAGE II - Estimated Stratospheric Aerosol Mass

Mass (Tg)

—— Estimated Aerosol Mass

---- 11-Month "Exponential" Decrease

1991   1992   1993   1994   1995
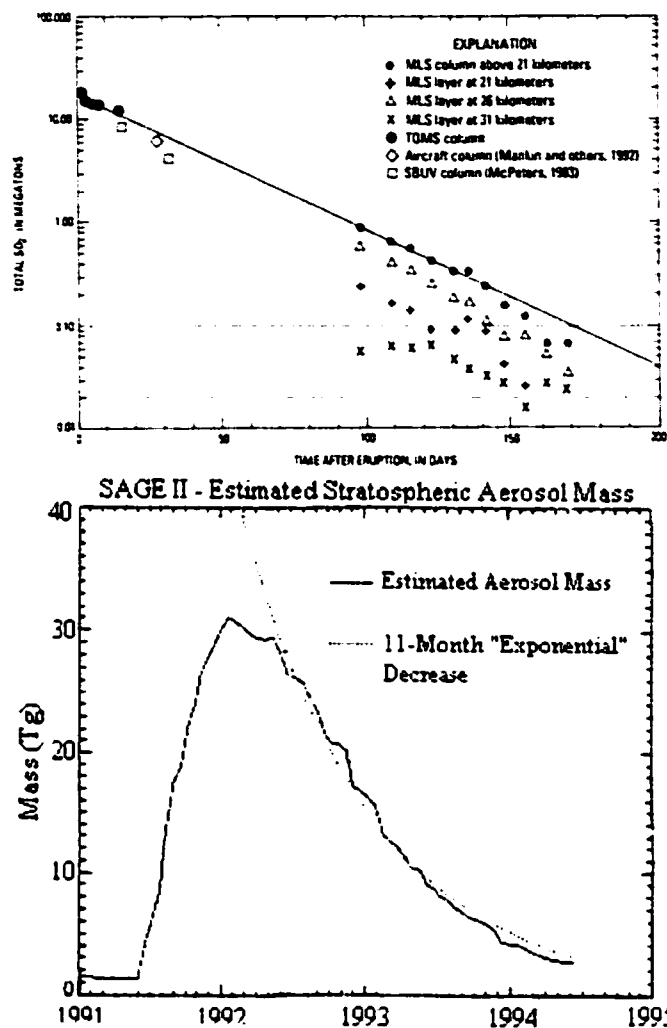
Figure 1.2: Buildup and decay of the sulfuric aerosol cloud from Pinatubo. Top: SO_2 concentration from different instruments and in-situ measurements after *Read et al.* (1993) showing a peak SO_2 mass of 18-20 Tg (=Mt). Bottom: presents the buildup of the sulfate aerosol (H_2SO_4 and H_2O) mass in Tg (=Mt) from SAGE II. with a peak mass of about 30 Tg in December 1991 - January 1992. when almost all SO_2 is transformed.

for transport. Second, one single archive - ice cores - is used to capture a record of explosive volcanic eruption occurrences in the tropics over the last 600 years. A new statistical technique will be applied to investigate the long term fluctuations in the occurrences of the large events. The conclusion will show that explosive volcanism is a non-stationary process in time and has the potential to influence climate on multi-decadal time scales.

1.2.3 Impact signals in proxy data

Impact studies of volcanic eruptions on climate are usually thwarted by both the small number of events for which data is available and large climate variability. New high resolution climate reconstructions significantly extend the time frame for such studies and allow investigations of an increased number of very large events in historic times, for which the signal to noise ratio is better. Depending on the type of reconstruction, different aspects of potential climate impacts can be investigated. For the interpretation of a signal, one has to remember the spatial and temporal resolution, as well as representation of the proxy data. Chapter 4 will make use of the global annual temperature reconstruction of *Mann et al.* (1998), which allows the study of the climate impact of large events going back to the year 1400. The twenty largest events are chosen from ice core and other records and their impact is analyzed. The general cooling and the pattern of the climate signals are compared with modes of natural climate variability. Short term effects and long term climate trends potentially influenced by the eruptions are discussed.

1.3 Modeling

More than 70% of the global surface is covered by oceans, for which high resolution climate information is extremely difficult to find. This adds to the difficulties of identifying climate signals from volcanic eruptions in instrumental and proxy time series. To circumvent this particular problem and to study mechanisms of signal propagation in detail, coupled ocean-atmosphere

climate models can be used. With the models, the spatial extent of data is no longer a problem, but the reliability of the representation of real world processes has to be evaluated. Since all approaches carry their own advantages and disadvantages, a combined approach would seem appropriate.

Therefore, a second approach to identifying the volcanic impact on climate, this study applies a state-of-the-art general circulation model (GCM). First, the volcanic aerosol physics are built into the radiation code, and the radiative forcing is evaluated. Second, the global climate response is studied for single and multiple events. The advantage of the climate model is to further enhance signal to noise ratio by running ensembles (i.e. using the same forcing but starting from different initial conditions). This allows us to isolate mechanisms of the climate response, be it in the direct radiative budget or the dynamic response to it in all parts of the system (atmosphere, ocean, land surface and sea-ice). They can be investigated in great detail in order to gain a more complete view of the highly complex coupled earth system response. The climate model also helps to put proxy data in a spatial perspective. At the same time, proxy data helps to test the models ability to represent certain climate responses, although the problem of local effects and random noise have to be taken into account. This leads to an iterative process, which is both needed and problematic. The need comes from the lack of detailed knowledge of the forcing, which can include total amount or duration of stratospheric aerosol, its composition, its size, its transport, all aspects the climate model will respond more or less sensitive to. On the other hand, the climate model also has the ability to identify where something is missing in our knowledge about a certain event. One particular event studied here (Krakatau) represents this case of cross-evaluation. In general, the cross-evaluation is of advantage for all disciplines involved, although it can sometimes be hard to reach a clear consensus:

Volcanoes. like the man in the fable.

can blow hot and blow cold with the same breath.

but that shall not provoke us to wrath.

(Humphreys. 1937)

Volcanic aerosol influence on climate has been modeled with almost all types of climate models. ranging from simple energy balance codes to the most sophisticated 3-D coupled ocean-atmosphere-sea ice General Circulation Models. Some models were used to study the transport of the volcanic dust (*Cadle et al..* 1976; *Capone et al..* 1983; *Boville et al..* 1991), others prescribe the volcanic forcing as a reduction in net radiation (*Crowley and Kim.* 1999; *Andronova and Schlesinger.* 2000). Since the actual forcing is dependent on the aerosol mass. its composition and size. as well as the underlying albedo. comprehensive solutions including two stream radiative transfer computations (one downward and one upward) with multiple scattering (allowing for direct beam and diffuse light treatment) and absorption will lead to the most accurate treatment of the direct effects (*Bohren and Huffman.* 1983). More difficult to evaluate are indirect effects which include the influence on stratospheric chemistry such as ozone (*Hofmann.* 1989; *Fahey et al..* 1993; *Turco et al..* 1993; *Solomon et al..* 1996; *Solomon.* 1999) and the influence on tropospheric cloud formation cloud droplet ice crystal properties (*Humphreys.* 1940; *Wexler.* 1956; *Jensen and Toon.* 1992; *Sassen.* 1992; *Minnis et al..* 1993). A nice summary of many applications can be found in *Kondratyev and Galindo* (1997).

1.3.1 Implementation

For this study. the physics of volcanic aerosol influence on the solar and terrestrial radiation were implemented in the National Center for Atmospheric Research - Climate System Model (NCAR-CSM). a state-of-the-art General Circulation Model. This allows the detailed study of what parameters of volcanic aerosols play important roles in influencing the global radiation budget

9

and climate. Chapter 5 describes in detail how the aerosol is treated in the climate model, what assumptions are used for its representation of the real world conditions and what limitations need to be kept in mind. Using the detailed knowledge of the aerosol produced by the 1991 eruption of Mount Pinatubo, the implementation is tested in a stand-alone version of the atmospheric GCM. The model is forced by a prescribed aerosol mass distribution in the stratosphere and observed sea surface temperatures over the oceans. Large emphasis is put on the radiative effects, which is at the core of the volcanic impact. Comparisons with observations will be used to evaluate the success of the simulation.

In order to use the climate model for eruptions prior to the period with detailed instrument measurements, a simplification of the aerosol characteristics is evaluated that should allow a generalized treatment suitable for all large explosive eruptions in the past. The primary parameter should be one that can be reconstructed from proxy archives, such as the sulfate mass from ice cores. Again, the radiative impact and subsequently, the climate perturbation are analyzed and compared with observations. Results show that for the Pinatubo event, a replacement of the detailed aerosol information with a simplified aerosol does not significantly change the impact, and hence, the method can be used in applications of other past eruptions.

1.3.2   Volcanic Impact during the 20th-Century

This conclusion is then put to the test in Chapter 6, where the 20th-Century volcanic impact is investigated. The forcing data (column integrated visible optical depth) described in Chapter 3.5 is used with the simplified aerosol characteristics. The GCM, now coupled to a dynamic ocean and sea ice model, is run keeping every other parameter constant at 1870 atmospheric conditions. The impact of the large explosive volcanic eruptions is described and analyzed for short and long term influences as compared to the control experiment with no volcanic influence. The climate impact from the Krakatau eruption is further analyzed in more detail and some general assumptions of the volcanic forcing implementation are evaluated and discussed.

10

1.4 Challenges

Despite a major improvement in measurement techniques and spatial coverage, fundamental uncertainties on general aerosol characteristics and their influence on the global radiative balance persist. This is not only true for the troposphere (*Charlson et al.*, 1992; *Hansen et al.*, 2000), but also for the stratosphere (*Russell et al.*, 1996). This problem is even more significant when eruptions prior to the beginning of the satellite period in 1979 are analyzed. The final Chapter 7 reiterates the main aspects of the proxy data and model simulations by evaluating the representation and confidence in each. The fundamental assumptions are also revisited and successful and less successful aspects of the simulations and our present knowledge about the impact of volcanic eruptions on climate are put against each other. Since only the direct forcing is included in the simulations, a brief discussion of possible indirect effects are also presented. Then, the contribution of volcanic aerosol in a GCMs simulation of short term and long term climate fluctuations over the recent past is discussed. Both single events and changes in temporal spacing between eruptions are found to be of importance for the real world climate, despite remaining limitations in our knowledge of the forcing and climate response.

Finally, a crucial property of the climate system, be it in the real world or in models, is discussed: the climate sensitivity. The question of what the large, but short lived, forcing and subsequent climate response from volcanic eruptions can tell us about the speed and magnitude of adjustments in the climate system is of high interest for a number of reasons. First, the climate models ability to represent past climates with years and decades of large climate variations beyond the background variations of the models internal climate variability. This aspect cannot be evaluated in a absolute sense, since the climate variations in the real world are only approximated by the reconstructions, often using proxies that are calibrated during the instrumental period. Both magnitude and spatial patterns of the climate response to the same forcing can change over time, a limitation that is still calling for caution in the interpretation of causes and effects of

past climates. Second, the climate sensitivity is important for the discussion and evaluation of global warming, as it will determine how fast and how strong the response to increased CO_2 is going to be. If there is such a property as *the* climate sensitivity, which as a general property would be unchanged over time, then a more accurate estimate of the future warming given an atmospheric forcing from greenhouse gases could be achieved. This would also imply that given global changes in the past, the forcing to reach these states could be estimated.

Chapter 2

RECORDS OF VOLCANIC

FORCING

2.1 Overview

Explosive volcanism releases large amounts of ash and gases into the atmosphere. Today, there are several ways to measure the mass and chemical composition, as well as the horizontal and the vertical location of these clouds remotely from the ground, from space, or directly in the air. Automatic observation platforms on satellites, together with volcanologic monitoring installations on and around selected volcanoes, are able to identify large activity and can immediately register perturbations in the atmosphere. Despite these available tools, only 20 years ago, just prior to the large eruption of El Chichón, these systems were initially not capable of identifying the source of an aerosol cloud that showed up unexpectedly (*DeLuisi et al.*, 1983; *Evans and Kerr*, 1983). Only after reanalysis of satellite data, the so-called 'Mystery Cloud' was later linked to an eruption of Nyamuragira in East Africa (*Krueger et al.*, 1995). In the past, much stronger 'mysterious hazes' have been reported repeatedly, but the link to volcanoes was probably done only in the

late 18th-Century, and instrumental data to directly analyze the volcanic forcing only starts in the late 19th-Century. Indirect techniques have to be applied for the earlier times. It is the task of this section to give an overview of the sources of direct and indirect information can be used for the reconstruction of past volcanic perturbations of the atmosphere. The brief description is organized to cover the data sources from today's most sophisticated satellite techniques backwards in time to early documentary data and indirect proxy archives. Different techniques or proxy records are shown to possess both advantages and disadvantages (see also *Bradley*, 1988; *Bradley and Jones*, 1995b). A successful reconstruction will have to combine as many archives as possible.

2.1.1 Background aerosol: Junge layer

Before discussing volcanic aerosol, a short note on background aerosol in the lower stratosphere is needed. *In situ* measurements of atmospheric particles from balloons in the late 1950s led to the discovery of a layer with, at that time, surprisingly high numbers of very small (i.e. $< 0.1\mu m$), mostly liquid particles with a dominantly sulfuric composition (*Junge et al.*, 1961). They tend to occur in a relatively limited layer above the tropopause, later called the Junge Layer. Because no large volcanic eruption preceded these observations, the particles in this layer were regarded as a background aerosol, primarily fed by sulfur fluxes from the troposphere (*Crutzen*, 1976; *Charlson et al.*, 1987; *Andreae and Crutzen*, 1997). The particle concentration in the Junge Layer can vary over time, with explosive volcanism having the most effective impact on it over short time scales. The aerosol burden in the Junge layer can quickly change by a factor of 10 and more. Between 1979 and 1992 it changed twice by a factor of at least 30 (*McCormick and Veiga*, 1992). Only few years are recognized to represent true 'background' conditions: the measurement period of *Junge et al.* (1961) 1959-60 and pre-El Chichón times 1978-79 (*Hofmann and Rosen*, 1981). Because of the very short timeseries of observational evidence, it is currently unclear if major long term fluctuations other than the volcanically generated ones exist. If this were the case, small to modest modifications of the radiative budget of the earth would be possible.

2.1.2 Direct versus indirect forcing

The sum of perturbations to the solar (incoming) and thermal (outgoing) radiative budget due to volcanic ejecta form the volcanic forcing. The more accurate one can capture the changes throughout the spectrum, the better one can describe the forcing. In this Chapter, emphasis will only be given to this direct forcing. The indirect radiative effect, which primarily includes impact on stratospheric chemistry and changes in cloud characteristics in the upper troposphere, is very complex and only poorly understood. While the indirect effect could modify the volcanic forcing, due to the much lower humidity it is not likely to carry the same weight in the stratosphere as was recently presented for the troposphere (*Charlson et al.*, 1992; *Kiehl et al.*, 2000; *Satheesh and Ramanathan*, 2000). For a brief discussion on cloud feedback, see Chapter 7.1.2.

2.1.3 Optical depth

A common quantity describing the aerosol perturbation of the atmosphere is the aerosol optical depth. It is usually given at one or several selected wavelengths. The optical depth, or τ, describes the integrated change in energy transmission (extinction, σ) through an incremental atmospheric layer (dz):

$$\tau_\lambda = \int_{\infty}^{z} \sigma_\lambda dz \tag{2.1}$$

or,

$$\tau_\lambda = \int_{\infty}^{z} \sigma_\lambda cos\Theta_s dS_b. \tag{2.2}$$

where $cos\Theta_s dS_b$ is the incremental distance along the solar beam, dS_b, scaled by the cosine of the solar zenith angle, Θ_s. Due to changing interactions (in form of scattering and absorption) of aerosol with different wavelengths, the optical depth is dependent on the wavelength λ. Given an aerosol size distribution, shape and composition, the optical depth can be regarded as a mass-scaled extinction over a certain path, or is often integrated throughout the atmospheric column. Under the assumption that the aerosol size distribution is the same after different eruptions,

15

the optical depth at different times can be inferred from the aerosol mass (and vice versa. But without knowledge of the aerosol properties, the optical depth at one specific narrow wavelength is not enough for solar or infrared energy budget calculations, since the wavelength-dependent extinction varies widely for different aerosol sizes. It will be shown below that once a specific aerosol size distribution and composition are selected, all the optical properties can be evaluated. For homogeneous distributions of spherical particles, the Mie approximation can be used to determine all parameters needed.

Often, optical depth is referred to as optical depth in the visible band. The human eye is sensitive to energy in the wavelengths from 0.38 to 0.75 μm (visible spectrum), which is generally approximated by 0.5 μm. This will be the wavelength of choice in the following chapters, when aerosol optical depth is prescribed for the climate model. Perturbations in this wavelength from ground based or space borne instruments can be compared with visual observations of atmospheric hazes, sunsets, etc., at least in a qualitative way. One needs to keep in mind, however, that the optical depth at visible wavelength is interchangeable with τ at any other wavelength, as long as there is an aerosol geometry and composition selected. Satellite sensors often measure at multiple wavelengths, many of which very different from 0.5 μm. Therefore, direct comparisons of the values of τ cannot be done easily.

2.2 Instrumental Records of Volcanic Aerosol

2.2.1 Satellite Data

Currently, a series of satellites with a host of different sensors are in earth orbit constantly monitoring composition, transmission and temperature of the atmosphere (see *Kidder and Vonder Haar*, 1995; *Harries*, 1995). For detecting volcanic aerosol in the atmospheric column, two different strategies are used. First, there are the *limb scanners*. These devices measure the diminishing light (occultation) as the sun (and moon for SAGE III) rises or sets behind the earth. With

this technique, vertical cross-sections through most of the atmosphere can be retrieved. Type, concentration and altitude of particles and gases can then be computed using specific algorithms based on known optical properties or assumed size distributions for the specific electromagnetic bands covered by the instruments. Some of the retrievals can turn out to be very sensitive to underlying assumptions such as aerosol size, which can bias the results. Common error estimates are around +/- 30% (*Krueger et al.*, 1995).

The second commonly used technique measures reflection and scattering characteristics and monitors certain absorption and emission bands of specific gases below the satellite's path (so called *nadir observation*). Because this scanning technique can measure large areas, they can be used to track spreading clouds in much detail. The large spatial coverage is a big advantage for early recognition and monitoring of volcanic gas and particles immediately after an eruption and therefore also widely used by air traffic controllers to divert air planes. Several instruments can measure sulfur dioxide, the climatically most important gas of volcanic origin (*Pollack et al.*, 1976; *Rampino and Self*, 1984) since it is one of the major sources for the formation of sulfuric acid after injection into the stratosphere (*Castleman et al.*, 1974; *Barth et al.*, 1983). The initial mass of injected SO_2 gas can give a good estimate on how much sulfuric acid droplets can be expected during the next months and years (see Figure 1.2). As mentioned above, it is important to measure the emissions early after the eruption, because SO_2 starts to diminish relatively quickly as the result of reactions with OH and H_2O (*Robock*, 2000). Because the sensors measure the integrated signal throughout the atmospheric column, there is no direct vertical resolution possible.

Stratospheric Aerosol and Gas Experiment (SAGE) : Figure 2.1 shows the compiled stratospheric sulfate optical depth at $1\mu m$ from the two limb-scanning instruments SAM II (*Mc-Cormick et al.*, 1979, 1981) and SAGE II (*Patrick and Wang*, 1987; *McCormick and Veiga*, 1992; *Rind and Liao*, 1997) for the period of 1979 to 1997. While SAM II, on-board of Nimbus-7, is ob-

serving the earth in a sun-synchronous orbit and therefore covers only the polar areas (64°-80°N and S). SAGE II was put on-board of ERBS (see below), covering the low and mid-latitudes, to complement the geographic pattern of SAM II (*McCormick et al.*, 1979, 1993). Two especially large volcanic eruptions occurred in this time: El Chichón in March and April 1982 and Pinatubo in June 1991. Sulfuric acid formation resulting from the eruptions can be readily recognized by strongly rising optical depth. Unfortunately, the sensors of SAM II were too sensitive to the strong aerosol injection from El Chichón. This deficiency in capturing large volcanic perturbations was fixed in SAGE II, so that the even larger Pinatubo cloud could be measured more accurately in 1991. The data collected by SAM and SAGE satellites is published in *Rind and Liao* (1997).

With the launch of SAGE III instrumentation in 2001, a significant further development will help capture the aerosol and gaseous species (e.g., O_3, water vapor) more readily. Eight different bands will be available for the aerosol retrieval. This will allow much more detailed spectral studies of the aerosol attenuation and will therefore reveal many more details regarding the particles' properties (size, shape, concentration, composition).

Earth Radiation Budget Experiment (ERBE) : Next to measurements directed towards the particle concentrations and mass in the atmosphere, energy budget instrumentation can evaluate the overall effect of the perturbation. The ERBE on board the Earth Radiation Budget Satellite (ERBS) offered an excellent way to verify the aerosol measurements during the Pinatubo aerosol perturbation (*Minnis et al.*, 1993). ERBE measured shortwave reflection integrated over a band of 0.2 – 5.0 μm (short wave length, SW) and total outgoing radiation from 0.2 – 50.0 μm (long wave length, LW). It showed that the increased SW reflection dominated over decreased outgoing LW radiation, especially in areas with low underlying albedo. This caused the earth system to lose energy and cool.

SAM II and SAGE II Stratospheric Aerosol
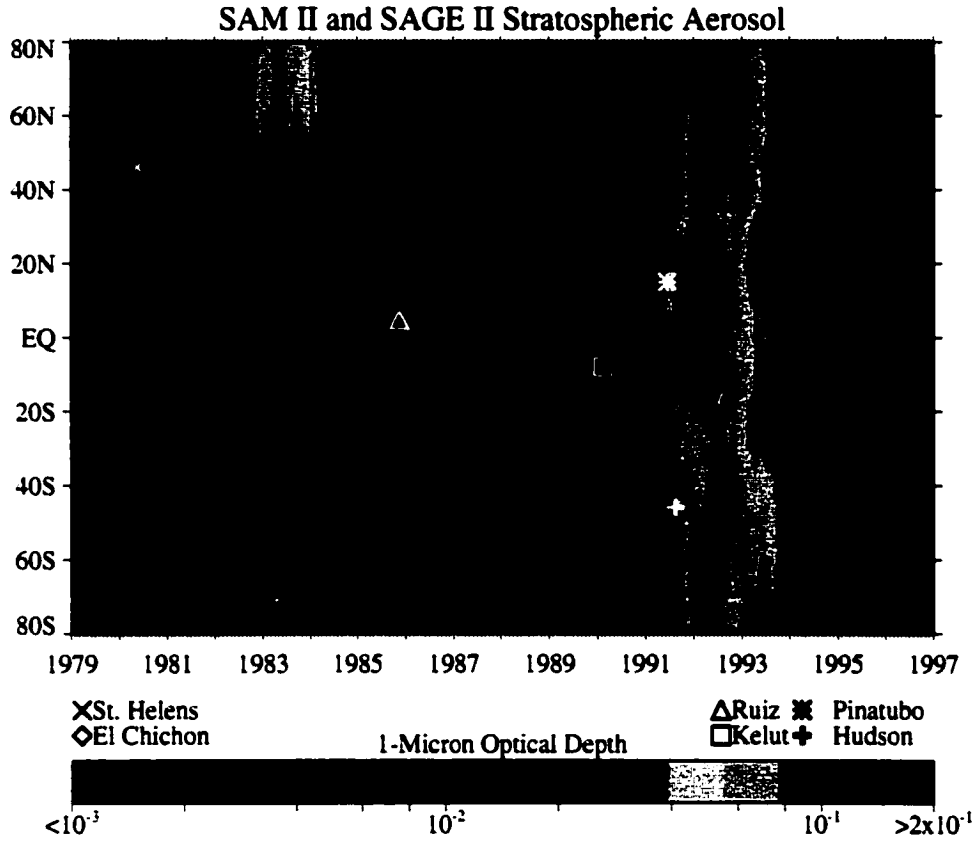
Figure 2.1: Column optical depth at 1 μm. compiled from SAM II. SAGE I and SAGE II (*Thomason et al.*. 1997). data published in (*Rind and Liao*. 1997). The black area is caused by failure of SAGE I. unfortunately just prior to the El Chichón perturbation. Data resumes in the low latitudes in October 1984 with SAGE II. Not indicated are saturation effects that happened to during the El Chichón and. to a lesser degree. also for Pinatubo (see *Thomason et al.*. 1997). Times and latitudes of significant volcanic eruptions are indicated by symbols.

19

2.2.2 Lidar

Lidar (standing for *light detection and ranging*), a combination of laser and radar makes use of the reflective characteristics of aerosols detected by laser pulsing at very specific wavelengths. The Lidar instruments measure the time delay of backscatter and its strength to compute the altitude of the reflector and its properties above a specific location.

From a number of long surface observation series, one can infer the spread of aerosol after a large eruption. Lidar not only records the timing of aerosol spread over a certain location, but it also captures the temporal evolution of layer altitude and a list of aerosol characteristics (*DeLuisi et al.*, 1983; *Thomas et al.*, 1983b; *Reiter et al.*, 1983; *Jäger et al.*, 1984, 1991; *Clemesha and Simonich*, 1984). Figure 2.2 shows the backscattering profiles during the El Chichón perturbation with the inferred visible optical depth from *Jäger et al.* (1984). The ratio of extinction-to-backscattering can be used to infer absorption profiles in the atmosphere (*Bohren and Huffman*, 1983). *Brock et al.* (1993) show a comparison of lidar with *in situ* measurements from aircraft demonstrating that lidar backscatter is a good predictor for aerosol volume and mass, whereas satellite extinction measurements in the visible and near-infrared (NIR) can capture the aerosol surface area very well.

Lidar measurements, like all remotely sensed data, suffer from a number of uncertainties in underlying assumptions (see *Bohren and Huffman*, 1983, p. 442-443). For example, the aerosol size distribution-dependent reflection can be difficult to disentangle from concentration changes (*Hofmann et al.*, 1983). Through combinations of different wavelengths, the problems can be reduced to estimate physical properties. Under idealized conditions, the lidars can provide very accurate results and allow for 24h measurements since they are not dependent on the sun. Long-term series are available at different locations (e.g. Mauna Loa, *Hofmann and Rosen*, 1982; *Hofmann et al.*, 1983; *Dutton and Bodhaine*, 2001, see also Figure 2.3).
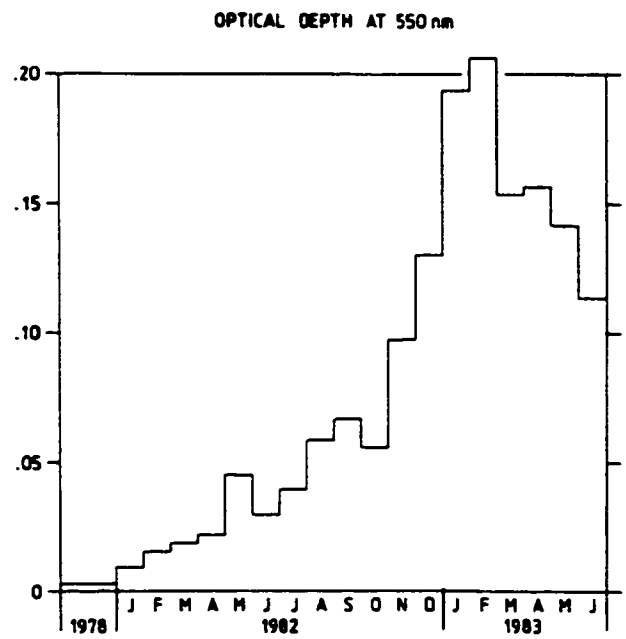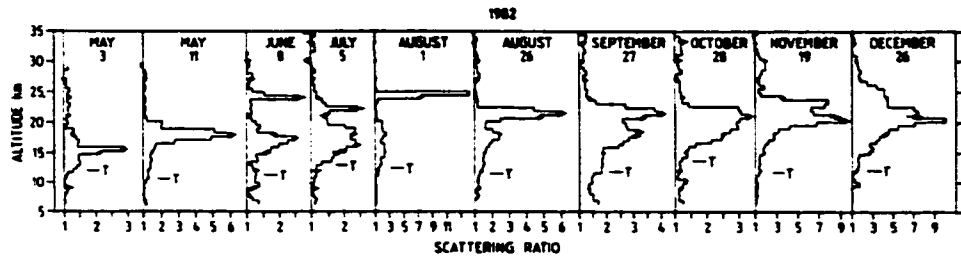
Figure 2.2: Top: Lidar profiles from Garmisch-Partenkirchen (Germany) during the El Chichón volcanic disturbance where elevated scattering clearly picks up sharp or massive aerosol layers. Note the changing scale between the different plots. Bottom: Plot of the inferred optical depth at mid-visible wavelength (0.5 μm) (*Jäger et al.*, 1984).

21
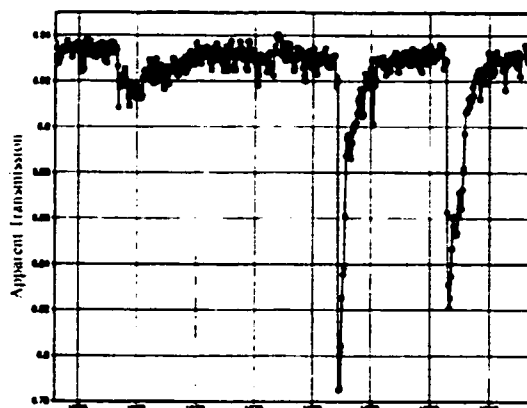
Figure 2.3: Atmospheric Transmission at Hawaii since early 1958 with a relatively small perturbation after Agung (1963) as only little mass was dispersed in the northern hemisphere, but much larger clouds are detected after the eruptions of El Chichón (direct ash cloud drifted over Hawaii!) and Pinatubo in 1991 (*Robock*, 2000).

2.2.3 Balloon- and Airplane-borne techniques

The best way of capturing aerosol properties is through *in situ* measurements from balloons or airplanes. *Bohren and Huffman* (1983, p. 439-440) describe techniques used to measure the critical values of backscattering with nephelometers and photo-acoustical measurements of absorption.

Another method is to actually sample the aerosol by collecting the particles, instead of using remote techniques. After large volcanic eruptions, filters and impact samplers captured large numbers of fluid particles (primarily sulfuric acids) in addition to the expected ash (*Mossop*, 1963, 1964). *Rosen* (1971), in an ingenious experiment, derived the concentrations of sulfate in water by heating the aerosol at the intake and comparing the temperatures of the boiling aerosol with the empirically calculated boiling points for different concentrations of sulfuric acid concentrations in water. He found that the aerosol was 75 wgt% sulfuric acid (H_2SO_4) and 25% water. This concentration also seemed to occur at other times and is now generally assumed to

be characteristic of all eruptions (*Toon and Pollack*, 1973; *Castleman et al.*, 1974; *Hofmann and Rosen*, 1984b; *Self et al.*, 1997a).

The evolution of the El Chichón cloud has been analyzed with *in situ* techniques, and the aerosol concentration and size variations have been shown in space (both vertically and horizontally) and time (*McCormick et al.*, 1983; *Hofmann and Rosen*, 1984a,c), although the spatial representation is loaded with uncertainties. Aerosol clouds, at least initially, spread in large elongated laminae instead of nicely diffusively mixed clouds. This can cause very large noise when sampling the aerosol during a flight. Later, the aerosol tends to be more evenly distributed. Particle counters and samplers were also applied to the Pinatubo cloud (*Deshler et al.*, 1997; *Pueschel and Kinne*, 1995; *Goodman et al.*, 1994) confirming remotely estimated chemical composition and size distributions. Figure 2.1 shows the evolution of the stratospheric aerosol size distribution as measured from an airplane with wire-impactors (*Goodman et al.*, 1994). Initially, only pre- volcanic aerosols of a small size (about $0.08\ \mu$m) were found. After the June 16 eruption of Pinatubo, slowly a larger mode ($> 0.1\ \mu$m) developed. This large mode accounted for around 30-40% of the total aerosol particles, but in terms of mass concentration the volcanic aerosol caused an increase of one to two orders of magnitudes (from initial values of about $0.03\ \mu$g/m^3). This bimodal size distribution dominated for more than two years, until the volcanic large mode disappeared.

2.2.4   Solar Radiometers and Pyrheliometers

A good source of data that reaches back into the past century is pyrheliometer measurements. The first long time series started around 1882 with observations in Montpelier, France and Berlin, Germany (*Stothers*, 1996b, and references therein). The French series is more widely in used, due to its better quality. The original goal of these instruments was to capture changes in the solar constant, not necessarily atmospheric particles. But very quickly, strong perturbations of the direct solar beam were recognized as having been caused by volcanoes (e.g., *Abbot*, 1902).
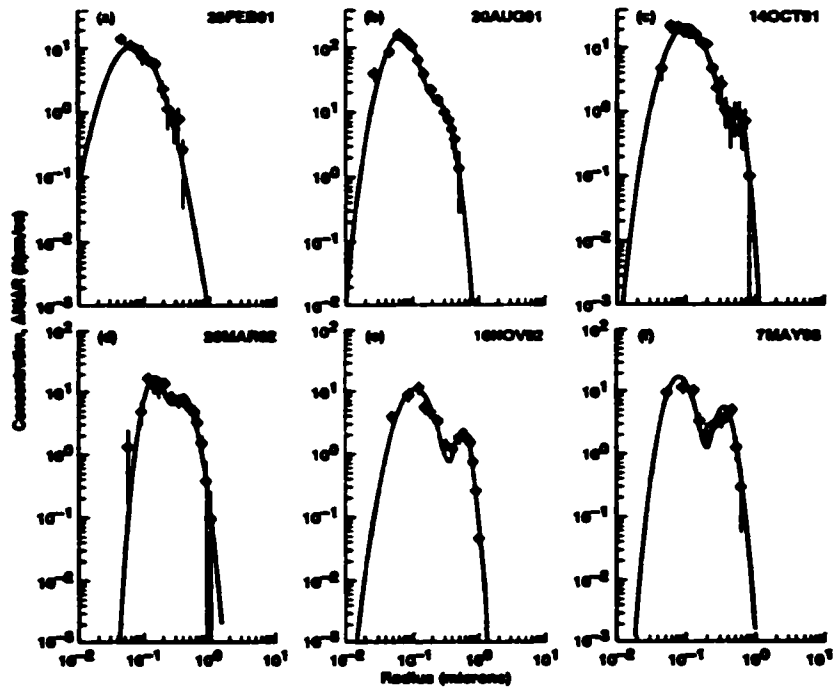
Figure 2.4: Aerosol size distribution from pre- to post-Pinatubo conditions from western North America. The growth of a large aerosol mode is clearly visible and continues into 1993 (*Goodman et al.*, 1994).

By the beginning of the 20th-Century, the first multi-spectral ('spectrobolometric') measurements were performed, allowing a look into the optical properties of the volcanic aerosol (*Abbot*, 1903; *Abbot et al.*, 1922; *Kimball*, 1924; *Kalitin*, 1926; *Abbot et al.*, 1932; *Kalitin*, 1938; *Volz*, 1975a; *Stothers*, 1997). Figure 2.5 shows the different atmospheric transmissions for 10 different wavelengths measured at Mount Wilson, California, during the strong perturbation from the 1912 Katmai-Novarupta eruption in Alaska. A particle perturbs the solar beam differently in each wavelength. The ratio of scattering efficiency (in Figure 2.5 the perturbation to normal transmission) between different wavelength can be used to compute the size distribution. This can be done using an assumption about the particles' composition (through refractive indices, here sulfuric acid in water solution is assumed) and type (liquid sphere) (*Stothers*, 1997, p. 6146). The measured scattering efficiency is then solely a function of the size parameter as shown by *Hansen and Travis* (1974). From these data *Stothers* (1997) concluded that the average size distribution stayed around 0.3 μm for at least two years. This is a slightly different behavior of the size distribution compared to Pinatubo, where the sizes grew to 0.5 μm and decayed later.

Long time series, up to the present day, allow for analysis of the evolution of transmission at a particular place, although careful correction of daily and seasonal cycles have to be performed. In addition, changing humidity and anthropogenic aerosols can perturb the picture. Examples of such series can be found in *Kimball* (1924), *Hand* (1937), *Pueschel et al.* (1972), *Hoyt* (1979), *Dutton and DeLuisi* (1983), *Dutton and Bodhaine* (2001) and others.

2.2.5 Sky polarization

Sky polarization is very sensitive to perturbations by volcanic particles (*Volz*, 1969). A linear relationship between the amount of decrease of the sky polarization and optical depth values over the mid-latitudes after the Krakatau eruption was recorded by *Cornu* (1885) and is described in more detail in *Stothers* (1996b)
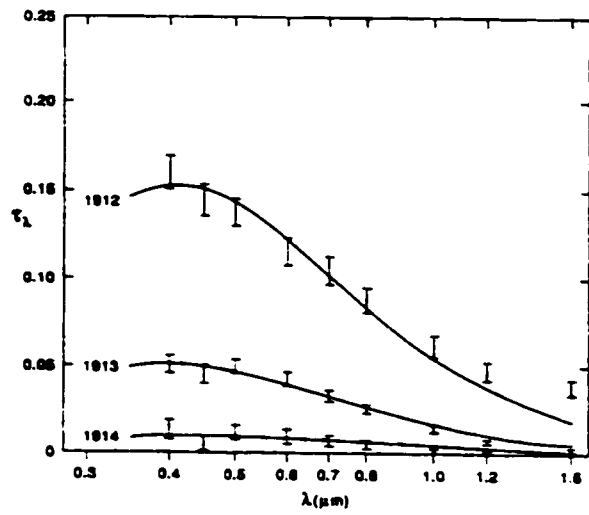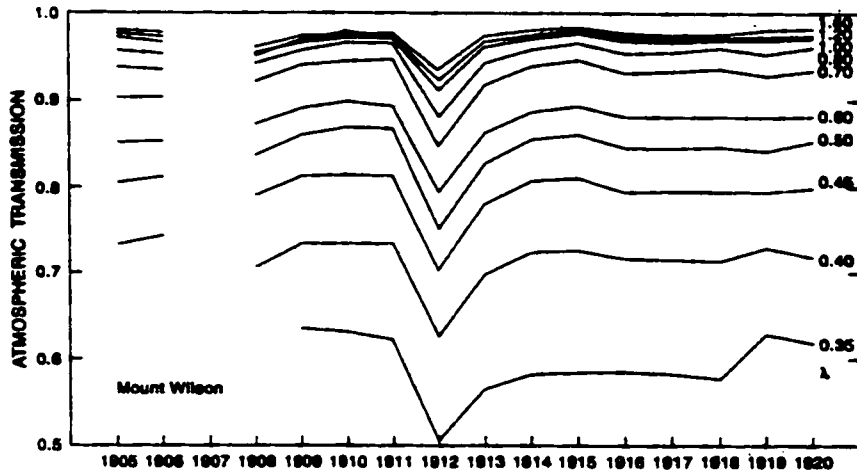
Figure 2.5: Spectrally dependent transmissions at Mount Wilson. California from 1905 to 1920 (top) and theoretical extinction-s fitted to pyrheliometric optical depth for peak Katmai-Novarupta perturbation in 1912 and two subsequent years (*Stothers*. 1997. bottom. from).

2.2.6 Lunar eclipse and stellar luminosity Observations

Although initially perhaps less intuitive, lunar eclipse observations, nonetheless, can provide reliable information regarding the global stratospheric loading of volcanic aerosol. *Keen* (1983, 1997) demonstrated that, for the interval 1960 to present, accurate measurements of the brightness of the eclipsed moon could be linked to the global optical depth as the solar radiation is refracted in the atmosphere into the earth shadow, but gets perturbed by the aerosol. This had already been proposed by (*Kepler*, 1604, p. 267-284). Detailed astronomical observations of the lunar brightness has been shown to be related to the global aerosol optical depth (*Matsushima et al.*, 1966; *Keen*, 1983, 1997), and is presented for the last 40 years in Figure 2.6. Since lunar eclipses are well documented, *Fisher* (1924) listed a number of these in relation to volcanic eruptions, covering the late 19th and early 20th-Century, including dark eclipses after Krakatau, 1883. Since about 1963, the 5 point *Danjon Scale* (a former Director of the Paris Observatory) measuring the amount of detail visible on the lunar disk with different sized telescopes (which turns out to be closely linked with the brightness of the moon) has been applied to observations from around the world. The results are commonly published in the Magazine *Sky and Telescope*, so that a continuous update will be available.

Since lunar eclipse events are rather unusual, lunar brightness anomalies have a good chance of being recorded in old diaries or logs. This is even particularly true when the moon almost disappears, as after large eruptions. A short list of particularly dark lunar eclipses is provided by *Hedervari* (1980) and *Link* (1961) : 1601, 1620, 1761 and 1816. The first can clearly be attributed to the large eruption of Huaynaputina, Peru in 1600 (*de Silva and Zielinski*, 1998), and the 1761 dark moon might have been caused by an eruption of Michoacan, Mexico in late November of 1759 and/or Makian, Indonesia in September 1760. The source of the 1620 perturbation is unknown. Although ice cores (see below) actually pick up a volcanic spike in 1619 in Greenland and in Antarctica, suggesting a large tropical eruption, the lunar eclipse in December 1619 was
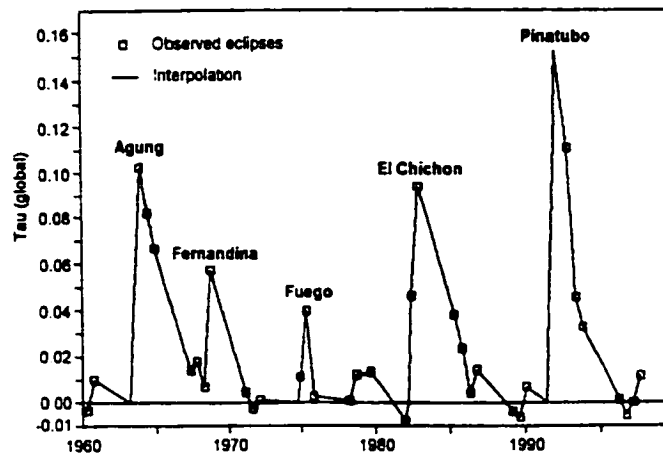
Figure 2.6: Global optical depth derived from the brightness of lunar eclipses (*Keen*, 1997)

reported as rather undisturbed (*Link*, 1961). The 1816 disappearance of the moon during the eclipse of June 10th can easily be attributed to the large eruption of Tambora in 1815. But there are also 'negative' results: the eclipse of 1783 was apparently not disturbed at all, despite the large aerosol mass ejected by the Laki eruption in Iceland. This could be explained by the large tropospheric and not stratospheric portion of the aerosol cloud (*Link*, 1961). One should also verify the path of the moon, which can favor perturbations in specific hemispheres.

Another technique is to directly measure the brightness of the stars. *Lockwood and Thompson* (1986) show stellar extinction for the periods after Agung (1963) and El Chichón (1982) in good agreement with other techniques.

2.2.7 Combined Indices

Compilations of data sets of measured or instrumentally-derived atmospheric optical depth are presented by *Sato et al.* (1993) and *Stothers* (1996b, 2001). A short summary is given here as they are a good basis for the derivation of a forcing data set for modeling purposes.

Sato et al. **1993** : Most widely used is the data set by *Sato et al.* (1993). They provide visible optical depth in a monthly resolution for different latitudinal bands from 1850 to 1990 (and updated to present: data available from GISS web page http://www.giss.nasa.gov/data/strataer/). Due to inhomogeneous source data over the whole time period. they separate the sequence into 4 periods.

The first. from 1850 to 1882. is not yet based on instrumental data. but is extrapolated from the relationship of derived optical depth during the subsequent instrumental period (1882 onwards) to the erupted volumes estimated in *Mitchell* (1970). Only a small number of eruptions are documented as important in this time interval. The largest is attributed to Cotopaxi. Ecuador in 1855-1856. although no modern records (see below: VEI and IVI) confirm this event. The dust veil reported in Lamb is probably from two rather large eruptions in far East Asia: Chikurachki. Kurile Islands (1853) and Sheveluch. Kamchatka (1854). both carry a VEI of 5 (*Simkin and Siebert*. 1994).

The second period of Sato et al. (1883-1959) includes the increasing record from pyrheliometric measurements with more reliable data since 1882. Although measurements in Arequipa. Peru. started already in 1912 (*Volz*. 1975a). the data are very discontinuous and difficult to use. Starting in 1920. the first good quality Southern Hemisphere station data are available for Mt. Montezuma. Chile. allowing for an extended spatial coverage. Previously. global extrapolations were done from the few series in the northern hemisphere. Especially for Krakatau the direct time series from the measurements at 44°N are used all over the globe (see Figure 3.5). The information about the 1895 Thompson Island eruption is not as stated in Sato et al. from *Dyer* (1974). but originally from *Lamb* (1967). where it is derived from temperatures at Punta Arenas alone. Since there is neither optical nor any ice core evidence (see below for description of ice core proxies) for this eruption. it seems rather uncertain.

The period 1960-1978 is then based mainly on extinction measurements from *Dyer and Hicks* (1968) and lunar eclipse data (*Keen*. 1983). The dominant eruption is clearly the relatively small.

but very sulfur rich eruption of Agung in 1963 (*Rampino and Self,* 1982). *Sato et al.* (1993) use the data provided by *Dyer and Hicks* (1968). although the eruption signal exhibits a rather unusual double peak, with actually largest optical depth in 1964. In the original publication. *Dyer and Hicks* (1968) comment on this strange phenomenon and attribute it to the very limited data in the tropics. No other single eruption is known to exhibit a double peak like this. Provided that no unknown eruption augmented the aerosol cloud, a more smoothed buildup and decay is more probable. The remainder of the 1960s is characterized by small but continuous loading. The main contributions probably resulted from Taal (1965). Awu (1966) and Fernandina (1968) with a remarkable caldera collapse very much in the style of Krakatau (*Simkin and Howard,* 1970). During the 1970s, the atmospheric perturbations originated mainly from Fuego (1974), as derived from *Keen* (1983).

Finally, the satellite period from 1979-1990 (later updated to present) contains excellent spatial and temporal coverage on a near global basis from SAM and SAGE instruments (see above), filled in with lidar and airplane-borne instruments. The limitation of these data is given by the saturation problems of the sensors by the strong perturbations from El Chichón (1982) and Pinatubo (1991). The values in Sato are calculated down to a level of 2 km above the tropopause and might therefore be closer to minimum optical perturbations rather than maximum. See also *Stenchikov et al.* (1998) and *Andronova et al.* (1999).

Stothers **1996b** The second period of *Sato et al.* (1993) (1883-1959) has been reevaluated in more detail by *Stothers* (1996b). Re-calibrating and comparing different data sources, the Stothers optical depth values exhibit significantly higher peak optical depth than the ones presented in *Sato et al.* (1993). Cross evaluation with sulfate mass from ice cores or in situ measurements was favorable. Additionally, the values are very homogeneous through time. Again, a good example for the differences can be seen for the Krakatau (1883) aerosol cloud (Figure 3.5).

In a recent paper *Stothers* (2001) reevaluated also the pre-satellite time period from 1961

to 1978. While qualitatively confirming the *Sato et al.* (1993) perturbations. he updated the temporal evolution of Agung significantly since *Dyer and Hicks* (1968). Yet, as in Sato, the Agung eruption is extraordinary in the way that the Southern Hemisphere saw about 4 times more aerosol optical depth than the Northern Hemisphere. Another change concerns the larger relative size of the well documented Fuego eruption (1974) (*Murrow et al.*, 1980; *Hofmann and Rosen*, 1977, 1980; *Volz*, 1975b; *Meinel and Meinel*, 1975; *Gras and Laby*, 1979; *Cadle et al.*, 1976; *Sedlacek et al.*, 1983) compared with the eruption of Fernandina (*Simkin et al.*, 1981; *Keen*, 1983).

Sato et al. (1993) and *Stothers* (1996b, 2001) are probably the most comprehensive data sets making use of available data. Major changes in the type and quality of the input data used by *Sato et al.* (1993) potentially introduce an artificial multi-decadal variation. This problem is already significantly reduced in *Stothers* (1996b, 2001). but limitations in the spatial coverage remain. To circumvent these issues of incoherent data coverage and to introduce the seasonal cycle, a simple model will be suggested below (see Chapter 3.3).

2.3 Documentary Data

Documentary data of volcanic aerosol clouds come in many forms. Some of earliest documents are discussed in *Stothers and Rampino* (1983). *Stothers* (1984b). *Rampino et al.* (1988) and *Self and Rampino* (1988). Of course, the most obvious sources are reports of the eruptions themselves. of complete darkness and of long-lasting strange dry hazes high up in the atmosphere (*Lamb*, 1970; *Stothers*, 1984b). More difficult to interpret are reports of colored sunsets. although the significant increase of such reports following large eruptions is well known (*Symons*, 1888; *Volz*, 1968; *Lamb*, 1970). Here. a few examples are presented to illustrate these data sources.

31

2.3.1 Times of Darkness

In the immediate vicinity of very large volcanic eruptions, it is a common observation that the sunlight is completely blocked. In fact, the larger the erupted mass, the larger the area that can encounter complete darkness over several days. Reports from Indonesia after the large Tambora eruption range from 19 to 72 hours of complete darkness (*Neumann van Padang*, 1971, cited in *Blong*, 1982). Figure 2.7 depicts the spreading ash cloud of Pinatubo in June 1991. Below the cloud, the sunlight was completely blocked, and ash rain caused tremendous damage. Because of the very strong impact of the ash on buildings and vegetation, such events have a good chance of getting recorded. Historical documents can help to date such events, and even oral histories can put some bracketing dates and estimates on big eruptions. A good example of the latter is demonstrated in *Blong* (1982), where oral histories of a 'time of darkness' were studied to estimate the large eruption of Long Island, a volcano off the eastern coast of New Guinea, some time in the mid-17th-Century. Another example is the reference in the *Book of Ancient Kings* (*Keys*, 1999, p. 253ff.), probably about an earlier eruption of Krakatau, though the exact date is unclear. Keys interprets it as corresponding to the year 536, responsible for the "*Mystery Cloud*", although the literal translation of the documented history would put it at least 100 years earlier.

2.3.2 Dry Fogs and Dust Veils

With increasing distance from the volcano, the aerosol cloud spreads out and large particles, mainly ash, fall out. If the cloud is still quite dense and contains a significant amount of large particles rather than a lot of small ones (*Paul and Jones*, 1951), the sun can appear in a strange blue or greenish color (though, according to *Bohren and Huffman* (1983), the optical effects are quite dependent on the actual size distribution). Blue sun and moon observations were very frequent after the large Krakatau eruption (*Symons*, 1888) which illustrates the density of the cloud and might additionally provide hints about the number of large particles. More attention
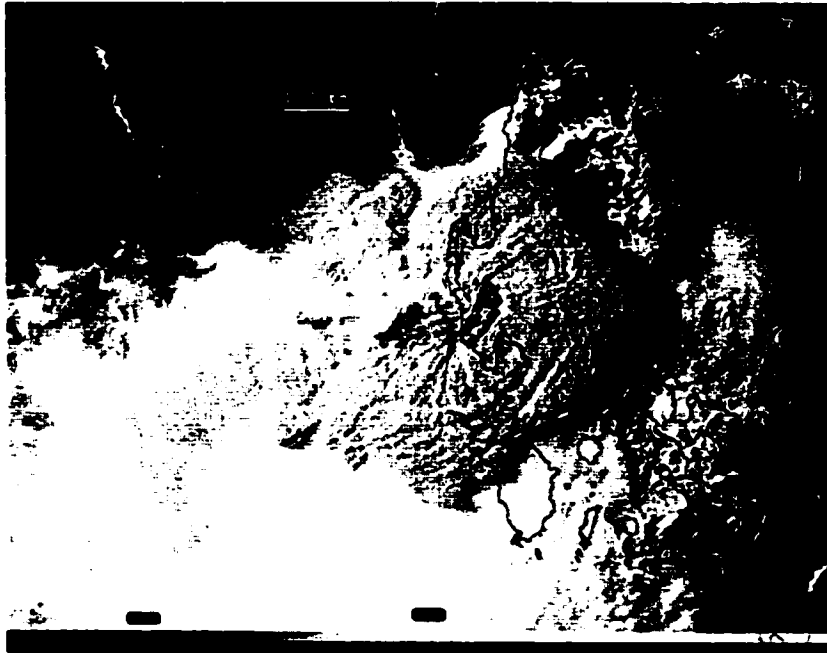
Figure 2.7: GMS visible satellite image roughly 16.40 local time on June 15. 1991. only a few hours after the paroxysmal Pinatubo eruption showing the spread of ash cloud quickly expanding beyond 100 km (*Self et al.*. 1997a).

to this will be given in Chapter 6.3.

The longer the time after the eruption, the more large and heavy ash will have been removed through sedimentation. Sulfuric acid droplets will start to dominate in the lower stratosphere. A whitish haze reducing the sunlight is commented on repeatedly in the past, and many of the hazes can actually be related to volcanic eruptions (*Symons*, 1888; *Lamb*, 1970). During the day, the sky can not reach its clear blue color, and sometimes the veil is so thick that

> "the sun was dark and its darkness lasted for eighteen month: each day it shone for
>
> about four hours, and still this light was only a feeble shadow...the fruits did not ripen
>
> and the wine tasted like sour grapes" (probably John of Ephesus, cited in *Stothers*,
>
> 1984b).

It is well known that, although the direct solar beam can be strongly perturbed, the indirect (or diffuse) skylight increases substantially due to the multiple scattering (*Dyer and Hicks*, 1968; *Baker et al.*, 1984; *Minnis et al.*, 1993). This effect is described in more detail below (Figure 5.12 and corresponding text).

The literature often credits Benjamin Franklin and his comments in May 1784 as the first to link the "dry fogs" and subsequent climatic anomalies with a volcanic eruption (*Franklin*, 1785). He noted:

> "During several of the summer months of the year 1783, when the effect of the sun's
>
> rays to heat the earth in these northern regions should have been greater, there existed
>
> a constant fog over all Europe, and great part of North America. This fog was of
>
> a permanent nature: it was dry, and the rays of the sun seemed to have little effect
>
> towards dissipating it, as they easily do a moist fog, arising from water. They were
>
> indeed rendered so faint in passing through it, that when collected in the focus of a
>
> burning glass they would scarce kindle brown paper." (*Franklin*, 1785)

This passage relates to the large Laki-Grimsvotn eruption on Iceland. The eruption ejected

roughly 122 Mt of SO_2, or about 250 Mt of H_2SO_4, over a period from June 8 to the end of November 1783 (*Thordarson et al.*, 1996). Others estimate the emissions to be somewhat lower (*Devine et al.*, 1984; *Clausen and Hammer*, 1988; *Fiacco et al.*, 1994; *Stothers*, 1996a). Franklin then linked the effects of the fog to the unusually frigid winter of 1783-84.

Still of unknown origin is the above mentioned 'Mystery Cloud' of 536 A.D. (*Stothers*, 1984b; *Rampino et al.*, 1988; *Baillie*, 1994; *Cole-Dai et al.*, 2000), although *Keys* (1999) hypothesizes an eruption of Krakatau, in the Sunda Strait. The dating of the large Krakatau eruption, which Keys envisions to be responsible for the haze and that formed a massive caldera of 7 km diameter beyond the 1883 rim, is too poor to be conclusive. A more probable source is an eruption of Rabaul, New Britain (VEI=6), radiocarbon dated at 540 AD.

Dust Veil Index (DVI) A large collection of reports of eruptions, dust veils and related phenomena were compiled by H.H. Lamb to generate an index, the *Dust Veil Index (DVI)* (*Lamb*, 1970, 1977, 1983). In his landmark paper (*Lamb*, 1970), he made use of earlier collections of information (e.g. R. Russell in *Symons*, 1888; *Sapper*, 1927, and others), and weighted the events according to their estimated volume erupted into the atmosphere, the depletion of the direct solar radiation, and the impact on surface temperature. The temperature criterion generated criticism because it caused circular argumentation. But *Robock* (1981) showed that when the events purely based on temperature perturbations were removed, the overall picture did not change significantly. In Figure 2.8, the DVI since 1500 shows the major volcanic events scaled to a DVI of 1000 over 4 years for the eruption of Krakatau. As can be seen in this plot, there are periods of higher activity and others with significantly less. The first half of the 20th-Century (after 1912) is almost without eruptions, but is followed by a rather active phase beginning with Agung in 1963. In the late 1960s and 70s, the link from volcanic eruptions to climate was quite popular, as intermittent glacial advances signaled an episode of cooling. Since the volcanic activity increased at the same time, the influence of volcanoes on climate was studied intensively

35
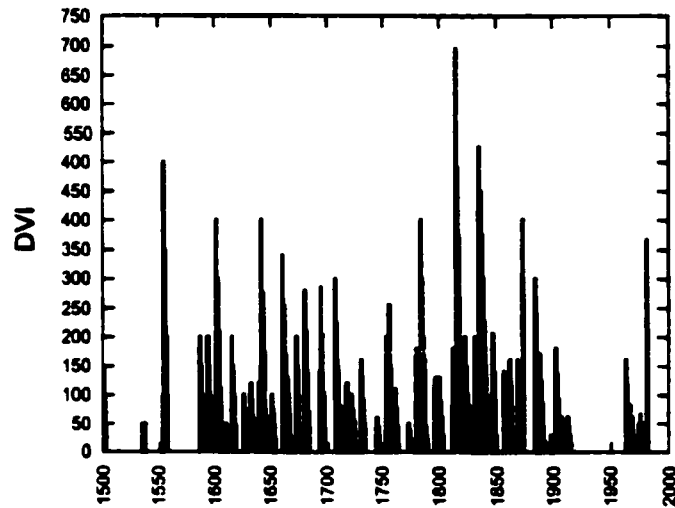
Figure 2.8: The *Lamb* (1970, 1977, 1983) Dust Veil Index modified for decay of aerosol loading over 1 years (*Bradley and Jones*, 1995b)

(*Schneider and Mass*, 1975; *Baldwin et al.*, 1976; *Oliver*, 1976; *Pollack et al.*, 1976; *Bray*, 1976; *Kelly*, 1977; *Robock*, 1978; *Bradley and England*, 1978a,b; *Robock*, 1979; *Porter*, 1986) (see also remarks in *Kelly et al.* (1998) on the circumstances prior to Lambs' publication). Subsequently, other volcanic timeseries, some quite similar to Lamb's, were generated (*Mitchell*, 1970; *Oliver*, 1976; *Schönwiese and Cress*, 1988).

2.3.3 'Fire in the Sky' : Colored Sunsets and Purple Skylight

When volcanic particles are small compared to the visible wavelength, they enhance the extinction of the blue part of the spectrum, increasing the 'reddening' of the remaining light. This is especially the case for low solar angles, causing brilliant red and orange sunsets. After some volcanic eruptions, the sunsets can get so intense that the sky appears on fire. After the eruption of Krakatau in 1883. *Hazen* (1884) reports that on October 30th, the sunset colors were so unusually spectacular and brilliant that "fire engines were summoned at Poughkeepsie [New

York] and New Haven [Connecticut] to quench the burning skies". Some of these impressions can be seen in the famous paintings of Krakatau sunsets of late 1883 by Ashcroft.

After several month to a year, these sulfuric acid clouds can become very smoothly spread over the globe and be diminished so that they are barely recognizable from the ground. Only during very low solar angles is the reflection (and sometimes some fine structure in the aerosol layer) visible. Very impressive red sunsets are a common phenomenon after large eruptions, and pink to purple skies can be seen long after sunset (*Symons*, 1888: *Volz and Goody*, 1962).

If one looks at the distribution of unusually increased sunset colorings during the early 19th-Century with perturbation of an unknown volcano during 1809/10 and then especially Tambora during 1816 (see Table 2.1), it appears that colored sunsets can also be suppressed if the aerosol loading is too high. This was described by *Stothers* (1996b) and put at an optical depth level of 0.16 or 0.17. Other examples of this phenomenon are Laki (1783). Krakatau (1883), and maybe Santa Maria (1902), and Katmai (1912) (*Stothers*, 1996b), although in the latter two cases, the seasonal variation of the aerosol concentration in the mid-latitudes might have played a role, as the colored sunsets disappeared (see below).

1810	4	1816	5
1811	33	1817	18
1812	17	1818	23
1813	31	1819	2
1814	21	1820	2
1815	24		

Table 2.1: Number of days per year where red sunsets, luminous twilights were noted by Howard, in (*Symons*, 1888, p. 402)

2.3.4 'Crows and Eggs in the Sun' : Bare eye sighted sunspots

There are repeated bare eye observations of sunspots in the rising or setting sun when large volcanic perturbations were present (*Stommel and Stommel*, 1983). *Deirmendjian* (1973) estimates that the minimum visible optical depth required for this is about 0.63, which is substantial and should therefore only apply to very large eruptions and potentially even only these with a significant amount of ash involved. These observations can, therefore, not help as an index of volcanic perturbation, but help to bracket the aerosol properties or magnitude. A long list of Chinese records exist. Here are three excerpts:

> 42 BC. May 5 / Jun 3 (China) : "The sun was whitish blue in color and cast no shadows. Right at its center, there were frequently shadows and no brilliance. That summer was cold until the 9th month, when the sun regained its brilliance."

> 188 AD. Feb 15 / Mar 15 (China): "The sun was reddish-yellow (orange) in color, and on it there was a black vapor like a flying magpie. After some months it gradually faded away".

> 1258 AD. SEP 15 (Korea): "Within the sun there was a black spot as large as a hen's egg. The next day (Sep 16) there was another one shaped like a man". (*Yau and Stephenson*, 1988)

Although these reports are almost randomly recording sunspot sightings, and don't include information about the zenith angle of the sun (below 5°over the horizon, no large perturbation is needed to make sunspots visible. *Stothers*, 1984a), their numbers can increase dramatically when the atmosphere is disturbed by a strong haze, as after volcanic eruptions. All observations shown above might have been supported by well known volcanic perturbations.

2.3.5 Other indicators

Other phenomena related to high level hazes and dust are Bishop rings (*Bishop*, 1884). These reddish to brownish rings surrounding a bright patch, with the sun at the center, were first described in detail after the eruption of Krakatau (*Symons*, 1888; *Deirmendjian*, 1973). They have since also been documented after eruptions in 1890, 1902, 1912 (*Stothers*, 1996b), 1963 (*Volz*, 1970), 1974, 1982 (*Meinel and Meinel*, 1983) and 1991 (*Sassen et al.*, 1994). The aerosol size distribution in these cases must have been close to a median particle radius of $0.6 - 0.9\mu m$ (*Deirmendjian*, 1973; *Sassen et al.*, 1994), and therefore at the larger end of observed distributions. Bimodal aerosol clouds are possible. These common phenomena might be a good proxy, but are not really recorded prior to Krakatau. Other halo effects might be related, but the lack of attributes, like the red color and the unusual radius ($11-23°$), makes it very difficult to distinguish halo observations in volcanic clouds from effects seen in cirrus and cirrostratus covers.

Although not generally precise in a quantitative way, these indices demonstrate the usefulness of documentary data to identify the periods of volcanic perturbations in the atmosphere, and in some cases to help bracket the atmospheric perturbation or optical properties (colorful sunsets, Bishop rings). Although quite patchy for smaller eruptions, they are in good agreement for the large events. Additionally, they help us to understand the impact of these eruptions on the cultures, a dimension not reflected in any other archive. From the failures of harvests to the occurrence of plagues (*Stothers*, 1999), the influence of the high-level veils covering the sun and reducing its strength can be substantial.

2.3.6 Years without a summer

As has been demonstrated extensively (*Bradley*, 1988; *Robock and Mao*, 1992; *Groisman*, 1992; *Graf et al.*, 1993; *Robock and Mao*, 1995; *Mao and Robock*, 1998; *Kirchner et al.*, 1998), the winter season over the higher latitudes might actually warm after large volcanic eruptions, despite a

39

clearer cooling during summer. Therefore, *years without summers* (*Stommel and Stommel,* 1983) are good candidates for years with strong volcanic perturbations. In fact, in a catalogue of weather extremes from central Europe (*Pfister,* 1999), 5 years are listed as exceptionally cool during the summer months (and therefore labeled as years without summer), including 1529, 1618, 1675, 1813 and 1816. Only 1529 cannot be readily attributed to a known large volcanic eruption. In the case of 1813, a series of eruptions might have been responsible for the cool summer. Snowfall events into the lowlands in the middle of summer, very late flowering of trees (e.g. the famous cherry blossoming in Japan), or destroyed harvests from frost are some of the related aspects of a 'missing summer'.

The most famous of the years without summer is clearly the year 1816, one year after the enormous Tambora eruption in Indonesia. Detailed descriptions can be found in *Stommel and Stommel* (1983), *Post* (1977), *Harrington* (1992) and *Chenoweth* (1996). Interestingly, the unusual cooling effects do not appear globally, but exhibit a regional pattern. As can be seen in Figure 2.9, the dramatic cooling in Western Europe is accompanied by a warming in Eastern Europe. The reason for these alleged 'inconsistencies' is investigated in Chapter 6.4. In the case of 1816, one has to keep in mind that the preceeding years had already been under substantial influence of volcanic perturbations since 1809 (*Legrand and Delmas,* 1987; *Dai et al.,* 1991) from a still unknown volcano.

As climate is inherently variable, the recognition of a volcanic signal in local to regional climates is not easy. When looking at vegetation-based proxies like tree rings, harvest statistics, or phenological data like flowering times of certain plant species, one needs to remember that a single cold front at a sensitive moment can strongly perturb the plants, although the average summer temperature was rather normal. During the summer of 1816, at least three distinct cold air outbreaks were recognized in eastern North America (Baron in *Harrington,* 1992). In mountainous areas, it is also not unusual that 'years without summers' are followed by flooding due to additional snowmelt (*Pfister,* 1999). The snowmelt during 1817, the year after the *year*
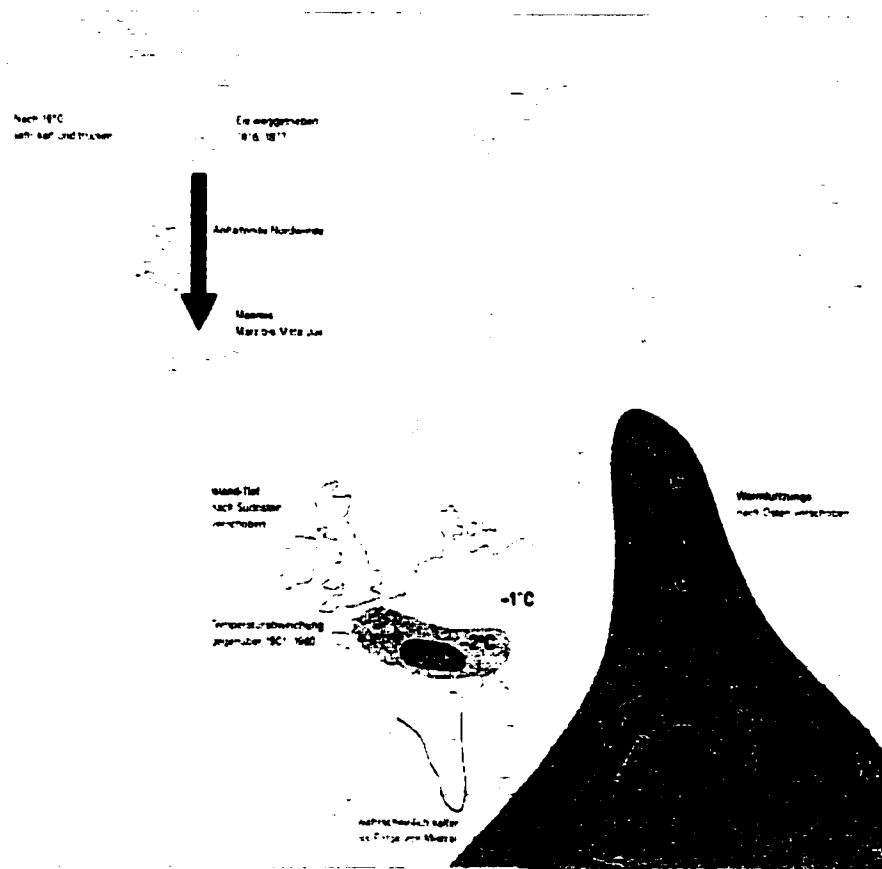
Figure 2.9: Reconstructed surface temperature anomalies based on documentary data for summer 1816 in Central Europe with marked cooling in western Europe but warming to the east (*Pfister.* 1999).

without summer caused dramatic floods in Switzerland and Germany.

Another example of delayed impacts are plague epidemics stimulated by cool and wet summers followed by rather warm winters (*Stothers*, 1999). This delayed process is not unusual and only exemplifies the problems when interpreting the indirect effects of climate on society. In the same way, most people who died as a result of the Tambora eruption in 1815 did not perish due to the direct eruptive processes, but due to starvation in the subsequent famine (*Simkin et al.*, 2001), as all vegetation was heavily damaged by the ash and released acids. [For extreme interpretation of delayed effects see *Keys* (1999).]

In general, while vegetation-based proxies might be a very good index on where and when to search for disturbances, they cannot by themselves be used conclusively. For example, the 1991 failure of wine in the French Bordeaux region is not due to the Pinatubo effects, but due to frost in April, two month prior to the eruption. The failure in the following year (1992), on the other hand, might have had significant contributions from the volcano (*Spellman*, 1999).

2.4 The volcanologic record

Observations of volcanic eruptions range far back in time. During the Antiquity, the volcanoes of Stromboli and Etna on the island of Sicily were very well known active volcanoes. In fact, the regularity of eruptions at Stromboli led to its use as a natural light house. Etna also caused repeated turmoil as it sent down long flows of lava. Another volcano in Italy gained even more fame: with its eruption in 79 A.D., Vesuvius buried the settlements of Pompeii and Herkulaneum, killing thousands of people. After the rediscovery of these towns in the mid 18th-Century, perfectly preserved snapshots of Roman life were unearthed.

Many catalogues exist (*Symons*, 1888; *Sapper*, 1927; *Shaw*, 1936; *Humphreys*, 1940; *Lamb*, 1970; *Mitchell*, 1970; *Oliver*, 1976; *Hirschboeck*, 1980; *Simkin et al.*, 1981; *Newhall and Self*, 1982; *Goodman*, 1984; *Simkin and Siebert*, 1994), though they are often at least partially based on the

same sources. They all exhibit the strong trend in increasing observations since about the middle of the second Millennium AD. Some are purely volcanologic in character, others add additional information, such as veils in the mid-latitudes, that can be related to a reported eruption in some location on the globe. Here, two aspects of volcanologic records are presented. The extended Volcanic Explosivity Index (*Newhall and Self*, 1982), as published in the Smithsonian Volcanic Catalogue (*Simkin et al.*, 1981; *Simkin and Siebert*, 1994), is the ultimate register of volcanic activity during the Holocene. Then, a technique (rather than an index) is briefly mentioned as an example of how properties of an eruption (or fingerprint thereof) can potentially be found in deposits at the other end of the globe.

2.4.1   Volcanic Explosivity Index (VEI)

Newhall and Self (1982) designed a purely volcanologic explosivity index that should measure the magnitude of an eruption. No climatic parameters were used, and even the criterion of 'stratospheric injection' of gas or ash is basically lowest in priority of nine distinct parameters. The record is continuously updated to the present day and cleared of errors (*Self and Rampino*, 1988), with *Simkin and Siebert* (1994) being the most up-to-date. Table 2.2 shows the scale of the VEI from 0 to 8 with the defining criteria. Note in the lowest row how quickly large eruptions decrease in numbers. The eruptions range from the smallest eruption recorded (an accidental 'man made' eruption of 1.5 m^3 of lava during a hydrothermal drilling operation, *Decker and Decker* (1991)) to the enormous flood basalt events, like Roza (4000 km^3, *Decker and Decker* 1991, about 14 million years ago) or the explosive Toba event about 72.000 years ago (estimated volume of 2700 km^3, *Rose and Chesner* 1990; *Rampino and Self* 1992, 1993; *Zielinski et al.* 1996b). Note: the Smithsonian Catalogue only includes eruptions of the Holocene. Among those, the largest VEI achieved is 7, containing eruptions of Tambora (1815), Baitoushan (1050), Kikai (4350 BC) and Crater Lake (4895 BC).

The VEI has been used as a index for volcanic forcing, although *Pollack et al.* (1976), *Rampino*

43

	0	1	2	3	4	5	6	7	8
General Description	Non-Explosive	Small	Moderate	Moderate-Large	Large	Very Large			
Volume of Tephra (m^3)	1×10^4	1×10^6	1×10^7	1×10^8	1×10^9	1×10^{10}	1×10^{11}	1×10^{12}	
Cloud Column Height (km) Above crater / Above sea level	<0.1	0.1-1	1-5	3-15	10-25	>25			
Qualitative Description	"Gentle,"	"Effusive"	"Explosive"	"Cataclysmic," "paroxysmal," "colossal" / "Severe," "Violent," "terrific"					
Eruption Type (see fig. 6)	Strombolian / Hawaiian	Vulcanian	Plinian / Ultra-Plinian						
Duration (continuous blast)	<1 hour / 1-6 hrs / 6-12 hrs	>12 hrs							
CAVW max explosivity (most explosive activity listed in CAVW)	Lava flow / Dome or mudflow	Phreatic	Explosion or Nuee ardente						
Tropospheric Injection	Negligible	Minor	Moderate	Substantial					
Stratospheric Injection	None	None	None	Possible	Definite	Significant			
Eruptions (total in file)	868	845	3477	868	278	84	39	4	0

Table 2.2: Criteria for VEI attribution. from *Newhall and Self* (1982) and *Simkin and Siebert* (1994).

and Self (1982), *Sigurdsson* (1990) and others have pointed out that it is not necessarily the volume and violence of the eruption that impact climate. but rather the gaseous components that form small, optically effective liquid particles in the stratosphere. These can remain aloft for months and years. Today, the VEI is more commonly used as a reference for the style of the eruption. and. together with the Smithsonian Catalogue. form the ultimate lookup table and reference list.

2.4.2 Petrologic sulfur estimates and chemical fingerprinting

A direct method of measuring the amount of sulfur released by an eruption can be estimated from gaseous inclusions in juvenile volcanic glass (*Devine et al.*. 1984; *Palais and Sigurdsson*. 1989). Two opposing factors need to be kept in mind. *Rose* (1977) pointed out that ash can effectively scavenge sulfuric acid aerosol. and *Tabazadeh and Turco* (1993) confirmed the same

for chlorine through very fast dissolution in the condensating water vapor in volcanic columns. Therefore, a significant amount of these chemical species are removed before or immediately after entering the stratosphere. Comparison of sulfate fluxes on ice sheets with the derived sulfur emissions from gaseous inclusions have shown large differences. While ice core derived sulfate estimates of a 'global' aerosol from Agung would amount to 40 Tg (*Legrand and Delmas*, 1987, using a hemispheric bias correction factor of 0.66), 53 Tg (*Delmas et al.*, 1992, no hemispheric correction) and 42 Tg (*Cole-Dai and Mosley-Thompson*, 1999) [all values multiplied with 1.33 to get to a 75% wt. sulfate in water concentration], the gaseous inclusions point to a minimum value of only 4 Tg of sulfate (*Devine et al.*, 1984; *Self and King*, 1996). Although known as only a minimum estimate (*Rose*, 1977), *Self and King* (1996) conclude that the petrologic method could underestimate the sulfur emissions by up to two order of magnitudes.

New studies looking into additional sources of sulfur that would not be represented well in the petrologic method (so called "excess sulfur") suggest hydrous fluids at the top of the magma chamber. These fluids are not in communication with the deeper chamber, and the sulfate is released early on in an eruption as pre-eruptive vapors (*Gerlach*, 1993; *Gerlach et al.*, 1994; *Wallace and Gerlach*, 1994; *Keppler*, 1999).

While being a clear minimum estimate, the technique can be used in an adjusted form as a chemical fingerprint analysis. *Palais et al.* (1990) show that it is a powerful tool for identifying source volcanoes, after finding volcanic deposits in polar ice cores. Previously mis-attributed eruptions can be recognized and then corrected. In this way, *Palais et al.* (1990) demonstrated that the two major sulfate spikes in the Dome C ice core, Antarctica, previously attributed to Tambora and Galunggung (*Legrand*, 1987) were actually from the now famous, yet still unknown eruption in 1808/09 (*Dai et al.*, 1991) and the 1815 Tambora eruption. Similarly, an eruption prior to Huaynaputina (1600) is probably attributable to Nevado del Ruiz (1595). Although the chemical composition of the very large 1258/1259 event resembles the 1980 El Chichón composition (*Palais et al.*, 1990), *Espindola et al.* (2000) find diverging calibrated dates of the

45

deposits in the vicinity of El Chichón. pointing to an eruption of El Chichón about 50 to 100 years later. Clearly, more needs to be done in this promising field.

2.4.3 Tephrochronologies

Tephrochronologies are used as stratigraphic time markers in areas of active volcanism. They are usually of local to regional importance. although markers of sulfate and ash in ice cores have gained wide acceptance. Fingerprinting of volcanic eruptions in ice cores. a very specific application of a tephrochronology. uses ash. especially volcanic glass. in analyses of the major chemical constituents (*Devine et al.*, 1984; *De Angelis et al.*, 1985; *Palais et al.*, 1990). The very small Reynolds number of these micron-sized glasses makes them good atmospheric transport tracers. Since some prominent layers in sulfate or ash deposition can be used for synchronization and age control. detailed chemical fingerprinting can confirm that the correct corresponding layers are used.

2.5 Ice core record

Large explosive volcanism can inject significant amounts of material into the lower stratosphere. *Pollack et al.* (1976). *Rampino and Self* (1982) and *Sigurdsson* (1990) have shown that. in order to influence climate. it's not the total mass but mainly the amount of sulfuric acid from the eruption that causes the climatic impact. They showed that relatively smaller eruptions like Agung in 1963. can emit very large amounts of sulfur (probably about 20 Tg of aerosol from about the 0.5 km^3 dense rock equivalent [DRE] erupted volume). In the stratosphere. small particles of sulfuric acid are formed primarily from condensation of SO_2 gas through oxidation and going into solution with water. The aerosol is small enough to remain suspended for many months. The average e-folding time is around 1 year. during which time the aerosol is transported poleward and downwards. Once entering the troposphere. the sulfuric acid is quickly washed out by rain

and snow. Over the polar ice sheets. it can get deposited and stored in the annual snow layers. By drilling into the polar ice. the sulfuric acid deposits can be measured (*Hammer*. 1977: *Hammer et al.*. 1980: *Legrand and Delmas*. 1987: *Clausen and Hammer*. 1988: *Delmas et al.*. 1992: *Zielinski et al.*. 1994: *Zielinski*. 1995: *Langway et al.*. 1995: *Zielinski et al.*. 1996a: *Cole-Dai et al.*. 1997a: *Clausen et al.*. 1997: *Stenni et al.*. 1999: *Cole-Dai et al.*. 2000). Several techniques are used to recover the volcanic signal. such as the electric conductivity. either of solid (*Hammer et al.*. 1980) or liquid samples (*Hammer*. 1977). acids (*Clausen et al.*. 1997). or by directly identifying sulfate species (*Legrand and Delmas*. 1987: *Mayewski et al.*. 1990). In order to obtain quantitative information of the volcanic forcing. several issues need to be resolved.

1. As many cores as possible must be analyzed in each hemisphere. In a single core. only about two thirds of the large eruptions are generally recorded (*Zielinski*. 1995). and additionally. each technique has its own problems of contamination of the volcanic signal (*Delmas et al.*. 1985).

2. The deposits need to be corrected for distance to the source volcano and for the transport mechanism of the aerosol. Volcanoes in the close vicinity of the ice sheet can leave a comparably larger signal than eruptions on the other side of the globe. Also. stratospheric transport has to be separated as much as possible from much more immediate tropospheric transport. where the material is immediately removed from the atmosphere. This separation is not easy.

3. Additional correction of the sulfate fluxes to snow accumulation rate. which differs substantially between sites (*Dai et al.*. 1991).

4. To compute the global forcing. *Hammer et al.* (1980) and *Clausen and Hammer* (1988) introduced a calibration that makes use of the large nuclear tests performed in the late 1950s and early 60s. During these tests. known amounts of radioactive isotopes were released and later deposited onto the ice sheets. Comparing the deposited mass flux (kg per km^2) with

47

the original amount produced in the tropics allows for an analogous calibration of the volcanic sulfate. Using an independent data set of atmospheric visible optical depth for calibration (e.g. *Sato et al.*, 1993), and assuming that all aerosol is of the same size and composition (see discussion below), each sulfate spike in the ice can be associated with an atmospheric optical depth, and therefore a direct forcing can be estimated. It turns out that roughly 0.1% of the total released mass is transported in the stratosphere and reaches the poles (*Pourchet et al.*, 2000).

Robock and Free (1995) and *Robock and Free* (1996) produced a multi-core volcanic index using eight Northern- and six Southern Hemisphere ice cores. They calibrated the volcanic optical depth similar to *Zielinski* (1995) for each core and averaged the computed forcing across the available cores. Although this technique only provides annual data, it is probably the most appropriate volcanic forcing data set directly derived from proxy data for climate modeling beyond the last century. But there are two important issues one needs to keep in mind. First, because of the limited spatial and temporal resolution, no seasonal distribution of the aerosol clouds is provided. Due to the exponential decay of the aerosol cloud, the atmospheric forcing could be very sensitive if a certain amount of sulfate of year x is deposited in one month compared to with much smaller fluxes over the whole year. A parameterization of the buildup and decay could add significant detail. The second important aspect concerns the the underlying assumption that the atmospheric optical depth is a direct function of the sulfate deposition as seen in the calibration time period (they use *Sato et al.* 1993). *Stothers* (1997) pointed out that the eruptions during the 20th-Century have not exhibited the exact same aerosol size distributions. Pinatubo aerosol, for example, grew from very small number to about 0.8 μm, where as El Chichón sulfates remained in the range of 0.3 − 0.4 μm (*Russell et al.*, 1996). For now, a constant treatment of the sulfate mass vs. optical depth (through aerosol composition and size distribution) is a valid approximation, but as will be shown below, that there is a potential bias in this assumption (see Chapter 6.3).

2.5.1 Sulfur isotopes

Isotopic composition of the sulfate has been analyzed from airplane sampling (*Castleman et al.*, 1974; *Rye et al.*, 1984) and more recently in Antarctic ice cores by *Patris et al.* (2000). It has been shown that volcanic sulfate can be distinguished from biogenic sulfate, thus opening a way to evaluate the volcanic contribution to the total sulfate.

2.5.2 Chlorines

Due to complicated chemical activity (*Solomon*, 1999; *Fahey et al.*, 1993), little is known about other chemical substances injected into the stratosphere. Chlorine could potentially be important in influencing stratospheric ozone concentrations (*Stolarski and Cicerone*, 1974; *Symonds et al.*, 1988; *Zerefos et al.*, 1994; *Angell*, 1997a). The chlorines, although sometimes ejected in very large quantities (for Tambora on the order of 10^{11} kg, *Sigurdsson and Laj*, 1992), generally cause only a small disturbance to the background loading (which is mostly of oceanic origin) in the atmosphere (*Mankin et al.*, 1992) and as found in ice cores (*Delmas et al.*, 1992; *Cole-Dai et al.*, 2000), suggesting that chlorine is scavenged out very quickly. This presumably happens efficiently in the rising volcanic plume, where large amounts of water vapor condense (*Tabazadeh and Turco*, 1993; *Turco et al.*, 1993). Also, ash can act as a scavenger, adsorbing and then removing chlorine through fall out (*Rose*, 1977; *De Angelis and Legrand*, 1994). The only exceptions, where large amounts of chlorine can be found in ice cores, may be due to deposition of tropospherically rather than stratospherically transported volcanic debris. *Hammer et al.* (1980). *Herron* (1982) and in much detail recently, *Clausen et al.* (1997) found exceptional amounts of chlorine in the GRIP ice core in the Katmai-Novarupta (1912) and Eldgja (934) deposits, all of which had a substantial tropospheric contribution. Nevertheless, *Stolarski and Butler* (1978) estimated, that a Krakatau-sized eruption could deplete ozone by almost 7%. Since Tambora emitted roughly 200 times the chlorine mass of Krakatau (*Sigurdsson and Laj*, 1992), an impact on

ozone would be quite possible. The eruption of El Chichón, a volcano underlain by a large salt dome, initially elevated the number of solid halite particles in the lower stratosphere (*Woods and Chuan*, 1983). *Mankin and Coffey* (1984) also report increased column amounts of gaseous HCl during the following months, probably originating from the erupted magma as well as from the halite (*Woods et al.*, 1985). Further investigations are needed, especially since the chemistry in the present anthropogenically perturbed stratosphere and for pre-industrial conditions are not necessarily the same (S. Solomon, personal communication).

2.6   Tree Ring data

Trees are very good proxies for climatic perturbations in relation to volcanic eruptions (*LaMarche and Hirschboeck*, 1984; *Lough and Fritts*, 1987; *Jones et al.*, 1995; *Briffa et al.*, 1998). Since the impact from volcanic perturbations on climate is most pronounced during the warm season (*Robock and Mao*, 1992, 1995) and because tree growth is very sensitive to climatic conditions during the growing season, especially at high latitudes and high elevations, it is not surprising that trees have a high potential to record these events quite accurately. However, not all trees and not in all regions respond the same way to environmental pressure. Some are more sensitive to stresses from the lack of precipitation, others, like those close to the upper tree line, are responding to temperature fluctuations. Also, different techniques exist to extract a climatic signal, such as looking at the ring width or at cell densities. Two excellent books present these techniques in detail: *Cook and Kairiukstis* (1990) and *Schweingruber* (1996). Here I shall focus only on some aspects related to volcanic perturbations from some recent work.

In a 600-year long series of Northern Hemisphere temperatures reconstructed from late wood density from 383 tree rings chronologies around the Northern Hemisphere (*Briffa et al.*, 1998), there are negative anomalies significantly below the the rest of the data (see Figure 2.10). Most of these years (note: mainly the warm seasons) are also years with or years following strong
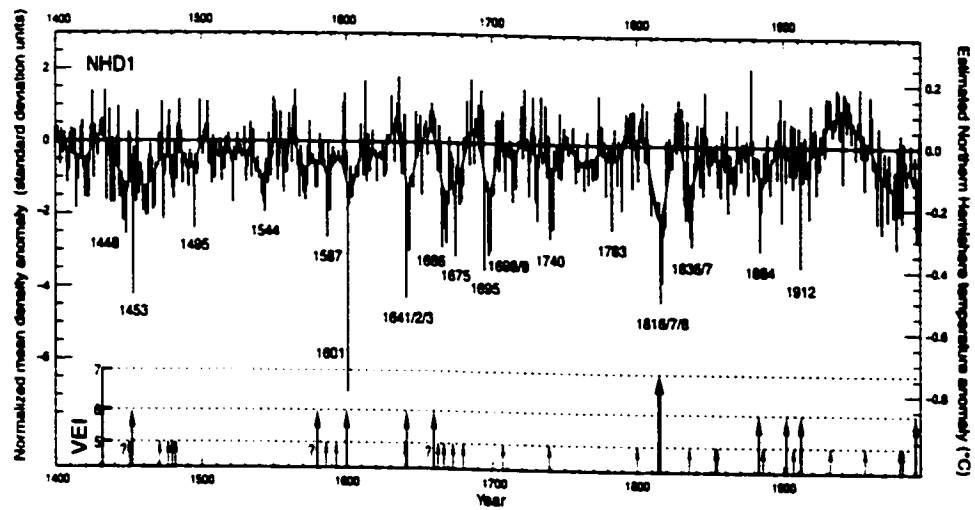
Figure 2.10: The Northern Hemisphere mean tree-ring-density and temperature anomalies reconstructed from a set of 383 chronologies (*Briffa et al.*, 1998). Arrows indicate large volcanic eruptions with associated VEI from *Simkin and Siebert* (1994).

volcanic perturbations. In fact. in Table 2.3. one can easily see that from the 30 coldest years (*Briffa et al.*, 1998. p. 450). the coldest eight years clearly follow large tropical events and only 11 occurred with more than a 2 year delay. From those years probably unrelated to tropical events. two followed VEI = 5 eruptions in the Northern Hemisphere. two are the years 1818 and 1819 floowing the large 1815 Tambora eruption (completing a cold series 1816-1819). and two fall into the last years of the 17th-Century. Overall. the volcanic influence on tree growth is significant. The question remains: how well are these volcanically perturbed years represented in a quantitative way? Were the temperatures during the growing season really so low or is the relationship to seasonal temperatures non-linear? Is it possible that short but severe coolings during the growing season cause the anomalous growth? In some tree ring series. there are a number of years where frost damaged the young cells (so called frost rings). which have been related to years with significant volcanic perturbations (*LaMarche and Hirschboeck*, 1984). This question of intra-seasonal to inter-annual variability and its impact is going to be discussed in detail in Chapter 7.1.1.

Rank	Year	σ Value	NHem T	Volcano	Reference
1	1601	-6.90	-0.81	Huaynaputina, Peru (1600)	*de Silva and Zielinski* (1998)
2	1816	-4.33	-0.51	Tambora, Sunda (1815)	*Stommel and Stommel* (1983); *Harrington* (1992)
3	1641	-4.31	-0.5	Parker, Philippines (1641)	*Delfin et al.* (1997)
4	1453	-4.24	-0.5	Kuwae, Vanuatu (1452/3?)	*Pang* (1993); *Delmas et al.* (1992) *Cole-Dai et al.* (1997a, 2000)
5	1817	-3.76	-0.44	Tambora, Sunda (1815)	see 1816
6	1695	-3.5	-0.41	Serua, Banda (1693)	*Simkin and Siebert* (1994)
7	1912	-3.33	-0.39	Katmai-Novarupta, Alaska (1912)	*Kimball* (1913); *Volz* (1975a) *Hildreth and Fierstein* (2000)
8	1675	-3.13	-0.37	Gamkonora, Indonesia (1673)	*Cole-Dai et al.* (1997a)
9	1698	-3.08	-0.36		
10	1643	-2.99	-0.35	Parker, Philippines (1641)	see 1641
11	1699	-2.96	-0.35		
12	1666	-2.89	-0.34	Long Island, New Guinea (1665?)	*Blong* (1982)
13	1884	-2.89	-0.34	Krakatau, Java (1883)	*Self* (1992)
14	1978	-2.80	-0.33		
15	1837	-2.78	-0.32	Coseguina, Mexico (1835)	*Williams* (1952); *Self et al.* (1989)
16	1669	-2.77	-0.32	Shikotsu (Tarumai Crater), Japan	*Simkin and Siebert* (1994)
17	1587	-2.64	-0.31	Kelut, Java (1586)	*Simkin and Siebert* (1994)
18	1740	-2.61	-0.30		
19	1448	-2.57	-0.30		
20	1992	-2.56	-0.30	Pinatubo, Philippines (1991)	*McCormick et al.* (1995). *Hansen et al.* (1996b)
21	1836	-2.48	-0.29	Coseguina, Nicaragua (1835)	*Self et al.* (1989); *Williams* (1952)
22	1818	-2.45	-0.29		
23	1495	-2.42	-0.28		
24	1968	-2.38	-0.28	Fernandina, Galapagos (1968)	*Simkin and Howard* (1970)
25	1742	-2.35	-0.27		
26	1783	-2.35	-0.27	Laki-Grimsvotn, Iceland (1783)	*Thordarson and Self* (1993)
27	1667	-2.35	-0.27	Long Island, New Guinea (1665?)	*Blong* (1982)
28	1642	-2.22	-0.26	Parker, Philippines (1641)	see 1641
29	1819	-2.21	-0.26		
30	1446	-2.20	-0.26		

Table 2.3. Volcanic eruptions represented in treering data. Rank and σ latewood density from *Briffa et al.* (1998) NHD1 as an average from 8 regional averages compiled from 383 individual chronologies. Volcanoes with potential influence on Temperature, and estimated northern hemisphere temperature anomaly from the σ value, representing mostly April through September growing season temperatures.

2.7 Coral Data

Rencently, coral records have been proposed to exhibit a volcanic signal similar to the tree rings (*Gagan and Chivas*, 1995; *Genin et al.*, 1995; *Crowley et al.*, 1997). If true, this would allow for the recognition of large radiative effects of volcanic eruptions over the tropical areas, where tree ring data are much less common due to the lack of a strong seasonal cycle. Additionally, the coral series, especially from the Pacific area, would tie in more closely than mid- to high-latitude tree rings with the El Niño - Southern Oscillation system, which is responsible for a significant amount of interannual climate variability. Although single events can be recognized, the technique is far from being as refined, as it is with tree rings. Dating problems might influence the comparison. For example, see Figure 8 of *Dunbar et al.* (1994), where a small age 'correction' could generate an incredible match with the largest volcanic eruptions during the represented period (1641, 1809, 1815, potentially 1883), although correlations with ENSO records might not support such a correction.

Nevertheless, corals could contain a volcanic signal, but many more series have to be collected and measured, and as with tree ring studies, areas sensitive to the volcanic forcing (surface temperature drop, shifts in precipitation) have to be identified.

Chapter 3

VOLCANIC FORCING

DURING THE

INSTRUMENTAL PERIOD

3.1 Overview

During recent years. a number of coupled climate model simulations have been performed to study the impact of increased greenhouse gases in the atmophere. Only a few of these experiments take external forcings into account (e.g. *Stott et al.*, 2000). although there are suggestions that the external forcing. and not the anthropogenic influence. has driven climate over the 20th-Century (*Friis-Christensen and Lassen*, 1991; *Lassen and Friis-Christensen*, 1995; *Svensmark and Friis-Christensen*, 1997). For the solar forcing. usually one of two different reconstructions are used (*Lean et al.*, 1995; *Hoyt and Schatten*, 1993). while the volcanic forcing is generally taken from *Sato et al.* (1993). These data are based on the important relation of aerosol visible optical depth to the forcing. as described by *Lacis et al.* (1992). They show that the radiative forcing on the
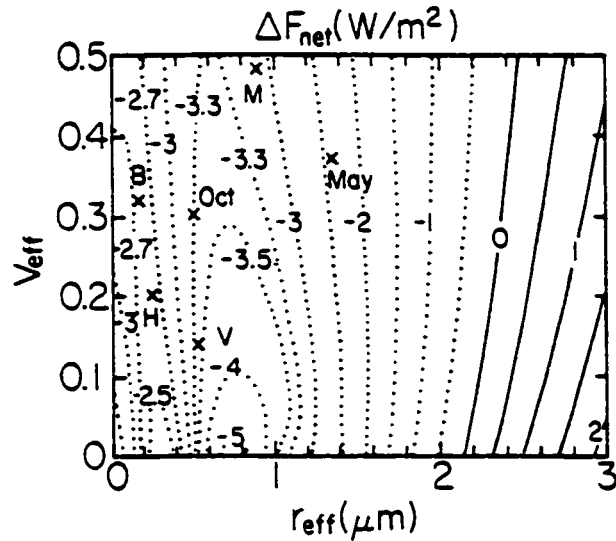
Figure 3.1: Aerosol net radiative forcing as a function of aerosol effective radius (x-axis) and effective variance (y-axis) at a visible optical depth $\tau_{v,i}$ = 0.1 from *Lacis et al.* (1992). It can be seen that particle sizes of larger than about 2 μm have a posive net radiative effect. whereas smaller ones have a negative net effect and therefore cause a cooling. Several observed aerosol distributions are indicated in the plot: May 1982 and October 1982 aerosol sizes of El Chichón (*Hofmann and Rosen*. 1983) with X. B and V from *Oberbeck et al.* (1983). and H and M are from *Deirmendjian* (1969).

climate system from volcanic aerosol is primarily dependent on the aerosol visible optical depth. and to a lesser degree by the aerosol size (see Figure 3.1). *Sato et al.* (1993) therefore present a timeseries of optical depth in the midvisible spectrum at 0.55 μm.

More recently. the originally published data of the earliest pyrheliometric measurements (1880-1960) have been re-analyzed by *Stothers* (1996b). The most important improvement presented by Stothers is the often ignored difference between visible optical depth and pyrheliometrically derived optical depth. He found that the pyrheliometric optical depth is lower. and a conversion factor k of about 1.6 needs to be applied (*Volz*, 1970. suggested 1.7). Stothers

combined this correction, together with improved calibration of the transmission data (seasonal cycle), into an alternative optical depth time series for perturbations exceeding the estimated $\tau = 0.04$ ($=\tau_{vis} = 0.07$) detection threshold. This limit is roughly equal to the lower end where the naked eye can detect a perturbation in atmospheric transmission. In any case, the radiative effect of transmission changes of this magnitude might not be completely negligible, especially over long timescales, but they are clearly much smaller than the impact from the big volcanic aerosol clouds released by a few very explosive events. At the same time, interannual climate variability at the earth surface is quite large, due to a number of internal mechanisms (like ENSO), and the detection of a potential impact of radiative perturbations at these low levels would be very hard, especially considering the poor historical knowledge of these events. Therefore, I follow the work of *Stothers* (1996b) and concentrate on the significant eruptions that produced a visible trace in the atmosphere.

To verify the higher optical depth values from *Stothers* (1996b) compared with *Sato et al.* (1993), an independent test can be performed. Based on the observed pyrheliometric optical depth perturbations *Stothers* (1996a) estimated an average aerosol size distribution for the eruptions and then computed the corresponding stratospheric sulfuric acid mass. The peak in the early month can then be compared with the independently derived sulfate emissions from either gaseous inclusions in erupted volcanic glass (*Devine et al.*, 1984; *Palais et al.*, 1990) or from ice core sulfate flux measurements (e.g. *Legrand and Delmas*, 1987; *Delmas et al.*, 1992; *Zielinski*, 1995; *Cole-Dai et al.*, 1997a). The sulfate mass derived from the higher optical depth values compare favorably with other estimates of volcanic sulfate, such as gaseous inclusions, supporting the higher visible optical depth values and with that, the higher radiative impact for many of the big events.

When looking at the temporal evolution of the visible optical depth in the combined Stothers-Sato data (see Figure 3.2) since 1870, one readily recognizes the main volcanic eruptions. In addition, there seems to be a higher temporal density of volcanic perturbations from 1883 to

about 1905. and again after 1963 to about 1995. The statistical significance of this distribution is investigated below (Chapter 3.6).

For modeling purposes in the climate change context. two disadvantages of these compilations need to be addressed. First. the spatial and temporal detail shows different decadal to multi-decadal episodes. which. in fact. represent changing data sources. For example. during the last 40 years. three distinct episodes (1960-1965. 1966-1979. and 1979-present) can be recognized. The first is based on a few ground based optical depth (transmission) measurements. the second mainly on optical depth estimates deduced from lunar eclipse data from *Keen* (1983). and the significantly increased detail in the most recent period is due to satellite coverage. For climate model experiments where multi-decadal climate change is to be analyzed. these unconformities in the forcing data could introduce an artificial signal. Second. the temporal evolution of the aerosol for eruptions mainly prior to 1960 is strongly simplified and either based on measurements in the Northern Hemisphere mid latitudes and kept constant over the globe. or made symmetric about the equator. This does not address the strong seasonality of the stratospheric circulation. where the dominant mass transport is towards the winter hemisphere.

These two limitations in the forcing data sets can be accounted for by the introduction of a simple seasonal parameterization that is applied to all eruptions since 1870. Such a model will be presented by using the aerosol evolution after the well-studied June 15. 1991. eruption of Mt. Pinatubo. Philippines and is subsequently applied to all significant (see above) eruptions since 1880. A few detailed examples are presented and validated against independent data.

3.2 Pinatubo, a reference eruption

The large 1991 eruption of Pinatubo. Philippines (15.1°N. 120.4°E). offered an ideal natural experiment for a wide variety of instruments and models to monitor and study the stratospheric aerosol cloud with its radiative and chemical effects. From space and from the ground. the
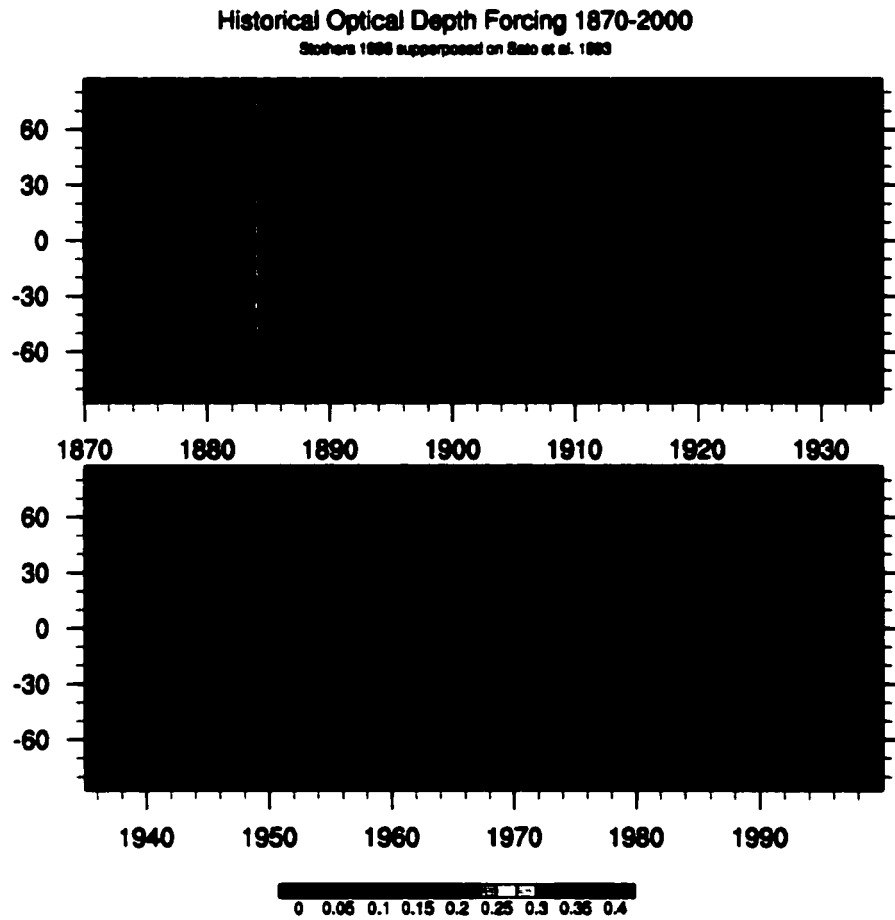
Figure 3.2: Combined visible optical depth data from *Sato et al.* (1993) [prior to 1880, and 1960-present] and *Stothers* (1996b) [1880-1959]. The temporal resolution is monthly, and the spatial resolution is in meridional direction only (assuming rapid zonal mixing).

59

aerosol cloud was closely tracked (*McCormick et al.*, 1995), and the different measurements allowed analysis of size distributions (*Russell et al.*, 1996), the impact on the radiative budget (*Minnis et al.*, 1993), ozone (*Fahey et al.*, 1993; *Zerefos et al.*, 1994; *Solomon et al.*, 1996), and surface climate (*Hansen et al.*, 1996a; *Parker et al.*, 1996).

Stenchikov et al. (1998) published a detailed data set of Pinatubo aerosol optical properties at a high spectral resolution, well adapted for modeling purposes. They combined different satellite data sets and a number of surface lidar time series into a spatially three dimensional data set at monthly resolution. In the electromagnetic spectrum, the data is available in 60 bands and can be averaged (binned) for different spectral bands of climate models. The data set takes the changing median in the aerosol size into account, but describes the size distribution at each point in time and space as log-normal and unimodal. *Russell et al.* (1996) showed that the properties can be well captured by a unimodal distribution. The composition of the aerosol is assumed to be a clean sulfuric acid aerosol at a concentration of 75% H_2SO_4 and 25% H_2O. The radiative properties are then fully described by Ψ_λ, the mass weighted aerosol extinction, ω_λ, the single scattering albedo, and g_λ, the asymmetry parameter. Given an aerosol size distribution and chemical composition, the mass extinction efficiency coefficient can be computed using Mie theory. This coefficient is weighted by the aerosol mass to receive the extinction at a specific wavelength. The Mie theory also relates the single scattering albedo (a measure of the absorption vs. reflection) and the asymmetry parameter (a term describing the separation of radiation scattered towards the earth surface vs the amount that is scattered back to space) to the size distribution and composition of the aerosol.

The aerosol optical depth (τ_{vis}) at a specific wavelength is equal to the column integrated extinction. The visible optical depth from *Stenchikov et al.* (1998) is presented in Figure 3.3-A for the time from June 1991 to May 1993. From the eruption latitude at 15°North, the aerosol immediately spread throughout the tropics. The buildup of the sulfuric acid droplets from the emitted SO_2 took place over a few months (although very fast rates have been observed

in the troposphere. *Oppenheimer et al.*, 1998). The maximum optical depth was reached over the equator around December 1991. after which time. the decay and further transport into the Northern and Southern Hemisphere took place. In the midlatitudes in each hemisphere. the aerosol optical depth increased during the respective winter season. when stratospheric circulation favors poleward transport through planetary waves (*Trepte et al.*, 1993). Over the polar areas. satellite data are often missing. as limb scanners like SAGE-II use sunrise or sunset times for their scans. or the satellite orbits don't pass directly over the pole. SAM II data can be used to fill in some information (*Wang et al.*, 2000). In winter. the interior of the polar vortex is cut off from inflow of aerosol (*McCormick et al.*, 1983). and the remaining particles are sedimented out by the general subsidence. Only in late spring. after the break down of the polar vortex. does aerosol concentration increase in the polar stratosphere (*Wang et al.*, 2000). The overall decay time of the Pinatubo aerosol follows quite closely an average e-folding time of about 1 year.

On August 12th 1991. an additional aerosol cloud was emitted by Cerro Hudson. Chile (45.9°S). Despite the large size of the event (VEI = 5). the aerosol loading was significantly smaller and at much lower levels than the Pinatubo aerosol. Nevertheless. some modification of the Southern Hemisphere perturbation resulted from this event and can be seen in Figure 3.3 as an increase in optical depth around October 1991. south of about 30°South.

3.3 Seasonality Parameterization

For eruptions prior to the satellite period starting in 1978. spatial information about spread of eruption clouds is very limited. and only for a small number of events is some temporal and spatial tracking of the spreading cloud possible (e.g. *Symons*, 1888; *Wexler*, 1951b; *Dyer and Hicks*, 1968). In order to provide a consistent data set of volcanic aerosol optical depth as a forcing for climate models with a focus back in time. events need to be treated consistently (i.e.. they carry a comparable background error). The parameterization should also introduce some

Visible Optical Depth

Infrared Optical Depth
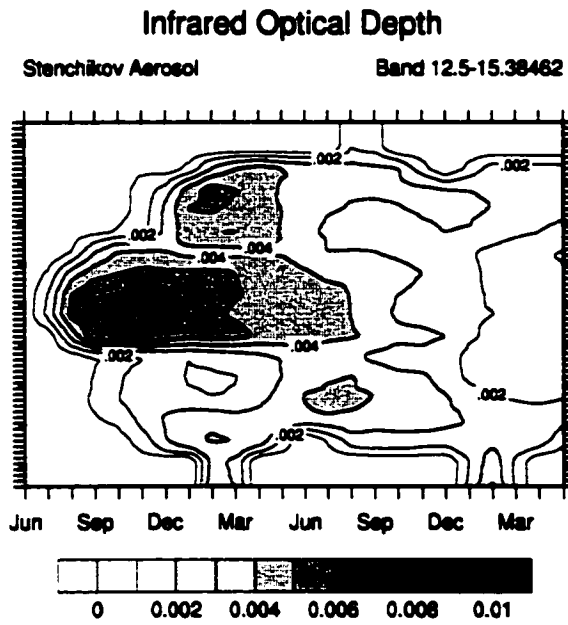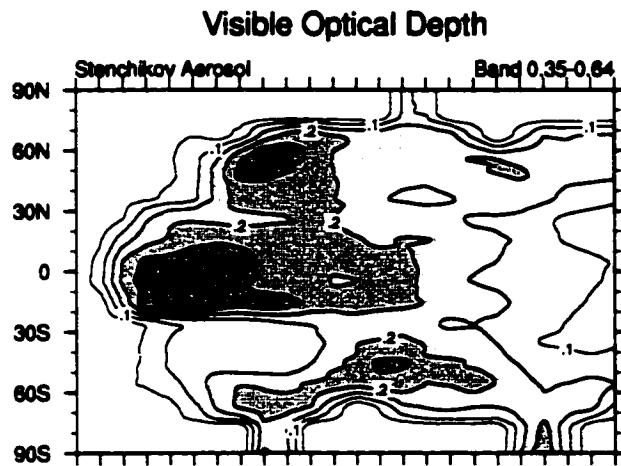
Figure 3.3: Pinatubo column optical depth. Top: the visible band of the National Center for Atmospheric Research Community Climate Model (NCAR-CCM) (*Kiehl et al.*, 1996, 1998b), representing the band width from 0.35 − 0.64 μm. Bottom: infrared optical depth at 12.5 − 15.4 μm. The monthly data is plotted at the a meridional resolution of 3.75 degrees.

first order spatial distribution over time to simulate some of the seasonality effects (*Dyer and Hicks*, 1968; *Post et al.*, 1996). Therefore, a very simple parameterization with only two input parameters is proposed :

- Maximum optical depth reached by the eruption (estimates can be based on observations, geologically or ice core derived amount of emitted sulfate)

- Month of the eruption (which is either directly observed, or estimated from timing of aerosol cloud appearence in mid-latitudes, or estimated from the timing of sulfate depositions in polar ice cores)

It is assumed that the zonally averaged aerosol formation takes place over a time of 4 month (*Grant et al.*, 1996) with subsequent decay at an e-folding time of 1 year. Any possible interannual variability in stratospheric circulation is ignored. Additionally, it is also assumed that the main stratospheric circulation and with it the aerosol transport, is not dramatically changed by the presence of the aerosol, despite quite significant heating. Therefore, this parameterization should probably be applied with caution for eruptions like Toba (about 72,000 years BP), where erupted volumes of the order of 2000-3000 km^3 were involved. Also, the potential influence of the stratospheric quasi-biennial oscillation (QBO) on the meridional transport (*Grant et al.*, 1996) is ignored because reliable information on the QBO is only available since the mid-20th-Century.

The transport model distinguishes between tropical and extra-tropical eruptions. Here, I first describe the model for tropical eruptions, which considers three zonal bands: tropics, mid-latitudes, and polar areas. In this hierarchical order, the computation is performed, as the aerosol is transported out of the tropics into higher and higher latitudes.

Tropics The tropical aerosol follows a build-up and subsequent decay. The values are set equal between 20°N to 20°S, assuming rapid intertropical mixing. The buildup is performed linearly in 4 months, reaching the specified peak optical depth. Thereafter, decay at an e-folding time of

1 year to background levels of 0.0001 is computed.

Mid-Latitudes Two months after the eruption. aerosol is allowed to spread outside of the tropics. The meridional expansion only takes place into the winter hemisphere (Northern Hemisphere winter : Nov-April. Southern Hemisphere winter : May - October) and as long as the aerosol optical depth in the tropics is above background. The increase in the respective winter hemisphere is at a rate that permits the mid-latitudes to catch up with the tropical optical depth by the end of the winterseason. During the summer season. the aerosol decays at a slightly faster pace than 1 year. due to stratospheric transport into the polar areas and back into the tropics.

Polar Areas During the core of the winter season. the polar areas are regarded as more or less cut off from the mid-latitudes though an efficient barrier formed by the polar night jet. Inside the polar vortex. remaining aerosol is deposited quickly. generally leaving a clean column (*Flowers and Vierbrock*. 1965: *McCormick et al.*. 1983: *Herber et al.*. 1993: *Di Donfrancesco et al.*. 2000). In spring. the breakdown of the polar vortex allows transport of aerosol over the poles. causing an incease in optical depth at a time when the mid-latitudes start to encounter a decrease. The maximum optical depth can not exceed the mid-latitude optical depth at the spring break down of the vortex.

This temporal evolution of the aerosol cloud is performed over four years. after which all aerosol levels have reached background again. Subsequently. an interpolation scheme generates a more smooth distribution from these three 'bins' into the requested latitudinal grids (i.e.. the meridional grid resolution of a climate model). As an additional improvement. latitudes from 25 and 40° in each hemisphere are treated with a special 'zamboni' filter to represent the reduced column aerosol due to very efficient divergence over the subtropical high pressure systems (*Trepte et al.*. 1993). see Figure 2.1. This reduction is introduced for the winter season.
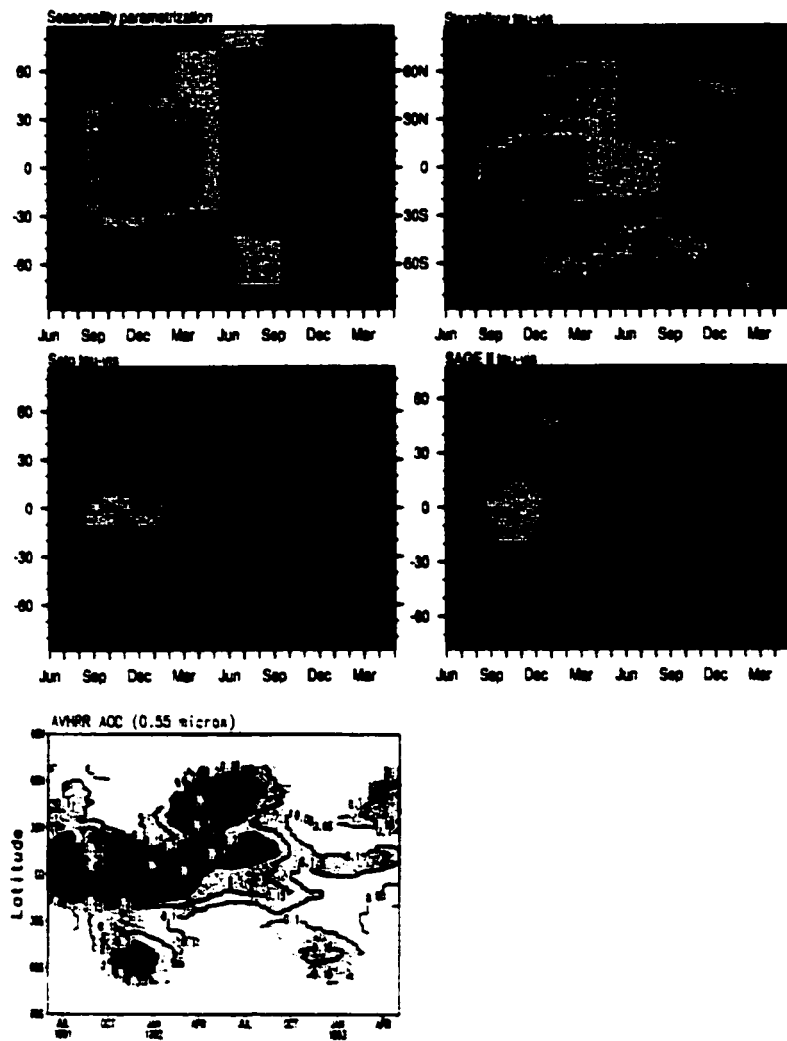
Figure 3.4: Spatial evolution of the Pinatubo cloud spread shown as visible optical depth from the simple parameterization using peak optical depth (τ_{vis}) of 0.35 and June 1991 as eruption month, compared with *Stenchikov et al.* (1998), *Sato et al.* (1993), SAGE II (*Rind and Liao,* 1997) and AVHRR (*Long and Stowe,* 1994).

3.3.1 Test with Pinatubo aerosol distribution

In Figure 3.4. the simple transport model is compared with the data from Stenchikov et al. (1998). the AVHRR (*Long and Stowe*. 1994). and SAGE-II and Sato (*Sato et al.*. 1993). First. we are concerned with the qualitative performance of the parameterization. After the prescribed tropical evolution of the optical depth. the main feature is the increased perturbations in the mid-latitudes during the winter season. While the buildup of the aerosol clouds in the mid-latitudes is somewhat slow compared to Stenchikov et al. (1998). it compares quite well with the other data sets. Note. the seasonality parameterization does not include the aerosol contribution of Cerro Hudson in the Southern Hemisphere. and therefore the lack of aerosol optical depth in January through April 1992 south of 40°South is misleading. The continued buildup in the winter seasons also simulates the 'persistence' of the aerosol clouds quite well. although it underestimates it slightly. From a quantitative view point. the core of the aerosol cloud over the tropics is initially somewhat large compared to Stenchikov and SAGE. but smaller than from AVHRR. *Russell et al.* (1996) comment on the tendency to underestimate the inner-tropical optical depth of the SAGE instrument due to too strong extinction in the aerosol layer (saturation). but also the tendency for overestimation from the AVHRR. This observation is supported by the detailed spectral measurements of *Dutton et al.* (1994) at Mauna Loa. Hawaii. The reconstruction of *Stenchikov et al.* (1998) seems therefore closest to the real perturbations and we concentrate on the comparison to Stenchikov. Here we see that the aerosol optical depth in our model are slightly underestimated in the mid-latitudes. The optical depth over the polar areas are larger than the satellite derived data sets. but compare more favorably against ground based estimates (*Herber et al.*. 1993). The reason for this is that the limb-scanners like SAGE II cannot measure during summer time. as there are no sunsets or rises over the polar areas during that time.

Overall. the distribution of the aerosol with the simple parameterization. which is only based on the month of the eruption and the peak optical depth in the tropics. is not far off the target of *Stenchikov et al.* (1998).

3.3.2 High-latitude eruptions

High-latitude eruptions. like the Katmai-Novarupta eruption in June 1912 in Alaska. are much simpler to describe. There is a buildup over 4 month of aerosol optical depth in the mid-latitudes with subsequent decay (e-folding of 1 year). While the treatment over the pole is the same as for tropical events. the equator ward extent of the aerosol is limited to the subtropical boundary described above. No further expansion into the tropics or even the other hemisphere is allowed. As no aerosol mass can flow in from the tropics to replace loss through sedimentation. the life time of the volcanic clouds is relatively short. This is done despite results from a two-dimensional model of aerosol transport for the 1956 eruption of Bezymianny (*Cadle et al.*. 1976). which exhibited spread from the very high reaching aerosol into the southern hemisphere. But observations from this and also from the much more massive Katmai-Novarupta event of 1912 do not show any transmission changes south of about 30°N (*Volz*. 1975a). There is also no event recorded in ice cores that would prove otherwise.

3.4 Examples of past eruptions

Given the simplicity of the parameterization. other eruptions further back in time can be simulated to get a temporal and spatial pattern. If the month of the eruption is unknown. usually a first guess can be made by looking at the timing of sulfate doposition in polar ice (making use of the seasonal dependence of stratospheric transport). First. the famous eruption of Krakatau (1883) is simulated with the simple parameterization and compared to a host of independent records. The second example is a proposition of Colima Volcano. Mexico in 1890 to be the source

of an unknown aerosol cloud over the northern hemisphere, illustrating the idea of evaluating the seasonal timing of eruptions. Additionally, the unusual real world aerosol distribution after Agung and somewhat El Chichón are briefly discussed to show that the simple parameterization is not without problems.

3.4.1 Krakatau 1883

The discussion of this exceptional event is separated into two parts. Here, some facts about the eruption itself, the ejecta as identified in different archives, and the optical phenomena described around the world are presented. This information is used to deduce the magnitude of τ_{vis} and its temporal evolution. Later, (see Chapter 6.3), when the the climate impact of Krakatau is simulated, some aspects of the eruption will be revisited. It will be shown that the visible-optical depth is a good, but not an exclusive parameter for describing the radiative effect of volcanic eruptions on earth's climate.

The cataclysmic eruption of Krakatau in the Sunda Strait (6.1°S, 105.4°E) in August 1883 is probably one of the most famous eruptions of all times. Krakatau was the first large volcanic event immediately made known around the world. Despite ample discussion on the feasability of a tropical volcanic source for the high level dust veils, the dramatic optical effects were in the news and scientific literature (Journals of *Nature, Science, Monthly Weather Review, Meteorological Magazine*) for many months (see summaries in *Symons* (1888) and *Simkin and Fiske* (1983)). The newly invented telegraph allowed the message of the enormous explosion on August 27, 1883, to be transmitted around the globe within hours of the cataclismic phase. The sounds of the eruption were heard up to 4653 km away in the Southern Indian Ocean (Rodrigues Island), and air pressure waves were observed to travel around the globe several times (*Symons*, 1888). In addition, up to 40 m tidal waves, which caused a disaster in the vicinity of the volcano and claimed a large percentage of the 36,000 lost lives, were later tracked travelling across the Pacific and even up the Atlantic Ocean. Outstanding compilations of the eruption history and the subsequent

68

wide spread effects were presented in the formidable work of the "Krakatau Committee of the Royal Society" (*Symons*, 1888) and in the detailed analysis onsite of *Verbeek* (1885). Newer summaries can be found in *Simkin and Fiske* (1983) and *Self* (1992).

From the beginning of the eruptive phase through the violent explosions due to caldera collapse (*Self*, 1992), the volcano released material in the order of 20 km^3 of bulk material (*Self and Rampino*, 1981; *Self*, 1992), or about 9 to 12 km^3 of dense rock equivalent (DRE) as also suggested by *Sigurdsson et al.* (1991) and *Mandeville et al.* (1996b). For comparison, Pinatubo ejected roughly 8.4 to 10.4 km^3 bulk volume and 3.7 to 5.5 km^3 of DRE (*Holasek*, 1995; *Scott et al.*, 1997). A very large ash and gas column rose into the stratosphere, giving birth to large pyroclastic flows depositing substantial ignimbrites and causing ash rain in a large area around the volcano. Estimates of the peak altitude reached by the cloud vary, but range from 30 to 50 km. Descriptions of the zenith angle of the earth shadow reflected by the aerosol long after sunset show that, at least initially, the aerosol reached close to 50 km (120,000 - 160,000 feet, Archibald in *Symons*, 1888). Blue and green suns were observed throughout the tropics (Archibald in *Symons*, 1888), and subsequently as it spread into the mid-latitudes in late September and October 1883, unusually intense sunsets were observed in North America and Europe alike. Filaments of dense aerosol clouds (initially probably carrying significant amounts of ash) and a more subdued fine, milky shining layer, which would glow in extaordinary pink to purple colors (even 90 minutes after sunset), were reported for almost a year. The phenomena recurred mainly during the winter season for at least another year or two, although with reduced intensity.

Estimates of the emitted amount of sulfate aerosol varies widely depending on the methods used. Generally accepted values range from 30 to 50 Mt $[= 30 - 50 \times 10^{12}$ g $\equiv$ Tg] (best estimate closer to 50 Mt, Self, personal communication). Ice core estimates of the total sulfate mass are probably the best available (see Table 3.1). These values put Krakatau clearly ahead of Pinatubo, which generated about 30 Mt of sulfuric acid aerosol (*McCormick and Veiga*, 1992; *McCormick et al.*, 1995; *Self et al.*, 1997a). The maximum aerosol optical depth (τ_{vis}) in the tropics was

69

Reference	Tg	archive, method
Ice cores		
Hammer (1977)	60	Greenland
Hammer et al. (1980)	73	total aerosol
Legrand and Delmas (1987)	10 – 50	total aerosol
Delmas et al. (1992)	45	Antarctic ice
Langway et al. (1988)	64	Antarctic ice
Zielinski (1995)	58	max. estimates hydr. aerosol mass
Gas inclusions or tephra		
Devine et al. (1984)	> 1	from g of Sulfur in inclusions (multiplied by 4)
Mandeville et al. (1996a)	> 10	from g of Sulfur in inclusions of different tephra
Mitchell (1970)	50	from total erupted tephra
Optical perturbations		
Stothers (1996b)	14	from optical depth reconstruction
Deirmendjian (1973)	48	about 2 weeks after eruption referring to total dust

Table 3.1: Estimates of maximum aerosol mass erupted from Krakatau 1883

estimated at 0.63 from naked eye sunspot observations (*Deirmendjian*, 1973). Although this high value agrees with the blue sun appearance from southern India (many other observations can be found in *Symons*, 1888, p. 199ff). *Deirmendjian* (1973) comments on the unreliability of the color impressions to determine the true optical properties and spectral radiance, especially when evaluated against an abnormal skylight background. Krakatau must have depleted the red end of the solar spectrum by an amount larger than the normal background aerosol, which points to slightly larger than average aerosol. *Stothers* (1996b) took this optical depth as the initial value in the tropics and decreased it then by an e-folding time of 1 year.

A couple of months after the eruption, the typical loading from Krakatau was reduced to about 0.55 (*Deirmendjian*, 1973), probably a more representative value for the developing sulfate cloud. This value is close to the decreasing aerosol as presented in *Stothers* (1996b). Therefore, a value closer to this (0.5) is assumed for the maximum optical depth. Figure 3.5 compares the data set of *Sato et al.* (1993), *Stothers* (1996b), and the simple parameterization using $\tau_{vis-max} = 0.5$ and *month* = August 1883. *Sato et al.* (1993) and *Stothers* (1996b) aerosol evolutions have been discussed before. The difference by using the seasonality parameterization is quite obvious.

Two major features stand out: the strikingly larger perturbation compared to Sato et al., and the seasonal variation in the parameterization. The difference in magnitude has been discussed before. For the seasonality, different latitudinal bands have to be looked at. In the tropics, the volcanic cloud spread very quickly, surrounding the globe in 13 days and covering the area between 33°S and 22°N within a very short time. By October and November, the cloud started to spread to mid- and finally to higher northern latitudes (*Symons*, 1888; *Wexler*, 1951b). In the higher latitudes of the southern hemisphere, observations are not available. For the polar areas, *Langway et al.* (1995) comment that the sulfate from Krakatau reached southern Greenland after only 1 year delay, and that in the following year, still a 'strong residual' can be found. This delay into the northern hemisphere summer month is well reflected in the temporal distribution given in the seasonality parameterization. Figure 3.6 shows SO_4 as recovered in the well dated

Krakatoa (Aug. 1883) Optical Depth (vis)

Comparison of different data sources
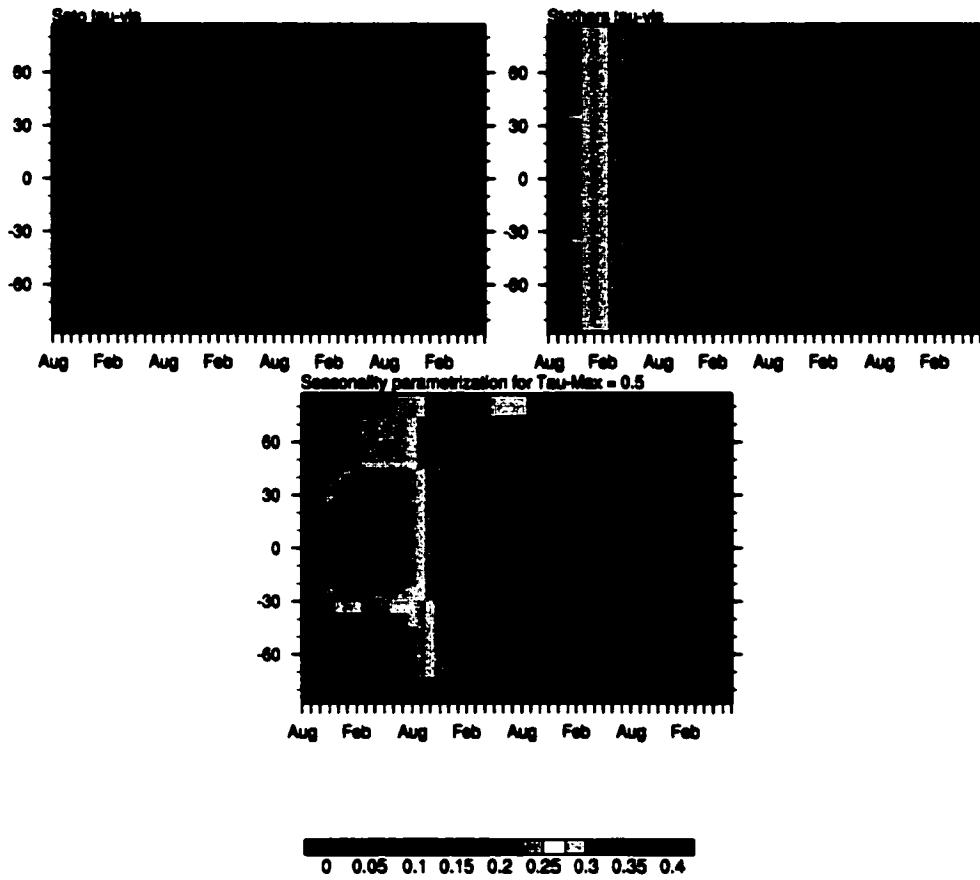
Figure 3.5: Temporal evolution of τ_{vis} after the large eruption of Krakatau in August 1883 as represented in *Sato et al.* (1993), *Stothers* (1996b) and the seasonality parameterization using August 1883 as month of eruption and 0.5 as peak τ_{vis}.

Krakatau Sulfate Deposition
Observed vs derived from optical depth
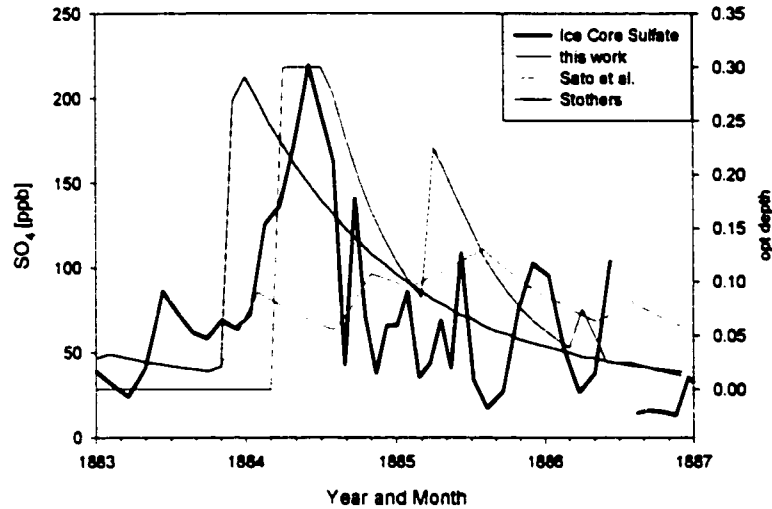
Figure 3.6: Volcanically perturbed sulfate [ppb SO$_4$] concentrations in GISP2 core B (*Mayewski et al.*, 1990, 1997) for 1883 to 1886 in subseasonal resolution compared with timing and magnitude of aerosol optical depth in the polar atmospheric column from *Sato et al.* (1993). *Stothers* (1996b) and the seasonality parameterization using $\tau_{v13} = 0.5$, and eruption month is August 1883.

GISP-2 ice core, and the clear 1884 summer signal is visible in the observations. While the Sato et al. optical depth over the polar area is much lower than the others, it also peaks in 1885, clearly one year later than the maximum deposition and other indices including lunar eclipse data (*Flammarion*, 1884; *Fisher*, 1924), colored sunset occurrences (*Symons*, 1888) and sky polarization (see summary in *Stothers*, 1996b).

Overall, τ_{v13} from the seasonality parameterization agrees well with independent data, at least from the tropics to the high northern latitudes.

3.4.2 Possible atmospheric impact of an eruption of Colima in 1890?

A nice feature of the seasonality parameterization is its potential to help evaluate sources of observed atmospheric perturbations. This can be illustrated with the optical effects observed starting in May 1890 from sky polarization and starting in late 1890 in the pyrheliometric data from Montpellier (France). lasting until early 1892 (*Stothers*. 1996b). Figure 3.7 shows the peak optical perturbations over the northern mid-latitudes in winter 1890/91 as presented by both Sato et al. and Stothers. *Simkin and Siebert* (1994) list only one eruption with VEI 4 or larger: an eruption of Colima. Mexico (19.5°N) on February 16. 1890. If we conservatively use the peak optical depth of Stothers and use February 1890 as the eruption month. the simple parameterization produces a temporal distribution that qualitatively matches the observations in the mid-latitudes. We can again use ice core information to verify relative hemispheric timing. The *Robock and Free* (1995) IVI. a compilation of eight northern and six southern hemisphere ice cores. lists perturbations in the southern hemisphere in 1891. and in the northern hemisphere one year later. The same relative timing is suggested by the simple model. given a tropical eruption in February 1890. although deposition in the northern hemisphere should be in mid-1891. A reason for this discrepancy could be in the relative age estimates from the different ice cores. In conclusion. an atmospheric impact from the 1890 eruption of Colima. Mexico would fit with observations.

3.4.3 Santa Maria 1902

The eruption of Santa Maria. Guatemala (14.77°N) in October 1902 is classified at a comparable magnitude to the Pinatubo eruption in 1991 (*Williams and Self*. 1983). The sulfate aerosol mass is estimated to have been at least 30 Tg (*Hammer et al.*. 1980: *Mitchell*. 1970: *Legrand and Delmas*. 1987: *Zielinski*. 1995: *Stothers*. 1996b). The contribution of the two other explosive eruptions in 1902. Soufrière and Pelée. were visible. but significantly lower. The optical perturbations

? Colima (Feb. 1890) Optical Depth (vis)

Comparison of different data sources
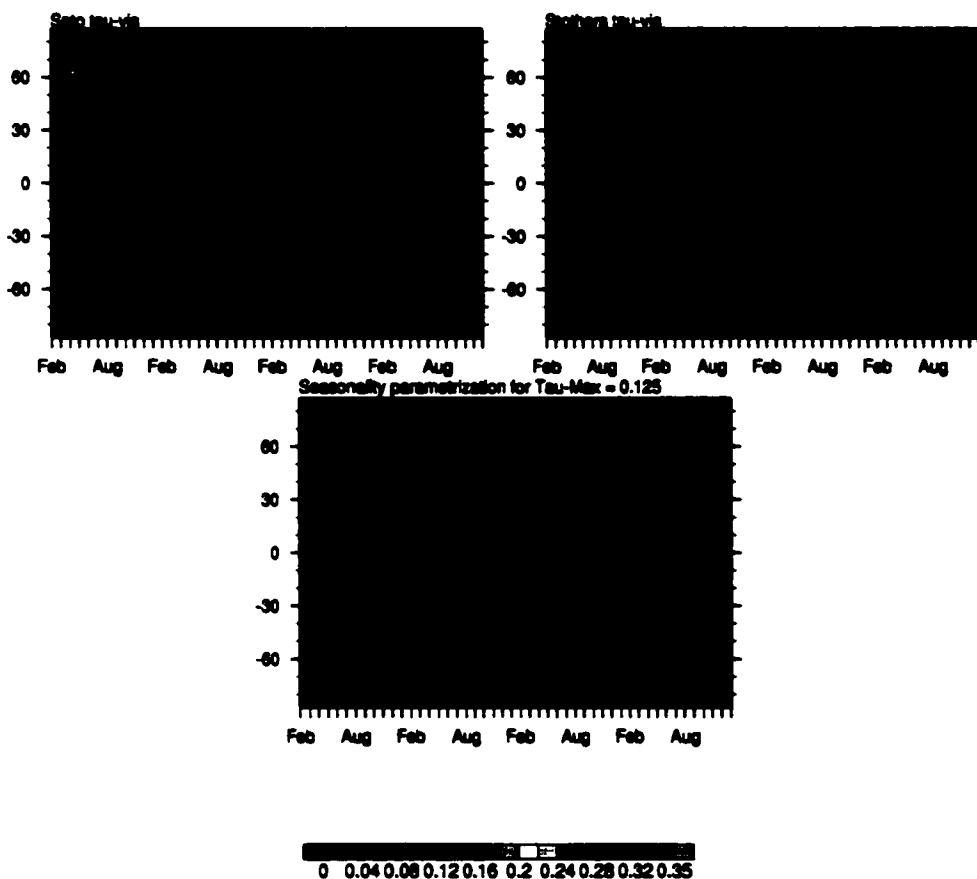
Figure 3.7: Optical depth parameterization for an eruption in February 1890. as would fit for the eruption of Colima. Mexico on February 16 at a latitude of 19.51°N. The observed optical perturbations in the northern hemisphere mid-latitudes are reasonably reproduced and together with the earlier arrival over Antarctica compared with Greenland support a proposition of Colima as the source volcano.

observed in the northern mid-latitudes started during summer 1902. but were greatly enhanced towards the end of the year due to Santa Maria. faded somewhat during summer but appeared enhanced again towards the end of 1903 (*Stothers*, 1996b). This temporal behaviour of the aerosol optical depth is nicely reproduced by the seasonality parameterization shown in Figure 3.8. Two very dark solar eclipses (see also *Fisher*, 1924) are used by *Stothers* (1996b) to argue that the cloud spread far into the southern hemisphere to cause the perturbation in the light refraction into the earth shadow. The parameterization reproduces also this feature. In fact. it is suggested. that the southern hemisphere. due to the seasonal timing. received a slighly larger mass of aerosol.

3.4.4   Katmai-Novarupta 1912

The June 6. 1912. eruption of Katmai and especially Novarupta in Alaska (58.27°N) produced very large volumes (around 13 km^3 DRE. *Hildreth and Fierstein* 2000) and emplaced an ashflow that became famous as *the Valley of the 10,000 smokes*. Due to its high northern latitude. no aerosol spread south of roughly 30-35°N (*Volz*. 1975a). Very quickly large optical perturbations were recorded around the mid-latitudes though. and in many places the sky appeared in a strange whitish. silky color and "at times one could look at the sun without discomfort" (J.R. Eastman in *Kimball*. 1913). The visible optical depth at the peak in late summer 1912 is around 0.35 to 0.4 (*Volz*. 1975a: *Stothers*. 1996b). I use the timeseries by Stothers and generate a decay with an *e*-folding time of 1 year fitted to the monthly data of *Stothers* (1996b). The resulting optical depth is plotted in Figure 3.9. and compared with the very low values of *Sato et al.* (1993) and the data of *Stothers* (1996b). The high optical depth values in the first few month after the eruption are probably overestimating the stratospheric optical depth due to significant tropospheric ash transport. which is confirmed by direct deposition of large amounts of chlorine preceeding the main sulfate deposition on the Greenland ice sheet (*Clausen et al.*. 1997). The best fit to the decay in the values of Stothers is found at a peak optical depth of 0.3.

Pele, Soufriere (May) and Santa Maria (Oct 1902) Optical Depth (vis)
Comparison of different data sources
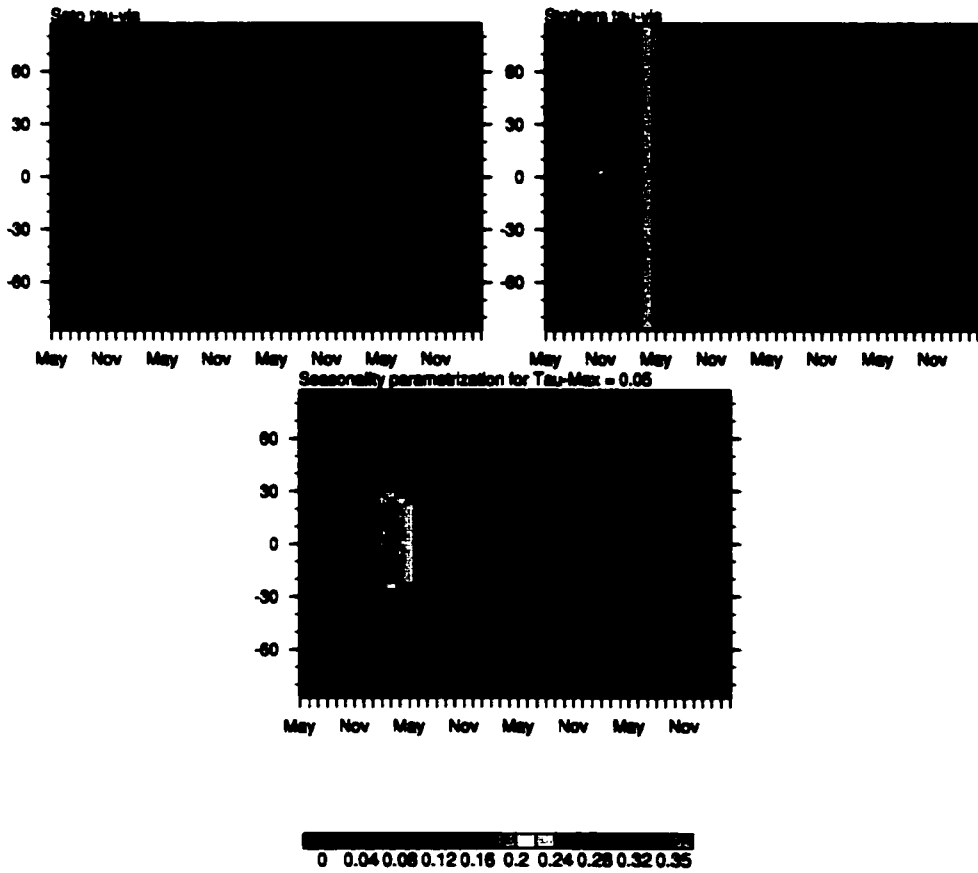
Figure 3.8: Optical depth parameterization for an eruption for the eruption of Santa Maria,
Guatemala (Oct. 1902, 15°N) and subsequent years. Previous eruptions of Soufrière and Pelée
are much weaker (*Williams and Self*, 1983).

Katmai-Novarupta (June 1912) Optical Depth (vis)

Comparison of different data sources
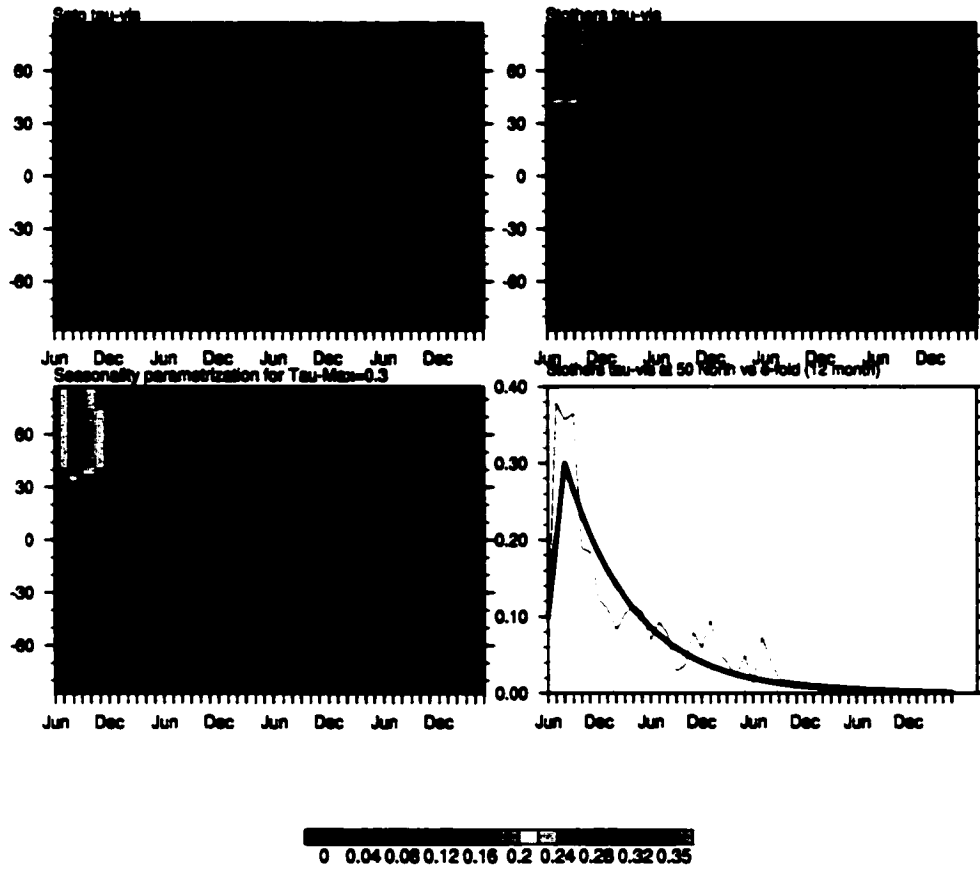
Figure 3.9: Optical depth parameterization for an eruption for the eruption of Katmai-Novarupta, Alaska (June. 1912. 58°N) and subsequent years. The lower right panel shows the monthly data of Stothers in red and in black the fitted smoother decay of the seasonality parameterization. The best fit was achieved by selecting a peak visible optical depth of 0.3

3.4.5 Agung 1963 and El Chichón 1982

The eruptions of Agung (1963) and El Chichón (1982) are two difficult cases because the aerosol cloud evolution of these tropical eruptions was rather unusual. While the Agung cloud was strongly concentrated in the southern hemisphere (*Flowers and Vierbrock*. 1965: *Moreno et al.*. 1965). with a possible north to south ratio of 1 to 3 (*Dyer and Hicks*. 1968) or even 1 to 8 (*Volz*. 1970; *Stothers*. 2001). the El Chichón optical depth on the other hand was probably about double or triple in the northern hemisphere compared to the south (*Stothers*. 2001). The simple parameterization shown in Figure 3.10 does not resolve these strong hemispheric biases very well.

Agung. Bali (8.34°S)   Although the Agung simulation is in terms of a temporal hemispheric weight largely correct. the simple model underestimates the much higher aerosol concentration in the southern hemisphere. as compared with the north here shown by *Sato et al.* (1993) and the timeseries of *Stothers* (2001). On the other hand. it also needs to be emphasized that the northern hemisphere did experience optical perturbations as spectacularly shown with extended colored sunsets and purple sky glare long after the eruption (*Meinel and Meinel*. 1964; *Volz*. 1964; *Mendonca et al.*. 1978). Perturbations measured in the northern polar areas showed an increase in diffuse and decrease in direct radiation. indicating the effect of volcanic aerosol (*Bradley and England*. 1978a,b). It is not clear. however. if eruptions in the high northern latitudes could have contributed to this effect. A list of eruptions in Alaska are registered in the Smithsonian Catalogue. and starting in November 1963. Surtsey. off the Icelandic coast. started to be very active in an explosive manner. The seasonality parameterization in Figure 3.10 does exhibit a maximum in Spring of 1964 from the Agung aerosol. a time when *Volz* (1970) observed weak Bishop rings in the Swiss Alps. But the optical depth of about 0.1 is probably about double from the real $\tau_{\nu,\lambda}$ of 0.05. Long time series of atmospheric transmission from Russia do exhibit some perturbations during this time as well (*Budyko and Pivovarova*. 1967). but many stations suffer from a increasingly strong trend in tropospheric pollution that might overstate the effect of

Agung (Mar. 1963) Optical Depth (vis)   El Chichon (Mar. 1982) Optical Depth (vis)

Comparison of different data sources   Comparison of different data sources
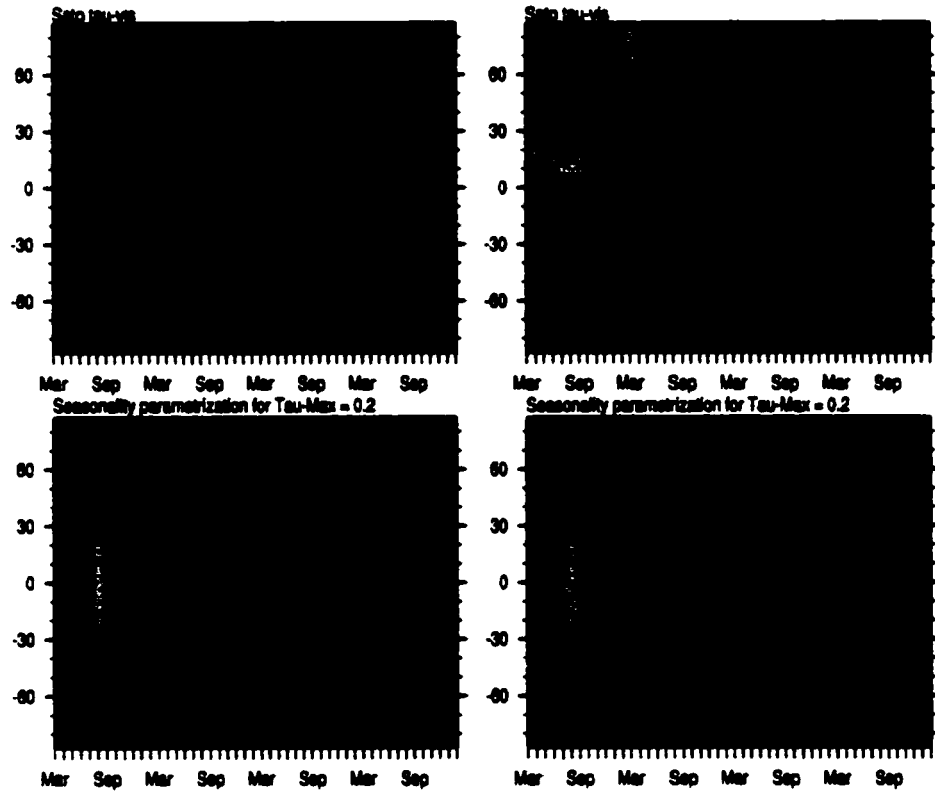
Figure 3.10: Optical depth parameterization for Agung, Sunda (8.34°S) compared to *Sato et al.* (1993) shown in the left two panels, and in the right column for El Chichón. Mexico (17.36°N). Note, the El Chichón eruptions started in late March but the largest events took place in early April. This delay was taken into account here to evaluate if the slightly different timing could be responsible for the different hemispheric distribution.

80

stratospheric aerosol (*McCormick and Ludwig*, 1967; *Pivovarova*, 1975). *Dyer* (1974) also reports significant perturbations in Japan during 1964, but the absence of a comparable signal in Hawaii (19°N) or Albuquerque (35°N) put doubt on Agung as the source of the aerosol.

El Chichón, Mexico (17.36°N)   : The El Chichón simulation fails to predict the hemisphere of maximum optical depth. This problem has shown up in other modeling experiments where transport models were given the challenge (*Cadle et al.*, 1976; *Capone et al.*, 1983), all with quite similar results to the parameterization shown here. It has been a puzzle why the El Chichón aerosol was so stongly confined to the northern tropics (*Thomas et al.*, 1983a).

The reason for the unusual spread for both eruptions can probably not be linked to the latitude of the eruption (Agung 8.34°S, El Chichón 17.36°N), since the Pinatubo (15.13°N) cloud was dispersed more or less evenly into both hemispheres. The season of the eruptions is also not a convincing argument, as the large Tambora eruption, from basically the same latitude as Agung (8.25°S) and only a couple weeks later in the year, did not exhibit this strong very bias. Possible influences could include :

- Regional meridional components in the lower stratospheric circulation mostly around subtropical high pressure systems that extended into the lower stratosphere (see *Trepte et al.*, 1993). Here, no longer perfect zonal conditions exist and parts of the cloud could get diverted into higher latitudes where their heating further enhances dispersion.

- QBO through differences in general meridional transport efficiency depending on easterly or westerly phase (*Trepte and Hitchman*, 1992; *Grant et al.*, 1996), where the altitude of the aerosol/gas cloud could play an additional role (*Hitchman et al.*, 1994): easterly phase favors detrainment from the tropics into the higher latitudes mostly above 22 km, whereas the westerly phase causes relative descent and poleward transport more in below.

- and finally, ENSO and inter-annual changes in the monsoon strength through modification

81

of the large scale Hadley circulation (*Meehl*, 1997).

3.4.6 Summary

In conclusion, we can summarize that while the simple parameterization is not perfectly repro-
ducing the distribution of aerosol, it offers a reasonable way to put directly and indirectly derived
proxies for atmospheric perturbations by volcanic eruptions into a useful context. It is especially
useful when applied to information from long time series of volcanic sulfate in polar ice sheets
that provide an estimate of peak optical depth (*Zielinski*, 1995). Using the same procedure back
in time provides a consistent approach to this rather intracable problem. The parameterization
(with reasonable spatial and temporal evolution of the aerosol throughout the time period of
interest) provides a significant improvement over the other records, where the quality of source
information changes dramatically over time.

3.5   Volcanic Forcing 1870 to present

The seasonality parameterization is now applied to all large eruptions since 1870. We follow
the assessment of *Stothers* (1996b) for identifying which eruptions did perturb the atmosphere
measurably, and only the event of Mt. Spurr is added in the Northern Hemisphere (*Enger and
Fritz*, 1956; *Wexler*, 1956; *Roosen and Angione*, 1984). The list of eruptions is presented in Table
3.2, and the resulting optical depth time series are shown in Figure 3.11 and Figure 3.12 showing
the spatial evolution.

Assuming an aerosol size distribution and composition, *Lacis et al.* (1992) showed that the
optical depth is the most important factor to determining the the forcing and with this the impact
on climate. The constructed forcing data set will be compared with observed climate data and
model simulation in the following chapters.

Historical Visible Optical Depth 1870-2000

Annual Global/N-Hem/S-Hem Optical Depth

Global Optical Depth (annual)

N-Hemispheric Optical Depth (annual)

S-Hemispheric Optical Depth (annual)

year AD
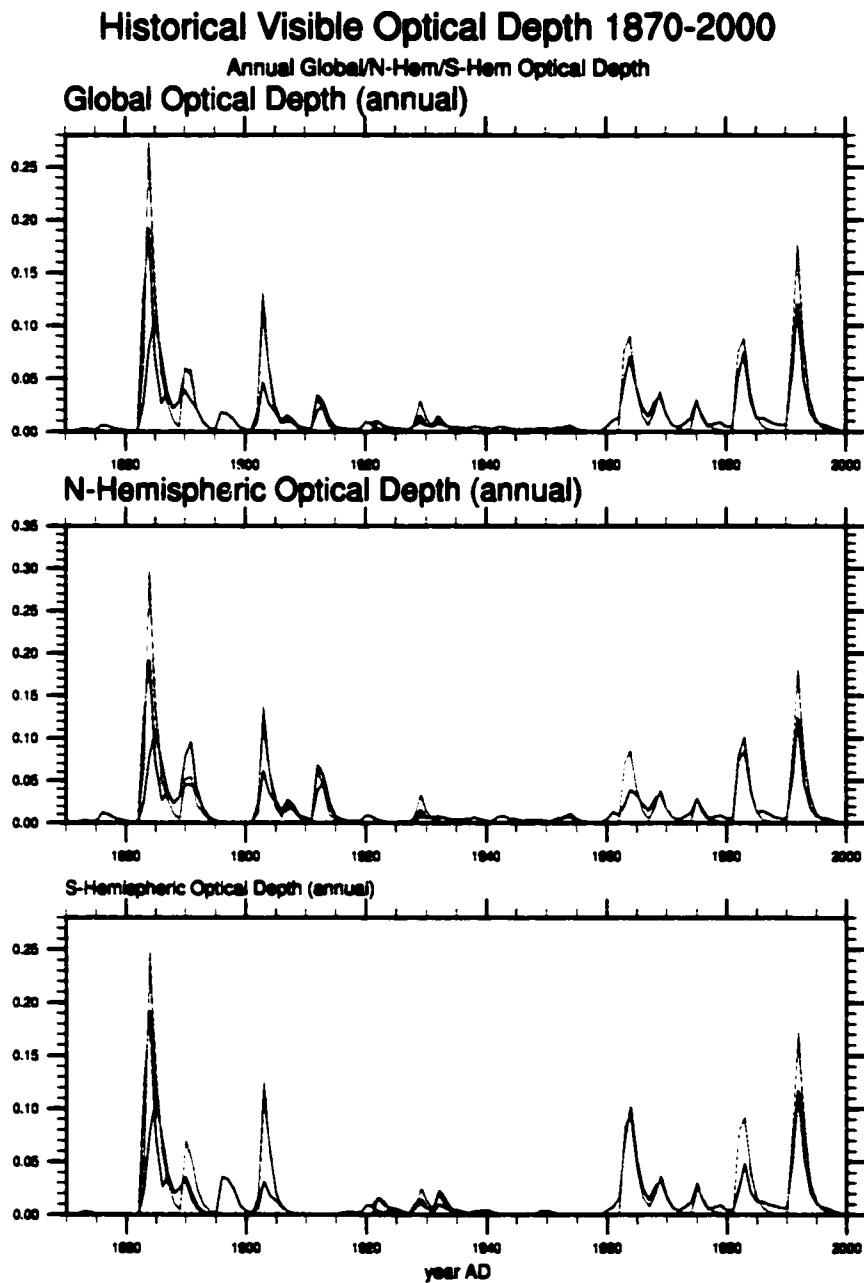
Figure 3.11: Globally averaged annual optical depth (τ_{vis}) for the seasonal parameterization (red) compared to *Stothers* (1996b) (blue) and *Sato et al.* (1993) (black).

Historical Optical Depth Forcing 1870-2000

Optical Depth with Background at 0.0001
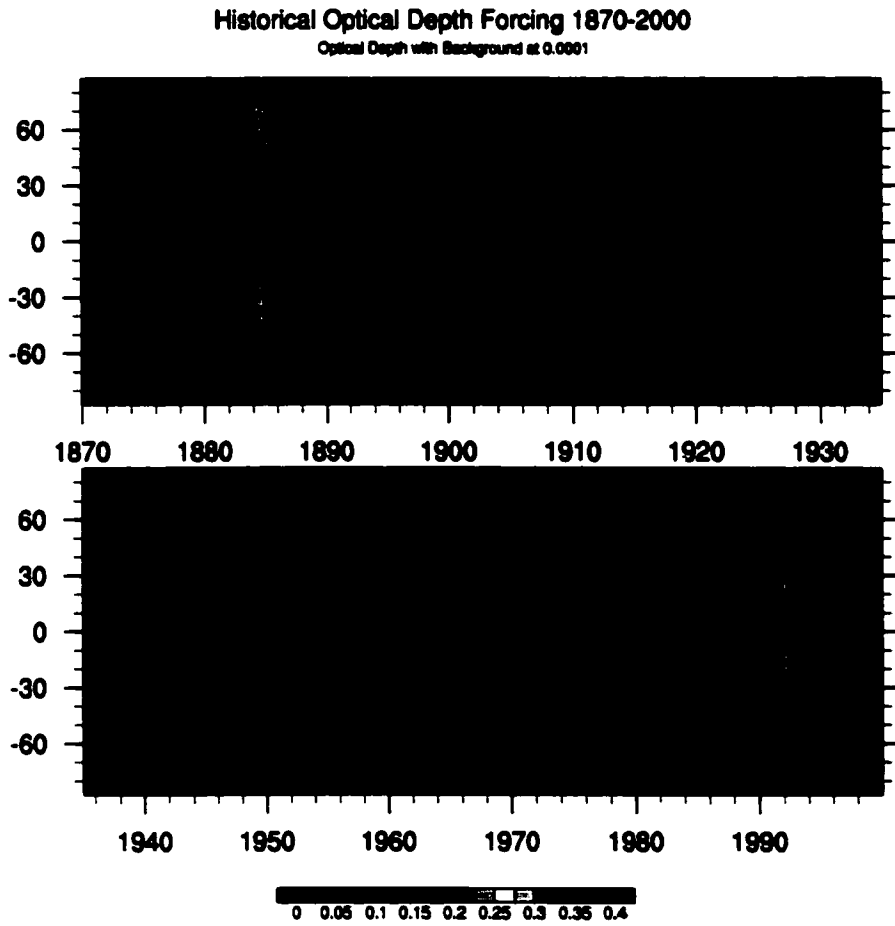
Figure 3.12: Spatial evolution of τ_{vis} using the seasonal parameterization

Volcano	Latitude	Date	Sulfate	References
Krakatau	6.1°S	Aug. 27, 1883	40-50 Tg	*Symons* (1888) *Self and Rampino* (1981); *Simkin and Fiske* (1983)
Colima (?)	19.51°N	Feb. 16, 1890	24 Tg	*Kimball* (1924)
Soufrière and Pelée	13.33,14.82°N	May 7 and 8, 1902	5 Tg	*Bullard* (1976); *Self et al.* (1981)
Santa Maria	14.76°N	Oct. 25, 1902	30 Tg	*Williams and Self* (1983); *Self et al.* (1981)
Ksudach	51.8°N	Mar. 28, 1907	4 Tg	*Macias* (1994), *Macias and Sheridan* (1995) *Braitseva et al.* (1996)
Katmai-Novarupta	58.27°N	June 6, 1912	11 Tg	*Kimball* (1913); *Volz* (1975a) *Hildreth and Fierstein* (2000)
Cordon Caulle, Puyehue	40.5°S	Dec. 13, 1921	2 Tg	*Gerlach et al.* (1988); *Abbot et al.* (1932)
Paluweh	8.32°S	Aug. 4, 1928	3 Tg	*Abbot et al.* (1932); *Hand* (1939) *Hoyt* (1978)
Komagatake	42.08°N	Jun. 17, 1929	4 Tg	*Abbot et al.* (1932)
Quizapu	35.7°S	Apr. 10, 1932	3 Tg	*Hoyt* (1978)
Spurr	61.3°N	July 9, 1953	<3 Tg	*Enqer and Fritz* (1956); *Wexler* (1956); *Bluth et al.* (1997)
Agung	8.34°S	Mar. 17, 1963	15-20 Tg	*Dyer and Hicks* (1965), *Cadle et al.* (1976) *Kern* (1983)
Fernandina	0.37°S	June 11, 1968	<3 Tg	*Simkin and Howard* (1970), *Castleman et al.* (1974)
Fuego	14.47°N	Oct. 10, 1974	2-5 Tg	*Hofmann and Rosen* (1977), *Cadle et al.* (1976) *Rose* (1977), *Lockwood and Thompson* (1986)
El Chichon	17.36°N	Apr. 3 1982	12-15 Tg	*McCormick and Swissler* (1983); *Bluth et al.* (1993) *Eparvier et al.* (1994)
Pinatubo	15.13°N	June 15, 1991	30 Tg	*McCormick et al.* (1995)

Table 3.2: List of significant eruptions since 1870, based on *Stothers* (1996b); *Sato et al.* (1993); *Robock and Free* (1995). Colima : estimate after *Stothers* (1996b) using the value for Colima as a tropical eruption. High latitude eruption aerosol mass was estimated to have been 6 Tg, and mid-latitude mass about 12 Tg. Katmai-Novarupta : Delayed part of sulfate deposition in Greenland. Much larger amount probably tropospherically transported but with very short atmospheric lifetime.

3.6 Multi-decadal periodicity in tropical explosive volcanism and its influence on climate

Caspar M Ammann[*t] and Philippe Naveau[*t]

[*] NCAR, Climate and Global Dynamics Division

[t] University of Massachusetts, Department of Geosciences

[t] Laboratoire de Météorologie Dynamique

3.6.1 Overview

During the last millennium, complex and often non-uniform patterns of cool phases with embedded warm intervals have characterized climate (*Bradley*, 2000). Explosive volcanism has been demonstrated to cool climate on inter-annual time scales (*McCormick et al.*, 1995). It has also been proposed that a series of temporally closely spaced eruptions could extend their influence on climate (*Robock*, 1978; *Porter*, 1986). However, the lack of appropriate statistical models and relatively poor records have not allowed this idea to be fully explored. Here, we present a new analysis of volcanic eruption occurrences during the past 600 years based on a compilation from recent ice core data. We demonstrate for the first time the existence of a very strong 76-year volcanic eruption cycle in the tropics. All episodes of high volcanic activity from 1550 to the present coincide with cooling periods in the Northern Hemisphere. Hence, this result supports the proposition that tropical explosive volcanism contributes significantly to multi-decadal climate variability.

3.6.2 The volcanic record from ice cores

Large explosive eruptions can inject a substantial amount of sulfur dioxide into the lower stratosphere (*Rampino and Self*, 1982), where sulfuric acid droplets form over the time period of a few

months (*Castleman et al.*, 1974). While most of the ash and the large acid droplets fall out rather quickly, a substantial amount (few to over hundred Tg $[= 10^{12}g]$ for some very large events) remains in the stratosphere. In the case of tropical eruptions, the aerosol cloud spreads into both hemispheres and is transported around the globe. Effective scattering of incoming short-wave radiation by the sulfuric acid droplets results in a decrease in the direct solar beam, but an increase in the diffuse skylight. Nevertheless, volcanic aerosol clouds can reduce the surface net flux in the short wavelengths by several Wm^{-2} (*Minnis et al.*, 1993). Absorption of upwelling long-wave radiation is generally smaller (*Minnis et al.*, 1993), leading to the overall surface cooling effect of volcanoes on climate (*McCormick et al.*, 1995; *Rampino and Self*, 1982). During the time frame of a few years, meridional transport spreads the aerosols poleward, where they are deposited through general subsidence onto the polar ice sheets. Ice cores (mostly from Greenland and Antarctica) have revealed long and continuous records of volcanic sulfate (*Hammer et al.*, 1980; *Zielinski et al.*, 1994). Significant spikes from a few very large events are often used as time markers to verify the age down core and for core-to-core correlations (*Langway et al.*, 1995). Unfortunately, due to local depositional effects, up to a third of the volcanic event signals can be missing in a single core (*Zielinski et al.*, 1997). Therefore, to obtain a complete volcanic record, a large number of well-dated ice cores have to be compiled, and the sulfate spikes have to be inter-compared. *Robock and Free* (1996) constructed the Ice-core-Volcanic-Index (IVI), based on eight cores from the Northern and six from the Southern Hemisphere. For identification of the volcanic origin, these records can be compared to the extensive Smithsonian Catalogue (*Simkin and Siebert*, 1994). For a large tropical eruption with a significant sulfate component, a signal in both polar ice caps is to be expected. However, the aerosol transport for individual events can in some cases be strongly biased towards one hemisphere (e.g. Agung, *Dyer and Hicks* (1968)).

To analyze the distribution of volcanic eruptions over the last 600 years, we complement the IVI of *Robock and Free* (1996) with the most recent ice core sulfate data. We concentrate on the climatically important eruptions in the tropics ($30°N$ - $30°S$), using corresponding sulfate signals

in both polar ice caps as the selection criterion. Instead of studying the magnitude of individual events, we focus our attention on the easier problem of analyzing the frequency of large tropical volcanic eruptions. This approach allows us to significantly reduce the difficulties in core-to-core comparisons and to simplify the construction of our compilation. We find 54 explosive eruptions in the tropics since 1400, which produced a global aerosol cloud and left a recognizable sulfate signal in ice. The data is presented in Table 3.3. For the remainder of this report we concentrate on these events.

In the early part of the record, definitive identification of the source volcano was not always possible (see Table 3.3). These identification problems decrease towards the present but still persist for a few recent eruptions. Despite traces in corresponding annual layers, one cannot exclude that some peaks in both Greenland and Antarctica could represent two independent events in the higher latitudes. For example, Icelandic eruptions pose a chronic problem for many Greenland sites, and little is known about sub-Antarctic volcanism. Further problems that can affect the cross-correlation among cores include the different temporal resolution and the inhomogeneities from the various techniques applied to detect the volcanic signal (*Robock and Free*, 1996). Nevertheless, large reference events, such as Tambora (1815), Huaynaputina (1600) and Kuwae (1452), help to 're-calibrate' the chronology of the different cores through time (*Langway et al.*, 1995). Also, the multiple ice core data in conjunction with a recorded tropical event in the Smithsonian Catalogue lend confidence to the compilation.

For the most recent ice/firn data from the Northern Hemisphere, the anthropogenically produced sulfate has caused a significant rise in the background concentration (*Neftel et al.*, 1985; *Mayewski et al.*, 1990; *Goto-Azuma and Koerner*, 2001). Since the detection of volcanic peaks is consequently more difficult, we complemented the ice record of the 20th-Century with compilations of observed atmospheric perturbations after tropical eruptions.

To analyze the eruption frequency, each year from 1400 to 1998 was coded by a one if sulfate spikes were recognized in both hemispheres, and zero otherwise. This binary tropical volcanic

Year	Volcano	Lat	Lon	VEI	NHem-Ice	SHem-Ice	Dust Veils
1443	' Soufriere de Guadeloupe (C-14c 1440)	16 05	61 7W	P	I.R	I.Co	
1452	Kuwae Vanuatu	-16 8	168 5E	6	I.C.R'.Lw	I.Co.Lw	
1459	' Pele.W-Indies	14.82	61 17	*	I.G.C R.Lw	I	
1463	' Kelut. Java	-8 0	112 3E	3	I.R	I	
'1490	' unknown	trop		*	I	I	
'1504	' Atitlan. Guatemala	14.58	91 2W	3*	C.R	Co'	L
1512	' Sangeang Api Sunda	-8 18	119 1E	3			
	' Gunungapi Wetar. Banda	-8 64	126 7E	3	G'.R	I	
1522	' Santa Ana. El Salvador	13 85	89 6W	3			
	' Arenal. Costa Rica (C-14 1525)	10 46	84 7W	4	I	I.M	
1554	' Merapi. Java	-7 54	110 4E	3	I.G'.R.A	Co'.M'	L
1568	' Savo. Salomon Islands	-9 13	159 8E	3			
	' Billy Mitchell (C-14 1580)	-6 09	155 2E	6	I.G'	I	
1571	' unknown	trop		*	I.G.C	Co'	
1586	Kelut. Java	-8 0	112 3E	5*	I.G C.R	I.Co'	L
'1595	Raung. Java	-8 1	114 0E	5*			
	Ruiz. Colombia	4 9	75 3W	4	I.G.R'	I.Co.Pa	L
*1600	Huvnaputina. Peru	-16 6	70 85W	6*	I.G.C R.Lw'	I.Co.Pa.Lw'	L
**1605	Momotombo. Nicaragua	12 42	86 5W	3	I.G' A	M	L*
*1619	' unknown	trop		*	I.G.R'	I.Co	
*1622	' Colima. Mexico	19 51	103 6W	3			
	Raoul Island. Kermadec (C-14 1630)	-29 0	177 9W	3	I'.C.R	I.Co	
1641	' Parker Indonesia	-6 06	124 5E	6	I.G.C R	I.Co	L
1660	' Teon. Banda	-6 92	129 1E	4*			
	' Guagua Pichincha. Ecuador	-0 17	78 6W	4	I.G	I.Co'	L
1665	' Long Island. New Guinea (C-14 1660)	-5 35	147 1E	6*	I.G.R	I.Co'	L
1674	Gamkonora Indonesia	1 48	127 5E	5*	I'.G.C R	Co.M'	L
1680	Tongkoko. Sulawesi	1 5	125 2E	5*	C.R'	I.Co'	L
1693	Serua. Banda	-6 3	130 0E	3*	I.G.C.R'	I.Co	L
1712	' Awu. Indonesia	1 67	125 5E	3	I.G' C	I.Co'	L
'1721	Raoul Island. Kermadec (C-14. 1720)	-29 0	177 9E	3	I.G' C.A' R'	I	
	Cerro Bravo. Colombia (T)	5 09	75 3W	3	I.G' C.A' R'	I	
1728	' Sangay Ecuador	-2 03	78 1W	3	I.G C.R	I.Co	
'1737	Fuego Guatemala	14 47	90 88W	4*	G C	Co'	
1744	Cotopaxi Ecuador	-0 68	78 4W	4	I.C.R'	I	L
'1749	' Taal. Philippines	14 0	120 9E	3	I'.R'	I	
1752	' Little Sunda. Indonesia (Tambora')	-8 0	118E'	3	G' C	I.Co'	L
1760	Michoacan. Mexico	19 48	102 3W	4			
	Makian. Indonesia	0 32	127 4E	4*	I.G.R'	Co' Lw'	L
1774	' Papandajan. Indonesia	-7 12	107 7E	3			
	' Tungurahua. Ecuador	-1 47	78 4W	3	G'.C'.R'	I	L
1789	' unknown	trop		*	I.C	I	
1794	' San Martin. Mexico	18 57	95 2W	4*	I'.G	I	
1808	unknown	trop		*	I.G.C.A' R.Lw Da	I.S.Co.Da.Pa.Lw	L
1813	Soufriere St Vincent W-Indies	13 33	61 2W	4			
	Awu. Indonesia	1 67	125 5E	4*			
	Suwanose-jima. Japan	29 5	129 7E	3	I.R	I.Da	L
1815	Tambora. Sunda	-8 25	118E	7	I.G.C.A' R Da.Lw	I.S.Co.Da.Pa.Lw	L
1823	Galunggung. Java	-7 25	108 1E	5	I.G' C' A'	Co' Da M	L
1831	Babuyan Claro. Philippines	19 52	121 9E	4*	I.G.C A' R Lw	I.S' Co Lw	L
1835	Coseguina. Nicaragua	12 98	87 6W	5	I.G C Lw	I.S' Co Lw	L
1861	Makian. Indonesia	0 32	127 4E	4*	I.G R'	S Co	L
1880	Fuego. Guatemala	14 47	90 9W	4*			
	Cotopaxi. Ecuador	-0 68	78 4W	3	I.C	I	
1883	Krakatoa. Sunda	-6 1	105 4E	6	I.G C.R.Lw	I.S.Co Lw Bu	L.St
1890	Colima. Mexico	19 51	103 6W	3	I.G.A' R'	I.S' Co.Bu'	St
1902	Pelee W-Indies	14 82	61 2W	4			
	Soufriere St Vincent W-Indies	13 33	61 2W	4	I.G C	I.Co	L.St
1903	Santa Maria. Guatemala	14 76	91 5W	6*	I.G C R	I.Co Bu	L.St
'1911	Lolobau SW-Pacific	-4 9	151 2E	4			
	Taal. Philippines	14 0	120 9E	4			
	Semeru. Java	-8 1	112 9E	3	I.C	I.Co' Bu'	Ha
1928	Paluweh. Sunda	-8 32	121 7E	3	I.G A' St	LF' Bu'	St
1951	Ambrym. Vanuatu	-16 0	168 1E	4-			
	Lamington. New Guinea	-9 0	148 1E	4			
	Bagana. SW-Pacific	-6 0	155 2E	4	I.G' A'	I.LF'.Bu'	L*
1963	Agung. Sunda	-8 34	115 5E	4	I' C A'	I.Co LF Bu	L.DH.Sa
1968	Fernandina. Galapagos	-0 37	91 5W	4	I.G C A.R	I'	L.Sa
1974	Fuego Guatemala	14 47	90 9W	4	C R'	LF' Bu	HR.V Sa
1982	El Chichon. Mexico	17 36	93 2W	5	I.G' A.R Z	LF	Th.Ho Sa
1991	Pinatubo Philippines	15 11	120 1E	6	A.Z	CoD Di.Kr	Mi.Mc.Sa

Table 3.3: Tropical eruption List derived from ice cores - Year: Year of sulfate deposition. ∗ = 1 year due to different seasonality of eruptions. *age correction of −2 or −3 years for GISP2 probable *de Silva and Zielinski* (1998). Volcano: potential source volcano from the Smithsonian Catalogue (*Simkin and Siebert*, 1994). Lat: Latitude of eruption. trop: tropical eruption due to sulfate deposition in both hemispheres. VEI: corresponding Volcanic Explosivity Index from Smithsonian Catalogue, listed for comparison, but not a criterion for the selection process. P: Plinian eruption. NHem-Ice: Ice core data indicating a sulfate spike in a Northern Hemisphere core. SHem-Ice: Ice core data indicating a sulfate spike in a Southern Hemisphere core. Dust Veils: Label L if a eruption is registered in Lamb's Dust Veil Index (*Lamb*, 1970), and in 19th and 20th-Century for observed perturbations in the lower stratosphere. L*: *Lamb* (1970) refers to a note from Arakawa and Tsutsumi (1956) that no volcano but nuclear bomb tests in the tropical Pacific might be responsible for the veil. (Sources: A Agassiz ice (*Fisher and Koerner*, 1994; *Zheng et al.*, 1998); Bo Boutron (1980); Pb and Zn as proxies for volcanic deposits; C *Crowley* (2000); Re-evaluation of Crete data by *Hammer et al.* (1980); Co *Cole-Dai et al.* (1997a); CoD *Cole-Dai et al.* (1997b); Da *Dai et al.* (1991); DH *Dyer and Hicks* (1968); Di *Dibb and Whitlow* (1996); G GISP2 (*Mayewski et al.*, 1993; *Zielinski et al.*, 1994; *Zielinski*, 1995); Ha von Hann (1915); Ho Hofmann (1987); HR *Hofmann and Rosen* (1977); I IVI (*Robock and Free*, 1996); Kr *Kreutz et al.* (1999); L *Lamb* (1970); Le *Legrand and Delmas* (1987); LF *Legrand and Feniet-Saigne* (1991); Lw *Langway et al.* (1995); M *Moore et al.* (1991); Mc *McCormick et al.* (1995); Mi *Minnis et al.* (1993); Pa *Palais et al.* (1990); R GRIP ECM and Acidity *Clausen et al.* (1997); S *Stenni et al.* (1999); Sa *Sato et al.* (1993); St *Stothers* (1996b). Th *Thomas et al.* (1983a); V *Volz* (1975b); Z *Zielinski et al.* (1997).

data set is represented by green spikes in Figure 3.13. To detect the low frequency signal present in this binary time series, a weighted moving average (blue line) was applied to the data. The dominant feature of this curve is a striking cycle of approximately 76 years.

3.6.3 Statistical method

3.6.3.1 Statistical model

To complement this graph and to provide a more exhaustive statistical analysis of the frequency of the eruptions, we developed a probabilistic model which has the advantage of summarizing the key features present in our time series. Its binary nature and non-stationarity imply that a classical spectrum analysis is not appropriate and a tailored statistical model has to be developed. There exists a long history of modeling binary data in the statistical literature ($Agresti$, 1990). In particular, the $logistic$ model has received special attention because of its flexibility and simplicity. The basic idea is to define the probability of observing an eruption during the t-th year as a function of time, $p(t) = \pi(\lambda(t))$ where $\pi(x) = \exp(x)/(1 - \exp(x))$ and $\lambda(t)$ is called the $logit$-$link$. The main difficulty is to find a reasonable and simple logit-link. Motivated by the moving average in Figure 3.13, we choose to decompose the logit-link function into the sum of two components, $\lambda(t) = \lambda^{(A)}(t) - \lambda^{(B)}(t)$. The first term represents periodicities, i.e.

$$\lambda^{(A)}(t) = \sum_{i=1}^{m}(\theta_{1,i}\cos(2\pi t/T_i) - \theta_{2,i}\sin(2\pi t/T_i)).$$

where m is the number of cycles, T_i the length of the i-th cycle, and the θ's are the parameters to be estimated. The second component corresponds to the long-term fluctuation (black line in Figure 3.13 and is modeled by $\lambda^{(B)}(t) = \theta_1 - \theta_2(1 - \exp(-\theta_3 t))$ (note $\lambda^{(B)}(t)$ increases from θ_1 to $\theta_1 - \theta_2$ for t large). Hence, the global logit-link can be written as:

$$\lambda_\theta(t) = \text{cycles} - \text{overall trend.}$$
$$= \sum_{i=1}^{m}(\theta_{1,i}\cos(2\pi t/T_i) - \theta_{2,i}\sin(2\pi t/T_i)) - [\theta_1 - \theta_2(1 - \exp(-\theta_3 t))]. \quad (3.1)$$

90

The next step is to estimate the unknown parameters $(\theta_1, \theta_2, ...)$ in (3.1) for a given multi-decadal set up, i.e. for different m and T_i.

3.6.3.2 Parameters estimation and model selection

The estimation of these parameters is carried out by maximizing the likelihood function $l(\theta)$, which is the probability of observing our data relative to θ. This classical procedure consists of selecting θ which maximizes $l(\theta)$. If we assume that eruptions occur independently, then $l(\theta) = \prod p_\theta^{v_t}(t)(1 - p_\theta(t))^{1-v_t}$ where v_t represents a volcanic event (0 or 1), $p_\theta(t) = \pi(\lambda_\theta(t))$, and $\lambda_\theta(t)$ is defined by (3.1). The maximization of $l(\theta)$ is undertaken by using classical optimization methods.

Although the moving average in Figure 3.13 varies with the window size, the 76-year cycle is also present for different windows (from 15 to 40 years). Here, the weights of the 36-year moving average are equal to $w \exp(-|t|/18)$ if $|t| \leq 18$ and 0 otherwise (w is chosen such that the sum of the weights equals to 1). These weights and the 36-year window have been chosen because of their excellent visual agreement with our models (red line), but they did not play any role in the parameter estimation. As can be seen in Figure 3.13, the logistic model with a cycle of 76 years (red curve) provides a very good estimate of the probability of observing an eruption over time. The probability oscillates significantly in time, from roughly 5 to about 17 percent, the peak phases being at least 3 times stronger than the low intensity phases.

In order not to rely exclusively on visual devices, another diagnostic tool for assessing the fit by (3.1) is needed. The problem of selecting a good model is related to the risk of over-parameterization, i.e. obtaining an excellent fit with an overly complex model that has the disadvantage of a very poor predictive quality due to the high number of parameters. One of the most popular criterion for model selection is the Akaike's Information Criterion (AIC) (*Petrov and Csaki*, 1973; *Stone*, 1977; *George*, 2000). The AIC is based on the likelihood function, which reflects the quality of the fit, and on a penalty cost proportional to the number of parameters.

In our case. the AIC can be expressed as

$$\text{AIC}(\theta) \quad = \quad \text{fit quality} - \text{penalty for adding parameters.}$$

$$= \quad -2 \ln l(\theta) - 2c(\theta).$$

where $c(\theta)$ represents the number of parameters. A small AIC indicates a competitive model. and the best model is the one with the smallest AIC. The "random" model (black circle in Figure 3.14) corresponds to the case where volcanic events are assumed to be completely random. Its AIC should be viewed as the reference (dotted line). Then. the model which only fits the overall trend (green cross) has 2 more parameters. This addition improves the log-likelihood by approximately 2 units. but the AIC is relatively unchanged. In comparison. the addition of 4 parameters with a 76-year cycle (blue circle) improves the log-likelihood by approximately 6 units and the AIC by 2.5 points. respectively. This net difference indicates a much better model. as seen in Figure 3.13. The same type of reasoning can be used to interpret other models.

3.6.4 Results

Figure 3.14 summarizes the selection process among different logistic models. in particular the ones that incorporate the cycles previously proposed in volcanic eruption data sets. *Stothers* (1989) recognized two week cycles of 80 and 11 years in an acidity record from Greenland as well as in the VEI. The AIC clearly shows that neither a 11 nor a 80-year cycle provide a good fit for our data set. the 76-year cycle being the most efficient to fit the tropical volcanic eruption occurrences. Note. *Stothers* (1989) did not take advantage of the binary nature of volcanic occurrences and dismissed an overall trend by stating that "it is reasonable to regard the record as roughly stationary for the VEI > 3". We also make use of significantly improved data from both ice cores and VEI (see Table 3.3. Besides the cycle of 76-years. both much shorter and longer cycles could be present in our compilation. The length of the time series given here does not allow us to study long-term variability much beyond about 100 years. and the rarity of large

Frequency of Tropical eruptions (30N,30S)
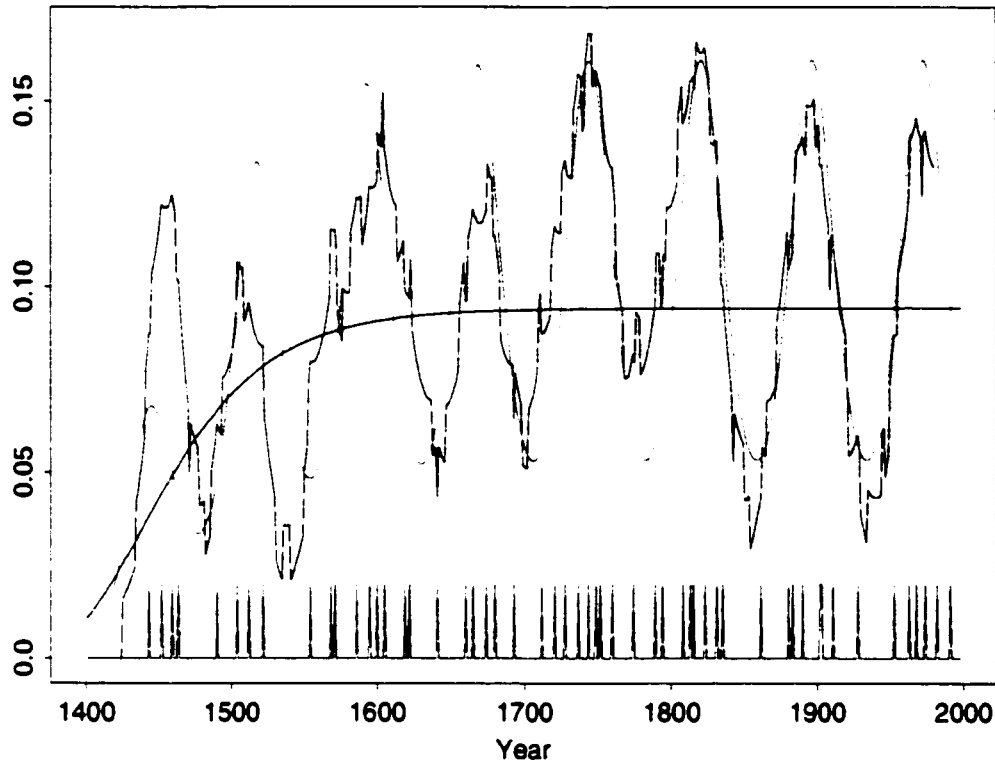
Figure 3.13: Logistic regression model with a 76-year cycle (red line) and a 36 year moving average (blue line) through binary eruption data (green spikes). The black line represents the overall trend.

tropical eruptions (around one per decade) makes the investigation of short cycles (<20 years) difficult. For example. the 11-year sunspot cycle proposed to be present in the data (*Stothers.* 1989) might not be properly resolved with this data set. Keeping this limitation in mind. we evaluate the possible contributions of the lunar nodal cycle of 18.6 years (*Currie.* 1994) to the eruption frequency. But it cannot provide a better AIC. Overall. the best model combines a trend with a 76-year cycle (blue circles).

While from a visual and statistical point of view. it is very difficult to refute the existence

Quality of fit of 10 logistic models
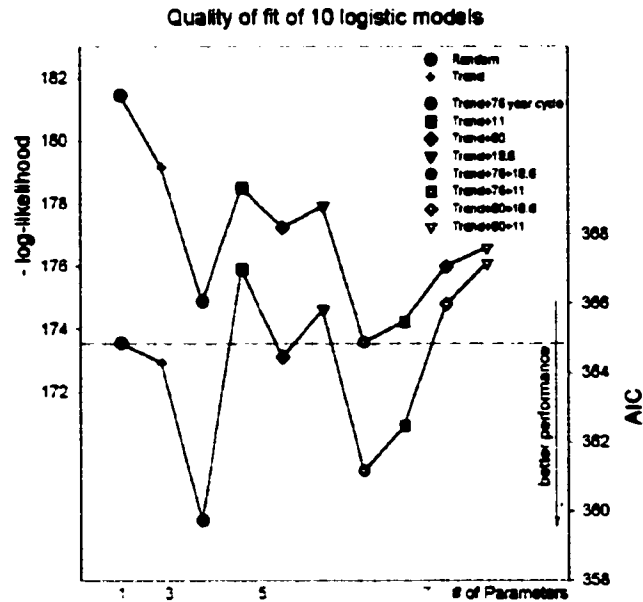
Figure 3.14: Selection among 10 logistic models defined by equation (3.1). The simplest model corresponds to the "random" model (black circle). The most complex models have 7 parameters and correspond to an overall trend with 2 cycles (red symbols). The quality of fit of these models is measured by the negative log-likelihood (upper curve) which has the disadvantage of not penalizing for the addition of parameters and by the more efficient AIC (lower curve) that penalizes for additional parameters. The smaller the AIC, the better the fit. The model with an overall trend and a 76-year cycle (blue circles) provides the best AIC, and therefore the best fit.

of this 76-year cycle in our compilation. we still need to confirm that no subtle changes in the background acidity. caused by an independent factor. could be responsible for this periodicity. To reduce this possibility. the same methodology is applied to the Volcanic Explosivity Index (VEI) (*Newhall and Self.* 1982) that was constructed independently from any climatic or ice-core records. We selected all tropical eruptions with a VEI > 3 from *Simkin and Siebert* (1994). which correspond to large and violent events that most probably injected ash and gases in the stratosphere (*Newhall and Self.* 1982). A similar statistical study (not presented here but available from the authors) indicates that the same 76-year cycle is also present in the VEI. although with somewhat less clarity. We conclude that changes in the background level of sulfate are clearly not responsible for the 76-year cycle.

3.6.5 Potential climate impact?

Large stratospheric sulfate injections from explosive volcanism have been shown to significantly impact climate on inter-annual time scales (*Kelly and Sear.* 1984; *Bradley.* 1988; *Briffa et al..* 1998). To assess the multi-decadal climate impact of the strong 76-year volcanic cycle. we compare our statistical model in Figure 3.15 with the Northern Hemisphere annual temperature reconstruction of *Mann et al.* (1998). The key feature from this comparison is that *all* episodes of high eruption frequency from 1550 to the present correspond to local minima in the temperature reconstruction (the converse being false). In comparison. the association between solar activity (represented in Figure 3.15 by sunspots group numbers from *Hoyt and Schatten* (1998) and secularly smoothed aurora observations from *Gleissberg* (1965)) and the temperature minima is visible. but not as clearly as with volcanic occurrences. Hence. sulfur rich explosive volcanism. acting beyond the influence of individual events. appears to be an essential component for driving multi-decadal climate variability. It is interesting to note that many of the high volcanic activity phases seem to coincide with solar indices showing at least local minima (see Figure 3.15). If there is indeed a link and how it would work is purely speculative at this point. Interestingly.

the multi-decadal changes of the solar radius proposed to exhibit a cycle of 76 years (*Gilliland,* 1981; *Fröhlich and Eddy,* 1984) are almost in phase with the volcanic eruption probabilities.

In conclusion, we have demonstrated that the temporal distribution of global volcanic sulfate forcing exhibits a strong cycle of about 76 years, with large explosive eruptions occurring every 5 years at its peaks. Short temporal spacing has been previously invoked as a necessary condition for volcanism to perturb climate on decadal time scales (*Bradley,* 1988; *Wigley,* 1991). Besides validating such conditions, we show that all peaks in the volcanic cycle coincide with Northern Hemisphere temperature depressions, at least from 1550 to present. Our results also suggest repeated conjunction of increased volcanic activity with lower solar activity. Therefore, isolated correlation analysis between either solar or volcanic forcing and climate have to be performed with caution. Additionally, further research is required to investigate potential mechanisms responsible for the 76-year cycle.
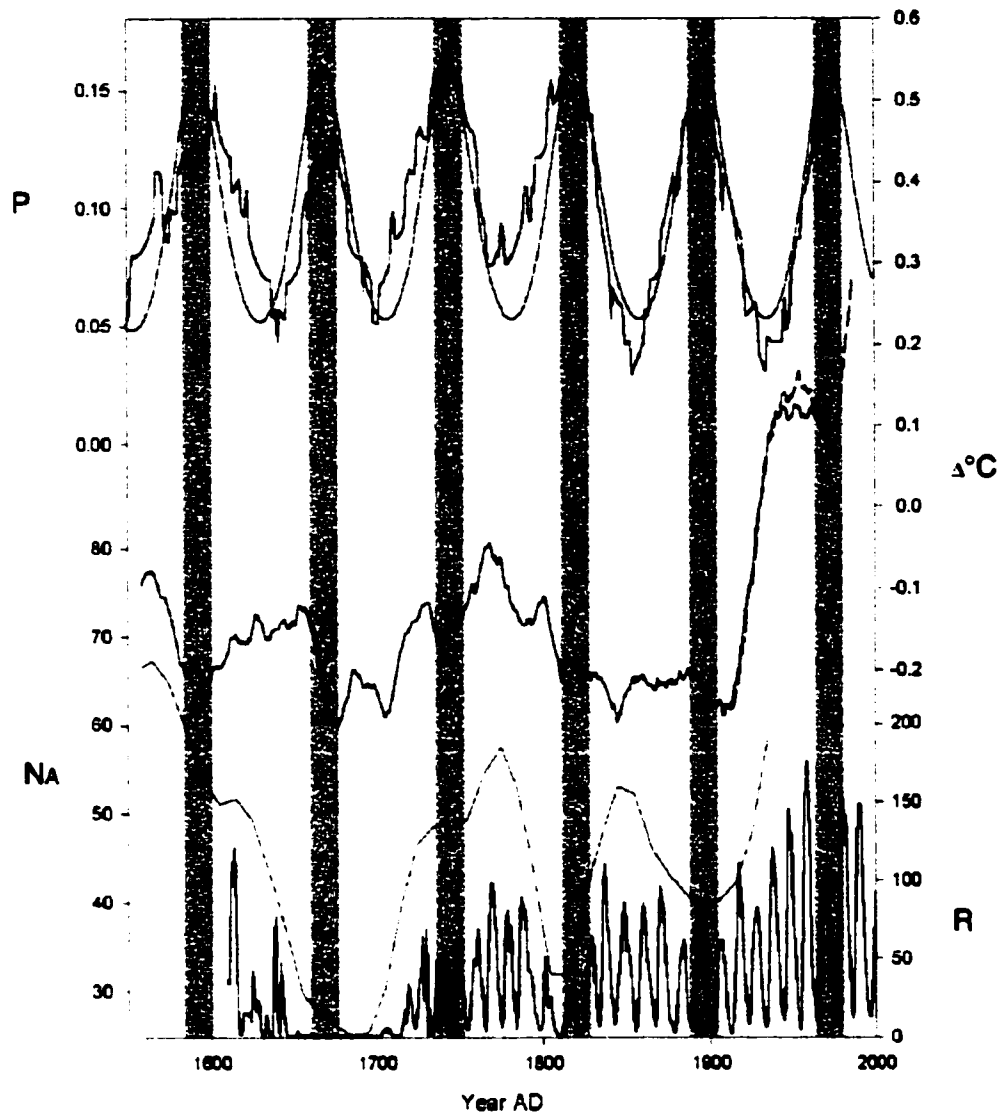
Figure 3.15: External climate forcing on multi-decadal scale. Top: Annual probability P for an explosive volcanic eruption in the tropics (blue line) with a logistic model (red line) from Figure 3.13. Middle: Reconstruction of annual Northern Hemisphere temperature anomaly ($\Delta°C$) of *Mann et al* (1998) relative to the average from 1902-80 smoothed with a 20-year running average (dark green line). Bottom: Group-sunspot numbers R since 1610 (*Hoyt and Schatten.* 1998) (black line). and secularly smoothed auroral frequency numbers N_A (*Gleissberg.* 1965) (purple line).

Chapter 4

CLIMATIC IMPACT OF EXPLOSIVE VOLCANISM FROM PROXY DATA

4.1 Introduction

Large volcanic eruptions in the tropics can significantly perturb the atmospheric radiative budget. The eruption of Pinatubo in 1991 caused a negative net radiative flux of 3-4 Wm^{-2} (*Minnis et al.*, 1993; *McCormick et al.*, 1995), resulting in a global surface cooling of several tenths of a degree Celsius. The temperature drop started almost immediately after the eruption and peaked roughly one year later, in fall 1992 (*Hansen et al.*, 1996a; *Parker et al.*, 1996). Many studies have focused on identifying intermittent climate cooling due to large volcanic eruptions (*Franklin*, 1785; *Humphreys*, 1940; *Mitchell*, 1961; *Lamb*, 1970; *Oliver*, 1976; *Pollack et al.*, 1976; *Baldwin et al.*, 1976; *Hansen et al.*, 1978; *Robock*, 1981; *Self et al.*, 1981; *Kelly and Sear*, 1984; *Bradley*, 1988; *Parker*, 1988; *Robock and Mao*, 1992, 1995), as well as the spatial distribution of

the anomalies (*Groisman*, 1992; *Kelly et al.*, 1996). Many of these studies suffer from the lack of enough significantly large events, where a separation of the signal from the climate background noise is possible.

Recently, a new climate reconstruction with unprecedented spatial coverage and resolution was constructed, offering a new opportunity to substantially extend the time frame in which large events can be studied, and to achieve a more viable look at this statistical problem. Here we want to make use of the nearly 600-year global climate reconstruction of *Mann et al.* (1998), which allows us to extend the study significantly in time and space. The reconstruction is based on a diverse, globally distributed proxy network, allowing not only a look at climate variability at a specific location, but also at the level of large scale patterns which could carry additional information (*Bradley and Jones*, 1993; *Barnett et al.*, 1996; *Mann et al.*, 1998, 2000). We analyze the signal of the 20 largest tropical eruptions covered by this reconstruction. We then compare the response pattern to natural modes of climate to see if the volcanic forcing tends to enhance or suppress some of the major modes of climate variability or if a distinct response pattern can be found. The response pattern to large volcanic eruptions will be evaluated on the interannual and multidecadal time scales. Finally, the potential differences between climate signals (as found in single proxy time series) and large scale pattern reconstructions are discussed.

4.2 Volcanic Eruption Data

Although explosive volcanic eruptions occur quite frequently (see *Simkin et al.*, 1981; *Simkin and Siebert*, 1994), events with discernible (radiative) effects on the earth energy balance are much less common, maybe on the order of one event per 1-2 decades (*Bluth et al.*, 1997). *Rampino and Self* (1982), *Sigurdsson* (1990) and others have shown that it is not primarily the magnitude of the eruption that is responsible for influencing the global climate but, more specifically, the amount of sulfur injected into the stratosphere. Only a relatively small number of large events

meet this criteria (*Stothers*, 1996b). A relatively detailed record of explosive volcanism can be constructed from sulfate deposits identified in ice cores (*Hammer*, 1977; *Hammer et al.*, 1980; *Legrand and Delmas*, 1987; *Delmas et al.*, 1992; *Zielinski et al.*, 1994; *Zielinski*, 1995; *Robock and Free*, 1995; *Clausen et al.*, 1997; *Cole-Dai et al.*, 2000; *Ammann and Naveau*, 2001). In order to obtain a sufficiently complete and reliable record, information from a large number of ice cores has to be compiled (*Zielinski et al.*, 1997; *Robock and Free*, 1996). Additionally, an important issue involves the identification of the source volcanoes responsible for the sulfate deposits. Given a certain sulfate flux, the derived atmospheric perturbation would be very different for a high latitude eruption compared to a tropical source (*Legrand and Delmas*, 1987; *Zielinski*, 1995). A way around this problem is to combine ice core information of both polar ice caps. All years with sulfate deposition in both hemispheres are candidates for tropical events. A number of problems including accurate chronologies of the individual ice cores, hemispheric biases in the sulfate transport, as well as independent high latitude eruptions can perturb the record. But if the ice core data are compared with additional volcanic information, such as the Dust Veil Index (DVI, *Lamb*, 1970, 1983) or the Volcanic Explosivity Index (VEI, *Newhall and Self*, 1982; *Simkin and Siebert*, 1994), most of the large events can be identified. Additionally, a compilation of latewood density data from tree rings collected in the Northern Hemisphere has been shown to be extremely sensitive to volcanic perturbations during the summer season (*Briffa et al.*, 1998). Comparison of the sulfate events with this tree ring record lends further confidence in the selection procedure.

Table 4.1 lists the selected eruptions of this study and how they are classified in the various volcanic indices over the last 600 years. The ice-core volcanic index (IVI) of *Robock and Free* (1996) was used as the main selection criteria because it is least biased towards observational coverage and takes the important sulfur content of volcanic emissions directly into account. Years with volcanic sulfate in both polar areas were selected and ranked by their respective radiative forcing computed from the standard-deviation of sulfate above the background level at each site

100

(see *Robock and Free*. 1995). For comparison. the corresponding values of other commonly used volcanic indices are listed in Table 4.1.

Very clearly. the two largest events. Tambora (1815) and Kuwae (1452/3) tower over the other events. They are followed by the eruption of Parker (1641) and the still unknown volcano that erupted at some point during 1808. Then. a group containing Huaynaputina (1600). Krakatau (1883) and Pinatubo (1991) form the next well recognized set of events. Careful consideration of available information then leads to the conclusion that starting with Kelut (1586). the confidence decreases significantly in the association and therefore the forcing estimate of smaller events. This is supported by a host of observations:

- Source Volcano: The large deposit of 1587 and 1588 has not been related to Kelut with high certainty. Kelut is a volcano with a large crater lake that has the tendency to cause dangerous mud flows. Although the eruption of 1586 is classified as '5?' in the VEI and is known to have claimed thousands of life's (*Sapper*, 1927). it cannot be excluded that the major part of the volcanic perturbation of the global atmosphere in that year is from another source. *Zielinski* (1995) suggested the very large eruption of Billy Mitchell (VEI = 6). a candidate yet to be precisely dated (tentatively set to the ^{14}C date of 1580). Further association problems are clearly visible with the increasing number of question-marks in the list. especially the early ones.

- VEI values: While all the eruptions up to Krakatau were very clearly of enormous magnitude. carrying VEI values from 5 to 7. this is no longer the case for some of the lower ranked events. Smaller. less known eruptions. but with high sulfate amounts. such as the eruption of Agung (1963). are included.

- DVI classification: The general decrease in the DVI as one moves down the list confirms the decreasing uniqueness of these smaller events. Nevertheless. there are a couple events missing that were classified with a DVI of 1000 or larger. One event is Mayon (1766)

Rank	Volcano	year-used	Lat	Lon	IVI	DVI	VEI	Rank$_{tr}$
1	Tambora, 1815	1816	8.3S	118E	15	3000	7	2
2	Kuwae, 1452/3	1453	16.8S	168.5E	10	-	6*	4
3	Parker, 1641	1641	6.1N	124.9E	6.7	1000	6	3
4	'Unknown, 1808	1809	'	'	5.6	1500	6^{k}	-
5	Huaynaputina, 1600	1601	16.6S	70.9W	4.1	1000^{a}	6	1
6	Pinatubo, 1991	1992	15.1N	120.4E	4*	> 1000	6	20
7	Krakatau, 1883	1884	6.1S	105.4E	3.7	1000	6	13
8	Kelut, 1586	1587	7.9S	112.3E	3.2	1000	5?	17
9	Coseguina, 1835	1836	13N	87.6W	3.2	4000	5	21/15
10	Babuyan, 1831	1832	19.5N	121.9E	2.8	1400	4?	-
11	'Unknown (Awu?)	1714	'	?	2.6	-	3	-
12	'Serua, 1693	1695	6.3S	130E	2.6/1.9	400*	4?	6
13	Ruiz, 1595	1596	4.9N	75.3W	2.4	1000	5?/4	-
14	'Gede, 1717	1718	6.8S	107E	2.1	-	3	-
15	El Chichón, 1982	1982	17.4N	93.2W	1.9	800	5	-
16	'Rabaul, 1630^{C14}	1621	4.3S	152.2E	1.9	-	4?	-
17	Agung, 1963	1963	8.3S	115.5E	1.8	800	4	-
18	Santa Maria, 1902	1903	14.8N	91.6W	1.6	900	6	-
19	'Arenal, 1525^{C14}	1522	10.5N	84.7W	1.5	-	4	-
20	'Long Island, 1665	1666	5.4S	147.1E	1.5	500	6	12

Table 4.1: List of the largest tropical volcanic eruptions in last 600 years as derived from the IVI of (Robock and Free, 1996). Data: IVI: Robock and Free (1996); DVI: Lamb (1970, 1983), ^{a}: attribution of DVI of eruption associated with Omate in 1660, a synonym for Huaynaputina, which is mentioned already in Sapper (1927) in the same sentence as activity around 1600; VEI: Simkin and Siebert (1994); Tree-Ring ranking: Briffa et al. (1998). VEI association for Kuwae and unknown event 1808 are based on comparison of sulfate flux with other events. Kuwae might need to be upgraded to VEI=7. Double IVI value for 1695 is due to 1 year shift in southern hemisphere deposition which delivers the larger value. This event has been recently recognized as large (Cole-Dai et al., 1997a).

with a DVI of 2300 (but only VEI=3), and Galunggung (1822) with 500 for the individual event, but 2200 for the period. No clear sulfate signals are present in the IVI for both of these times, and a major climate perturbation from these eruptions must therefore remain questionable.

- Tree ring signal: The same decreasing trend can be seen in the ranking of northern Hemisphere perturbation of growing season perturbations for trees. With the exception of Santa Maria (1902), all events of the top 20 eruptions left very clear cooling signals in the tree ring data (*Briffa et al.*, 1998). A clear cooling in the year 1673 (rank 8), possibly related to the eruption of Gamkonora (VEI=5, DVI=1000), is not in the list because there is no sulfate recorded in the Southern Hemisphere in the IVI of *Robock and Free* (1996). But in a more recent study, *Cole-Dai et al.* (1997a) registered a clear signal during 1673 and 1674 in Antarctica. Using their fluxes, an updated ice core index would put Gamkonora roughly into the area of the events of 1714 and 1695, around rank 11 or 12.

Interestingly, three eruptions of the late 20th-Century are present within the top 20 events of the last 600 years. In particular, Pinatubo is ranked among the major events. Its flux was conservatively estimated to be 25% larger than the available fluxes from El Chichón (*Zielinski et al.*, 1997) in the Northern Hemisphere and set equal to the Agung deposits in the Southern Hemisphere from (*Robock and Free*, 1995). This is probably a conservative estimate, given that *Dutton and Christy* (1992) estimated optical perturbations during the first 10 months after Pinatubo to be roughly 1.7 times stronger than after El Chichón. In terms of IVI, Pinatubo is placed into the neighborhood of Krakatau. But since especially the El Chichón fluxes are taken from a single source, a re-ranking, when more ice cores covering this period will be available, cannot be ruled out. Nevertheless, Pinatubo will probably remain within the 10 largest sulfate-producing tropical eruptions during the last 600 years. El Chichón might be moved down, but the Agung signal is very prominent in all Southern Hemisphere ice cores. Its ranking, therefore,

is likely to remain more stable.

4.3 Method

We use the Superposed Epoch Analysis (subsequently SE) method (*Panofsky and Brier*, 1965) to isolate the volcanic impact on surface temperatures as reconstructed from a multi-proxy network (*Mann et al.*, 1998). So as not to bias the data towards the changes in climate, we scale the temperature anomalies of the climate reconstruction for each of the selected events at each grid cell to its preceeding 10 years. In this way, each event added into the SE-composite represents the deviation from the climate of that time rather than from an arbitrary mean. When using shorter average periods, the interannual variability dominates the signal and interpretation of the result is obscured, although the primary conclusions remain. Longer averages give results very close to the 10 year window used here. To evaluate the significance of the temperature changes, we employ the Monte Carlo technique using 10,000 iterations to subsample the climate reconstruction in the same way as for the volcanic events.

4.4 Results

Figure 4.1 shows the SE analysis of all eruptions from Table 4.1, except El Chichón and Pinatubo. These two eruptions were excluded because no consistent spatial proxy-based temperature reconstructions are available. The superposition of temperature anomalies after the 18 remaining events shows a generally clear cooling signal. The strongest temperature perturbations are found over the Northern Hemisphere continents, especially eastern North America and western Europe. A similar pattern has also been identified for the aftermath of Pinatubo, although the cooling over Europe was shifted more to the east (NCEP, not shown). Cooling is also present over the tropical Atlantic and in the western Pacific warm pool area. On the other hand, warming anomalies appear in the eastern Pacific, Alaska and areas in central Asia and the tropical Indian

Superposed Epoch of 18 Large Tropical Eruptions
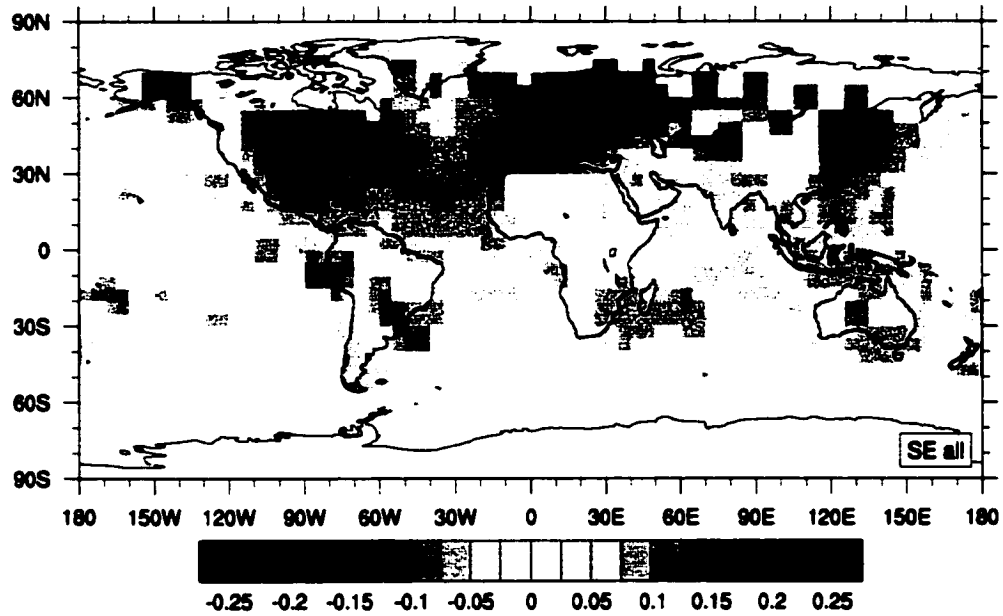
Figure 4.1: Superposed epoch analysis of 18 largest volcanic eruptions in the tropics since 1400 derived from *Robock and Free* (1996) IVI data shown in Table 4.1 with exception of 1991 Pinatubo and 1982 El Chichón. because they are not included in the proxy series used by *Mann et al.* (1998).

Ocean. To analyze which of the superposed temperature anomalies are significant. we performed a Monte Carlo simulation. applying 10.000 iterations of 18 randomly sampled years for which anomalies to the previous 10 years were computed. The procedure was performed exactly the same way for this as for the volcanic events. Figure 4.2 shows the same surface temperature anomalies. but only for areas with significant temperature changes. A significance level of 90% was chosen. Note. these significance levels apply only under the assumption of stationarity of El Niño variations over time. A more conservative approach might be required.

Clearly. the cooling found in the northern hemisphere is very unusual as compared to a random selection of any 18 years. Most of the cooling from eastern North America to western Europe is actually significant above the 95% level (see Figure 4.3). Also significant is the somewhat smaller

Superposed Epoch of 18 Large Tropical Eruptions
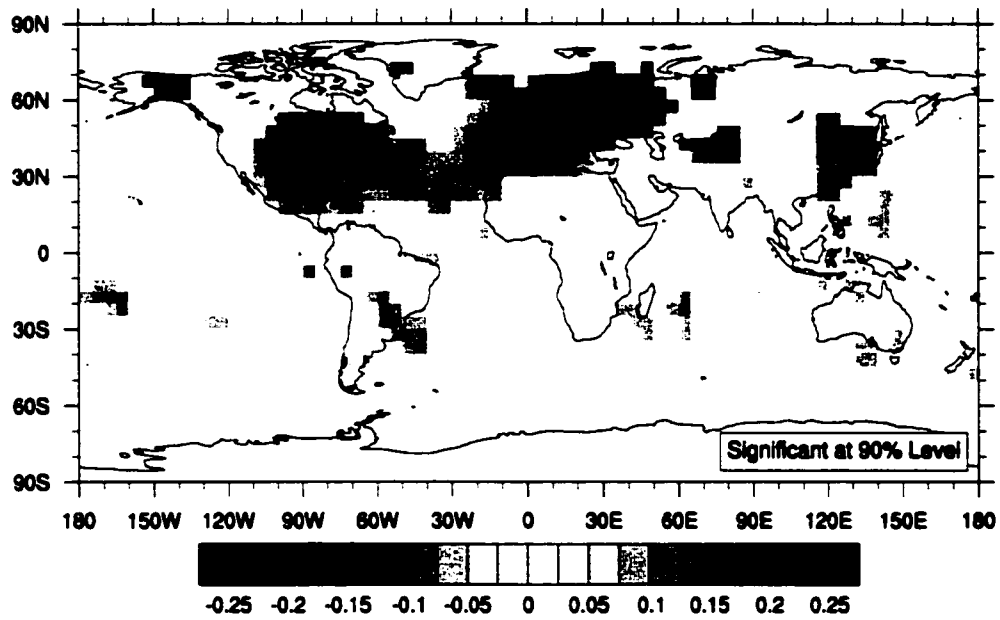
Figure 4.2: Same as Figure 4.1 but exclusively areas with anomalies significantly (> 90%) different from random. The level was determined in a Monte Carlo study sampling 10.000 times superposed anomalies of 18 random events.

Superposed Epoch of 18 Large Tropical Eruptions
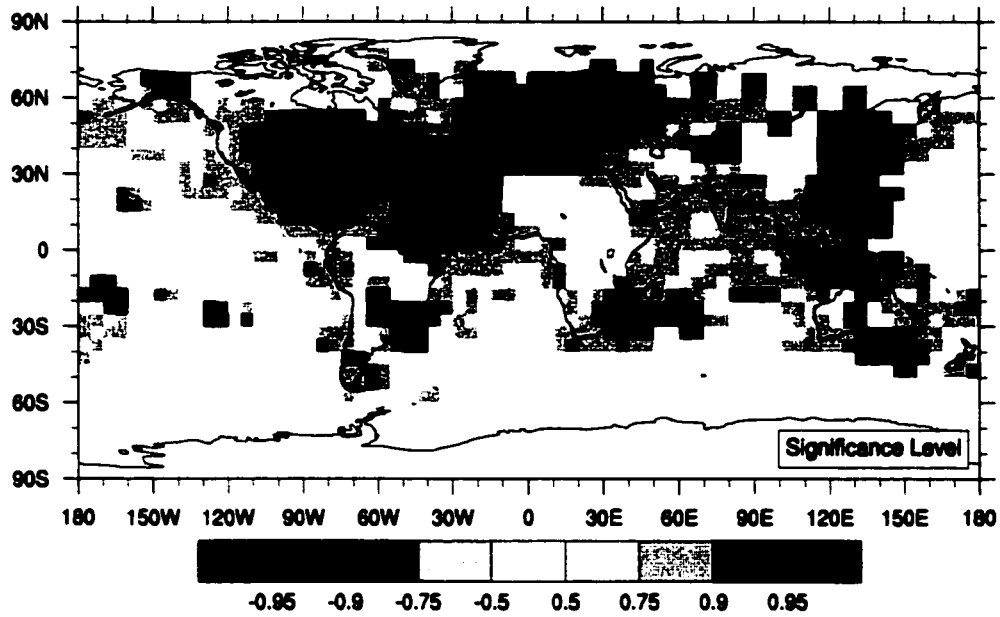
Figure 4.3: Significance level for volcanic composite anomalies determined in a 10.000 iteration Monte Carlo study.

cooling in far eastern Asia. as well as a spotty distribution of single grid cells in the southern hemisphere. Warm anomalies are significant mainly in Alaska and central Asia. again with some locations in the eastern Pacific and adjacent South America.

4.4.1 Pattern in the North Atlantic sector

In general. the cold anomalies are dominating the signal and confirm the expectation of volcanic cooling. The spatial pattern gained from the multi-proxy network reproduces a similar structure found in composite studies of *Groisman* (1992) and *Kelly et al.* (1996). both of which used instrumental time series. The differences. as compared to the cited studies. generally include their patterns of winter temperatures. where they identify warming tendencies over a large part of the area. The reconstruction of *Mann et al.* (1998) is annual mean temperatures. and hence.

opposing signals between summer and winter might tend to cancel each other. The anomalies after the largest volcanic events seem to be dominated by the summer cooling. whereas the winter warming might be smaller. or at least not that well captured by the proxy time series. Generally. compared to the two summer temperature reconstructions of northern hemisphere of *Briffa et al.* (1998) and *Jones et al.* (1998). the *Mann et al.* (1998) is less sensitive to volcanic cooling. suggesting that it might retain a winter warming component in the data. For more detailed investigation of the North Atlantic area response to volcanic eruptions see Chapter 6.4.

4.4.2 Anomalies in the eastern equatorial Pacific

The spatial pattern of warm anomalies in Figure 4.1 is somewhat surprising. A large area of uninterrupted warm anomalies emerges in the eastern equatorial Pacific. where warming is commonly connected with El Niño events. A general similarity to the El Niño pattern can also be seen in other locations (e.g.. *Halpert and Ropelewski.* 1992): Warming in Alaska and cooling over the western Pacific are common teleconnections. The tendency for cooling over the south eastern US completes the large scale anomalies expected for El Niño years. Less El Niño like are the anomalies seen in other areas. primarily over some ocean basins. While a general warming in the Indian Ocean could be expected. a strong cooling in the tropical South Atlantic would be more common than the warming in the SE-composite. The warming in the eastern equatorial Pacific would generally also penetrate into the Caribbean. Despite these differences and the fact that the warm anomalies in the eastern equatorial Pacific are significant only in a few grid cells (see Figures 4.2 and 4.3). an El Niño fingerprint seems to be present in the composite. We now evaluate this signal by looking at individual events to verify if a few of them could dominate the composite as pointed out by *Nicholls* (1990). We then compare the *Mann et al.* (1998) proxy composite with independent indices for sea surface temperature anomalies in the NINO3 area (5°N-5°S. 90-150°W). as well as for the atmospheric component of the Southern Oscillation.

4.5 Volcanic eruptions and El Niño. Is there a relationship?

El Niño events (here used as the coupled El Niño - Southern Oscillation system) are an important component of interannual natural climate variability. Similar to perturbations from volcanoes, El Niño events can influence climate for roughly a year (although either can last for a shorter or longer period), and their spatial impacts are recognized over most parts of the globe (*Halpert and Ropelewski*, 1992; *Philander*, 1990; *Glantz et al.*, 1991; *Allan et al.*, 1996). El Niños, responsible for a major part of the internal climate variability (*Philander*, 1990), recur over a range from about two to roughly seven or eight years. A number of instrumental (*Allan et al.*, 1996; *Können et al.*, 1998), documentary (*Quinn et al.*, 1987; *Quinn and Neal*, 1995; *Ortlieb*, 1994, 2000) and proxy records (e.g. *Thompson et al.*, 1984, 2000; *Cole et al.*, 1993; *Dunbar et al.*, 1994; *Stahle et al.*, 1998) are available that allow an evaluation of its occurrences during the last several hundred years. Problems include stationarity of the teleconnection patterns (*Meehl and Branstator*, 1992; *Mann et al.*, 2000) and exact dating of some of the records, especially coral data (*Dunbar et al.*, 1994). An alternative is to use a reconstruction based on a diverse, globally distributed proxy records, allowing not only a look at a specific location in the eastern equatorial Pacific, but at the same time at a large scale pattern, which could carry additional information (*Bradley and Jones*, 1993; *Barnett et al.*, 1996; *Mann et al.*, 1998, 2000).

There has been a discussion as to whether occurrences of El Niños and explosive volcanism are independent or somehow related. *Handler* (1984, 1986), *Parker* (1988) and *Handler and Andsager* (1990) have suggested that tropical volcanic eruptions since 1860 were followed by El Niño events, and even a close cause and effect relationship has been claimed to the extent that every El Niño was ultimately caused by a volcanic eruption (*Handler and Andsager*, 1990). This conclusion was reached looking at 11 tropical events between 1868 and 1980, taken from *Newhall and Self* (1982) and an updated version of the Smithsonian Catalogue of *Simkin et al.* (1981).

Using the SE method, a 'common' response, in the form of a warming in the eastern equatorial Pacific between $20°S-20°N$, was found for up to four seasons after the tropical eruptions, and an opposite trend was established for high latitude events (not discussed here). This link was then investigated for the large eruption of El Chichón in 1982, which was followed by one of the strongest El Niños on record. *Hirono* (1988) proposed a mechanism for how the direct radiative effect of the mainly tropospheric aerosol from the eruption could have weakened or even collapsed the trade winds in the eastern tropical Pacific, favoring the El Niño development. This response could not be confirmed in modeling studies of *Robock et al.* (1995), and clear trends towards El Niño onset prior to the eruption have been pointed out (*Nicholls*, 1988, 1990; *Self et al.*, 1997b) for several eruptions included in the study of *Handler* (1984). In addition, the selection of volcanic events in *Handler* (1984) and subsequent works does not reflect their radiative importance but more their volcanologic magnitude, as taken from the VEI index. Many of the eruptions did not exhibit any appreciable radiative signals (see compilations of *Sato et al.*, 1993; *Stothers*, 1996b) or leave sulfate traces in polar ice cores (*Robock and Free*, 1995), making a causality for El Niño development unlikely. Additionally, the use of the superposed epoch analysis technique has been criticized, since a few very large events can dominate the signal (*Nicholls*, 1990). Cross-validation by successively dropping single events out of the procedure and re-evaluating the significance could guard against this pitfall. The concurrence of El Chichón and Pinatubo perturbations with El Niño events was concluded to be coincidental.

Why would it be important to know if explosive volcanic eruptions in the tropics and El Niño events were linked in some way? The answer to this question has many dimensions. First of all, the question arose in the midst of the establishment of El Niño in climate research as an important natural variability factor. Then, for identifying a climate impact, be it from volcanic eruptions or from El Niño events, the time scales involved are roughly comparable and the magnitudes can be quite substantial (although with opposite sign for global average temperature). Furthermore, models used in climate studies cannot always internally produce El Niño events, and the claim

for an external driver might arise. On the other side, volcanologists and climatologists looking into impacts of some large volcanic events recognized that the size of the eruption and its climate impact don't seem to follow a simple linear relationship. Damping mechanisms seem to be involved that are able to trim down the impact of extremely large events. Although different mechanisms, such as enhanced sulfate removal by ash or chemical processes, as well as water vapor, were suggested. El Niño events could also mask the impact. The recent examples of El Chichón and Pinatubo show that the signal was probably reduced by the oceanic anomalies (*Wigley*, 2000). The question remains whether it was mere coincidence since El Niño events generally happen every 3 to 7 years, or if there might be some evidence for a more mechanistic link.

Other than in *Handler* (1984), the study presented here, only includes volcanic eruptions with clearly large radiative effects on the earth climate. If there would exist a relationship between eruptions and El Niño development, then it should show up primarily for these largest events. Figure 4.4a shows the occurrence distribution of NINO3 temperature anomalies for all years from 1400 to 1980 of the *Mann et al.* (1998) reconstruction simply using the appropriate grid boxes. (Note: this method does not take the varying uncertainty in the NINO3 area into account. *Mann et al.* (1998) regard the reconstruction of the El Niño pattern before 1700 as highly uncertain. Despite these limitations, we use the data as a first attempt for the very largest volcanic events. The procedure clearly needs to be repeated as more reliable reconstructions of pre 1700 become available.) Figure 4.4b presents the distribution for the year after each of the 18 tropical eruptions. Figures 4.4c and 4.4d evaluate the significance of the clear shift towards higher number of observations in the warmer bins in the histogram. While Figure 4.4c shows the anomaly distribution for 10,000 randomly sampled sets of 18 years as compared to their preceeding 10 years. Figure 4.4d combines the information of 4.4b with 4.4c, showing the percentages where the number of observed events per bin are larger in the volcanic series compared to the random set. The bin for anomalies from 0.2 to 0.4°shows a significant increase after volcanic eruptions

above the 95% level. From this, one could conclude that the warming in the eastern equatorial Pacific NINO3 area could be indeed significant.

Table 4.2 lists different independent indices for the El Niño - Southern Oscillation system for the 18 tropical eruptions from Table 4.1. The data used for the composite is shown in column MBH10 using a 10 year pre-eruption calibration for each event. The basic similarity to a reduced window of 5 years can be seen by comparing it to column MBH5. These values are based on the global temperature reconstruction of *Mann et al.* (1998). which uses dominant Empirical Orthogonal Functions (EOFs) as its base. The reconstruction using the main EOFs is very successful in reconstructing the hemispheric average annual temperature. explaining 70-80% of the variance after 1820. Before this time. the record suffers somewhat from reduced coverage of available proxy records. and fewer EOFs can be captured with necessary accuracy. Therefore. *Mann et al.* (1998) reconstructed a time series for the NINO3 area starting only in 1650. In a newer update. *Mann et al.* (2000) managed to separate their climate reconstruction into both a predominantly Northern Hemisphere winter and summer component. At the same time. they reconstructed a winter index for the NINO3 area (the time for which the development of El Niño is most relevant). which is shown in column MBH-Recon in Table 4.2. For the years available. the correlation between the winter index and the data from the annual reconstruction is quite good. though the former carries considerably higher skill (*Mann et al.*, 2000). Other records included here are two reconstructions of the atmospheric Southern Oscillation Index (SOI). The data from *Allan et al.* (1996) are instrumental time series starting in 1876. The data from *Stahle et al.* (1998) are a proxy record starting in 1706. is based on tree rings collected in southern North America and the Indonesian warm pool area. Note. for the two SOI indices. negative values represent El Niño conditions while positive numbers show the same for the sea surface temperature reconstructions in the *Mann et al.* (1998) data. Beyond these indices. two El Niño chronologies based on documentary data (observations of precipitation events). primarily from the South American Pacific coast. are shown (*Quinn and Neal*, 1995; *Ortlieb*, 2000).

NINO3 Temperature Anomalies
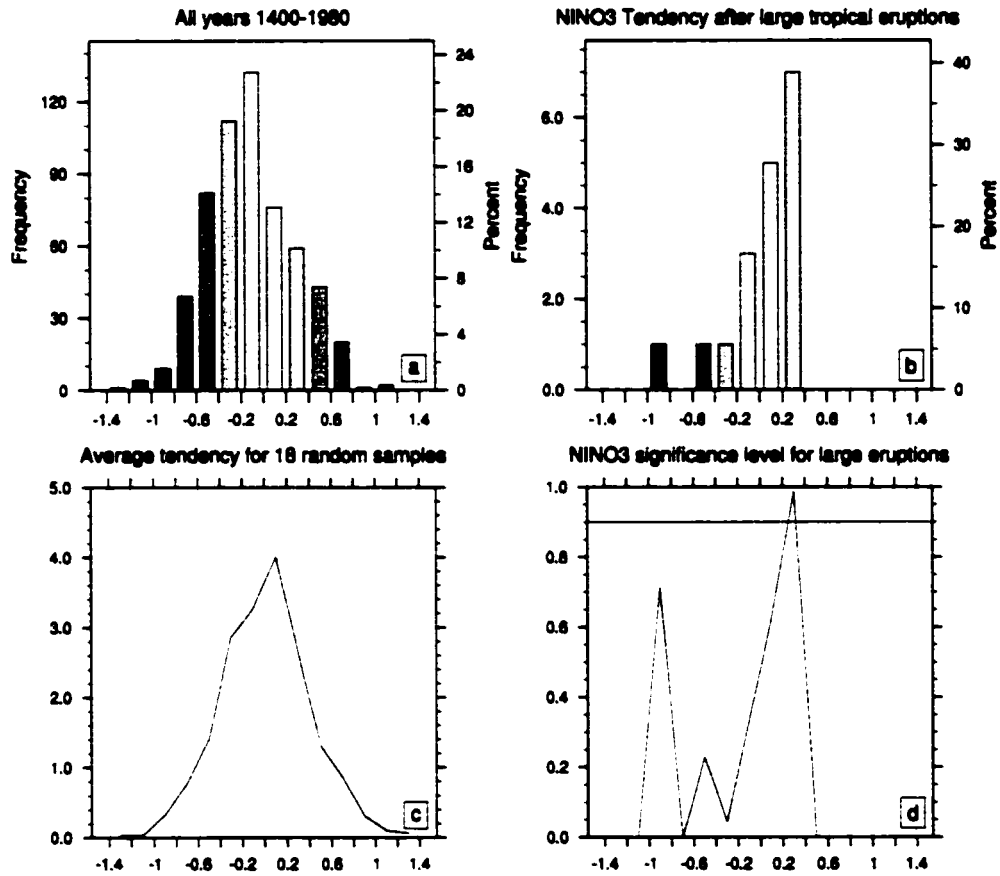
Figure 4.4: Frequencies of NINO3 anomalies from the *Mann et al.* (1998) reconstruction. a: all years. b: anomalies of the 18 tropical events from Table 4.1 compared to their previous 10 years. c: average of 10.000 random sets of 18 years as compared to their preceeding 10 years. and d: significance of increase in number of observations per bin after volcanic eruptions (b) as compared to c. (See text for limitations in the data).

Year	Quinn95	Ortlieb	MBH-Recon	MBH5	MBH10	Stahle	Allan
1816	no	no	0.26	0.08	0.18	-11.2	
1453	-			0.33	0.36		
1641	S	no		-0.1	0.03		
1809	no	no	-0.11	0.07	-0.06	2.3	
1601	no	no		-0.91	-0.94		
1884	S--	S	0.68	0.58	0.39	-2	-13.2
1587	no	no		0.06	0.33		
1836	no	no	0.32	0.08	-0.07	1	
1832	M--	M	-0.28	-0.36	-0.39	0.6	
1714	no	no	0.5	-0.05	0.04	-2.8	
1695	no	no	0.34	0.33	0.38		
1596	M--	S		-0.01	0.2		
1748	no	S	0.85	0.09	0.09	6	
1621	no	no		0.05	0.23		
1963	no		0.43	0.13	0.26	3.7	3.08
1903	no		0.34	-0.2	-0.01	-5.9	-9.42
1522	-			-0.52	-0.4		
1666	no	no	0.19	0.38	0.31		

Table 1.2: NINO3-Data for years after the largest volcanic perturbations of the atmosphere as derived from the ice core volcanic index of *Robock and Free* (1996). Proxy records: Documentary data from South America is used in *Quinn and Neal* (1995) and *Ortlieb* (2000). Multi-proxy reconstructions of *Mann et al.* (1998) include direct NINO3 reconstruction since 1650 [MBH-Recon] as well as spatial anomalies using 5 year [MBH5] and 10 year windows [MBH10]. *Stahle et al.* (1998) use a tree ring record from subtropical North America and Indonesia to estimate the atmospheric Southern Oscillation index [note: negative values stand for El Niño events]. *Allan et al.* (1996) constructed Winter SOI since 1876 from instrumental data.

From this list, the argument for a clear El Niño occurrence after large tropical eruption is far from convincing. Only for the post-Krakatau year (1884) are all indices clearly pointing to an ongoing El Niño event. Similarly, for the eruption at the end of the 17th-Century (maybe Serua?), 4 out of 5 indices point in this direction. For 1816, after the large eruption of Tambora, the proxy records seem to show an El Niño effect, although both of the records based on historical data do not show increased precipitation. These facts hint towards a complex relation between the different aspects of El Niño anomalies and the volcanically perturbed climate conditions. This interplay could be potentially important, since the atmospheric perturbations from an eruption like Tambora are quite dramatic. Only very few large volcanic events occurred during the calibration time period. A global net reduction of almost 15 Wm^{-2}, as estimated by the IVI of *Robock and Free* (1996) (with even stronger perturbation in the tropics), would clearly influence the convective activity in the tropics. For locations like the western Pacific warm pool, a reduction in precipitation could be directly interpreted as associated with El Niño conditions, as during these events the center of convective activity moves eastward into the central tropical Pacific and dry (or at least dryer) conditions prevail in Indonesia (*Stahle et al.*, 1998). Therefore, a proxy record sensitive to fluctuations in precipitation in this area would be prone to show signals common to El Niño events after volcanic eruptions. Similarly misleading connections could exist in other proxy locations, although with increasing numbers of diverse proxy records, the weight put on the principal component of the El Niño pattern should be balanced. Further evaluation of the sensitivity of the *Mann et al.* (1998) reconstruction to volcanic eruptions as compared with El Niño should be performed.

From the documentary records presented in Table 4.2, one also has to be careful not to over-interpret the data. While quite a number of locations along the South American Pacific coast are reasonably well covered with documentary data, rainfall can happen on a very local basis, and these records don't include information from the main convection in the central equatorial Pacific.

Overall. while the SE-composite produces many aspects of El Niño following large volcanic eruptions in the tropics, the conclusion of volcanically induced El Niño events is not so clear from a diverse set of NINO3 and SOI indices as the simple approach using SE-composites from *Mann et al.* (1998) would suggest. In fact. the number of El Niño associations, even with the 18 largest volcanic events is relatively small and appears random. This observation holds up even when considering that the two events not included in the composite (El Chichón and Pinatubo) were followed by El Niño events. Conclusions of more coincidental occurrences (*Robock et al.*, 1995; *Self et al.*, 1997b) seem more probable.

4.6 Evidence for a multidecadal component of the volcanic signal?

The general pattern of anomalies shown in Figure 4.1 has. as discussed, some resemblance to the El Niño pattern. When ignoring the positive temperature anomalies in the eastern equatorial Pacific, the overall pattern seems to closely match another major pattern of climate variability. For the decomposition of the spatial patterns of northern hemisphere temperature, *Mann et al.* (1998) present in their Figure 2 (p. 780) the leading 5 EOF patterns. EOF #5 carries many of the features described for the volcanic SE-composite: the same tendency of temperatures over the sector North-America - western Europe with temperature anomalies in the western Pacific. Opposite anomalies in the South Atlantic and parts of central Asia, as well as Alaska, are also present in Figure 4.1. The temporal contribution of EOF #5 (its principle component PC5) is described by *Mann et al.* (1998) to be "dominated by multidecadal variability in the entire Atlantic basin and neighboring regions that has been widely noted elsewhere". referring to *Schlesinger and Ramankutty* (1994). among others. *Schlesinger and Ramankutty* (1994) found a very robust oscillation of near global scale with a time period of roughly 70 years. This fluctuation has been recognized in many instrumental, as well as proxy records (*Kushnir*, 1994;

Mann and Park. 1994. 1996: *Shabaloba and Weber.* 1998: *Delworth and Mann.* 2000). The fact that the volcanic impact pattern resembles this large scale pattern raises the question if volcanic eruptions could (a) modify EOF #5 from *Mann et al.* (1998) on interannual time scales. and (b) influence this mode of climate variability on the much longer time scales by undergoing some multidecadal fluctuations in their occurrences.

In a recent study. *Ammann and Naveau* (2001) showed a multidecadal oscillation of tropical volcanic eruption occurrences in a new binary eruption record derived from a large set of polar ice core data. They documented a very robust cycle of roughly 76-years. covering the last 600 years. Since PC5 of *Mann et al.* (1998) is reconstructed back to 1650. a comparison with the statistical description of volcanic occurrences from *Ammann and Naveau* (2001) is possible. Figure 4.5 shows PC5 from *Mann et al.* (1998) together with the multidecadal fluctuations in eruption probabilities (including both smoothed data and statistical model) presented in *Ammann and Naveau* (2001). Additionally. the temporal location of members of the top 20 sulfate producing eruptions from Table 4.1 are indicated in vertical bars. Many of these events are immediately preceeding or directly at a clear drop in PC5. While not being responsible for all drops. the eruptions could be responsible for some.

When looking at the multidecadal time scale. one first needs to keep in mind that the eruption frequencies do not directly represent the forcing. but merely a statistical tendency when volcanic forcing can be expected to rise or decrease event occurrences versus magnitude. For example. the eruptions after 1800 are significantly larger than events during the mid-18th-Century or around 1900. The eruption of Krakatau has proven to be unique in terms of its forcing. Despite a very large sulfate flux. only a small signal (if any) is detectable and other factors such as aerosol composition and particle size distribution might have distorted the actual radiative forcing significantly. This is discussed in detail in Chapter 6.3 and *Ammann et al.* (forthcoming: Krakatau. A Challenge for Climate Modeling). Nevertheless. when adjusting for the magnitude of volcanic eruptions and allowing for a response lag of a few years. one might see a tentative relationship

between the eruptions and PC5 both on interannual and on multidecadal time scales. While this possibility exists, it could also arise from the influence of a common forcing responsible for the fluctuations in tropical eruption frequency on one side and, on the other side, through additional processes for climate as well.

That the pattern described by EOF $\neq 5$ is not only a response mode of the climate system to volcanic eruptions is shown in *Delworth and Mann* (2000). They report a multidecadal pattern similar to EOF $\neq 5$ from a completely un-forced coupled climate model integration. It is possible that this feature represents an important coupled climate mode involving an interaction between the atmosphere and ocean circulation. From this point of view, one wonders if volcanic eruptions could influence this mode and excite or suppress it. Clearly, a more detailed analysis should concentrate on this possibility of a volcanically driven multidecadal mode in climate. A preliminary comparison of the timing and sign of the fluctuation presented by *Schlesinger and Ramankutty* (1994) and PC5 from *Mann et al.* (1998), as shown in Figure 1.5, are promising, and, at least for the past 150 years, the findings of *Bertrand et al.* (1999) confirm the potential volcanic influence on this long, multi-decadal time scale. But one equally needs to keep in mind that even fully independent variations operating on multi-decadal time scales might accidently suggest a relationship as the degrees of freedom are very small given the short record at hand.

Volcanic eruption frequencies and PC #5 of Mann et al. (1998)
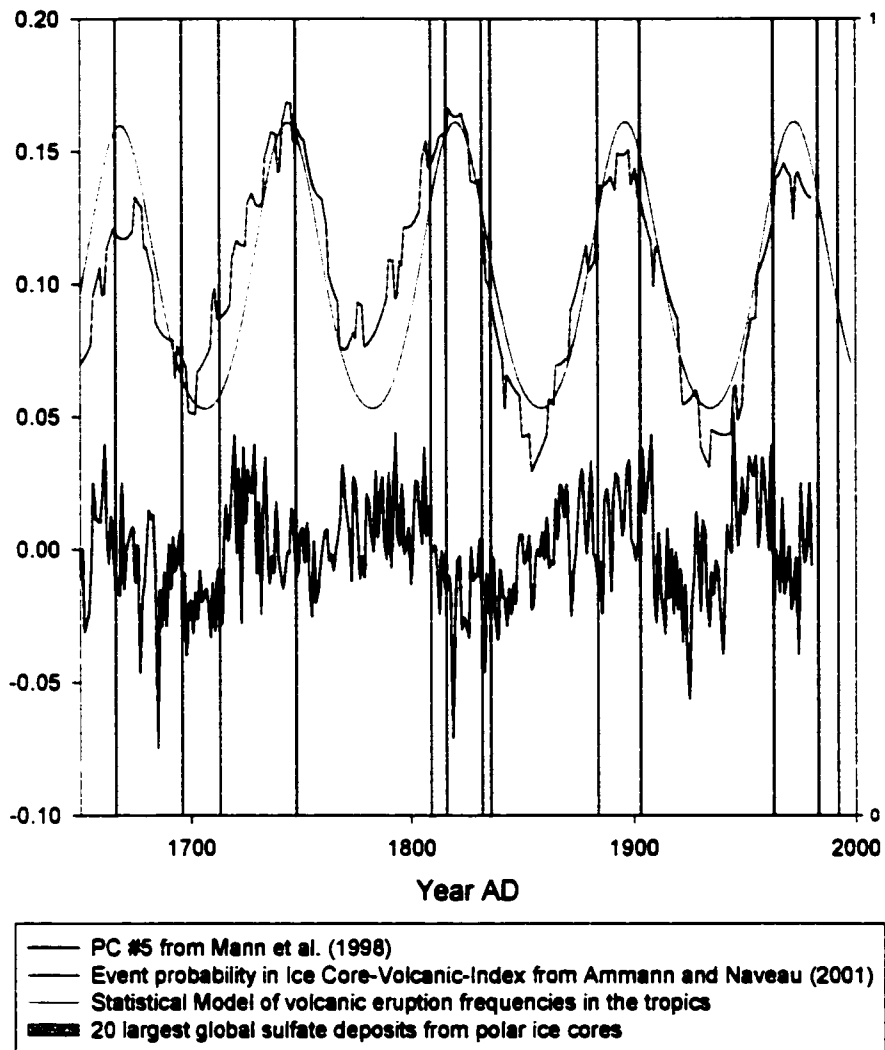
Figure 4.5: PC5 from *Mann et al.* (1998) (black line) are shown against volcanic eruption frequencies in the tropics described by a moving window over binary data of years with sulfate deposits in both polar areas (blue line). and a simple logistic model attempting to describe its behavior (red line). For details. see *Ammann and Naveau* (2001).

119

Chapter 5

IMPLEMENTATION OF VOLCANIC AEROSOL IN THE NCAR CCM/CSM

The purpose of including volcanic aerosol into the climate model is to add a major external forcing to the simulation of the climate system. The importance of volcanoes is illustrated in Figure 5.1. where the recent climate forcing is broken into its individual components. The lower panel shows that the volcanic forcing for a couple years after large explosive events, can reach the magnitude of all other forcings combined. Global average perturbation of the radiative balance from the Pinatubo aerosol cloud reached about -4 Wm^{-2} one year after the 1991 eruption (*McCormick et al.*, 1995). Therefore, one can expect that large eruptions have a strong impact on climate on the interannual time scales. Additionally, longer term perturbations cannot be excluded. The top panel of figure 5.1 shows the average forcing from the anthropogenically caused increases in greenhouse gas concentration since 1850, as compared to the influence from increased tropospheric aerosol, solar and volcanic forcing on multi-decadal time scales (*Hansen et al.*, 1998).

The volcanic forcing, ranging from +0.2 to -0.5 Wm^{-2}, compares the average volcanic forcing over the last 150 years with decades of no (positive forcing) explosive volcanic activity and the 1880s. a decade with very large volcanic perturbations of the atmosphere (negative forcing). As was shown in Chapter 3.6. there is also the indication of temporal fluctuations of this 'difference' as a result of changes in the temporal spacing of large events. If the 20th-Century can be taken as representative. Chapter 6.2.3.1 will show that volcanic fluctuations could rival the generally more accepted solar variations on these time scales.

This Chapter describes the implementation of volcanic aerosol treatment into a state-of-the-art climate system model. Simulations of the 1991 eruption of Pinatubo are used to verify the forcing to impact relationship. and Chapter 6 will then discuss simulations of the volcanic forcing on multi-decadal and century time scales in long coupled experiments.

5.1   The Model

The stratospheric aerosol is implemented into the National Center for Atmospheric Research - Community Climate Model (NCAR-CCM3) (*Kiehl et al.*. 1996. 1998b). This three dimensional general circulation model can be run *stand alone*. using either prescribed sea-surface temperatures or an interactive slab ocean model with a specified mixed layer depth and seasonally and geographically varying ocean heat fluxes. The land surface with specified vegetation types and a comprehensive treatment of the different fluxes to and from the atmosphere is integrated into CCM as the Land Surface Model (LSM). Sea ice is simulated by a multilayer thermodynamic model. In *fully coupled* mode. CCM3 fluxes are passed through a flux coupler (*Bryan et al.*. 1997) into a separate dynamic ocean (*Gent et al.*. 1998: *Holland et al.*. 1998). a now separate land surface model (*Bonan*. 1998). and a sea ice model (*Weatherly et al.*. 1998). The coupled configuration is called the National Center for Atmospheric Research - Climate System Model (NCAR-CSM) (*Boville and Gent*. 1998). The advantage of CSM over a number of other models
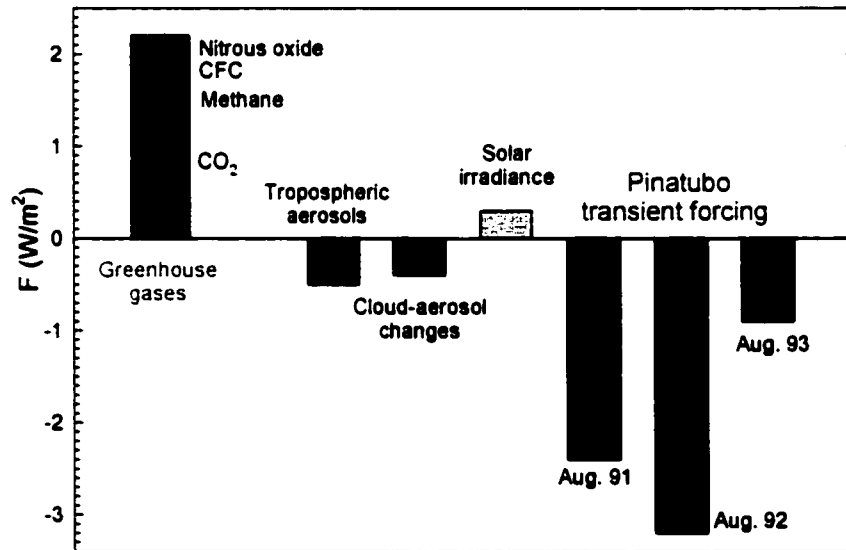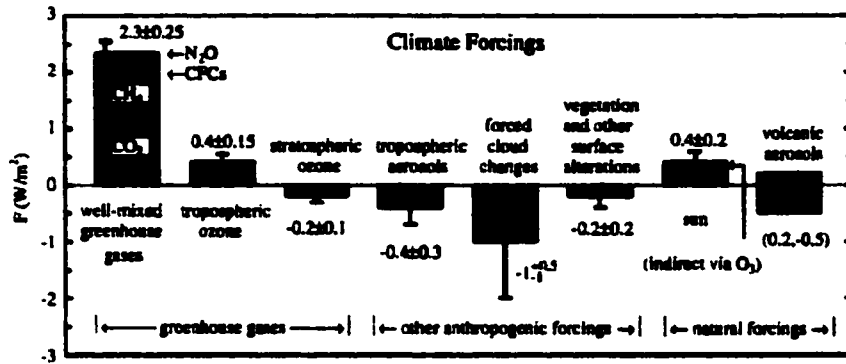
Figure 5.1: Summarized climate forcing. Top: 1850 to present change in forcing, broken down for individual contributions. The volcanic forcing is the difference of decades with no or very high forcing with the 150-year average (from *Hansen et al.*, 1998). Bottom: Short term forcing from Pinatubo (after *McCormick et al.*, 1995).

is the lack of a need for flux corrections (*Boville and Gent*, 1998; *Boville et al.*, 2001), while still producing a surface climate with a very small drift. The only significant drift was initially found in the deep ocean (*Boville and Gent*, 1998; *Bryan*, 1998; *Doney et al.*, 1998) but was drastically reduced in CSM version 1.3 (*Boville et al.*, 2001). This latest version with small modifications will be used here.

5.1.1 CCM3: Atmospheric Model

Of central interest for the implementation of stratospheric aerosol is, of course, the atmospheric component, CCM3 (*Kiehl et al.*, 1998b). The atmospheric model is a spectral model, solving the dry dynamical equations in spectral space but applying diffusion of moisture and all parameterizations in the Gaussian grid-point space. Therefore, all the aerosol parameterizations shown below are inserted and applied on a regular grid. The configuration of the model includes different horizontal resolutions. The spectral *T31* resolution is equivalent to a grid with 3.75 degrees resolution in latitude and longitude (48×96 gridcells), and *T42* represents roughly 2.8×2.8 degrees on a grid of 64 latitudes by 128 longitudes. In the vertical, 18 levels are included with a rigid lid at 2.9 mb as the upper boundary at the model top. The stratosphere is with five to eight layers (depending on latitude) only relatively poorly represented. This has implications for the volcanic implementation. While *Boville et al.* (1991) simulated the spread of Pinatubo aerosol after the initial injection in a middle atmosphere version of the model, such an attempt in the standard version is not appropriate. At this stage, the aerosol distribution is prescribed, using the parameterization presented in Chapter 3.3. Finally, depending on resolution, the time steps required vary from 30 (T31) to 20 minutes (T42), providing a full diurnal cycle with the computationally expensive radiative fluxes being calculated only every hour. In between, the radiative fluxes are held constant.

The solar, or short-wave (SW), part of the radiative spectrum, encompassing 0.2 to 5 μm, is treated using the δ-Eddington approximation (*Briegleb*, 1992). This method, after *Joseph*

123

et al. (1976) and *Coakley et al.* (1983), simulates multiple scattering both for an upward and a downward stream, separately for each of 19 SW bands. A globally uniform tropospheric aerosol formulation is used in the standard version as a place holder for detailed aerosol treatment, which is expanded in *Barth et al.* (2000). *Rasch et al.* (2000) and *Kiehl et al.* (2000). In the version used here, only a globally uniform sulfate aerosol with a visible optical depth ($\tau_{v,s}$) of 0.14 (or otherwise stated) and optical properties given in *Kiehl and Briegleb* (1993) are present.

The infrared, or long wave (LW), treatment for wavelength from 5 to 50 μm is performed using a broad band approach with 6 bands. This technique is based on the absorptivity/emissivity formulation of *Ramanathan and Downey* (1986) covering major absorbers like H_2O, CO_2, O_3, CH_4, N_2O. It also includes minor absorption bands of CO_2 (*Kiehl and Briegleb*, 1991), as well as an exponential transmission approximation for CFC11 and CFC12 (*Kiehl et al.*, 1996).

For the simulations of the Pinatubo eruption (Chapter 5.3), CCM3 is run stand alone in T42 resolution with prescribed sea surface temperatures (SST), using a dataset of the Atmospheric Model Intercomparison Project (AMIP). The long simulations (Chapter 6.2) were run in fully coupled mode in the more efficient T31 version used for paleo climate simulations (*Otto-Bliesner and Brady*, 2001).

5.1.2 Performance and shortcomings of the model

The performance of CSM is described in *Boville and Gent* (1998) and *Boville et al.* (2001). CCM3 is evaluated in detail in *Kiehl et al.* (1998a), *Hack et al.* (1998) and *Hurrell et al.* (1998). In general, CCM3 produces the large scale pressure and circulation patterns very well (*Hurrell et al.*, 1998). The top of the atmosphere (TOA) radiative fluxes shows very good agreement with ERBE observations (*Kiehl et al.*, 1998b). Similar to most radiative transfer models, the surface fluxes show an underestimation of the atmospheric SW absorption, probably due to insufficient cloud absorption (*Cess et al.*, 1995; *Ramanathan et al.*, 1995; *Pilewskie and Valero*, 1995; *Zender et al.*, 1997; *Kiehl et al.*, 1998a; *Collins*, 2001). Other deficiencies include some problems in

accurate representation of low level stratus and stratocumulus clouds over the oceans, a bias in the position of the deep convective activity over the western tropical Pacific and summertime convective activity over land areas (*Kiehl et al.*, 1998a). There are cold biases over the polar areas. causing a general overestimation of sea ice production in both coupled and uncoupled mode (*Briegleb and Bromwich*, 1998b,a; *Weatherly et al.*, 1998). A poleward displacement of the Beaufort High could be responsible for a shift of the highest sea ice concentration towards the Bering Strait as compared to the Canadian Arctic and North-Greenland known from observations. Nevertheless, the general performance is significantly improved compared to earlier versions, and the variability including the seasonal cycle. and interannual and low frequency variability is represented reasonably well, although some biases exist (*Gent et al.*, 1998; *Bonan*, 1998; *Hack et al.*, 1998; *Meehl and Arblaster*, 1998; *Saravanan*, 1998; *Capotondi and Holland*, 1998; *Otto-Bliesner and Brady*, 2001; *Meehl et al.*, 2001). Especially, the atmospherically implied ocean heat transport (the amount of heat transported by the ocean necessary to balance the high latitude energy budget given an atmospheric simulation) agrees well with the uncoupled transport simulated in the ocean model, which allows for a successful performance in fully coupled mode.

5.2 Strategy of volcanic aerosol implementation

The implementation of the volcanic aerosol into a climate model can be done with different goals in mind. For events like the recent Pinatubo eruption (1991), a large amount of detailed information is available about the aerosol cloud's buildup. spread. composition and decay. At the same time. comprehensive measurements did capture the radiative and climatic impact of the aerosol both from space and from the ground. Therefore. the aerosol and its temporal and spatial evolution can be put into the model in high detail. At the same time. the output of the model. the forcing and the climate impact can be compared and evaluated with high resolution data all over the globe.

125

The situation is quite different for eruptions in the past. Only crude, and often indirect, information is available about the aerosol, the atmospheric optical perturbation, as well as the climate impact. A number of simplifications have to be accepted. The two most crucial assumptions concerning the aerosol are:

(a) aerosol mass and its temporal and spatial distribution,

(b) the optical properties of the particles (i.e. the composition and size distributions).

While for (a) a number of proxies, like sulfate from ice cores and volcanologic records, can be used to make reasonable assumptions, it is much harder to do so with (b). There is no proxy that preserves the particles as they existed in the stratosphere. Only the general composition can be estimated from ice core data. Once deposited on snow, sulfate and other volcanic species can only be used to calculate a flux (mass deposition per unit time). Unfortunately, a given flux can be generated either by a few large or by many small particles. Since the radiative effects will vary widely depending on the size, shape and composition of the aerosol, it is a challenge to determine a useful distribution - especially one that should suit all events as would be the case for a generalized treatment of volcanic events over hundreds of years.

The following section will describe in how this problem is addressed in the implementation of stratospheric aerosol into CCM/CSM. Then, a comparison of simulations using very detailed and strongly simplified aerosol information is performed. This will help determine how important the detailed aerosol information is and how it might influence the potential of modeling eruptions in the past.

5.2.1 Stratospheric aerosol and its optical properties

5.2.1.1 Composition

Volcanoes emit large amounts of ash and gases into the atmosphere. Ash is most noticeable immediately after the eruption. Due to its size and high specific weight, ash will fall out rather quickly. There are some indications that a small amount of ash may stay afloat for some time. For example, Cole-Dai et al. (1997b) found some Pinatubo ash in snow layers from 1993, more than 1.5 years after the eruption. Nevertheless, the amount is generally very small and is not taken into account in this study.

Of all the gases injected into the stratosphere, water vapor and especially sulfur dioxide are most important. The latter is transformed over a few month into sulfuric acid droplets dissolved in water. The liquid particles are so small (sub-μm) that they can stay in the stratosphere for a few years. General e-folding times of around one year are commonly found. A list of collectors have isolated sulfuric acid to be the dominant aerosol after the fallout of ash. The same result was obtained through indirect measurements of the boiling point of the aerosol and through spectral information (see Chapter 2.2.3). Hence, sulfuric acid aerosol consisting of 75% H_2SO_4 and 25% H_2O is generally used as volcanic aerosol. The same approach is taken here.

Nevertheless, one needs to keep in mind that if, in the real world, the composition of the volcanic cloud of some eruptions would be markedly different, significant changes to the optical properties could arise. This is illustrated in Table 5.1. The list from Hansen et al. (1998) shows the calculated optical effects for sulfate and other particles (see also Pollack et al. (1976) and Lacis et al. (1992) for comparison of Basalt and Sulfate). While sulfate droplets were found to be very efficient scatterers, volcanic dust/ash of basaltic composition is a very strong absorber. They give extinction curves for the different aerosol types.

Aerosol	ϖ	$\Delta F(Wm^{-2})$	ϖ	ΔF (Wm^{-2})
sulfate	1	-0.28	0.95	-0.20
organic	1	-0.41	0.92	-0.22
dust	1	-0.53	wvl-dep	-0.12

Table 5.1: Mean net forcing of three different aerosol under two different assumptions of the single scattering albedo.

5.2.1.2 Size distribution

Generally, volcanic aerosols are assumed to be liquid spheres following a log-normal size distribution with a modal radius r and a geometrical standard deviation σ_r (*Hansen and Travis*. 1974; *Stothers*. 1996b). Although several modes could co-exist in a volcanic cloud. *Russell et al.* (1996) showed that they can be treated as a single distribution with reasonable accuracy. A useful descriptor of particle size distributions is also the area weighted mean radius (i.e.. effective radius. r_{eff}) (*Hansen and Travis*. 1974; *Lacis et al.*. 1992). which after *Russell et al.* (1996). can be determined for a unimodal distribution by

$$r_{eff} = r \; exp \left[\frac{5}{2} \; (ln\sigma_r)^2 \right] .$$ (5.1)

The advantage of r_{eff} is that it summarizes efficiently the theoretically infinitely large number of r and σ_r combinations that could be responsible for extinction at a specific wavelength. r_{eff} is relatively robust and therefore more useful for comparison of size distributions (*Stothers*. 1997). This is discussed and illustrated in more detail below in the section on optical properties.

For the simulations of past volcanism. no information on size distributions is available beyond the 20th-Century. During the period with multi-spectral extinction information from volcanic clouds since about the turn of the century. estimated r_{eff} remained in a remarkably small range from about 0.3 to 0.6 μm (*Stothers*. 1997). While for eruptions like El Chichón. Santa Maria and Katmai the aerosol seems to have remained relatively close to $r_{eff} = 0.3$ μm throughout the
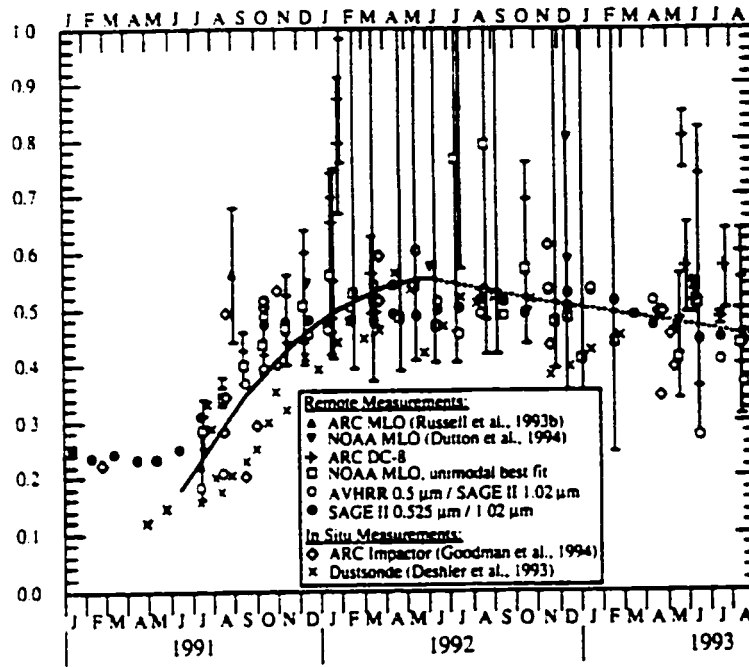
Figure 5.2: Pinatubo aerosol size evolution after injection into the stratosphere as observed from ground stations, satellites and in-situ measurements (*Russell et al.*, 1996).

time of atmospheric perturbation, the aerosol of Ksudach and Pinatubo did exhibit an evolution from $r_{eff} = 0.3$ to 0.5 or 0.6 μm (*Russell et al.*, 1996; *Stothers*, 1997). Figure 5.2 shows this size evolution for the Pinatubo aerosol as observed from different instruments.

Lacis et al. (1992) suggest that the aerosol forcing is rather independent from most aerosol parameters other than optical depth and to some degree from r_{eff}. If r_{eff} is larger than 1 μm, a strong reduction in negative net forcing is to be expected, and for r_{eff} larger than about 2 μm, the LW effect dominates, causing a net warming. This has already been shown in Figure 3.1. Therefore, as an approximation, a single, intermediate aerosol size distribution within the range of the observed particle sizes will be applied and evaluated in Chapter 5.3.3.

5.2.1.3 Computation of optical properties

Assuming the particles are homogeneously spread liquid spheres of a constant composition. Mie theory offers a useful way to obtain the key wavelength-dependent optical properties. which can be used to describe the perturbations of the direct solar beam as well as multiple scattering and absorption. The three parameters used in the SW δ-Eddington formulation:

Ψ_λ : the *mass extinction coefficients* or specific extinction. which describes how efficiently the particles disturb the direct beam.

ω_λ : the *single scattering albedo*. which defines the absorption efficiency.

g_λ : and the *asymmetry parameter*. which is a measure of the amount of radiation scattered in the forward direction as compared to backwards.

Mie theory evaluates these three properties based on a size distribution given as r and $\ln(\sigma)$. as well as the refractive indices and density of the substance under consideration. The refractive indices contain a real and an imaginary part. The real part describes the refractive strength as the ratio between the speed of light in a vacuum versus the speed of light in the substance. which is the ability of the substance to distort the direct path of light (basically the scattering). The imaginary part describes the absorption efficiency of the liquid spheres. In our case. this substance is a solution of sulfuric acid in water. Its refractive indices are presented in Figure 5.3. For the standard stratospheric aerosol of 75% H_2SO_4 and 25% H_2O. refractive indices are taken from *Palmer and Williams* (1975) and completed with *Hummel et al.* (1988) below 0.3 μm. as well as above 27 μm. The density was set to 1.69 for stratospheric conditions (*Timmermans*. 1960). Note. should the sulfate aerosol concentration vary between 50 and 85%. the error in the mass extinction would not exceed 3% (*Kiehl and Briegleb*. 1993). Additionally. *Niedziela et al.* (1998) describe the temperature dependence of refractive indices of sulfuric acid. For concentrations around 75% H_2SO_4. they find that temperature does not play an important role.

[See also *Mergenthaler et al.* (1995) for further critical evaluation of refractive indices of *Palmer and Williams* (1975).]

For the LW computation. the wavelength dependent mass absorption coefficients (a_λ) are needed for the six broad bands. These are used to compute the transmissions at each model level. which determine the radiative fluxes. Twice per day absorptivities and emissivities are reevaluated and then held fixed for the twelve hourly transfer calculations. Only temperatures and cloud concentrations are changed.

The computation of the optical properties has to be binned (resolved) for the radiative bands of CCM3. Figure 5.4 shows the theoretical high resolution (solid line) and model resolved (blue stars) mass extinction. single scattering albedo. and asymmetry parameter in the 19 SW bands for an intermediate aerosol size distribution with $r_{eff} = 0.42$ μm. $r = 0.3709$ μm and $\ln(\sigma_r) = 0.223$ μm ($\sigma = 1.25$ μm). These properties are later used as intermediate aerosol. This figure shows how well the properties of sulfuric acid of the theoretical curves are captured by the CCM bands. represented by the band centers. Additionally. the figure shows the absorption coefficients per unit mass (a_λ) for the standard CCM3 bands (dashed red lines). For comparison. the absorption coefficients of a higher resolution (10 band) Goddard Space Flight Center (GSFC) code of *Chou and Suarez* (1994) and *Chou et al.* (1999) is shown in green. When compared with the CCM3 bands. the GSFC absorptions are often somewhat higher than the wider CCM3 bands. especially and most significantly around 8 to 12 μm. where the largest terrestrial emissions take place and therefore. where most of the energy is absorbed. Because the higher resolution code can resolve more detail and is thus more accurate (measured against a precise line-by-line calculation). the CCM absorption coefficients were adjusted to reproduce the band weighted total absorptions averaged over the globe of the higher resolution GSFC code. This resulted in this case in a roughly 16% increase in the mass absorption coefficients (solid red line).

As mentioned before. there is uncertainty about the details of size distributions for past eruptions. although some constraints can be imposed in the 20th-Century (*Stothers.* 1997). How
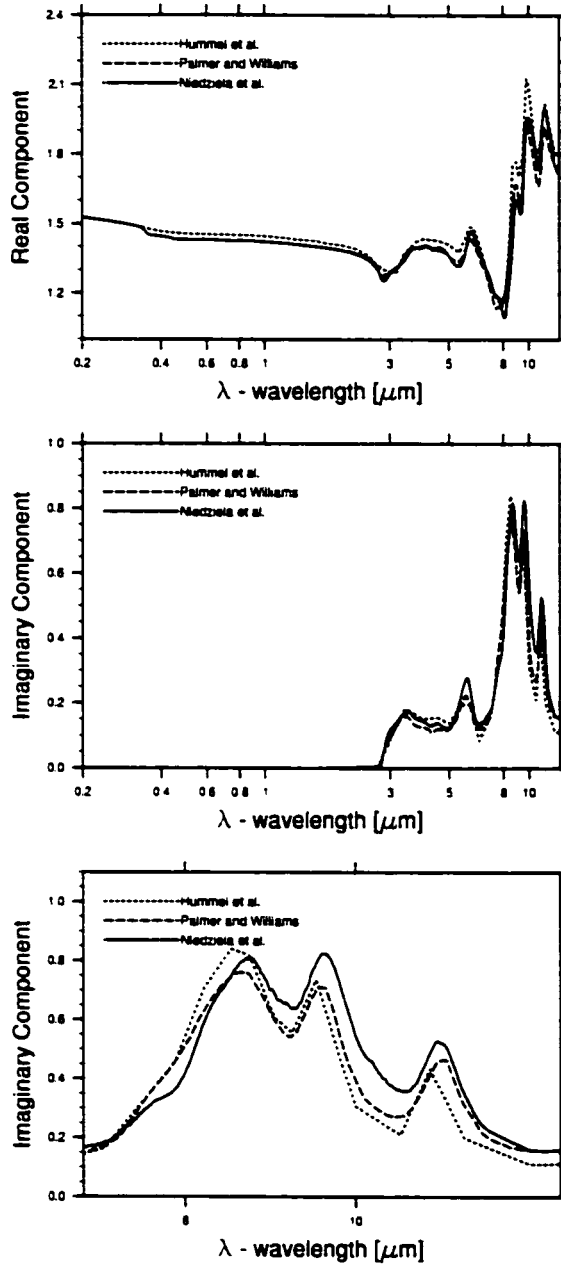
Figure 5.3: Refractive indices of sulfuric acid (75% H_2SO_4 and 25% H_2O) from different sources. Top: real component. middle: imaginary part. and bottom: imaginary part representing absorption in the window region.

132

(a) fixed ln(σ_r)

ln(σ_r)	0.223	0.223	0.223	0.223	0.223	0.223
r	0.177	0.353	0.442	0.530	0.883	1.325
r_{eff}	0.2	0.4	0.5	0.6	1.0	1.5

(b) fixed r_{eff}

ln(σ_r)	0.095	0.182	0.262	0.336	0.405	0.470
r	0.411	0.387	0.354	0.317	0.279	0.242
r_{eff}	0.42	0.42	0.42	0.42	0.42	0.42

Table 5.2: Aerosol size distribution parameters r. ln(σ_r) and r_{eff} with (a) fixed ln(σ_r) and (b) fixed r_{eff}. corresponding to Figures 5.5 and 5.6 respectively. All units are μm.

do these optical properties change with the size of the aerosol? Figures 5.5 and 5.6 show the theoretical properties for different sulfate aerosol size distributions. Table 5.2 summarizes the size parameters. Figure 5.5 shows the properties for different r_{eff} when the standard deviation of the distribution was held constant. It is apparent that the radiative effects of these different distributions are vary quite significantly. Figure 5.6 shows less significant differences when r_{eff} is held constant and widely different standard deviations are evaluated. Although some differences exist, the various distributions behave very similarly over the whole spectrum. This better determination of the aerosol distribution through r_{eff} was used by *Stothers* (1997), as shown in Figure 2.5.

Given its optical properties for the different treatments in SW and LW computation. the aerosol can now be fully described in the model if its concentration at the different model levels (i.e.. its mass) is known. This is achieved by prescribing the optical depth at a mid-visible wavelength of 0.5 μm. The same Mie computation is performed to calculate the mass extinction coefficient at a narrow interval around 0.5 μm. With a known (i.e. prescribed) optical depth

Standard Aerosol of 0.42
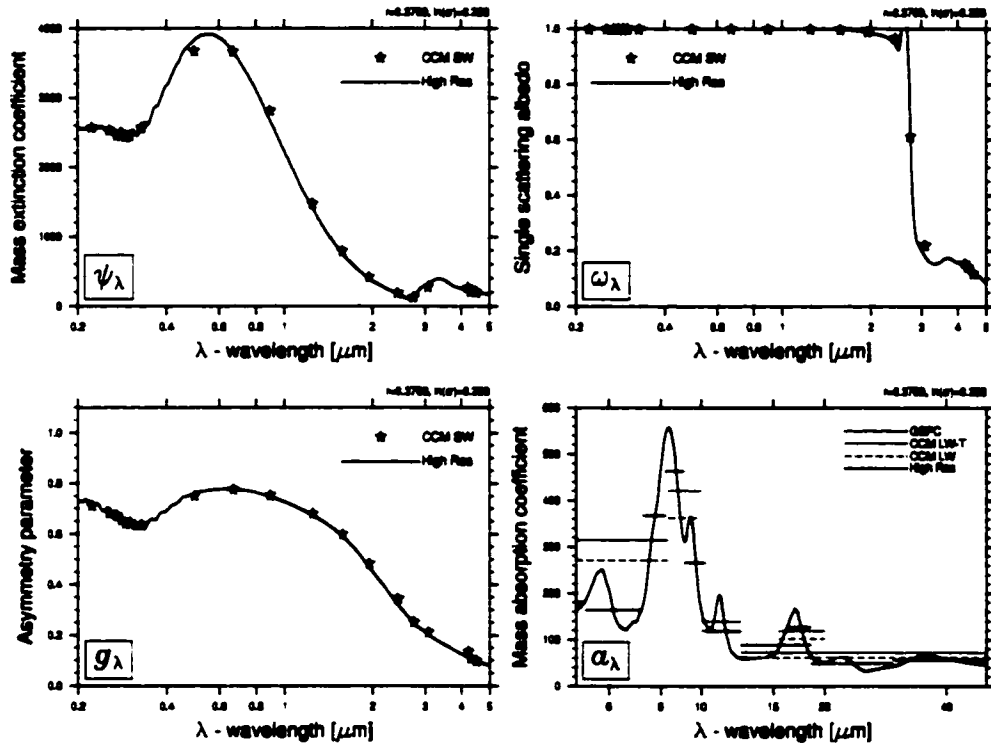
Figure 5.4: Optical properties of sulfuric acid aerosol. The solid line represents a high resolution (1000 bands) mie calculation. and the blue stars show the properties at the CCM SW band centers. The mass absorption coefficients (a_λ) is also shown in high resolution versus broadband implementations. in red the six CCM bands and in green the 10 bands of *Chou and Suarez* (1994). See text for further discussion.

Aerosols with fixed sigma of 1.25
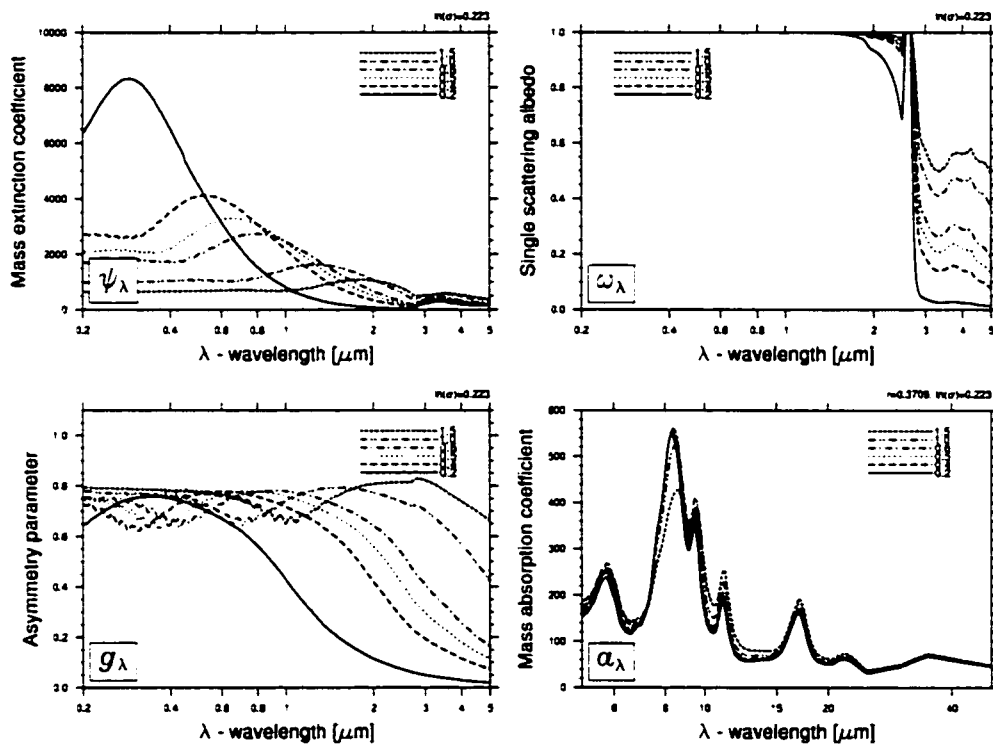
Figure 5.5: Optical properties of sulfuric acid aerosol similar to Figure 5.4 with constant σ_r. Lines are labeled by resulting r_{eff}.

135

Aerosols with fixed reff 0.42
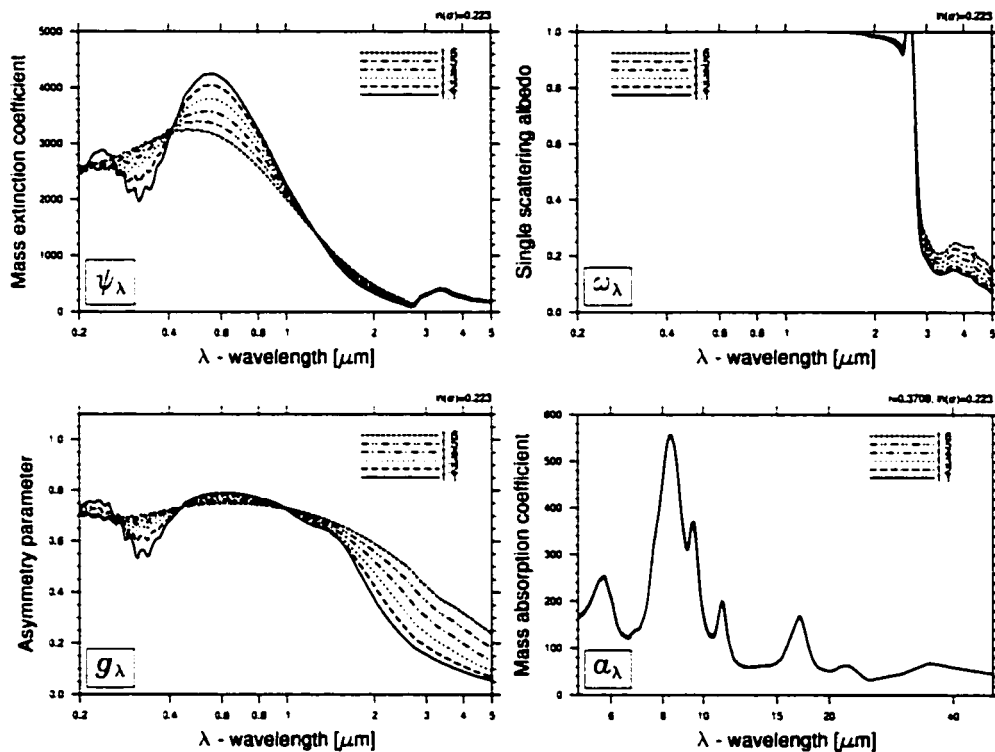
Figure 5.6: Optical properties of sulfuric acid aerosol similar to Figure 5.4 with constant r_{eff} Lines are labeled by resulting σ_r.

136

at this wavelength and a selected number of model levels. where the aerosol is homogeneously distributed. the mass mixing ratio can be calculated for each model level. This mass mixing ratio is independent of wavelength and will be used with the level thickness to compute the aerosol mass present on each model level. where it interacts with radiation. either scattering or absorbing a certain amount. The two following sub-chapters explain this procedure during SW and LW radiative transfer calculations.

5.2.2 SW implementation

The radiative transfer in the SW bands is performed in each atmospheric column (over one gridpoint) at every model hour over the sunlit part of the globe. For each column. the solar zenith angle and the surface reflectivity (albedo) in each SW band are known. The solar irradiance is set as constant. but can be changed over time. Given these boundary conditions. together with the vertical distribution of all atmospheric constituents (e.g. clouds. aerosol). the transfer calculations are performed for cloudy and clear sky conditions in each column separately. For all 19 SW bands. the δ-Eddington formulation (*Briegleb*. 1992) uses scaled extinction and scattering properties of the atmospheric constituents to compute reflectivity and transmissivity at each layer in the vertical for direct and scattered (i.e. diffuse and assumed isotropic) radiation. Additionally. the different layers are then combined to account for multiple scattering between the layers. This allows for the computation of the differences in upward and downward radiative fluxes at each level interface. which. in turn. offers the evaluation of solar heating rates.

The stratospheric aerosol mass and optical properties at different wavelengths must be known during the calculation. As mentioned above. before entering the radiative transfer computation. the mass mixing ratio is determined from the prescribed mid-visible optical depth and vertical distribution. Then. the inclusion of aerosol into the code is rather trivial by calculating the parameters for the δ-Eddington computation. which is the extinction optical depth at each CCM

SW band.

$$taustr_{i,\lambda} = aermmr \times path_i \times \Psi_\lambda \times k. \tag{5.2}$$

where $taustr_{i,\lambda}$ is the extinction optical depth on model level i and CCM band λ. $aermmr$ is the mass mixing ratio of sulfuric acid aerosol. $path_i$ is the vertical extension of layer i (i.e. layer mass path). Ψ_λ is the mass extinction coefficient at CCM band λ. and k is a conversion factor to adjust the extinction coefficients to cgs units for the δ-Eddington calculation. The other required aerosol properties ω_λ (single scattering albedo) and g_λ (asymmetry parameter) are mass independent and read in as a lookup table which is separated into each CCM band. All downward and upward radiative fluxes are then computed through the δ-Eddington approximation

The most significant modification to the SW code had to be done in the clear sky computation where previously only two layers were considered: A top level exclusively containing ozone and a lower level containing all other absorbers and scatterers. In order not to interfere with the cloud radiative forcing. the prime reason for the clear sky computation. the stratospheric aerosol was entered into the top level.

5.2.3   LW implementation

The CCM LW code uses a broadband approach to calculate the absorption by the different atmospheric constituents at different levels and bands. This quantity, in general, is a function of the absorber mass, the local emitting temperature and the pressure, or the absorber density and level temperature. Details of the calculation follow *Ramanathan and Downey* (1986) and are presented in *Kiehl et al.* (1996), and for the 15 μm band system, in *Kiehl and Briegleb* (1991).

The goal is to compute the transmission of energy radiated from each level (the level emission) to every other level throughout the column and through both the top (into space) and bottom interface (into the ground) of the column. Due to absorption in the different layers through a variety of absorbers. the upward and downward flux differences at each level can then be used to determine the heating rates. which in turn then drive the atmospheric dynamics.

138

The calculation of absorptivity α and emissivity ϵ at each layer and band is very cpu intensive. In fact, this process takes up about 90% of the longwave computation (*Kiehl et al.*, 1996). Fortunately, the factors that determine changes of α and ϵ on short timescales, such as changes in layer cloud amount (water vapor and clouds), changes in the layer heating rates and ozone, are mostly accounted for. The clouds are directly included in the cloud parameterization, and the inclusion of the Planck function largely compensates for changes in the heating rates. Ozone is held at its prescribed distribution, including an annual cycle. Else, α and ϵ change slowly and, therefore, can be calculated much less frequently. In the standard setting, this is done twice per day. The less frequent computation of these variables causes no problems for the treatment of the very smoothly distributed (both in space and time) stratospheric aerosol. The situation is different for tropospheric aerosol, where the daily cycle plays a crucial role activating, lifting, transporting and finally, depositing dust and other aerosol particles. Absorptivity and emissivity change dramatically and probably should be calculated much more frequently.

Focusing on the stratospheric aerosol treatment, three main steps are involved in the LW computation.

First, a large data array is built (5 dimensional, although internally only 4D in the code since the different latitudes are treated separately on different processors) containing the spectrally resolved, mass-scaled transmission ($aer\_trn\_ttl_{lon,k1,k2,\lambda}$) from each level $k1$ to each other level $k2$:

$$aer\_trn\_ttl_{lon,k1,k2,\lambda} = exp\left(-1.66 * odap\_aer\_ttl\right) \tag{5.3}$$

with

$$odap\_aer\_ttl = a_\lambda * path_{k1,k2} \tag{5.4}$$

where $odap\_aer\_ttl$ is the absorption optical depth as the product of the mass path ($path_{k1,k2}$) and the mass absorption coefficient at the specific wavelength (a_λ). [Note, the latitudinal dimension is omitted here.] The transmission data basically describes the local aerosol absorption efficiency

from emissions coming from any other level, throughout the column.

The second step during the LW transfer, which is only done twice per day, consists of calculating ϵ and α at each level given their temperature, composition and density. Here, the total transmissions from the surface up to the layer of concern are used to scale (simple multiplication) the transmission from other absorbers, carefully including and adjusting for spectral overlaps. The emissivities in each of the bands can then be derived from the total upward transmission. The layer absorptivities can then be summed up throughout the column from the residual of the transmission from each model level. After the evaluation of α and ϵ, their values are stored in a lookup table which is used for the next twelve hours in step 3.

Finally, in the third step, which is again performed on the standard one hourly radiation time steps, the radiative fluxes in upward and downward direction are evaluated. This process corrects the fluxes for cloud occurrences at the different levels. For this, precomputed emissivities and absorptivities from step 2 are used, either directly after their calculation, or for eleven additional hours as lookup values.

As for the SW computation, radiative fluxes can then be used to calculate TOA and surface interface net fluxes, as well as infrared (LW) heating rates throughout the column.

5.2.4 Forcing versus feedback simulations

Generally, there are two different areas of interest when simulating volcanic eruptions in a climate model. On one side, one wants to know what the radiative effects of the aerosol, or in other words, the forcing on climate. On the other side, the climate response is the key issue. The difference between the two is that the first tries to isolate the radiative effect of the aerosol without actually changing the climate. Since the forcing from a stratospheric aerosol cloud is not only dependent on the aerosol cloud and its optical properties, but also on the surface albedo and cloud cover, it is not necessarily useful to have the aerosol modify the climate and with it the surface albedo and cloud distribution. In each column, the identification of the aerosol forcing would be quite

difficult. *Hansen et al.* (1997, p. 6835) presented different ways of expressing climate forcing. Here, only the the most simple (instantaneous) and the one closest to the real world (all feedback response) are considered. The others include additional treatment of a separated stratosphere and troposphere, which in a 3-dimensional GCM is not necessarily easy to perform. Nevertheless, it is important to point out that since 1990 the Intergovernmental Panel on Climate Change (IPCC) adopted a definition of radiative forcing as "the perturbation to the net irradiance (in Wm^{-2}) at the tropopause after allowing for stratospheric temperatures to re-adjust (on a time-scale of a few months) to radiative equilibrium, but with the surface and tropospheric temperature and atmospheric moisture held fixed." (*Schimel et al.*, 1996, p. 109).

The instantaneous forcing can be computed if the stratospheric aerosol in CCM is run in *forcing mode*. This mode does not allow the climate to respond to the aerosol and will result in a exact reproduction of a control run without the aerosol formulation. The forcing can be calculated if, in each time step, the radiation code is run twice: once including the stratospheric aerosol, for which the corresponding vertical fluxes and heating rates are stored, and then a second time with the stratospheric aerosol turned off. The difference between the first (with aerosol) and the second (without aerosol) radiative transfer with resulting fluxes is due to the presence of aerosol only. While it is rather costly to run the radiation twice, it is the only way to receive the instantaneous forcing that is only dependent on the aerosol.

The second mode the aerosol can be run with is the full *feedback mode*. In this case, the stratospheric aerosol is an intricate part of the atmosphere and perturbs the simulated climate. Feedbacks can now either enhance or dampen the direct effect of the volcanic aerosol.

Depending on the mode used in a simulation, a number of additional diagnostic fields are written to the history tapes. When running with the volcanic aerosol formulation turned on, independent from forcing or feedback mode, several additional fields will be stored. First, the optical depth in the visible band (SW band number 8) is retained as column integrated value in ODXC_VIS. Further, to provide at least an approximate forcing comparable to the example of

adjusted stratospheric temperature (*Schimel et al.*, 1996; *Hansen et al.*, 1997), net fluxes in both SW and LW are interpolated for a globally constant level of 200 hPa, roughly a global average of the tropopause. While, for LW bands, the fluxes are available for cloudy and clear sky conditions, the SW numbers can only be calculated for cloudy conditions, since the clear sky computation only distinguishes between two levels.

If the stratospheric aerosol is run in forcing mode, all radiative fluxes, atmospheric absorption and heating rate differences between the first full aerosol run and the second column transfer calculation where aerosols are absent are retained and saved with the postfix _FRC. All values are monthly averages, but may be saved in higher frequency for other purposes.

5.3 Pinatubo: A test case

An ideal test case for the implementation is the well observed eruption of Pinatubo in June 1991 (*McCormick et al.*, 1995; *Self et al.*, 1997a). Many details of this eruption have been previously mentioned (see Chapter 3.2) and are only briefly summarized here.

Pinatubo (15.13°N/120.35°E) erupted on June 15, 1991. The sequence of major explosive phases emitted a total volume of about 5 km^3 (DRE) and injected SO_2 in the order of 17 to 20 Mt into the lower stratosphere. Subsequently, this gas was transformed into sulfuric acid aerosol, which reached a peak mass of about 30 Mt (see Figures 1.2. The aerosol spread over the globe and perturbed the radiative budget for several years. Satellites and surface measurements tracked the buildup and decay of the volcanic aerosol cloud in much detail.

5.3.1 Forcing

5.3.1.1 Aerosol data set

A set of two year integrations from June 1991 to May 1993 were performed with monthly resolved, zonally averaged evolving stratospheric aerosol. The main aerosol data used for the experiments

was supplied by G. Stenchikov (Rutgers University) and is an adaptation to the CCM radiation bands from their data set with high spectral resolution (*Stenchikov et al.*, 1998, subsequently called ST98). The data set was built using satellite and lidar data from many different sources, trying to correct for some of the instrument dependent biases. One important difference to SAGE II (e.g. *Sato et al.*, 1993) is a higher optical depth in the visible wavelength. As discussed by *Thomason et al.* (1997) and ST98. SAGE II profiles were repeatedly saturated starting in late 1991 and with decreasing frequency until 1993 (*Thomason et al.*, 1997). SAGE II mid-visible optical depth estimates are, therefore, minimum values and range clearly below optical depth estimates from the ground (e.g. *Dutton et al.*, 1994) or, at the peak perturbation, are only about half of the NOAA-AVHRR satellite estimates of τ_{vis} (*Long and Stowe*, 1994), although the latter is potentially overestimated. The ST98 peak optical depth in the tropics is estimated at 0.35 (ST98, *Andronova et al.*, 1999). When the extinction is interpolated to the CCM spectral grid and vertically integrated, using either climatological column thicknesses (AMIP II data) or the thicknesses of an feedback run with aerosol, a peak optical depth (τ_{vis}) of just above 0.3 is reached (Figure 5.7, top left). This number is about 10% lower than ST98, and somewhere in the middle between ST98 and *Sato et al.* (1993). For later steps including simulations with aerosol data derived from the simple parameterization presented in Chapter 3.3, peak aerosol optical depth in the tropics was set to 0.35 to better match the original data (see Figure 3.4).

5.3.1.2 Optical properties

Figure 5.7 summarizes the main SW properties of the aerosol from ST98. The left column demonstrates optical depth and radiative properties for the visible band, the right column for the near infrared (NIR) band from 1.409 to 1.749 μm. Note the markedly different scales for the corresponding panels. The top row shows the column integrated optical depth, the second through fourth rows represent vertical profiles of aerosol optical properties needed for the δ-Eddington computation in the densest part of the cloud at the equator. One can see that the

smallest particles, which more efficiently perturb the shorter wavelength, dominate at the highest levels of the aerosol cloud (almost at 10 hPa pressure level), whereas larger particles reside below. The single scattering albedo with values almost at unity clearly demonstrates that the aerosols were almost pure scatterers in the visible band, and only at well past 1 μm start to absorb, as the single scattering albedo starts to decrease. The asymmetry parameter shows an increase in forward scattering efficiency in the visible, whereas in the NIR, it exhibits a decrease over time.

In Figure 5.8, longwave optical depth in a band from 12.5 to 15.38 μm is compared to the 12.66 μm optical depth derived from the cryogenic limb array etalon spectrometer (CLAES) on board of the UARS satellite (*Roche et al.*, 1993; *Grainger et al.*, 1995). Although the CCM optical depth is slightly higher, the two agree reasonably well, ensuring that the aerosol distribution is also acceptable in the longer wavelength where one can expect absorption of upwelling terrestrial radiation.

5.3.1.3 Simulated forcing in CCM

CCM was run in forcing mode at $T42$ horizontal resolution with AMIP SSTs applied as surface boundary conditions over oceans. Initial conditions for the atmosphere were taken from a June 1991 restart file of an AMIP-II simulation of a similar version of CCM3.6, but without strato-spheric aerosol. The land surface was initialized in the same way. The aerosol was assumed to be zonally uniform. In the vertical, ω_λ and g_λ were available in standard lookup tables resolved for latitude, level and time. The extinction was not supplied as column optical depth but as extinction per meter and CCM hybrid sigma level. Therefore, the individual layer thickness had to be computed during the run in order to calculate the layer optical depth for each time step. All aerosol was supplied in monthly resolution and was linearly interpolated to each radiation timestep (1 hour) during the integration. The aerosol data is shown in Figure 5.7.

Using these data, the instantaneous radiative forcing was stored for the simulation as the difference in radiative transfer at each time step between a disturbed and an undisturbed atmo-
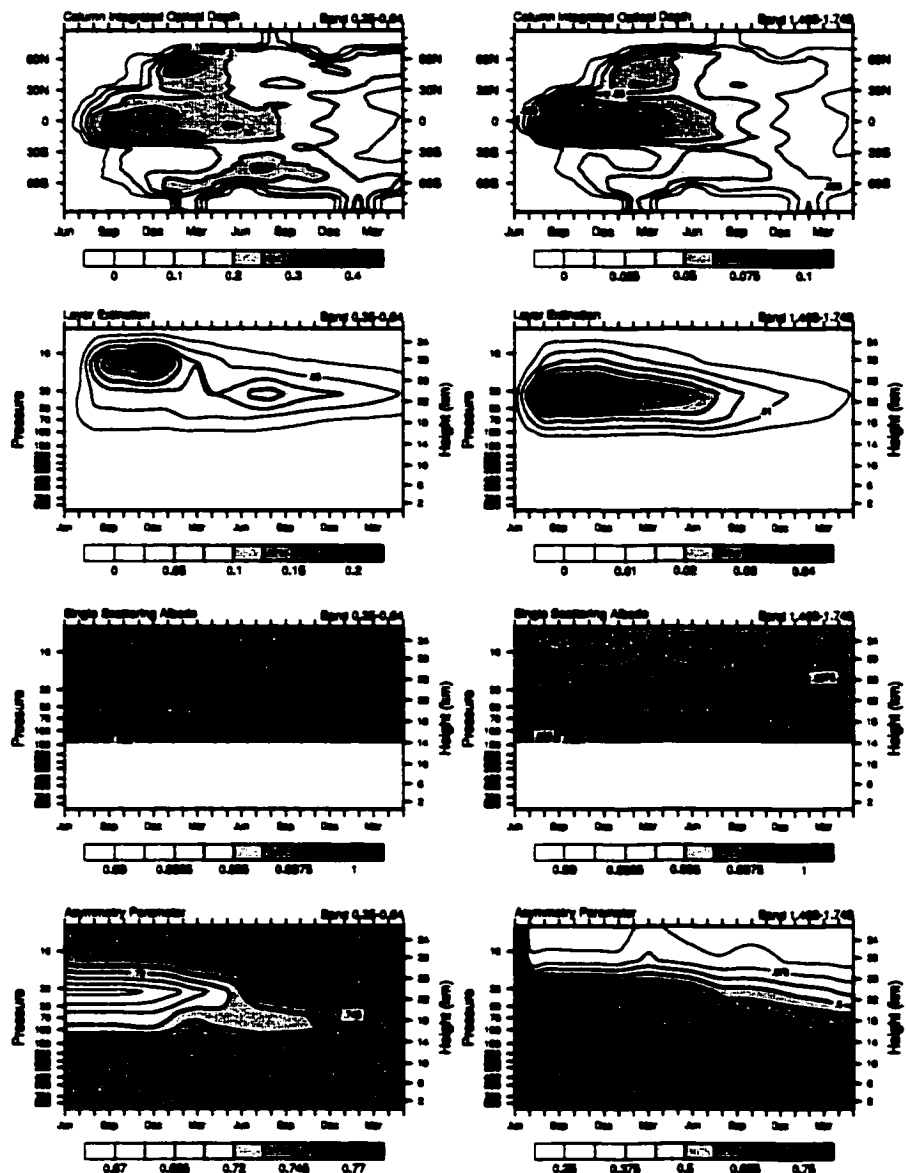
Figure 5.7: Optical properties of ST98 aerosol binned for the CCM3 radiative spectrum. Left column: mid-visible band (0.35 to 0.64 μm). Right column: CCM3 band 12 (1.408 to 1.749 μm). Rows from top: column integrated optical depth, vertical profiles of layer extinction, single scattering albedo and asymmetry parameter over two years starting in June 1991.
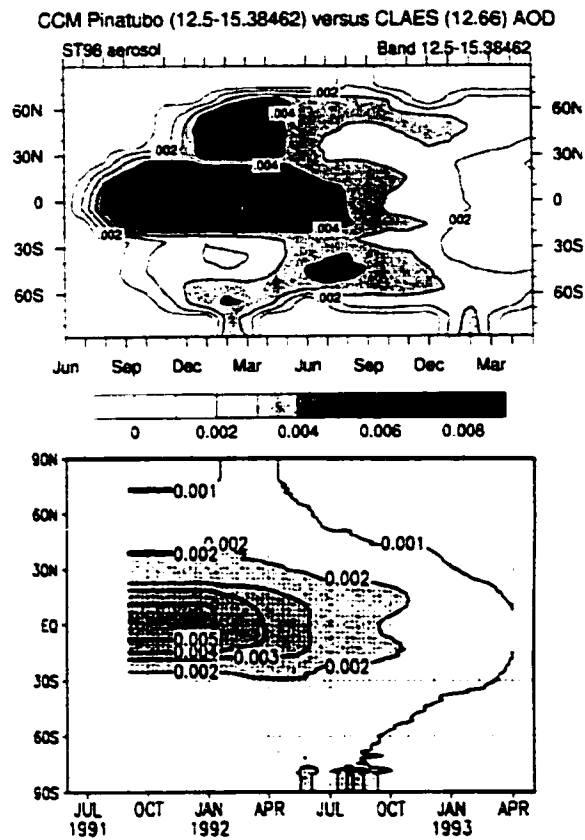
Figure 5.8: Optical depth at 12.66 μm from CLAES satellite (source: ST98) as compared to the CCM3 optical depth in a band from 12.5 to 15.38 μm. Note, the gray shadings are slightly different.

146

spheric column. The climate was not allowed to respond to the forcing (see above).

Figure 5.9 shows the zonally averaged distribution of the all sky forcing from spectrally weighted SW and LW computations. as well as the resulting total forcing both for TOA and the surface. The rapid increase in solar radiative perturbation resulting from the volcanic aerosol can be seen in the tropics. with peak SW forcing at TOA of just about -8 Wm^{-2} in September and October of 1991. This zonally averaged value is exceeded locally by values over 10 Wm^{-2} (not shown). They occurred especially over cloudless areas with dark underlying albedos (mostly ocean areas), similar to observations from *Valero and Pilewskie* (1992) and *Minnis et al.* (1993). During Northern Hemisphere spring and summer of 1992. the aerosol is finally globally distributed. The tropical forcing has dropped to about one third. whereas the northern mid-latitudes reach their maximum forcing. The Southern Hemisphere is additionally perturbed by aerosol from the eruption of Cerro Hudson (eruption on August 12. 1991). which is responsible for a counter intuitive southward 'transport' during the last part of 1991 (see discussion of meridional transport in Chapter 3.3).

In general. the LW forcing is similar to the SW distribution. but significantly smaller. This results in a negative total forcing. For example. the LW forcing in October 1991 reaches not quite 4 Wm^{-2} in the tropics. resulting in a negative net forcing of over 4 Wm^{-2}. The exceptions are polar night areas. where due to absence of insolation. no SW forcing can exist. but where LW absorption of upwelling terrestrial radiation can still take place. Note. the surface LW forcing is an order of magnitude smaller than the other flux perturbations (see also Figure 5.11) and also exhibits a drastically different pattern. This is due to the large absorptions from frequent cloud cover and large amount of water vapor in the vertical column. reducing the downward penetration of a rather small temperature anomaly.

Not surprisingly. the computed forcing patterns agree well with the patterns from ST98. *Andronova et al.* (1999) and *Ramachandran et al.* (2000). All these investigations used the same original data. but with different atmospheric resolutions in both horizontal and vertical space as
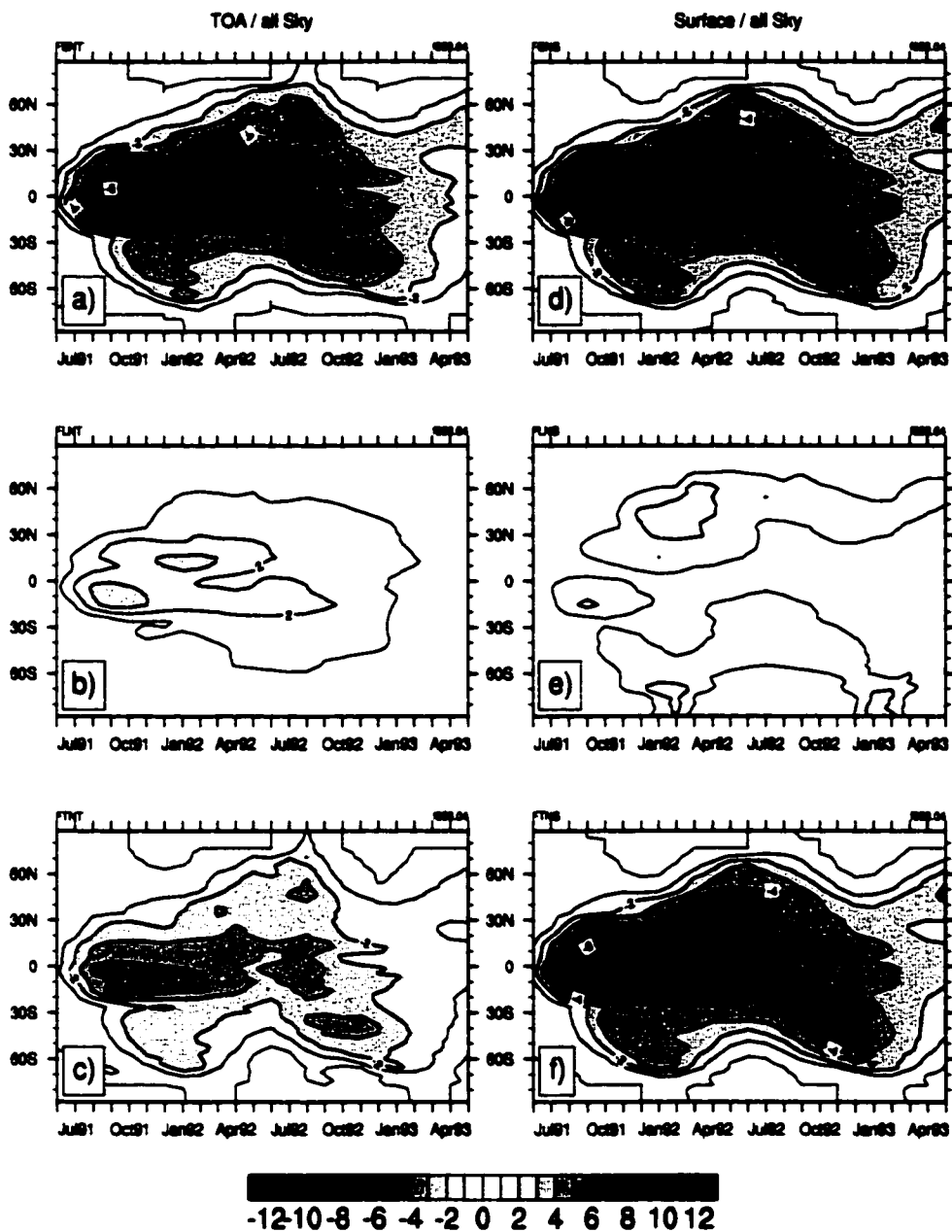
Figure 5.9: Temporal evolution of all sky aerosol forcing from Pinatubo using CCM3 with aerosol data from ST98. a-c are showing the SW. LW and total forcing at TOA. and Column d-f for surface respectively.
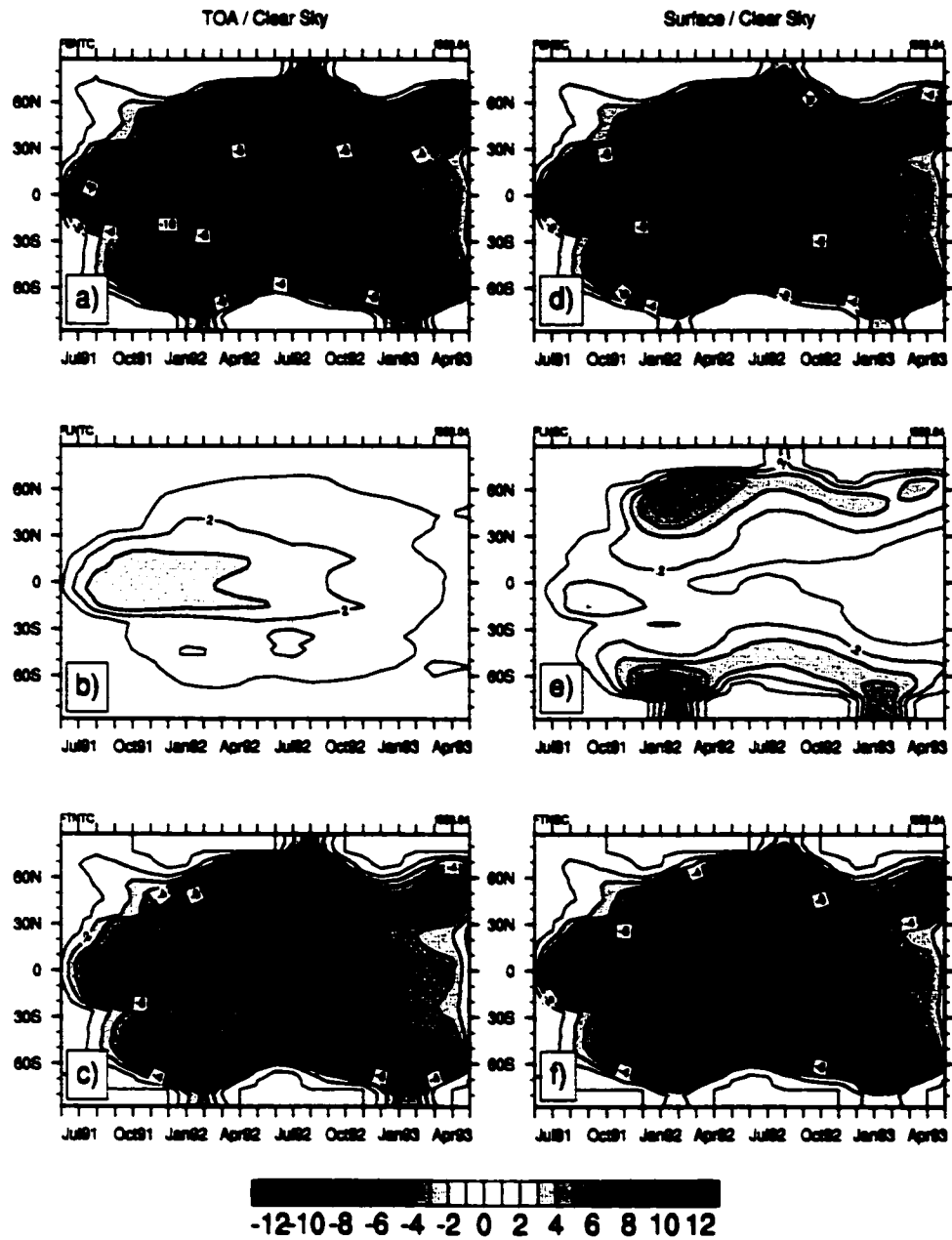
Figure 5.10: Same as Figure 5.9. but for clear-sky conditions.

well as in the radiative treatment. If looking at the obtained forcing at TOA and the surface, clear differences appear. The forcing in CCM is in many ways very close to the results from the Sky-High model of the Geophysical Fluid Dynamical Laboratory (SKYHI) (Ramachandran et al., 2000). This includes both all-sky (Figure 5.9) and clear-sky conditions (Figure 5.10). The CCM results are slightly higher in the perturbations, although much detail of the spatial evolution is similar. Looking at the all-sky conditions first, the CCM SW forcing reaches over 7 Wm^{-2} in the tropics, while SKYHI gets 5 to 6 Wm^{-2}. In the LW, again CCM is only slightly higher, resulting in a 4 vs 3 Wm^{-2} total TOA forcing. For clear-sky conditions, the total forcing of 7.5 (CCM) vs 8 Wm^{-2} (SKIHI) in the tropics around October 1991 to January 1992 is basically identical. Additionally, there are equally large forcings in the summer hemisphere high latitudes, both in the North and South with forcing at 60 to $70°$ reaching initially over 12 Wm^{-2} in January 1992 in the Southern Hemisphere, and roughly 10 Wm^{-2} in the Northern Hemisphere. These large high latitude forcings coincide with the high insolation times at these latitudes during the respective summer season, and represent an extended influence of the dominating SW signal. The forcing is so so strong that the clear sky effect is also strongly reflected in the all-sky results.

If Figure 2 of Andronova et al. (1999) represents clear sky conditions, then the results are almost identical to those obtained here, although the high latitude peaks are markedly smaller. The forcing values obtained with CCM are higher than those received from a relatively coarse resolution radiation treatment in ECHAM3 shown in Stenchikov et al. (1998), as discussed in Andronova et al. (1999) and Ramachandran et al. (2000).

Figure 5.11 shows a comparison of the SW, LW and combined total forcing in the tropics (area averaged from $40°N$ to $40°S$) with measurements from ERBE (Minnis et al., 1993). Very good agreement is achieved during the buildup phase, reaching a correct peak forcing of about 3 Wm^{-2} (comparison of ERBE has to be done with the TOA forcing, since this is what the satellite measures). The decay of the forcing over time is somewhat faster in ERBE. The reason for this is probably twofold. First, the model is run in forcing mode only, therefore the climate and with

150

it cloud distribution is not allowed to adjust to the forcing. Second, the development and decay of El Niño/Southern Oscillation, an important aspect for tropical cloud distribution and albedo, could have easily caused a further perturbation. Generally, good agreement in radiative forcing is achieved. This is also true for the global average SW forcing, which *Minnis et al.* (1993) estimate at 2.7 Wm^{-2}.

Due to the δ-Eddington formulation, the strong effect of the aerosol in the SW can also be split into the perturbation of the direct solar beam and the change in diffuse sky light. Figure 5.12 shows the total SW changes in direct, diffuse and total radiative flux at the surface for January 1992, the month close to the maximum global aerosol forcing. A strong decrease in the direct solar beam on the order of 10 to 20 Wm^{-2} in the clear sky areas of the tropics can be seen. At the same time, the diffuse sky light compensated for the loss, but by a somewhat smaller amount, resulting in a net loss of downward radiation at the surface. This very effect has been observed since the earliest documentations of hazes high in the atmosphere (see Chapter 2.3.2). The decrease in the direct beam with an accompanying increase in diffuse light is responsible for the often reported lack of clear shadows, and the hazy color of the sky. Due to an inconsistency in the data storage, the fields are shown of the simplified aerosol (run f060.14), but it will be shown below that the radiative forcing is almost identical between these two runs, and therefore the plot is not only qualitatively informative, but basically quantitatively correct.

5.3.2 Climate impact

Now that the forcing is reasonably captured in the aerosol implementation, the next step in the model-based investigation of volcanic effects on climate is to let the climate respond to the forcing. In the following, the same experiment was performed using prescribed SSTs and identical initial conditions. This time, the aerosol parameterization was run in feedback mode and no forcing fields were stored. The forcing can now be estimated by differencing the fluxes from the unperturbed run with the fluxes from the feedback run. Note, due to climate response

Tropical and Global Radiative Forcing
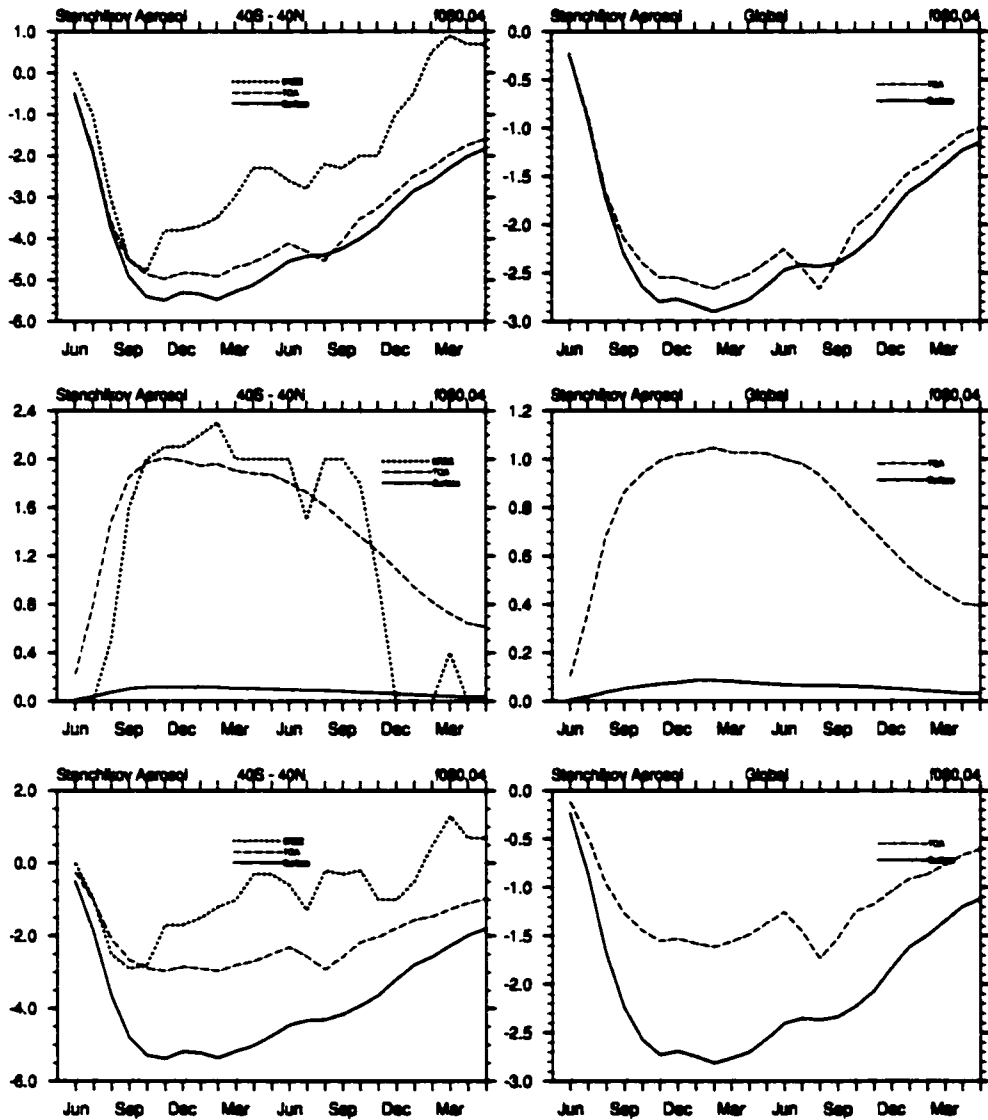
Figure 5.11: Simulated radiative forcing separated into SW (top row). LW (middle row) and total forcing (bottom row). for the tropics from 40°N to 40°S (left column) and global (right column). The model data was area weighted. A comparison of modeled and ERBE observed radiative forcing is shown for the tropics. Note that the ERBE satellite data should be compared with the top of atmosphere fluxes (red lines). rather than the surface fluxes (blue lines).

January 1992 direct and diffuse beam perturbations (VIS/NIR)
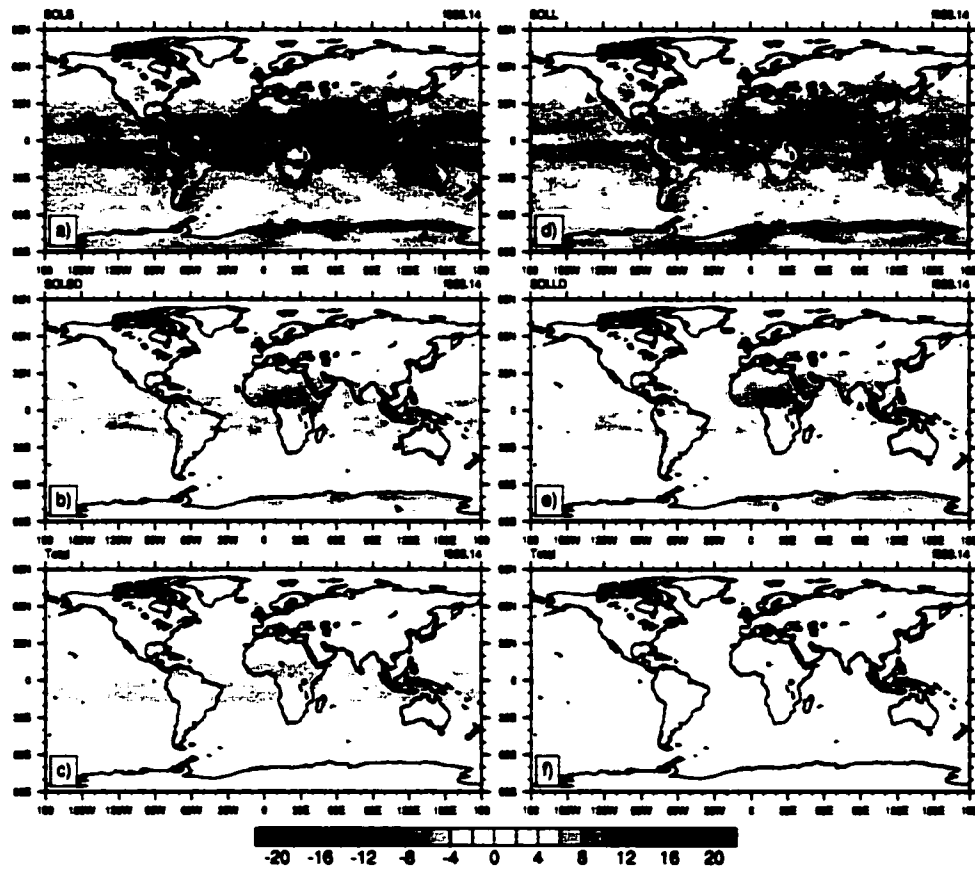
Figure 5.12: Direct (a.d), diffuse (b.e) and total solar flux changes (c.f) for cloudy skies due to volcanic aerosol for visible (a-c) and NIR (d-f) wavelength. Note: data from run f060.14.

153

(feedbacks). no exact agreement with the forcing numbers presented above would be reached and noise can blur the signal.

5.3.2.1 Heating rates

The first direct effect of the aerosol forcing concerns the vertical heating rate anomalies due to the aerosol. Since the radiation code distinguishes between SW and LW. one can also look at their individual contributions. The heating rate changes. in turn. will cause the temperature profile to adjust. which influences the density of the air throughout the atmospheric column and therefore. the dynamics.

Figure 5.13 shows the obtained CCM3 heating rates. The maximum heating using the Stenchikov aerosol occurs in the SW in the uppermost part of the aerosol cloud. where a large number of very small particles are present (around 10 hPa. or roughly 30 km altitude). For a generic aerosol (see below). the heating rates get closer to *Ramachandran et al.* (2000). Due to the low vertical resolution in CCM. the maximum in visible and NIR heating fall together causing the very high heating of over 0.4 K/day. somewhat higher than in *Ramachandran et al.* (2000). but quite similar to idealized model calculations using an observation-derived single scattering albedo of 0.99 compared to unity (*Kinnison et al.*, 1994). No detailed analysis similar to SKYHI can be done here. as the vertical resolution does not allow the detailed separation of vertical sections of the aerosol cloud. Despite this fact. the LW maximum heating of over 0.2 K/day occurs clearly in the lower half of the cloud. The large heating persists until early 1992 when it starts to decrease and by early 1993. is around 0.1 K/day. During this time. the maximum heating that initially occurred at the top of the cloud is reduced and continues to decrease in altitude (see Figure 5.14). although limited vertical resolution does not allow this process to be fully explored. Figure 5.14 also shows how the heating is largely confined to the low latitudes. Already at 45°North. the heating is more than 50% lower. and in polar areas basically absent.

Vertical Distribution of Spectral Heating Rates
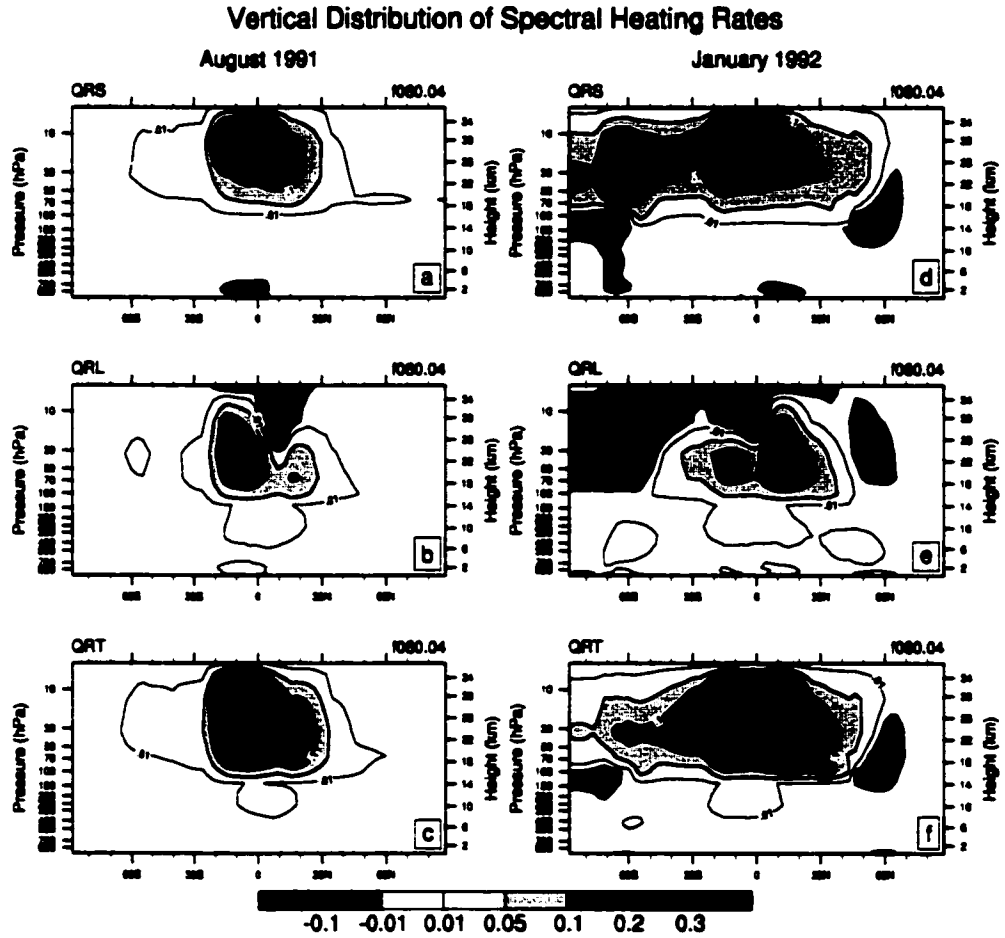
Figure 5.13: SW and LW heating rates due to stratospheric aerosol derived from forcing experiment using AMIP II SSTs. Shown are zonally averaged values for August 1991 (a-c). January 1992 (d-f). August 1992 (g-i) and April 1993 (j-l).

Vertical Distribution of Spectral Heating Rates
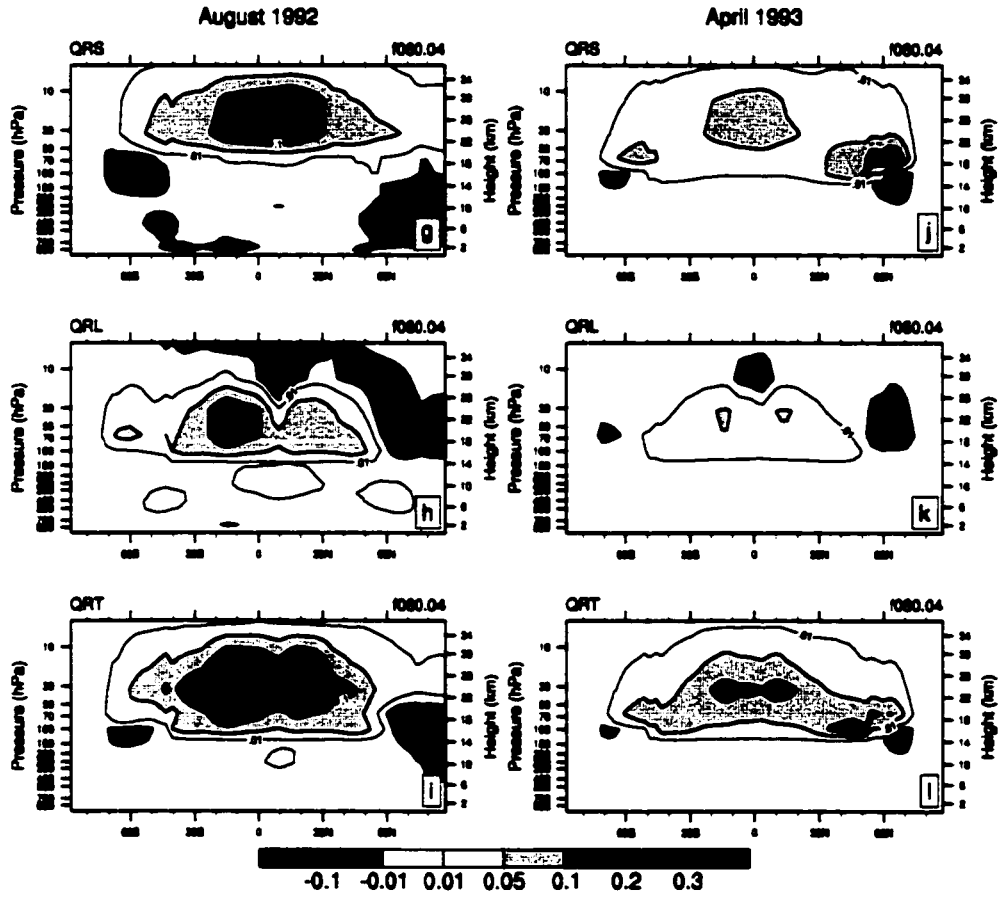
Figure 5.13: (continued)
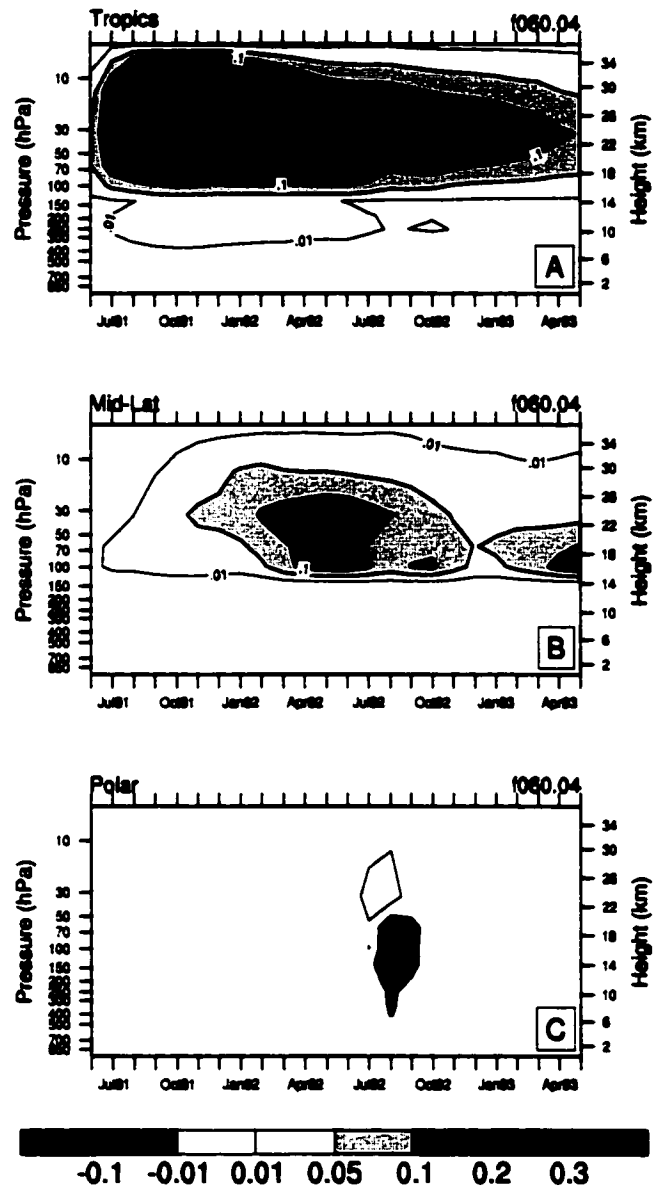
Figure 5.14: Vertical distribution of total heating rates over the two years of simulation in the a) tropics. b) mid-latitudes and c) polar areas.

5.3.2.2 Atmospheric temperatures

Figure 5.15 shows a north-south cross section through the zonally averaged atmosphere for two winter seasons. Plotted is the temperature anomaly at each level to the volcanically unperturbed control run. The presence of the lower stratospheric aerosol can be readily detected as the area of temperature increase. The maximum heating occurs in the tropics during the largest optical perturbation, in December through January 1991/92 with almost 4°C warming. This warming can also be seen in Figure 5.16. where the 50 hPa level temperature anomalies are presented in zonally averaged form throughout the two years of simulation. Striking is the warming in the tropics with a semi-annual pulsing forced by the shift of the sun. At the end of the simulation, the stratospheric temperatures are still perturbed by at least 1°C. The high latitudes, especially in the northern hemisphere, also show some strong anomalies. One needs to keep in mind, however, that the high latitudes, particularly during winter time, exhibit a very strong natural interannual variability. In Figure 5.16b. therefore, only the anomalies larger than one standard deviation to a 14 year AMIP simulation are retained. The northern hemisphere winter cooling and warming immediately after the eruption turns out to be not significant. Figure 5.16c shows an example of unforced sudden stratospheric warming in the northern polar areas during the AMIP run.

As seen in Figure 5.15. the polar areas cool indicating an initial intensification of the polar vortex as compared to the corresponding conditions in the AMIP simulations where the SSTs were identical, but no stratospheric aerosol was used. The early winter 91/92 simulation resembles closely results obtained by *Kirchner et al.* (1998), when they used observed SSTs, and the National Center for Environmental Prediction/National Center for Atmospheric Research NCEP/NCAR reanalysis (*Kalnay et al.*, 1996: *Kistler et al.*, 2001), subsequently NCEP. Note. the first northern hemisphere winter is only represented by December and January, as CCM experienced a strong sudden stratospheric warming during February, strongly perturbing the zonally averaged temperatures. From the available data, the significance of this event cannot be

Pinatubo Meridional Temperature Profile
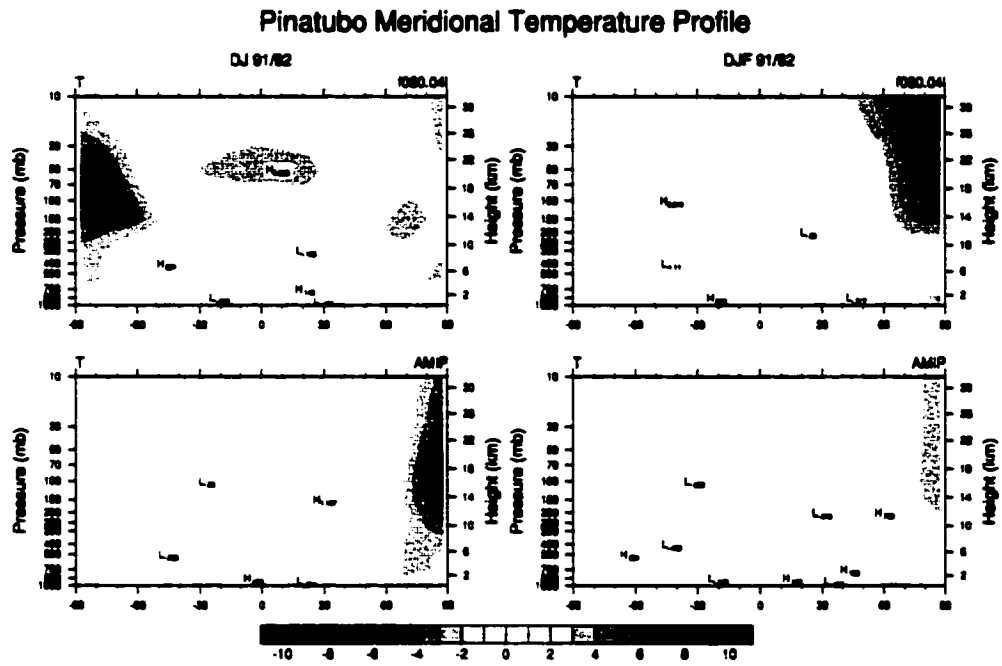
Figure 5.15: North-South profile of temperature change due to Pinatubo aerosol zonally averaged for two winter seasons in each hemisphere as compared to the same years (same SSTs) of the AMIP simulation.

159
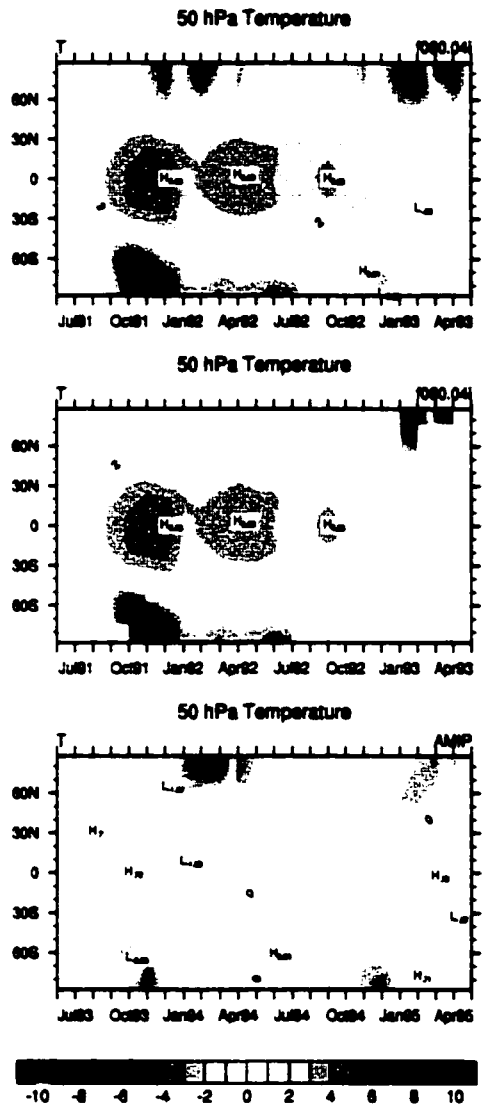
Figure 5.16: Temperature perturbations on the 50 hPa pressure level. a) anomalies after removal of seasonal cycle in Pinatubo simulation. b) only areas of change larger than one standard deviation from 14 year AMIP simulation are shown. c) shows a section for of the AMIP II simulation with a stratospheric warming independent from aerosol.

established. Yet. in the second winter. a similar warming occurred in the simulation. this time during two of the winter months causing a warm anomaly.

5.3.2.3 Zonal wind

These vertical temperature anomalies drive the dynamic response to the aerosol. Figure 5.17 shows the zonal wind perturbations in the same cross section as the temperature profile in Figure 5.15. In red are increased zonal westerlies. and blue represent decreased westerly strength. The colored regions are areas of more than one standard deviation anomalous winds.

5.3.2.4 Seasonal surface temperature response

How are the surface climate conditions simulated? If one first looks at globally area averaged temperatures. as simulated using AMIP SSTs and two observational time series (NCEP and the globally gridded data merged of *Jones* (1994) (land stations) and *Parker et al.* (1995) (ocean surface temperatures). updated with *Rayner et al.* (1996). subsequently Jones-Parker). The success of the simulation can be seen in Figure 5.18. Initialized to zero for June 1991. observations and the simulation show a seasonal cycle in the global temperature with cool conditions in northern hemisphere fall but relative warm averages during the following winter. The magnitude of the temperature fluctuations is reproduced well in the feedback simulation as compared to NCEP and Jones-Parker. The spatial distribution of the temperature anomalies are presented in Figure 5.19. In the left column. the northern hemisphere winter conditions are compared between the model simulation and the two observational data sets. Most prominent are marked warmings over the northern hemisphere continents that were related to the volcanic aerosol (as reported in *Groisman* (1992). *Robock and Mao* (1995) and *Kirchner et al.* (1998)). The difference from the aerosol feedback run to the unperturbed control (panel a) shows a strong influence from the aerosol in CCM. In addition. the magnitude of the temperature changes are well reproduced in the simulation. The spatial location is more difficult to match as the planetary wave structure

161

Pinatubo Zonal Wind Profile
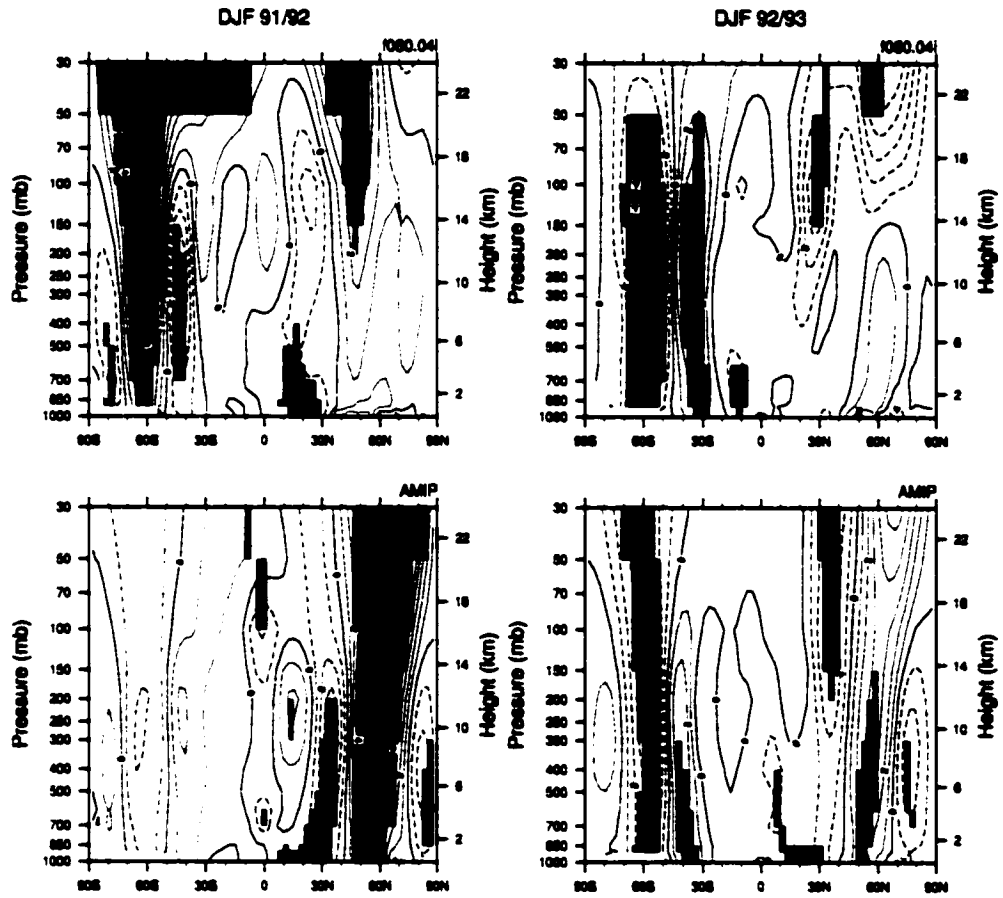
Figure 5.17: North-South profile of zonal wind strength for two northern hemisphere winter seasons. Colored areas are changes more than one standard deviation different from the 14 year AMIP simulation.
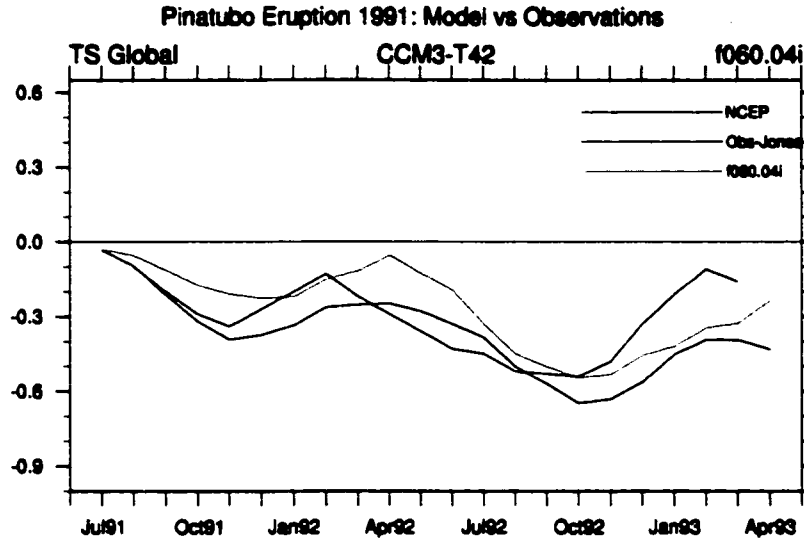
Figure 5.18: Global area averaged temperatures from the CCM3 simulation as compared to NCEP reanalysis and observational data from Jones-Parker

shifts continuously.

The good match is also true for the summer conditions of 1992, when large areas of slight continental cooling are more prominent than areas with warming. In the model, a slight shift of the wave structure over the northern hemisphere is found, although, again, the difference to the control run shows the correct tendency with warming in western Europe and cooling to the east.

5.3.3 Simplification

The above reported results from the Pinatubo simulation using the ST98 aerosol were to verify the implementation. The general success permits us now to move to other eruptions. Since, for other events the detail in aerosol properties is no longer known, a intermediate step will evaluate the potential of simplifying the aerosol description and generalize to a point, where the majority of impacts still are preserved and the simulation can be regarded as 'close enough'. One needs to keep in mind, that for paleo climate applications, basically no aerosol information apart from

Seasonal Surface Temperature Anomaly
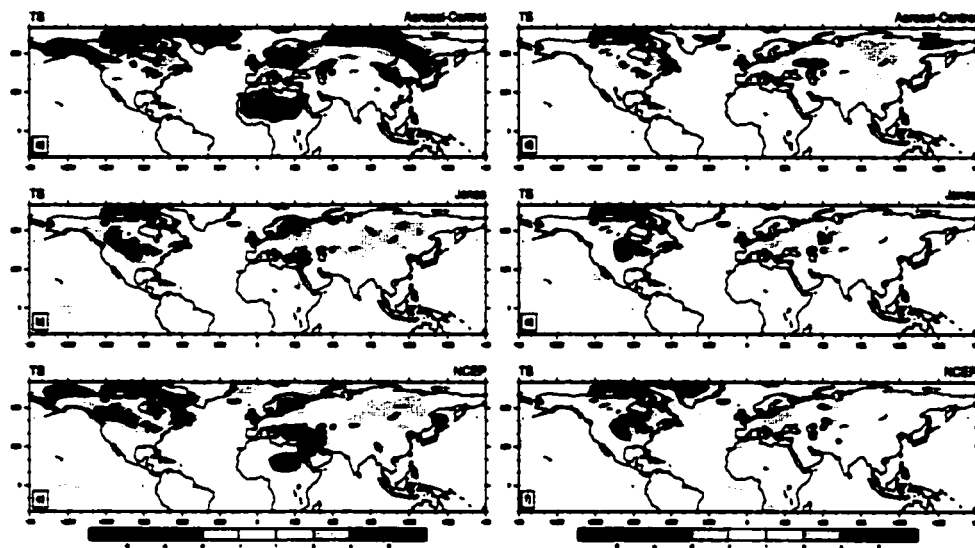
Figure 5.19: Spatial distribution of northern hemisphere winter 1991/92 and summer 1992 as compared to Jones-Parker and NCEP

perhaps the total aerosol mass will be available.

This problem was addressed in Chapter 3.3. Here an intermediate step is used. While preserving the visible optical depth as found in ST98, the detailed aerosol information is replaced by a single aerosol distribution which is held constant throughout the run and at all levels. It consists of an intermediate sized aerosol ($r_{eff} = 0.42$ μm and $\sigma = 1.25$ μm, as in ST98), and a limitation to model levels 3 through 6, or roughly from 30 to 150 hPa. The aerosol properties for this distribution were computed in a Mie code and then added into the model as lookup tables for each radiative band for CCM.

Here, the simplified Pinatubo aerosol distribution is compared against the run with fully described aerosol. In order not to repeat too many discussions from above, only two analyses are shown. The first step is, of course, the crucial aerosol forcing. Figure 5.20 shows the TOA and surface radiative forcing over two years of simulation, broken down into SW and LW parts. The peak TOA SW forcing also reaches 8 Wm^{-2} and the LW maximum just about 4 Wm^{-2}, resulting in almost identical TOA total forcing of around 4 Wm^{-2} in the southern tropics and in good agreement with ERBE observations (*Minnis et al.*, 1993). The surface forcing is slightly smaller than for the run, with detailed aerosol mostly due to a slightly reduced SW forcing. This is no surprise, as in the single aerosol experiment no high numbers of very small particles are present at the top of the aerosol cloud, as in the ST98 data. Nevertheless, the radiative forcing at TOA and the surface due to the aerosol is basically identical between the detailed aerosol data of ST98 and the simplified, single aerosol distribution with the same optical depth in the visible band.

The climate impact of the single aerosol distribution is shown in Figure 5.21. The winter warming over the Asian continent is not particularly well reproduced as in the previous experiment, although a clear warming is simulated in the northern most areas. Over North America, a similar warming is produced, again slightly shifted to the north east of observed warming as represented by Jones-Parker or NCEP. In summer, the overall performance is better over North
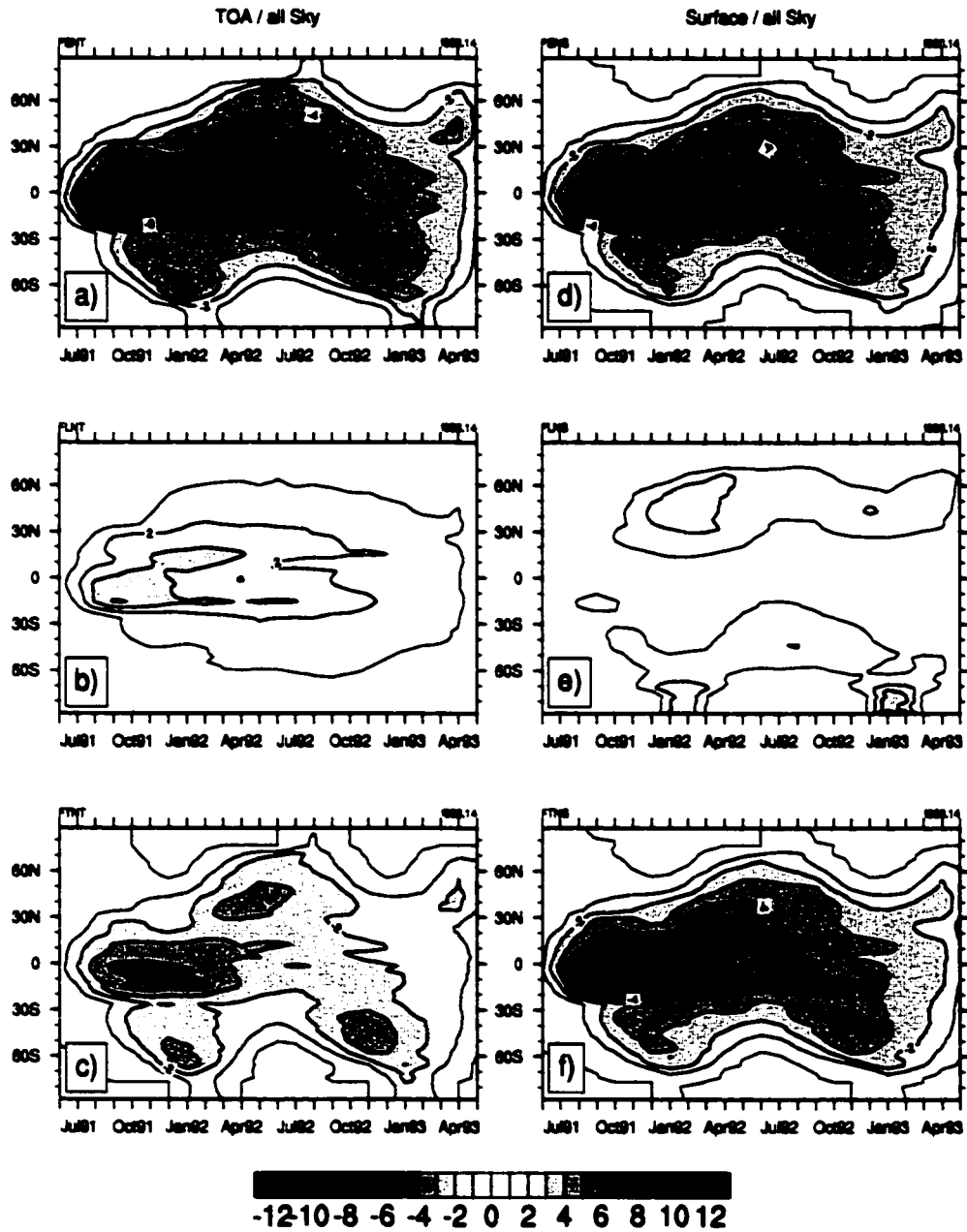
Figure 5.20: Radiative forcing as shown in Figure 5.9 but for single aerosol size distribution of $r_{eff} = 0.42$ μm. and $\sigma = 1.25$ μm

Seasonal Surface Temperature Anomaly
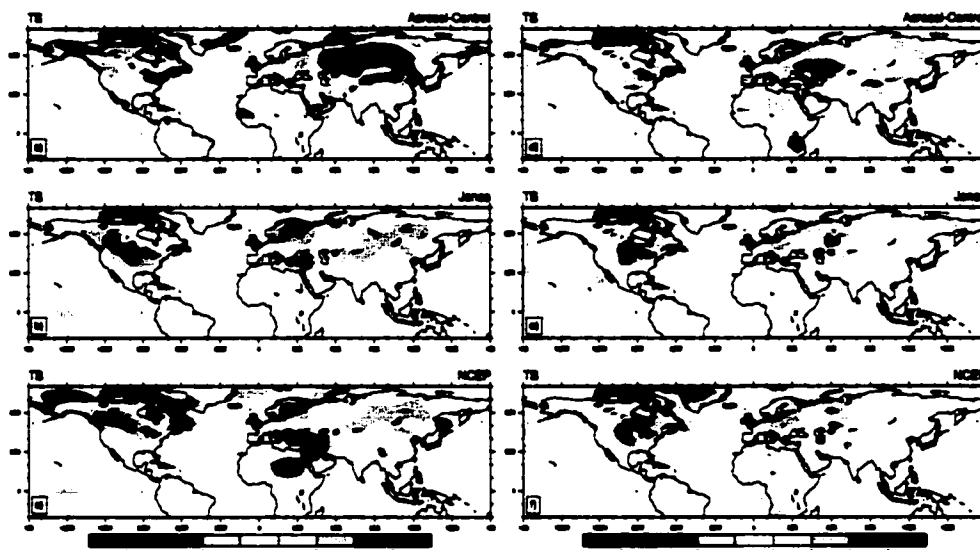
Figure 5.21: Surface temperature response during first winter and summer season as compared with observations. Same as Figure 5.19. but for single aerosol size distribution.

America. with a more pronounced cooling over the central US. extending towards the Labrador Sea and Greenland. Warm anomalies over Europe are not well captured. although the stronger cooling over western Russia is very similar to the previous experiment.

The surface climate response to the aerosol seems reasonable. and not much detail is lost when replacing the detailed aerosol properties with a much simplified. single size distribution. This is encouraging for the following experiments of eruptions where no aerosol size information is available.

Chapter 6

CLIMATE IMPACT OF HISTORIC ERUPTIONS IN CSM

6.1 Overview

Once we have implemented the volcanic aerosol physics into the NCAR-CCM and tested the model's response to the well-known Pinatubo aerosol (Chapter 5), we can then use the aerosol module in fully coupled mode. Only when the entire climate system can respond to the large but transient perturbation of the volcanic aerosol will the climate impact be more internally consistent and there will be less external biases present in the solution. This should lead to an outcome that more accurately resembles the conditions in the real world.

The previously presented Pinatubo simulations were run with observed SSTs, which led to a "fudged" coupled climate experiment. By now imposing the atmospheric forcing on the coupled climate system model and replacing the prescribed SSTs with a fully dynamic ocean model (in

the configuration of the NCAR-CSM), the response will be somewhat different. as the ocean

model. together with the sea ice component. will leave their own imprint. But this configuration

will now allow for feedbacks from the coupled system to participate in the response and recovery.

In addition. for the simulations presented below. the aerosol will no longer be the highly detailed

aerosol data of *Stenchikov et al.* (1998). but the simplified parameterization presented in Chapter

3.3. The reason for this is that no detailed aerosol information is available for eruptions prior

to Agung (1963). The simplified parameterization uses optical depth estimates from the small

number of observations since 1882 and follows the assumption that aerosol particles always form

in a similar way as for the eruptions since 1963. This also implies that sulfate fluxes from the polar

ice sheets can be used to describe the atmospheric perturbations from explosive volcanism (e.g..

Zielinski, 1995). since the total emitted sulfur mass can be estimated from the linear relationship

to the deposition mass flux measured in the ice. The validity of this assumption will be discussed

later.

This chapter will focus on three main questions:

How large is the volcanic aerosol forcing and its impact on climate during the 20th-Century?
Using the aerosol dataset produced in Chapter 3.5. the NCAR-CSM was run at T31-x3° resolution

for the time period of 1870 to 2000. First. a control experiment was run out using an atmospheric

composition of 1870 but without any external forcing. Then. the experiment was repeated. this

time using the volcanic aerosol to perturb climate. Using these runs. the volcanic forcing over

time will be described and compared to other natural forcings. The climate impact of the volcanic

aerosol on interannual and decadal time scales is then documented.

*What determines the magnitude of the climate impact of a specific eruption in a coupled
experiment?* The climate impact of a single tropical event (Krakatau. 1883) was analyzed in

more detail. and sensitivity experiments evaluated how important different boundary conditions

were in determining the effect on climate of a particular eruption. The general assumptions put

forth in Chapter 5 were revisited and critically analyzed.

In what way can volcanic eruptions excite, suppress or pace internal modes of climate variability? Volcanic eruptions impact not only the radiative budget, but with this also influence the temperature and pressure gradients that are generally modulated by internal modes of climate variability. Using the ensemble simulations of tropical and high-latitude events, a first description of their impact on one of the major modes of variability, the North Atlantic Oscillation, is presented. The results are compared with previously suggested relationships in the area of the eastern North Atlantic (*Defant*, 1924; *Lamb*, 1970).

To summarize, the conclusions from the different simulations as well as the implications of successful and less successful aspects of the simulations are discussed. General implications for modeling of past volcanic eruptions and their climate impacts will be highlighted.

6.2 Coupled simulations of the 20th-Century

6.2.1 Spinup procedure

The first task in performing simulations is to get the coupled model to spinup towards an equilibrium, at which point, the response to an imposed forcing can be studied. The spinup is particularly important for coupled climate model simulations, since strong drifts or fluctuations could hamper the signal-to-noise analysis. While the Pinatubo experiments described in Chapter 5 were run as a branch off from a long AMIP simulation with the T42 resolution of CCM3, the experiments of the 20th-Century make use of the coupled T31 (Paleo) version of the NCAR Climate System Model (CSM). This model in its current configuration has not yet been run for 1870 conditions. Therefore, a spinup procedure had to be performed to equilibrate all components of the coupled climate system to the conditions of 1870 (i.e., the atmospheric composition of that time with ocean heat transport and sea ice in, or close to, a stable equilibrium with the atmospheric flow).

The standard spinup procedure of the paleo CSM includes three distinct steps: atmospheric spinup, ocean spinup, and then an initial coupling.

First, the atmosphere is spunup using observed or otherwise prescribed SSTs and by setting the atmospheric composition to the selected values for CO_2 and the other greenhouse gases. For 1870, the following concentrations were set (data from IPCC, Wigley, pers. comm., 2000):

- CO_2 : 289.263 ppm

- N_2O : 281.351 ppb

- CH_4 : 901.355 ppb

- CFC-11 : 0.

- CFC-12 : 0.

Additionally, the solar constant was lowered from 1367 Wm^{-2} in the standard configuration to 1365.5 Wm^{-2}. This value was chosen for later transient simulations, where the solar constant would be ramped towards present day, following suggestions of *Lean et al.* (1995) and *Hoyt and Schatten* (1998). The fixed, globally uniform tropospheric aerosol optical depth was lowered to 0.035 from the standard 0.14, according to estimates of reduced tropospheric aerosol (*Rasch et al.*, 2000). The initial SST data were taken from GISST version 2.3a in 1°resolution for 1870 conditions and combined with present SSMI sea ice distributions, since sea ice reconstructions in the last century are not assumed to be very accurate. The data were interpolated to the CSM-x3' ocean grid and combined into 12 monthly time slices that were then repeatedly used during the 10 years of simulations of the atmosphere.

From this 10-year atmosphere-only simulation, the last 5 years were subsequently used to repeatedly force the dynamic ocean and sea ice models during their spinup. Since the atmosphere adjusts much faster to changes in boundary conditions, the second 5 years of a 10 year run are usually sufficient. The reason that not only one single year is used comes from the fact that

the atmosphere undergoes quite substantial interannual variability, and it would not be suitable to spinup the ocean to one single atmospheric mode (e.g., one extreme in the North Atlantic Oscillation). For the ocean spinup, the surface was forced with winds, radiation and temperatures of the atmospheric spinup. To allow the deep ocean to adjust, a process normally taking hundreds of years, an acceleration function into depth was applied (see *Bryan*, 1984), ranging from 1 (no acceleration) at the surface continuously to a factor of 50 for the lowest 5 of the total 25 ocean layers of the x3˚ model version. The run was extended for 20 surface years, which has the deep ocean go through an equivalent of 1000 years due to the factor of 50 in acceleration. Over the 20 years of integration, several diagnostic fields show the strong adjustments taking place in the ocean, namely deep ocean temperatures, volume integrated salinity, and circum Antarctic flow strength. Most of the drifts decreased significantly towards year 20, suggesting an approximation towards an equilibrium. The same was the case for sea ice.

The spinup, so far, was trying to bring all models as close as possible to the new conditions, but only through coupling can a stable mode be reached. This was achieved by the initial coupling step, where acceleration was no longer used, and the models find an equilibrium trough a coupled (i.e. interactive) process. This initial coupling was run out for 70 years. During this time, the model underwent further adjustments. In the first 10 years, sea ice volume increased roughly 20%, while northern hemisphere temperatures increased by over 0.5˚C. After 70 years of coupled run, again diagnostics such as sea ice, surface temperature, ocean potential temperatures, radiative net fluxes seemed to come close to equilibrium conditions. After a total of 100 years of spinup procedures, the T31-x3˚ Paleo CSM was reasonably spun up to conditions viable for the experiments.

6.2.2   Control Experiment

In order to analyze forced experiments in terms of climate variability on interannual and longer timescales, a control experiment containing no external forcing is needed. This is basically

an extension of the initial spinup. and as such. was run for an additional 130 years. Figure 6.1 shows the coupled portion of the initial spinup and subsequent control for absolute surface temperatures and their relative change compared to the average of the first 10 years for the globe. the tropics as well as the northern and southern hemisphere. The strong adjustments during the first 70 years (during the spinup) are clearly visible. with the most important changes taking place roughly around 1920. where the northern hemisphere temperature increases while the southern hemisphere temperature decreases. Around 1940. the run looks reasonably stable. although further trends can be seen around year 1990 to 2000. Figure 6.2 shows the sea ice conditions throughout the initial spinup with subsequent 130 years of control experiment. The increase followed by dramatic decrease in northern hemisphere sea ice area and volume is probably primarily responsible for the hemispheric temperature changes.

An important measure of the global ocean circulation is the overturning in the North Atlantic. After an initial increase to over 32 Sverdrup (Sv). the control shown in Figure 6.3B seems to level out around 26 to 28 Sv. although with continued slight negative trend. This is similar in behavior to the 300 year coupled performance reported in *Donabasoglu* (1998). but clearly less than the 30 to 40 Sv in *Boville et al.* (2001). All these values are higher than observations (around 20 Sv). probably due to somewhat higher surface wind stress after coupling (*Donabasoglu.* 1998). The simulation of the Antarctic Circumpolar Current (ACC) is with roughly 145 Sv significantly improved towards the standard model (236 Sv compared to 118-148 Sv from observations *Whitworth.* 1983).

The run is not in full radiative balance. As can be seen from Figure 6.3A. the ocean heat content is slighly negative (about 0.6 to 0.7 Wm^{-2}). causing the coupled system to cool slightly (about 0.15°C per century). This trend is marginally larger than the performance of the 300 year coupled integration at higher resolution (*Bryan.* 1998).

Interannual variability in the control is represented quite well. NINO3 SST variability exhibits a standard deviation of 0.66°C. somewhat lower than observations. which range from 0.7°C for the
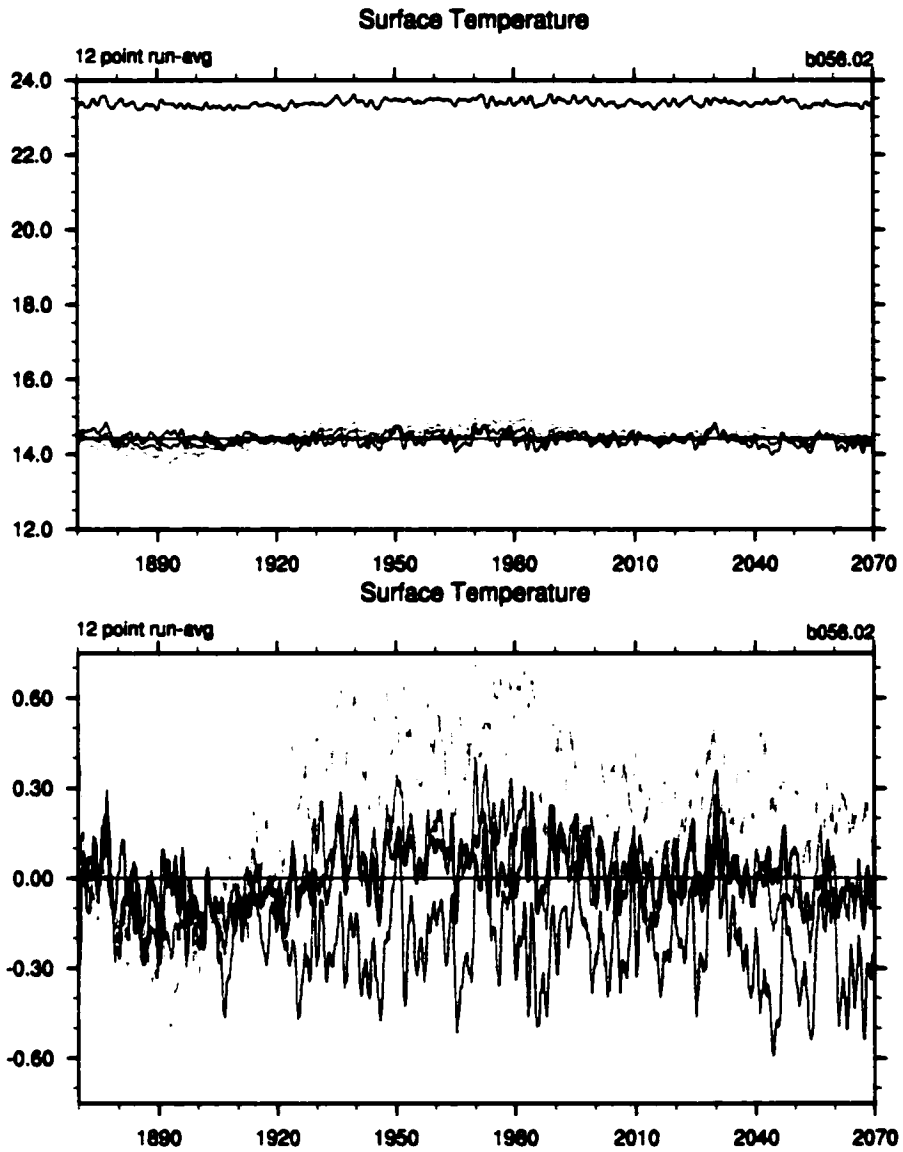
Figure 6.1: Coupled spinup and control experiment for surface temperatures for globe (dark red lines), the tropics from 40°N to 40°S (blue), the northern (orange) and southern hemisphere (green).

174
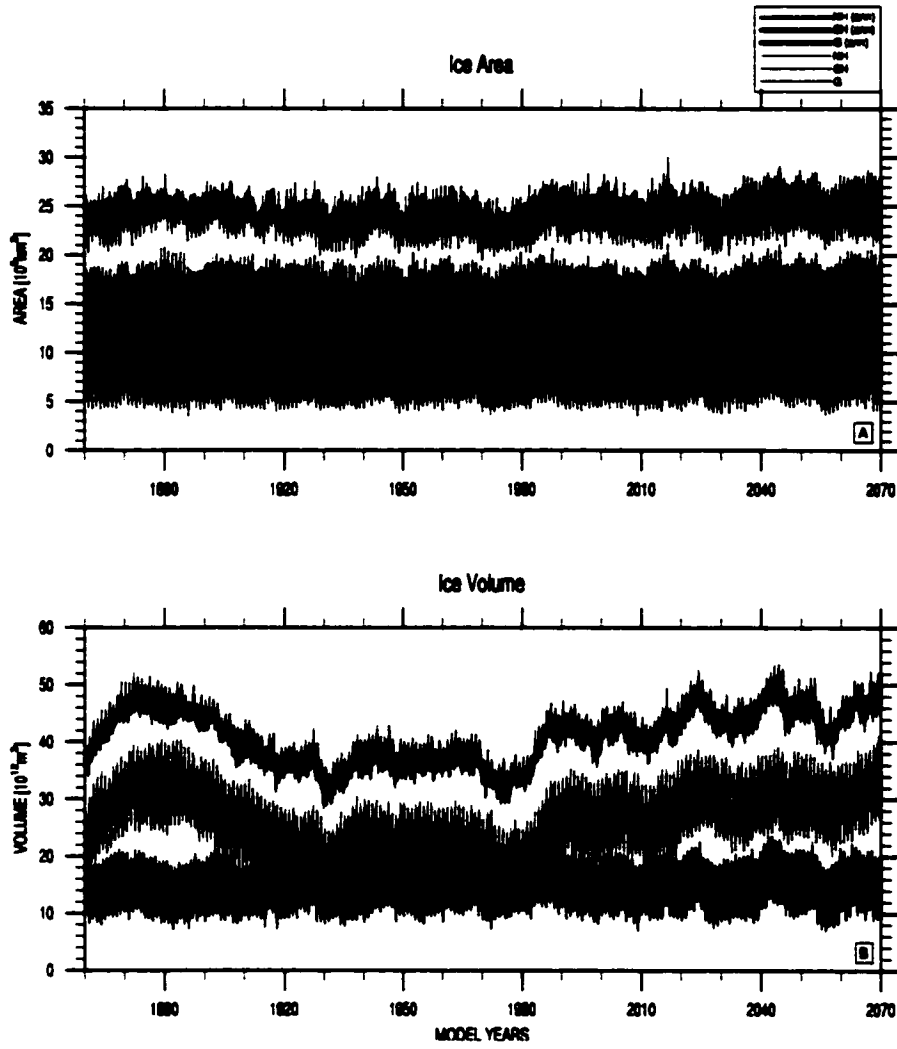
Figure 6.2: Coupled spinup and control experiment for sea ice area and volume for globe (black lines). the northern (red lines) and southern hemisphere (blue lines).
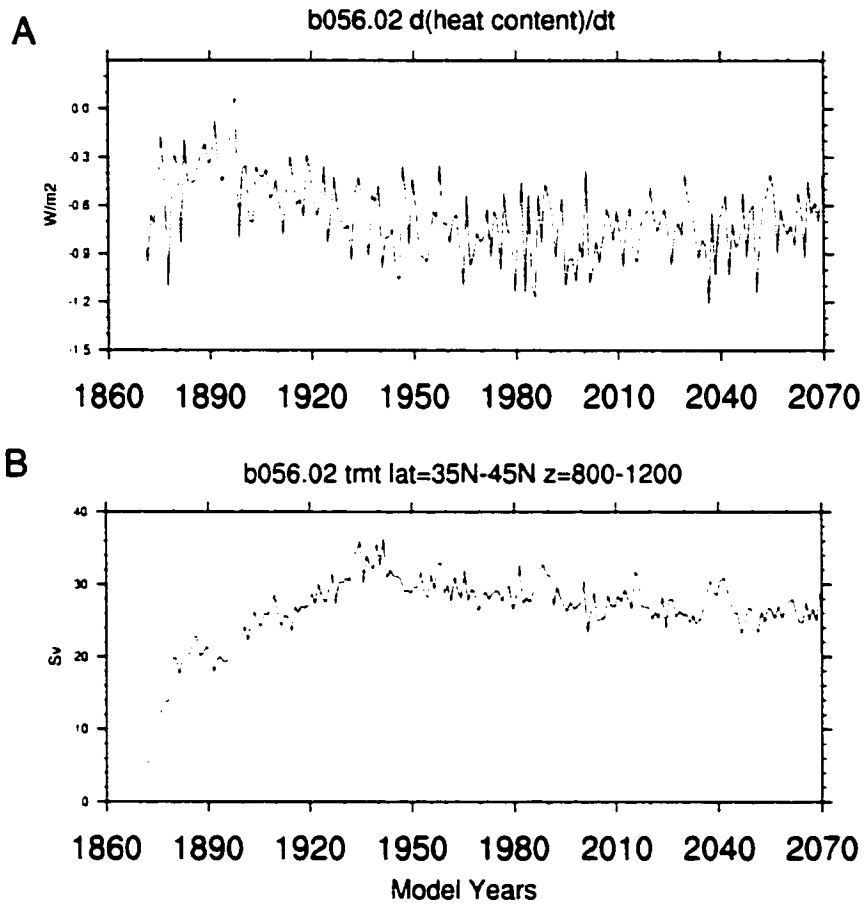
Figure 6.3: Ocean response: A: Ocean integrated mean heat content change per month: B: Barotropic streamfunction around 35-45°N and 800-1200 m depth as approximation of maximum North Atlantic overturning.

period 1950-1979 to 0.86°C for 1950-1998, although the run exhibits clear decadal variations with episodes of larger variations. NINO4 variability is 0.56°C within the range of observations (0.55-0.6°C). The features of thermocline displacements during El Niño episodes are also well captured. For a more detailed description of the El Niño - Southern Oscillation in this model configuration, see *Otto-Bliesner and Brady* (2001). Another important variation, the North Atlantic Oscillation (NAO), is also reproduced quite well, exhibiting interannual to decadal fluctuations.

Overall, the model was performing well, reproducing major modes of climate variability. The slight negative radiative imbalance and the somewhat strong overturning in the North Atlantic are features to keep in mind when looking at the response in the forcing experiments.

6.2.3 Volcanic Forcing Experiment

The volcanic aerosol loading of the time period 1870 to present has been discussed in Chapter 3. Using a simple seasonality parameterization, a spatial and temporal distribution of atmospheric optical depth in the mid-visible (around 0.5 μm) has been proposed (Chapter 3.5). In the following, this forcing dataset was used to describe the volcanic perturbation of the atmosphere during two 130-year experiments. It is assumed that the aerosol optical depth in the mid-visible is a good descriptor of the aerosol and can be used for all the eruptions, since it is relatively insensitive to aerosol variations (*Lacis et al.*, 1992). Further, the aerosol was put into fixed model levels and prescribed for their temporal evolution according to the seasonality parameterization. For each radiation timestep (every hour), the total column aerosol optical depth at each latitude was interpolated linearly between two monthly values. This technique has been proven to work reasonably well for the well known Pinatubo eruption (see Chapter 5).

In the following, the main aspects of the coupled aerosol experiments are described, and the forcing and impact are compared to observations and other modeling studies.

6.2.3.1 Radiative Forcing during the 20th-Century

Figures 6.4 and 6.5 show the variations in TOA and surface net solar fluxes. Several aspects can be recognized immediately. First, the five largest volcanic eruptions [Krakatau (1883). Santa Maria (1902). Agung (1963). El Chichón (1982) and Pinatubo (1991)]. can readily be recognized in the field of zonally averaged radiative fluxes. As observed by *Minnis et al.* (1993). the volcanic aerosols for these large eruptions cause the TOA radiative budget to significantly exceed the normal interannual variations. The signal is less clear for the high-latitude eruptions, such as Katmai-Novarupta, despite a visible optical depth of 0.3 in summer 1912 at latitudes north of 40°N. Secondly, the TOA SW flux perturbations are stronger than the surface fluxes, which is primarily due to cloud and water vapor responses in the troposphere. The opposite is the case for the total net fluxes, because the longwave perturbations are acting against the SW (see below). The volcanic perturbations are, of course, even easier to identify after removing the clouds (Figure 6.5). Here, all perturbations, other than from the volcanic aerosol, are due to surface albedo changes. Therefore, one would expect the largest changes to occur where the albedo can vary most dramatically. This is the case in areas where either snow cover (continents) or sea ice (ocean) can form or disappear. It can be seen from Figure 6.5 that the largest changes are indeed present in the high latitudes of both hemispheres. They not only show up intermittently but seem to follow a particular trend. The surface fluxes show an increasingly negative radiative budget in the Arctic compared to the first 10 years. This is mainly due to increasing Arctic sea ice, as is demonstrated in Figure 6.6. The reason for this general increase of ice volume and, to a lesser degree of the sea ice area as well, is probably due to the negative radiative balance mentioned above. The positive tendency pattern immediately southward of the negative radiative fluxes in the Arctic also hints at some reorganization in the mean sea ice distribution, probably in the North Atlantic versus North Pacific area. The radiative flux fluctuations in the equatorial areas are rather small (note: these are zonally averaged values). The perturbations primarily reflect

El Niño - Southern Oscillation events.

The total net radiative fluxes are presented for TOA in Figure 6.7 and the surface in Figure 6.8. Again, the perturbations from the volcanic aerosols are clearly visible. In fact, when looking at global and hemispheric values, even the smaller eruptions are now relatively easy to identify. When looking at total net fluxes, the clear interannual variability in net radiative flux is due to climate noise and natural modes of variability, such as El Niño and others. The total surface net flux perturbations are larger than the TOA net fluxes (note difference in scale of the plots), because the LW buffering of the volcanic aerosol does significantly reduce upwelling LW radiation. However, the warming signal from the stratospheric aerosol cannot penetrate down to the surface, and therefore, the LW variation at the surface is minimal. Only the large Krakatau perturbation (1883-85) can be identified out of the interannual noise.

When looking at individual volcanic eruptions in the direct comparison shown in Figure 6.9, the magnitude of the events can be recognized. This figure shows the total net radiative fluxes for the surface in relation to the time of the year. The buildup of the aerosol cloud until 5 months after the individual eruptions can be seen. For example, Pinatubo erupted in June (1991) and Santa Maria in October (1902). Also, the general decrease of the forcings follow a more or less parallel line, in agreement with the 1-year e-folding time of the aerosol clouds. Compared to the tropical eruptions, the small radiative effect on the global scale of the large high-latitude eruption of Katmai-Novarupta (1912) is remarkable.

Figure 6.10a shows the radiative perturbations from 55-60°N. This is a latitude where a series of observations for the time of the Katmai-Novarupta aerosol cloud are available (*Kimball*, 1913; *Volz*, 1975a; *Stothers*, 1996b). At this latitude, two important aspects of the aerosol perturbation need to be pointed out. First, the high-latitude injection of aerosol from Katmai-Novarupta (Alaska) immediately impacts the radiative budget, only a few month after the eruption in June 1912 (*Kimball*, 1912). This is in sharp contrast to the tropical eruptions, whose aerosol does not reach the high northern latitudes until late in the year due to the seasonal cycle in meridional
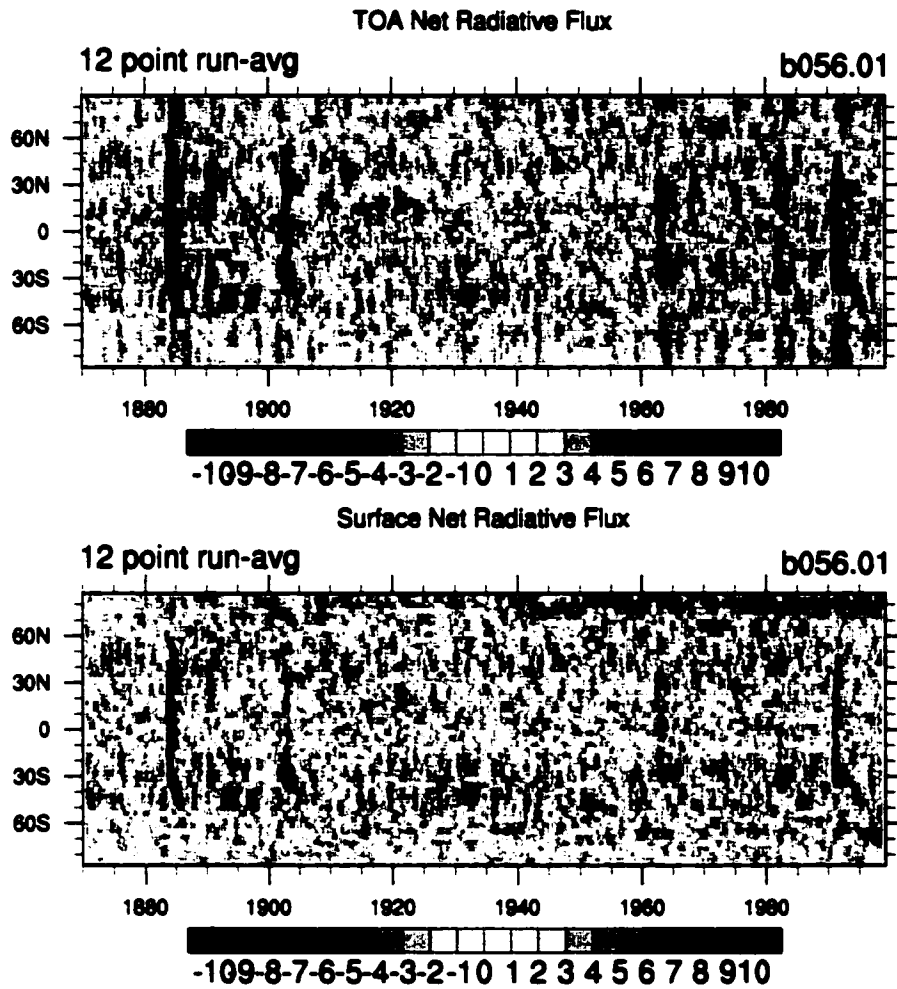
Figure 6.4: SW flux perturbations during the 130 year experiment using volcanic aerosol forcing. Upper panel shows zonally averaged 12 point running average net flux changes relative to the mean flux from 1870 to 1880. Lower panel: same as upper panel except for surface radiative fluxes.

TOA Clear Sky Net Radiative Flux

12 point run-avg   **b056.01**

-109-8-7-6-5-4-3-2-10 1 2 3 4 5 6 7 8 910

Surface Clear Sky Net Radiative Flux

12 point run-avg   **b056.01**

-109-8-7-6-5-4-3-2-10 1 2 3 4 5 6 7 8 910
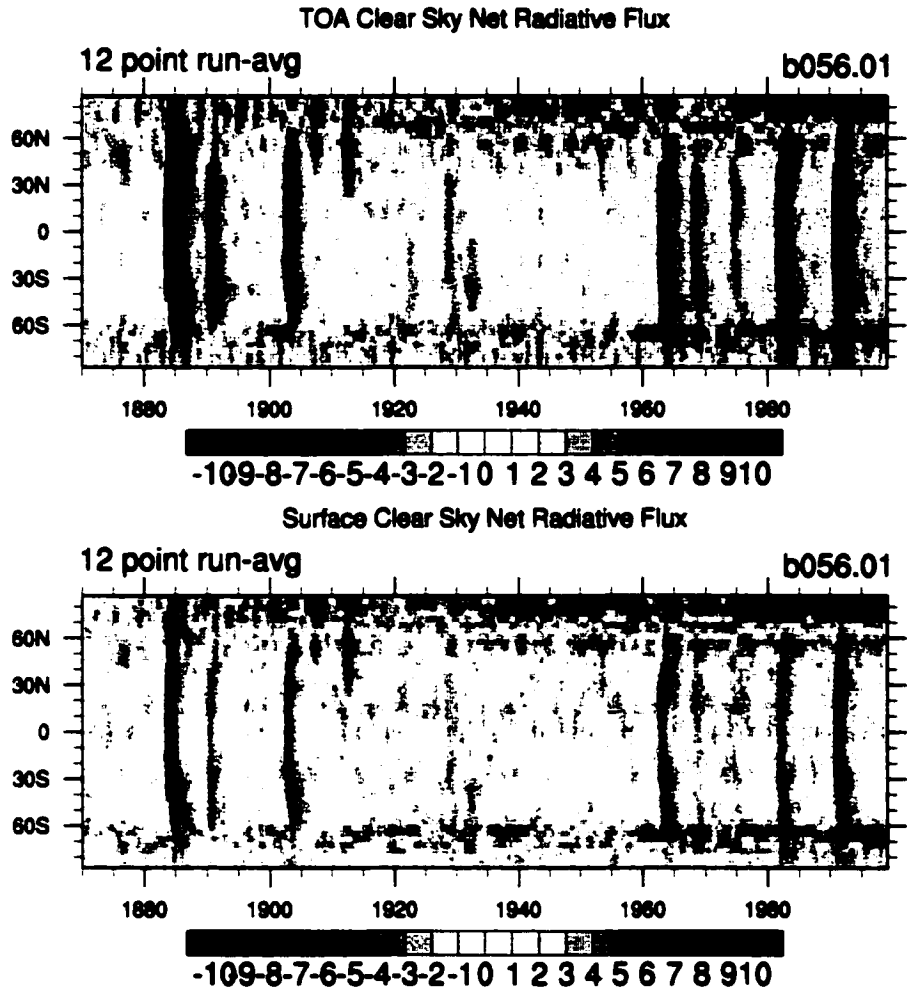
Figure 6.5: Same as Figure 6.4. but for clear sky conditions.
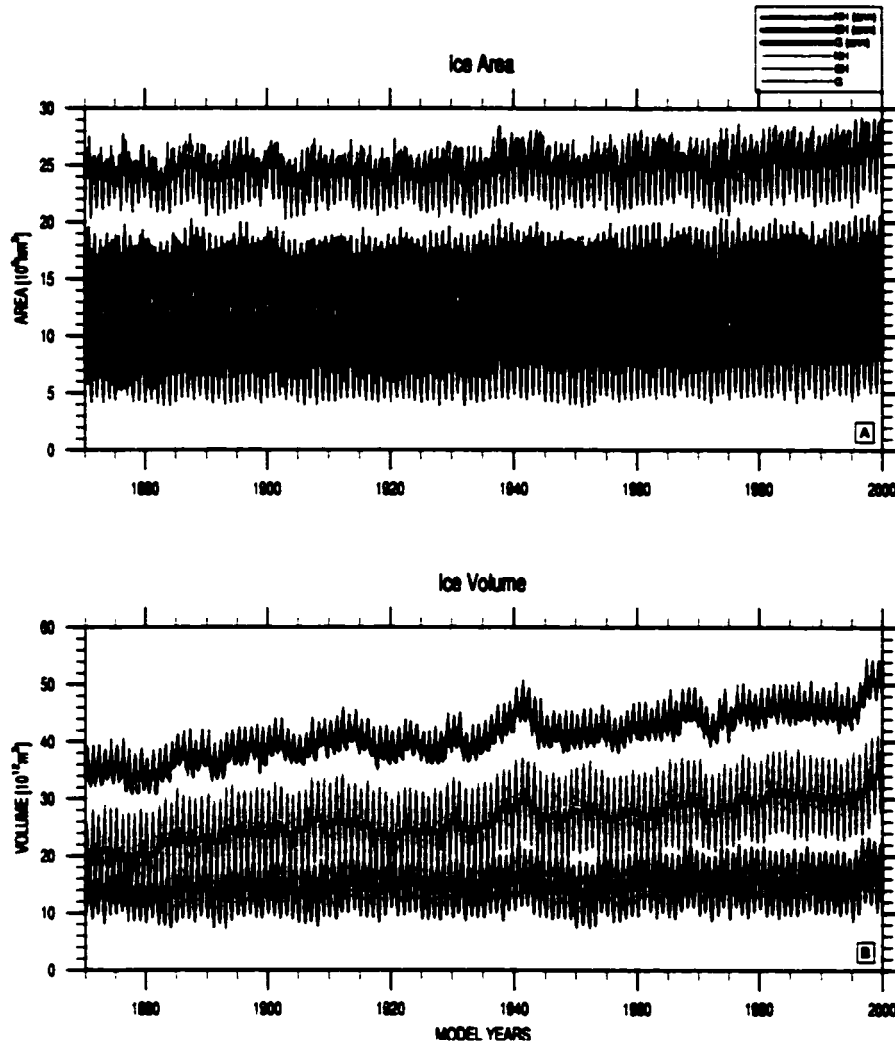
Figure 6.6: Sea ice area and volume separated for global (black lines), northern hemisphere (red lines) and southern hemisphere (blue lines).
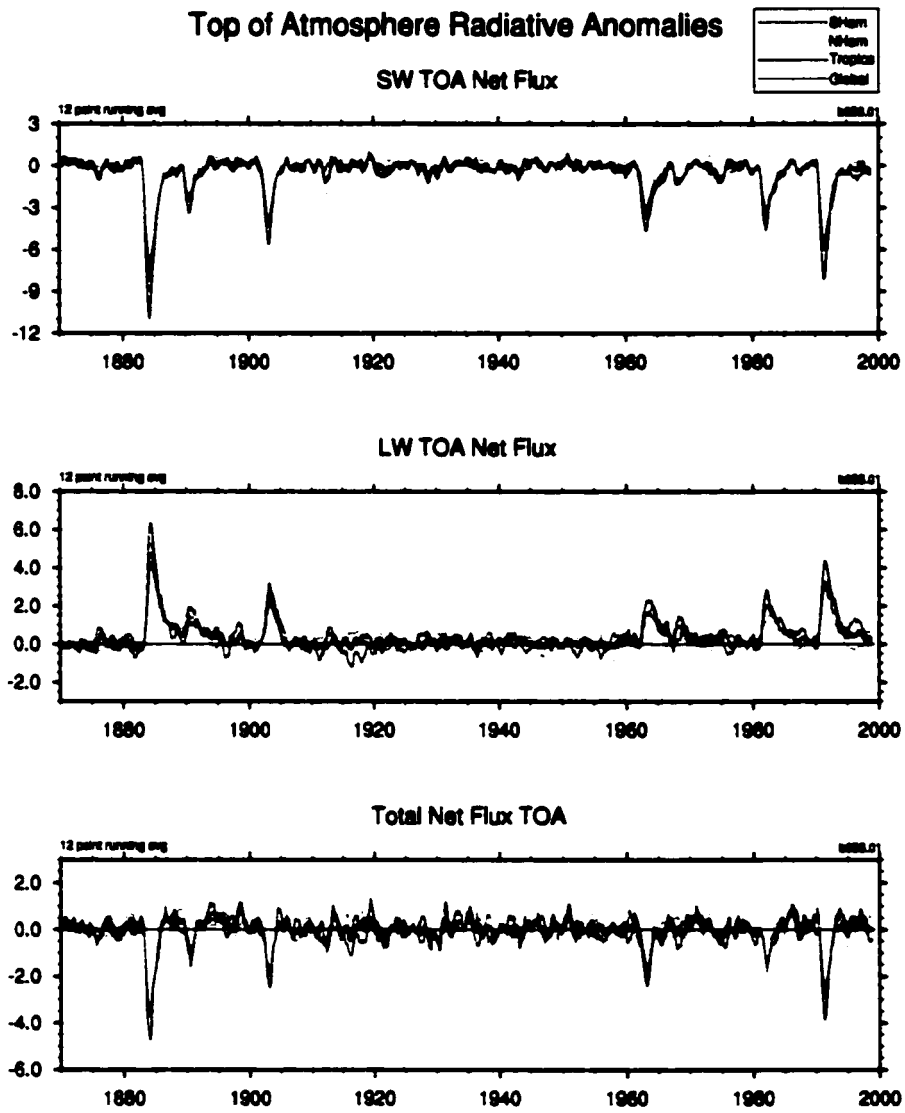
Figure 6.7: TOA flux perturbations for the globe (red line), the tropics (blue) and the northern (orange) and southern hemisphere (green).

Surface Radiative Anomalies
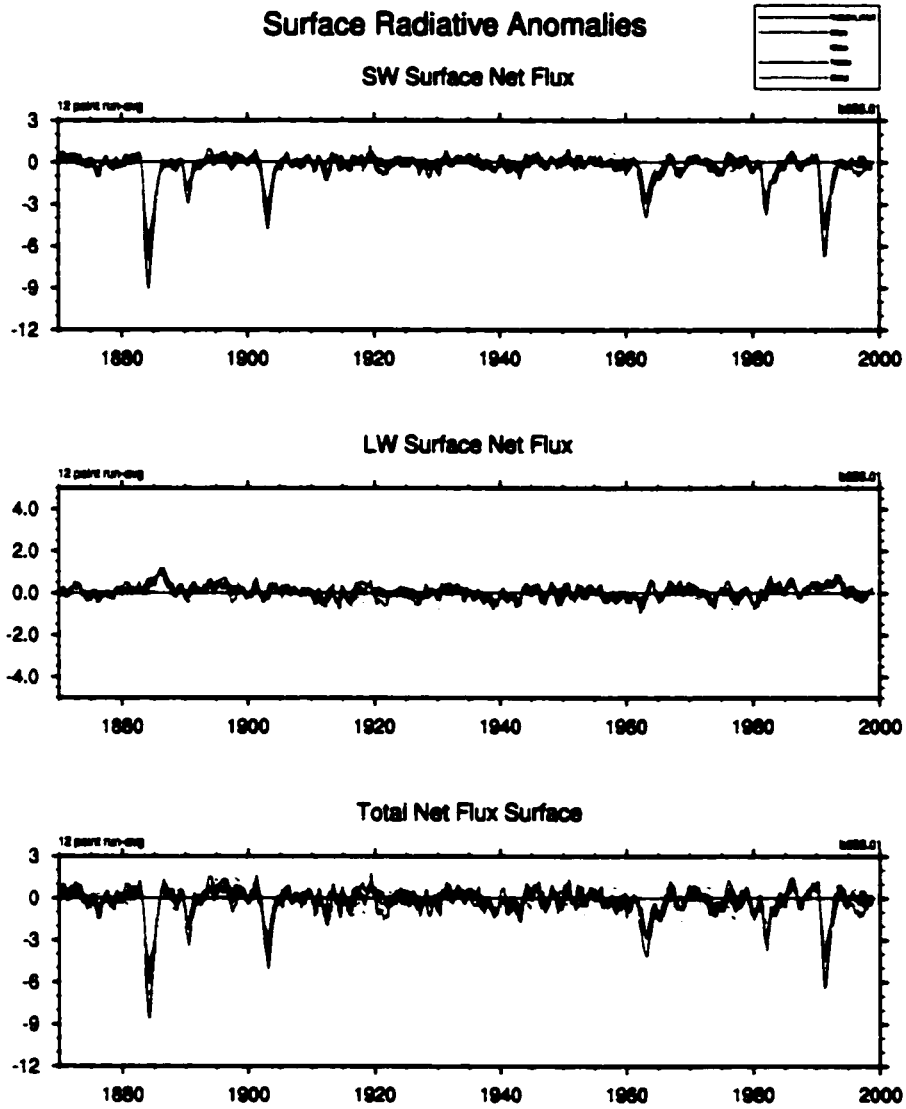
Figure 6.8: Same as Figure 6.7. but for surface.

184
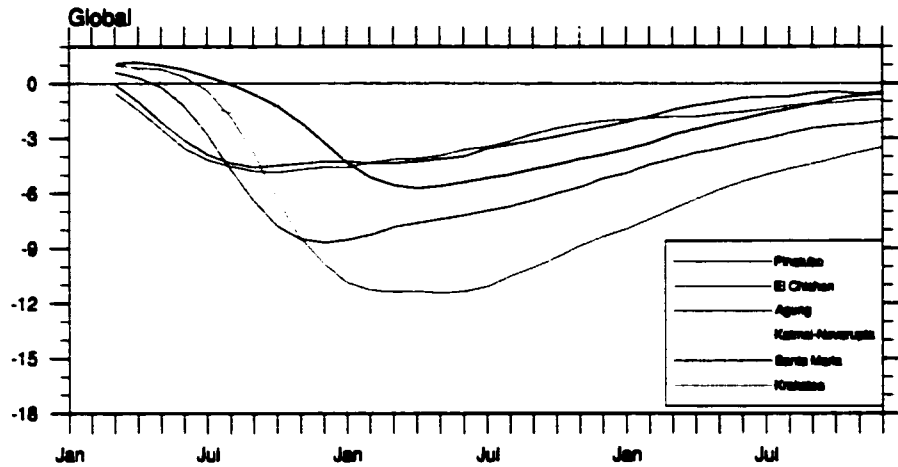
Figure 6.9: Globally averaged surface net flux changes in Wm^{-2} after selected eruptions. The temporal order is in calender month. ranging from the year of the eruptions to 3 years later. The data was smoothed with a five point moving average.

transport in the lower stratosphere. Direct radiative effects from low- and high-latitude eruptions are. therefore. not directly comparable. but require the correction of a lag for the tropical events. This is important when comparing climate signals in some proxy series. such as tree rings. The second interesting aspect of the radiative flux perturbations in the high latitudes is the markedly different decay between aerosol clouds from tropical and high-latitude eruptions. While the Katmai-Novarupta areosol decays within roughly a year. the aerosol perturbations after low latitude eruptions repeatedly regain some strength during the winter season. This is due to the fact that aerosol after low latitude eruptions can continuously receive mass from the tropical stratosphere. which may act as a reservoir. This effect has been incorporated in a very simple manner in the aerosol seasonality parameterization by setting a somewhat faster decay rate in the high latitudes than in the tropics. During the respective hemispheric winter season. new aerosol from the tropics can therefore lead to an intermittent increase in aerosol mass in the mid- and high-latitudes. That this different decay behavior of tropical versus high-latitude eruptions

185
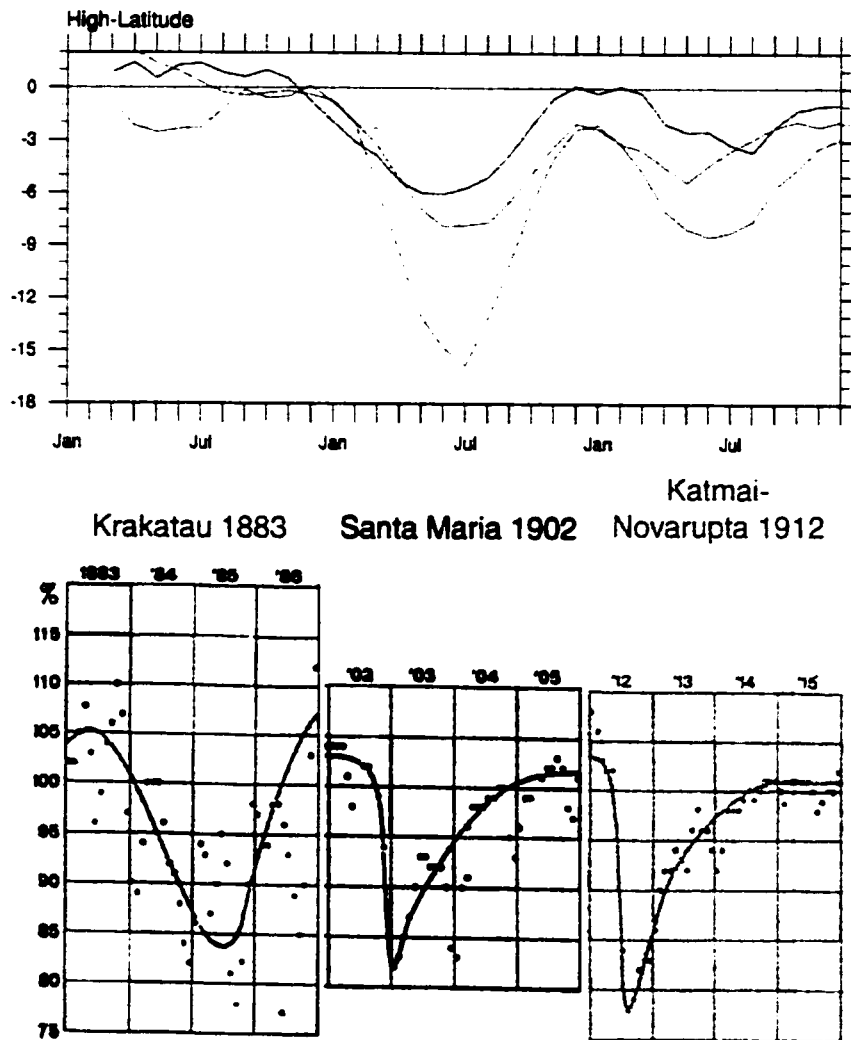
Figure 6.10: Top: Temporal evolution of the surface net flux perturbations between 55 and 60°N after high-latitude (Katmai-Novarupta) and tropical eruptions (Krakatau. Santa Maria. Pinatubo). Lines are selected eruptions are the same as in Figure 6.9. Bottom: Early observations of atmospheric transmission from *Kimball* (1924) for two tropical eruptions Krakatau (red), Santa Maria (1902) and the high-latitude eruption of Katmai-Novarupta (1912). Note the recurrence of low transmission during the winter time for the tropical but to a much lesser extent for Katmai-Novarupta.

186

is not just an artefact of the model, but actually can be deduced from observations, is shown in Figure 6.10b. Here, a compilation of the early observational time series from *Kimball* (1924) exemplifies this for the two tropical eruptions of Krakatau (1883) and Santa Maria (1902) versus the evolution of atmospheric perturbation from Katmai-Novarupta (1912). Despite the noise in the early time series (especially for Krakatau, where only one single series from Montpelier is available), the clear recurrence of optical perturbation in more than one winter following the eruption is clearly captured. Very different is the decay of the Katmai-Novarupta aerosol cloud, which does not experience these re-intensifications. The parameterization captures this behavior remarkably well.

Before addressing the climate impact from the reported forcing, two important conclusions can be drawn from the forcing results already presented. First, the volcanic eruptions since 1870 have repeatedly imposed a significant forcing on the earth radiative balance. Interannual variations in total radiative fluxes in the order of several Wm^{-2} are not unusual for volcanic eruptions. Second, the coupled climate model allows us to look into the real forcing effect of the volcanic aerosol on the climate as it responds. Compared to the interannual variability the volcanic eruptions not only show up as short lived perturbations, but clearly exhibit a long term component. As has been suggested before, more closely timed eruptions can perturb the radiative balance on decadal time scales. Figure 6.11 shows both of these forcing effects as TOA net flux anomalies for annual averages. The volcanic run is shown in red. Despite internal noise, clear evidence of volcanic aerosol perturbations can be seen. The red dashed line is a 10-year average through the data. Two episodes of strong deviations from zero are visible, one from 1880 to 1905, the other at the end of the century between 1960 and 1995. The negative forcing during these decades is on the order of 0.4 Wm^{-2}. It has been suggested that variations in solar radiation could have a substantial impact on the longer term behavior of climate and that the warming in the 20th-Century could be explained by solar variations alone (*Friis-Christensen and Lassen*, 1991; *Lassen and Friis-Christensen*, 1995). For comparison of the solar irradiation

Volcanic Forcing vs. Solar Irradiance Changes 1870-1999
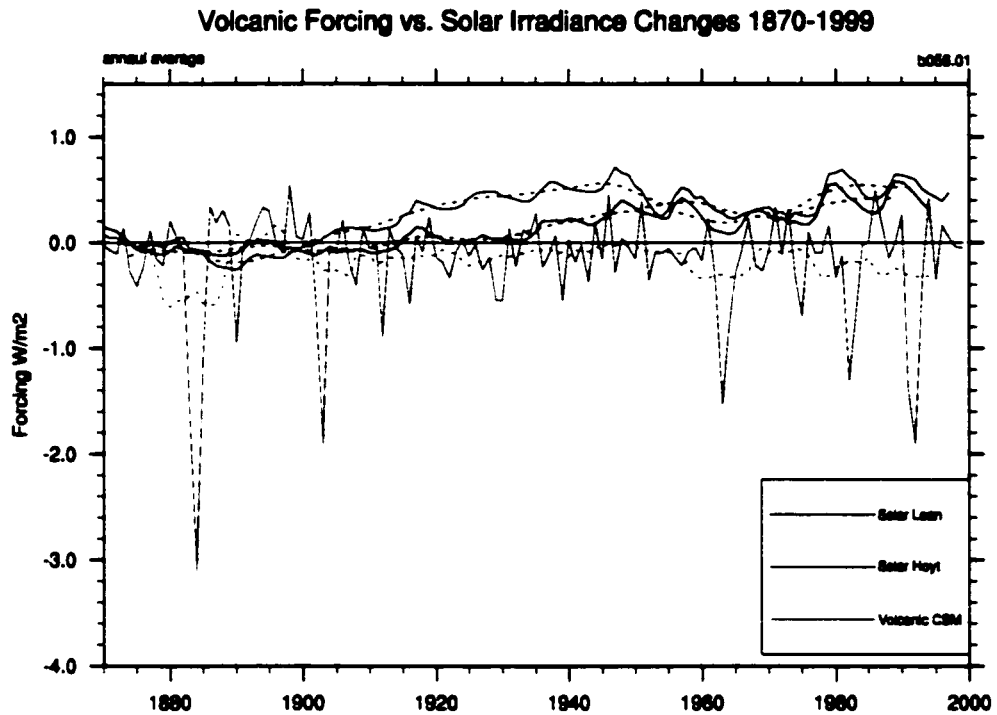
Figure 6.11: Volcanic versus solar forcing during the 20th-Century. Data is shown as annual averages and for 10 year moving averages.

changes as reconstructed by *Lean et al.* (1995) and *Hoyt and Schatten* (1998) with the volcanic perturbations. Figure 6.11 shows that the solar irradiation indeed exhibits an increase, starting either at the turn of the 20th-Century or later during the 1930s, depending on the time series under consideration. The first maximum, reached around 1940, occurs at a time when no volcanic forcing is present. The positive solar forcing on earth climate after 1960, on the other hand, is matched by an equally strong, but opposite in sign, volcanic forcing. While an active contribution from the solar irradiation can be expected for the first half of the century, the same can not be claimed after 1960, when the volcanic forcing offsets increased solar irradiation.

6.2.3.2 Climate impact of volcanic eruptions

The volcanic eruptions with their individual perturbations to the radiation budget cause a number of impacts on climate. Although the aerosol particles efficiently scatter the solar beam, they also absorb some SW (mainly near infrared, NIR) and LW radiation. This absorption raises the temperature of the atmospheric layer they are located in. Figure 6.12 shows the averaged temperature anomalies throughout the global atmosphere for the 130-year experiment. The seasonal cycle has been removed. Absorption by intermittent volcanic aerosol in the lower stratosphere leaves a clear signal in the temperatures causing substantial warming. The strongest warming, as well as the longest perturbation, occur at the bottom of the aerosol cloud. This is mainly the result of two factors. First, the bottom of the aerosol cloud is the place of first absorption of upwelling longwave radiation and has, therefore, a larger share. Secondly, the relaxation time in the tropopause area is significantly longer than higher up in the stratosphere (see Figure 5 of *Kiehl and Solomon*, 1986). Stratospheric warming in connection with volcanic eruptions has been observed since the time of the Agung eruption in 1963 (*Labitzke et al.*, 1983; *Labitzke and van Loon*, 1996; *Angell*, 1997b). The global perturbations reported here of up to $2°C$ (and more than $2.5°$ for Krakatau) is in good agreement with observations (*Spencer and Christy*, 1993; *Angell*, 1997b; *Thulasiraman et al.*, 1999; *Parker et al.*, 2000).

Below the heated stratosphere, the temperatures are clearly reduced. This effect is due to both a reduction in transmitted solar radiation from above and climatic feedbacks such as reduced convective activity, transporting less latent heat into the upper troposphere (see also *Coakley and Cess* (1985) or *Hartman* (1994)). In fact, the temperature reduction in the troposphere is largest between 400 and 300 hPa. Next to the reduced convective activity, the damping from the large heat capacity of the worlds oceans reduce the signal towards the surface.

Interestingly, the perturbations persist for quite some time after the eruption and seem to last longer, even after the stratospheric aerosol is gone already. This delay might be due to the lagged
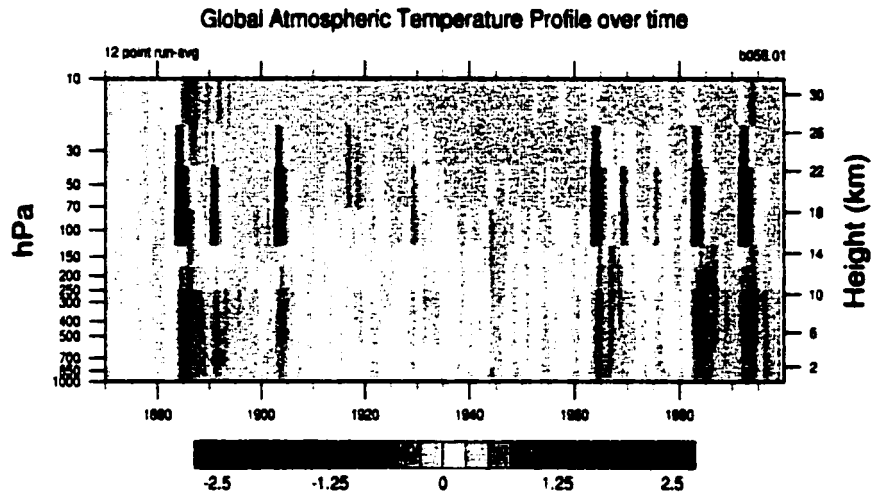
Figure 6.12: Vertical distribution of temperature anomalies during the 130 year experiment with volcanic aerosol.

response in the oceans. The temperature perturbations are also somewhat dependent on the latitude. Figure 6.13 shows a set of vertical crosssections from different latitudes during the large perturbations from Krakatau (1883). The stratospheric warmings are mainly in the tropics, and with decreasing aerosol and sunlight, the temperature perturbations are much smaller in the high latitudes. Additionally, the high latitudes undergo a strong seasonal cycle, which further perturbs the signal. Finally, dynamical responses can modify the radiative signal through advection.

The effects of these temperature changes on the zonal wind has been discussed for the Pinatubo experiments. Here, we now focus on the surface climate. The surface temperature response is shown in Figure 6.14. The five large volcanic eruptions of Krakatau, Santa Maria, Agung, El Chichón and Pinatubo are responsible for significant global surface temperature changes of several tenths of a degree Celsius. The large interannual variability that produces a strongly varying surface temperature comes from the internal climate variability of the coupled CSM. The five eruptions mentioned above cause the surface climate to exceed its usual inter-
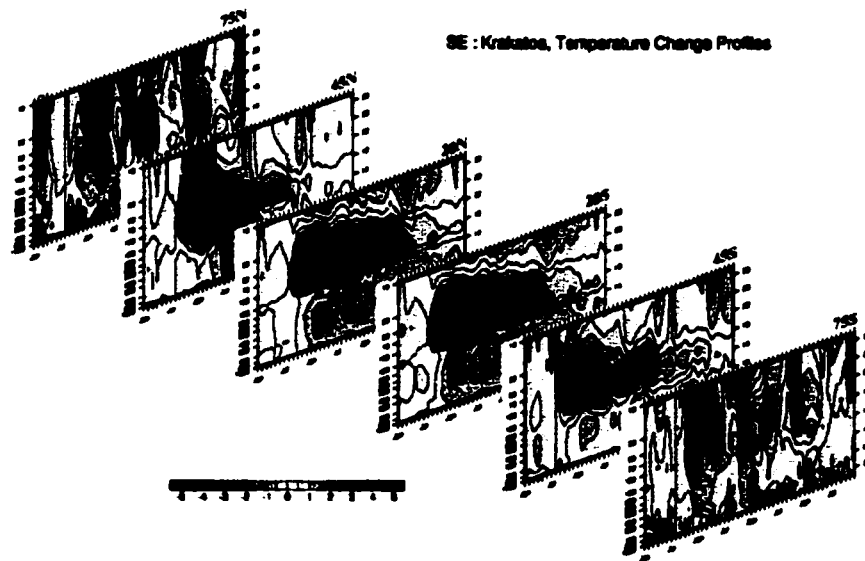
Figure 6.13: Latitudinal crosssections through the atmosphere after the large eruption of Krakatau showing temperature perturbations on different atmospheric layers.

annual variations and significant cooling occurs. The onset of the cooling is abrupt. while the recovery is slower and often undergoing clear fluctuations. These fluctuations are due to internal variations. such as El Niño. but also represent the winter warming effects over the Northern Hemisphere high latitude continents as discussed for Pinatubo. They are also discussed below for ensemble experiments. The second important feature of this plot is the long-term effects of volcanic eruptions. When comparing the duration of the forcing with the climate impact. it is remarkable that the large eruptions between 1880 and 1910. as well as between 1963 and 1995. cause the global average temperature to decrease so much that recovery in-between the individual events is not complete. The possibility of a decadal effect of closely spaced volcanic eruptions has been discussed in Chapter 3.6 and was mentioned in Chapter 4.6. Figure 6.14 strongly supports this idea and suggests that the effect is real. The decades with increased volcanic optical perturbations exhibit cooler average temperatures.

Paleo-CSM: Volcanic Aerosol Run 1870-2000 AD

Surface Temperature

12 point run-avg

b056.01
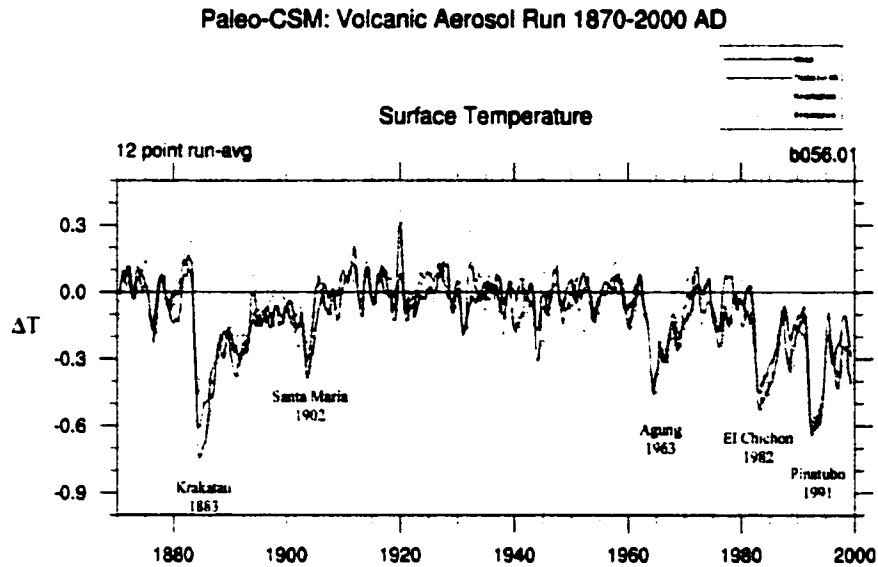
Figure 6.14: Surface temperature response from the coupled experiment with volcanic aerosol forcing. Large volcanic eruptions are marked.

Finally. one oddity that bears mentioning. is the shear magnitude of the impact of Krakatau (1883). While for all the other eruptions. the simulated impact is similar to observations. the strong cooling after Krakatau simulated in the coupled climate model is only seen as a small anomaly in the GISS temperature series (*Hansen et al.*, 1999) or is missing entirely in the combined land and ocean data from *Jones* (1994) and *Parker et al.* (1995). Given the large sulfate signal (and consequently large optical depth used as a forcing). a large signal could be expected. The possible reasons why there is such a large discrepancy with observations will be discussed below in Chapter 6.3. where ensemble simulations study different possibilities that might counteract an eruption's impact.

The second crucial parameter of surface climate is the precipitation. Given the strong radiative effects of volcanic eruptions (of the order of several to over 10 Wm^{-2} in the tropics). one

192

would assume that the hydrologic cycle. which is driven by the insolation, would get hit by the reduction in downwelling radiation at the surface. Figure 6.15 investigates this question. The upper panel shows area averaged interannual total precipitation fluctuations (sum of two model output fields: convective and large scale precipitation) in *mm* for different regions. While over the globe (red) and the entire tropics (blue) the precipitation changes from year to year are very small. in the Indian Monsoon area (green) and, for example, the British Isles (yellow), interannual precipitation fluctuations are much larger. Due to the large climatically driven variations in the two small areas, no perturbations from volcanic eruptions are visible. At the global and tropical scale, however, the averages seem to exhibit small, but recognizable, decreases, in agreement with observations after Pinatubo (*Spencer et al.*, 1998). In the lower panel of Figure 6.15, these perturbations of the globe and tropics are expanded. Here, only convective precipitation is shown and is scaled towards the total convective precipitation amount to obtain percentages of change. As for the surface temperature, the five major eruptions in the simulation introduce a clear precipitation decrease. on the order of a few percent. This signal also seems to be present in observations. *Dai et al.* (1997) show precipitation as collected from a large global network of stations. From their Figures 7 and 8 (p. 2951 and 2952) one can recognize a similar large scale pattern as shown for CSM in the lower panel of Figure 6.15.

Mukherjee et al. (1987) and *Mukherjee* (1990) have reported that large volcanic eruptions in the tropics influenced the Indian Monsoon. They found decreased precipitation in both summer as well as winter monsoon. While for the tropics as a whole CSM does confirm this observation. for single events the influence is not clearly visible over the Monsoon area. The interannual variability is too large. There are some events for which the correlation seems to hold well (El Chichón). but for others. there is no signal at all (Agung). Further detailed studies are needed to search for this effect. As in the real world. the climate model exhibits a large variability when looking at small areas. Clear volcanic signals only appear on the hemispheric scale. a dimension where observations. or at least early ones. suffered from significant gaps in spatial coverage.

193

Precipitation Changes
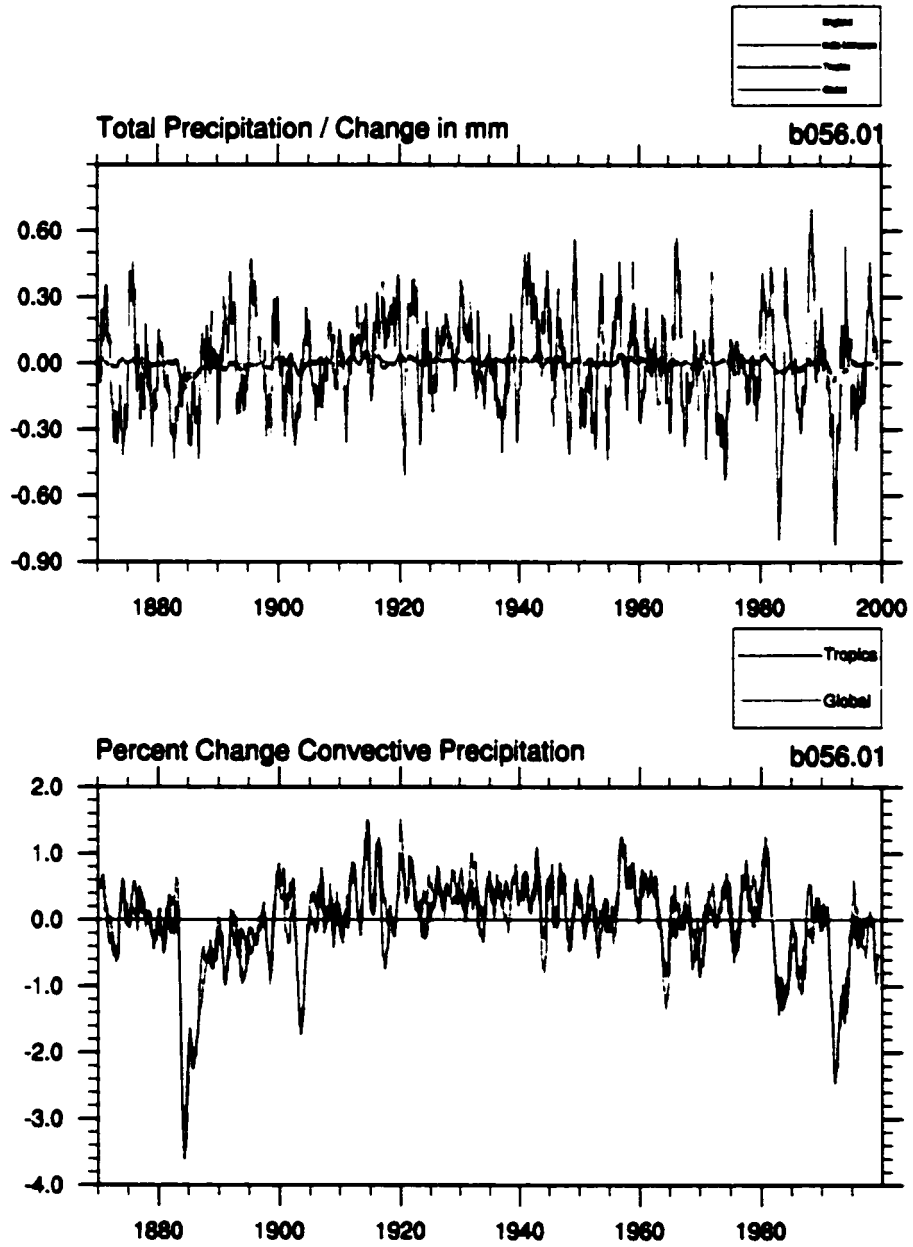
Figure 6.15: Precipitation analysis from CSM. Top: Total precipitation for different zones and areas in interannual changes compared to long term average. Bottom: Percent change in convective precipitation for the globe and tropics (40°N - 40°S).

194

In good agreement with observations the impact from volcanic eruptions in the coupled NCAR-CSM show significant transient perturbations of the climate. Next to these overall global and hemispheric scale impacts, another to investigate is in what way the volcanic eruptions perturb internal modes of variability, like ENSO and NAO. This topic is addressed below, where ensemble experiments try to shed some light on these questions.

6.3 Krakatau - A Challenge for Climate Modeling

The magnitude of the climate impact by the different eruptions is primarily a factor of optical perturbation (see Figures 6.1, 6.7 and 6.14). However, other factors, such as El Niño and the mode of the NAO (among others), could potentially modify the signal.

This question, as pointed out above, is particularly to consider when looking at the large impact simulated for the eruption of Krakatau (1883), which in the model is significantly larger than observed. It is important to know whether it were possible that internal climate mechanisms could suppress a large volcanic signal altogether. A well known example for such a masking occured during the massive El Niño of 1982/83, which basically cancelled the expected cooling from the spring 1982 eruptions of El Chichón. Some remnant cooling was only discovered after the decay of the El Niño (Wigley, 2000). When looking at the large impact of Krakatau in the CSM simulation (Figure 6.14), one wonders if the same effect could have happend in 1884. The exploration of candidate mechanisms for such a masking is the goal of this section. Using ensemble simulations and selected sensitivity tests, the Krakatau Challenge will be discussed. The significance of this problem should not be underestimated. From geologic, as well as other records, we know that Krakatau was a major explosive event, and as such the expected perturbations of the atmosphere should have been large. On the climate impact side, large events like this have the capacity to potentially disrupt the climate, impacting agriculture and water availability as the sensitive focus points for society. A series of closely spaced events could potentially extend

the time period of perturbations, further enhancing the pressure on society. It is important that climate models can accurately simulate these major events in order to give insight into regional and global impacts on the short time scales. Krakatau, as the largest event during the instrumental period (*Stothers*, 1996b), is a test ground for the ability of the models, and any difference to the observed climate impact should be understood.

6.3.1 Ensemble simulations of a large tropical eruption

The coupled climate system simulated in the CSM exhibits internal climate variability. In this configuration, it is very hard (if not impossible) to study events in a one-to-one comparison with the real world. Next to the fact that the climate model and the real world represent two different coupled systems, the states of internal modes (e.g., ENSO, NAO) within each system are probably never the same. Therefore, we cannot really reproduce identical situations. A way to look into the problem is to study ensembles. This precedure makes use of the same forcing but each experiment starts from different initial conditions. By varying the initialization, a 'common' direction of the response might be found. But one also needs to keep in mind that the real world could have 'chosen' an extreme pathway, rather than the 'common' middle way. Therefore, in order to explore all possible pathways, a large number of ensemble simulations might be needed. Here, a total of six experiments of tropical eruption of Krakatau (1883) and four of high-latitude Katmai-Novarupta (1912) event were performed.

6.3.2 El Niño as a buffer for volcanic cooling

The method for performing ensemble simulations is to use the same aerosol data with different starting conditions for each run. The selection of these initial conditions was done using the 130-year volcanic coupled simulation. The NINO3 surface temperature anomalies were used as selection criterion in order to choose years when the coupled system would head into an El Niño or a La Niña event. As suggested by the example of El Chichón, where the large El Niño of 1982/83

masked the impact of the stratospheric aerosol, this ensemble should test to what degree El Niño could be responsible to cancel the cooling effect simulated by CSM. Earlier, in Table 4.2, it was shown that all proxy and instrumental indices for the year after the large Krakatau eruption point to a reasonably strong El Niño event. Therefore, a possibility for the lack of a clear surface signal could be due to this internal climate mode. The ensemble experiments can help evaluate the validity of this hypothesis. Additionally, following the discussion of Chapter 4.5, the ensemble member selection with opposing states of ENSO could shed some light into the trends reported by *Handler* (1984). Table 6.1 lists the years of initial conditions used for the ensemble simulations and summarizes the main results. Figure 6.16 shows NINO3 anomalies in the long volcanic run with the ensemble member solutions for the individual events. The tropical eruptions using the Krakatau aerosol are shown in red, while the blue lines show ensemble members for high-latitude events follwing the Katmai-Novarupta aerosol perturbation (see Chapter 6.4 below).

The primary results from the ensemble simulations are illustrated in Figure 6.17, and corresponding maximum global temperature deviations can be taken from Table 6.1. Figure 6.17 shows the zonally averaged surface temperature response to the Krakatau aerosol forcing, starting off from the initial conditions of the long 130-year experiment in the years listed in Table 6.1. What becomes immediately clear is that, despite the different states in the ENSO cycle the coupled system was heading for, the general surface cooling signal remains very prominent. Therefore, from this plot, it can be seen that when using the aerosol forcing of Krakatau as described in Chapter 3.3, which is very similar in magnitude to *Stothers* (1996b), the surface signal is too large to be compensated for by El Niño. The lack of a surface signal in the observations is therefore unlikely to be due to El Niño alone.

Before discussing other options for masking a Krakatau signal, a short description of the influence of strong volcanic aerosol forcing on the development of El Niño in the coupled CSM is presented. First of all, one important aspect to keep in mind when looking at El Niño indices in connection with large volcanic eruptions is that the volcanic forcing can perturb conditions in

Tropical Eruptions using Krakatau aerosol data					
Run Number	Eruption Year	Max ΔT_{global}	MM/YY$_{\Delta T}$	NINO3	comment
b056.01	1883	-0.7	ND -1	0 - -	control experiment
b056.kr1	1881	-1.3	JF -2	- - -	eruption during El Niño
b056.kr2	1943	-0.8	ND -1	- 0 -	eruption into La Niña
b056.kr3	1956	-0.85	MA -2	- - -	eruption before El Niño
b056.kr4	1925	-0.8	D -1	- 0 -	eruption into no trend
b056.krL	1883	-0.7	N -1	(- - -)	see below Chapter 6.3.3

High-Latitude Eruptions using Katmai-Novarupta aerosol data					
Run Number	Eruption Year	Max ΔT_{global}	MM/YY$_{\Delta T}$	NINO3	comment
b056.01	1912	-0.2		- 0 0	control experiment
b056.ka1	1947	-0.2	AS -0	0 - -	eruption into La Niña
b056.ka2	1914	-0.2	JA -0	- - -	eruption during El Niño
b056.ka3	1912	-0.35	ON -0	- 0 0	Stothers (1996b) magnitude

Table 6.1: Ensemble runs. Top: Tropical eruptions using the aerosol optical depth of Krakatau. Shown are eruption years for ensemble branch off from the main 130-year volcanic aerosol run. with eruption in August of year 0. Each run was four years long. MM/YY$_{\Delta T}$ is the month and year relative to eruption of strongest temperature reduction compared to unperturbed b056.01 run. NINO3 lists winter NINO3 tendency for 3 consecutive winters. The NINO3 trends for b056.krL were reversed since this experiment compares a very large aerosol with minimal signal to the control experiment with the full Krakatau aerosol equal to all other ensembles. Bottom: same as above but for high-latitude eruption of Katmai- Novarupta in June of year 0.

NINO3
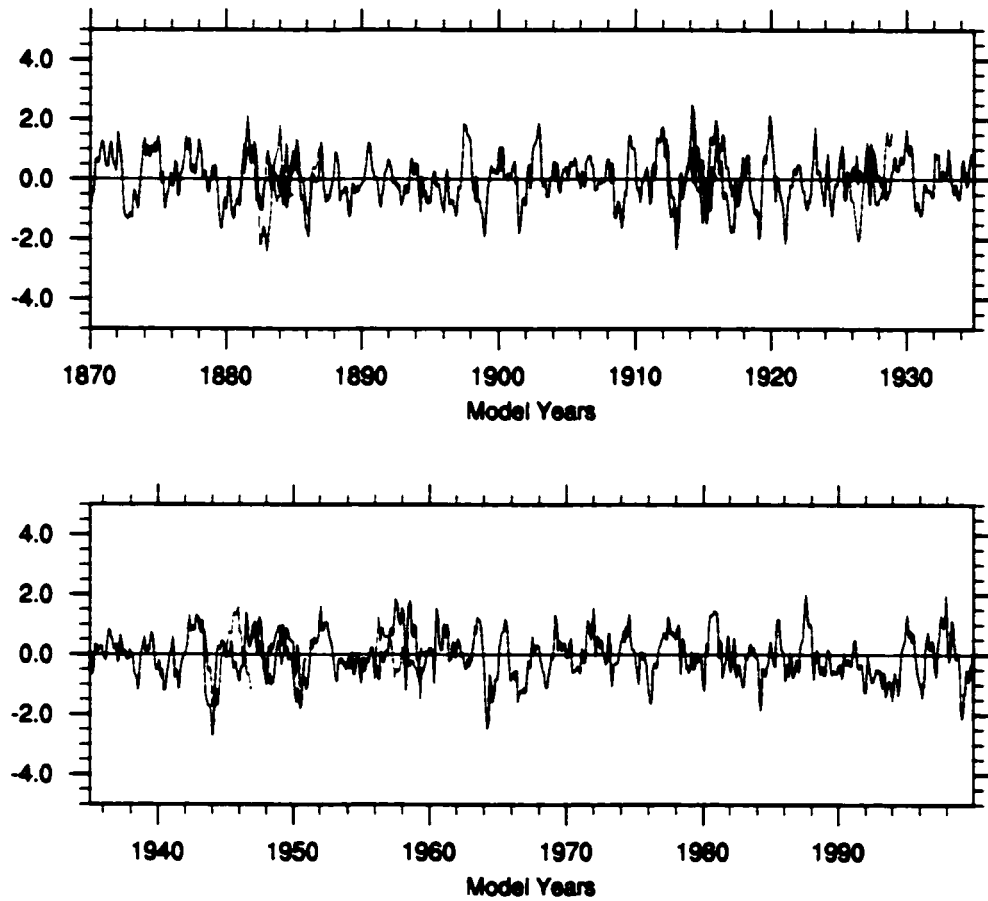
Figure 6.16: NINO3 SST evolution during volcanic experiment and ensemble memeber runs. Red lines are representing tropical ensemble experiments using the Krakatau forcing, blue lines are for the high-latitude events studied below (Chapter 6.4).

199
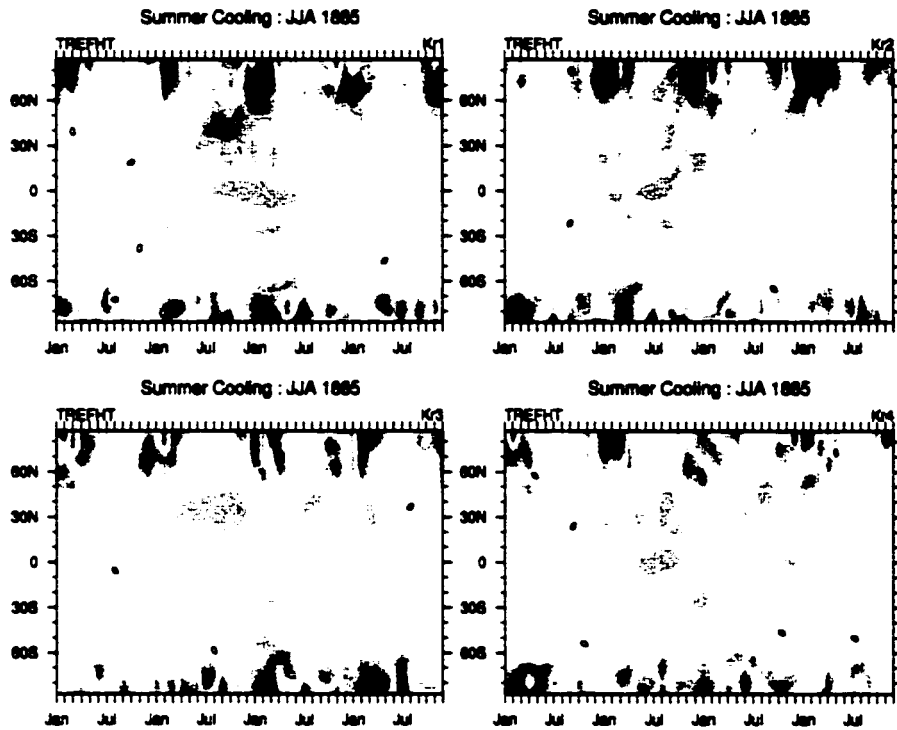
Figure 6.17: Zonally averaged reference height temperature response of 4 ensemble members to the Krakatau aerosol forcing. The seasonal cycle was removed and all data is an anomaly monthly zonal values. Each ensemble was forced with the same Krakatau optical depth starting in August of the initial year. Initial conditions are branched off the control run.

single locations to such a degree that looking only at the single time series following the usual connection to El Niño could be misleading. Two examples to illustrate the idea:

1. Assuming a large volcanic eruption causes widespread cooling in the tropics. When using the isolated SSTs from the NINO3 area, a cooling signal could mean two distinct things. Either it means that conditions of a La Niña events are causing the SSTs to fall, or that the direct cooling from the volcano could influence the SSTs more strongly than it is regulated by the upwelling process. The larger the volcanic forcing, the more important this second option could become.

2. Another situation could involve the western Pacific area. During El Niño, the general low pressure over the area (in the "normal" state of ENSO) is linked to the warm ocean conditions and strong convective activity. Again, a strong volcanic perturbation would reduce the surface temperature throughout the tropics, and with it, the convective activity would slow down. Without having the system fall into El Niño mode, reduced precipitation in the western Pacific area could solely arise from reduced insolation. This could be misinterpreted for an El Niño event, although in the eastern Pacific no precipitation would indicate such an event.

These two examples highlight the need for a critical evaluation of single proxy series used for climate modes like El Niño, particularly during time periods of significant perturbations of the normal conditions through volcanic aerosol. It is, therefore, more useful to use spatial expressions of the modes, including areas with teleconnections. But even for these spatial aspects, there are limits involving the stationarity of spatial correlations, as *Meehl and Branstator* (1992) and more recently, *Mann et al.* (2000) have shown. See also Chapter 4 for further discussions.

Focusing now on the NINO3 area and the results of tropical ensemble runs presented in Table 6.1, the primary influence of such a large tropical volcanic forcing follows a general cooling in the tropics. One year after the eruption, all five ensemble members show colder conditions in the

NINO3 area than initially seen at the beginning of the runs and colder than for the unperturbed condition (not shown). For the first winter. on the other hand. roughly four to five months after the eruption. a tendency to positive anomalies can be seen in Table 6.1. This tendency is similar to the suggestion of *Handler* (1984) as was discussed in Chapter 4. The only real exception in run b056.kr4. which was set at a time with almost zero NINO3 anomaly. Here. the cooling from the aerosol dominates already a few month after the eruption. For the other tropical simulations it seems to make little difference in what state the ENSO system is. or is heading. The second winter is less consistent in terms of a signal. although for most events the cooling still prevails.

As a further test of the suggestions by *Handler* (1984). an ensemble set of high-latitude events were run. Using the aerosol evolution of Katmai-Novarupta (1912). they indeed show a tendency to cool conditions immediately after the eruptions (see Table 6.1). as was found by *Handler* (1984). But we also need to keep in mind that the number of ensembles here is very small and despite showing a trend. it would be hard to make a case from these experiments. Nevertheless. these first results using a coupled model capable of internally producing El Niño events do not contradict *Handler* (1984) and warrent further investigation in this direction.

One additional aspect can be pointed out from the results in Table 6.1. The current state or trend in ENSO determines the timing of the maximum cooling compared to the undisturbed run. If the eruption takes place during an El Niño event (b056.kr1) or when the system is heading into an El Niño already prior to the eruption (b056.kr3). then the maximum perturbation is delayed by several month compared to the other cases. This agrees with observations of the El Chichón eruption in early 1982. which was followed by a very strong El Niño. The volcanic cooling signal was first completely obfuscated. but its remnants showed up slightly in early 1984 *Wigley* (2000). While the maximum cooling after a tropical eruption is delayed by a year or year and one half. the impact of high-latitude eruptions on the other hand is almost immediate. and the maximum cooling is reached within four of five months. More discussion on these high-latitude events follows below (Chapter 6.4).

6.3.3 Impact dependent on aerosol properties

Since El Niño. as the strongest natural mode of climate variability on the interannual time scale (*Philander*. 1990). did not provide adequate masking capacity for the large aerosol forcing from Krakatau. there appears no other option than to re-evaluate the aerosol mass. size distribution and composition with corresponding radiative properties. In doing so, one violates the assumption of universal application of a 'volcanic sulfate aerosol'. as derived from the most recent eruptions of Pinatubo and El Chichón. Together with Agung. these eruptions have been used to evaluate the appropriateness of using sulfate fluxes on the polar ice sheets to estimate optical depth during the atmospheric perturbation following the explosive events (e.g., *Zielinski*. 1995; *Robock and Free*. 1995).

In the following. two options will be evaluated. One is to change the size distribution. the other to evaluate a different composition of the aerosol. Both are based on the same optical depth in the mid-visible wavelength given by the seasonality parameterization. This allows us to comply with the large number of observations: the visible optical effects (reported as unusually colored sunsets and sky glow. whitish hazes. colored solar or lunar disks. and colored rings around the sun (Bishop Rings)). as well as the different instrumental measurements of atmospheric perturbations for more than two years after the Krakatau eruption (*Symons*. 1888; *Self and Rampino*. 1981; *Simkin and Fiske*. 1983; *Stothers*. 1996b). It also means that the large sulfate deposits recorded in polar ice cores. which allow the calculation of the total sulfate mass in the stratosphere (see Table 3.1). may be put into question (or the process to derive the global loading).

Reports collected by *Symons* (1888) from different places around the world. include observations of green suns after the eruption of Krakatau in August 1883. This could point towards a relatively large particle mode. which selectively reduced the more reddish part of the solar spectrum. Although *Deirmendjian* (1973) pointed out that the size distribution for these observtions most probably would not exceed an average aerosol size of 0.6 to 0.8 μm. here an experiment

is run using an aerosol size distribution very similar to the earliest El Chichón aerosol in May 1982 (*Hofmann and Rosen*, 1983). It consists of an effective radius of 1.5 μm (median radius is roughly 1 μm) with an effective variance of about 1.5 μm (see Figure 3.1). This size distribution is roughly 3 times larger than both the average Pinatubo aerosol and the aerosol used as the standard aerosol for the long volcanic simulation. Two important consequences of such an increase in aerosol size distribution need to be considered. First, such large particles would fall out of the atmosphere much more quickly then smaller ones (*Kasten*, 1968). This would clearly influence the decay rate. Second, since the optical depth in the mid-visible (CCM SW band 8) is fixed to the same value as for the standard aerosol experiment (in order to accomodate for the observations as reported in *Stothers* (1996b)), the total aerosol mass required to accomodate such an optical depth in the visible surpasses the standard aerosol mass by a factor of 5.58. Instead of 40 to 50 Mt, this would lift the total sulfate mass to almost 250 Mt. Since Krakatau's aerosol was observed for more than two years after the eruption (*Symons*, 1888), it is questionable if this simple switch to a larger size distribution is reasonable. And there is also no evidence whatsoever for sulfate deposits of that magnitude in polar ice cores (see Table 3.1). Here, we want to evaluate what the influence of a large particle size would be.

Tables 6.2 and 6.3 lists some selected sulfate fluxes and the total atmospheric mass for a number of aerosol size distributions, using 0.3 as the global optical depth during the peak month (January 1884) of aerosol loading from Krakatau.

Figure 6.18 shows the global average temperature response to an aerosol loading described by this large particle mode and a visible optical depth identical to the previous experiments. The large temperature signal at the surface is entirely gone. The particle size, therefore, has to be considered an important parameter when looking at these enormous eruptions. Nevertheless, the observed long duration of the optical effects following the eruption suggest that the size distribution and its dampening effect on the surface forcing can only be part of the solution.

A next component to be briefly evaluated is the composition of the aerosol. If a significant

r_{median}	σ_r	r_{eff}	kg m^{-2}	Mt H$_2$SO$_4$
0.07	0.41	0.1066	1.32e-4	67.1 Mt
0.3709	0.223	0.42	7.80e-5	39.8 Mt
0.408	0.223	0.45	8.32e-5	43.7 Mt
0.6	0.41	0.913	2.45e-4	124.9 Mt
1.0	0.405	1.5	4.65e-4	237.0 Mt

Table 6.2: Aerosol size distribution and total mass loading used with CSM given an optical depth of 0.3 (τ_{vis}) in the mid-visible wavelength of 0.5 μm.

r_{eff}	$\Phi_{0.5}$	H$_2$SO$_4$ [Mt]
0.2	4488	32.6
0.3	5005	29.2
0.4	4096	35.7
0.5	2880	50.8
0.6	2010	72.8
0.7	1540	95.0
0.8	1316	111.2
1.0	1082	135.2
1.5	682	214.6

Table 6.3: Change in mass extinction coefficient ($\Phi_{0.5}$ [m^2 Kg^{-1}]) depending on effective radius r_{eff} and corresponding mass loading to generate a mid-visible aerosol optical depth of 0.3.
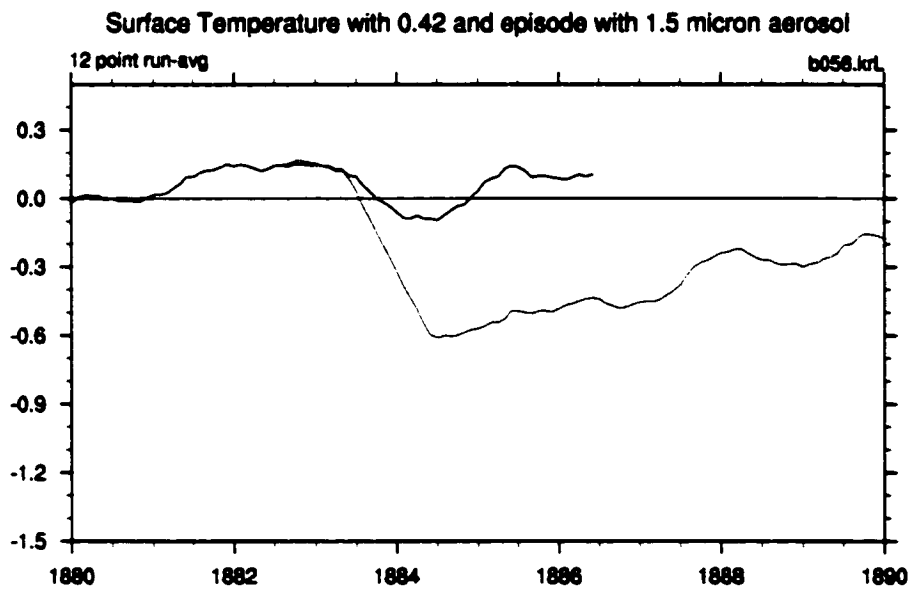
Figure 6.18: Globally area averaged surface temperature follwing the Krakatau eruption in the 130-year run using standard aerosol of $r_{eff} = 0.4$ μm (red line) and the large aerosol experiment using $r_{eff} = 1.5$ μm (blue line).

Volcano	SO$_2$	Ash	SO$_2$/Ash Ratio	function
Pinatubo	20 Mt	10.000 Mt	0.002	0.89
Ruiz	0.75 Mt	48 Mt	0.0156	0.094
El Chichón	7 Mt	3.000 Mt	0.0023	0.335
Agung	10 Mt	1.000 Mt	0.01	1.0
Krakatau	30 Mt	34/25.000 Mt	0.00086/0.0012	0.89/1.04

Table 6.4: Estimated sulfur dioxide and fine ash emissions. Using a function that is balancing the sulfur by the gas to ash ratio, like: Index = SO2 MT × SQRT of gas/ash

amount of the aerosol would have been something other than sulfuric acid, the optical properties can be dramatically different and, over all, can look much more similar to the large-sized sulfuric acid droplet mode presented above. If this were the case, for example, with a significant amount of fine tephra or silicate ash as part of the aerosol cloud early on and later fading into pure sulfuric acid for the long lived aerosol, the sulfate mass required to explain the optical depth in the mid-visible could be substantially smaller than for the example of the large aerosol mode, and, therefore, in better agreement with the ice core data. Gooding et al. (1983) reported collection of ash particles coated with sulfuric acid roughly half a year after the eruption of El Chichón. Note, this would not only influence the optical properties of the aerosol, but also raise questions about increased removal of sulfuric acid (Pinto et al., 1989, see also). Table 6.4 lists the sulfate and fine ash emissions from a few eruptions and shows the two ratios of sulfur-dioxide versus ash amount. These are total values that don't take any spatial distribution into account. They are meant to illustrate a possible scaling of the sulfate by the erupted fine ash. In this regard, Krakatau with by far the largest sulfur emissions, would not significantly exceed the ratios of Pinatubo and Agung (very small amount of solids!). Further investigationis needed.

Evidence for large amounts of ash in the Krakatau aerosol cloud is sparce. Nevertheless, reports of falling ash over Europe during late fall of 1883 were cited in Symons (1888), although

they could not be directly confirmed. Additionally, a large deposition spike of sulfate found in an ice core from the Peruvian Andes was interpreted by *Thompson et al.* (2000) as coming from the Krakatau cloud. Because the general motion in the lower tropical stratosphere is directed upwards, this observation could indicate rather large particle sizes, causing rapid fall out in the tropics. Repeated observations of a greenish appearence of the sun throughout the tropics could be a hint in the same direction. The continued optical phenomena reported all around the world (*Symons*, 1888; *Simkin and Fiske*, 1983) nevertheless suggest that the complete removal did not take place for more than two years.

6.3.4 Summary of Krakatau studies

The large response to the Krakatau forcing as simulated in the coupled CSM is significantly larger than observed (roughly 0.7°C in the model vs. 0.2-0.3°in observations). Different avenues for explaining the difference have been explored. El Niño as an internal mode of climate variability has the potential to partially off-set the cooling due to tropical volcanic eruptions. The simulations presented here point towards a possibility of a dynamical relation between volcanic perturbation and El Niño onset as was suggested by *Handler* (1984). One needs to keep in mind that the forcing used in the ensemble simulations was very large and the simulated climate signal diverges with the observations. The tendency towards El Niño formation in the first winter after large tropical volcanic eruptions can therefore only be regarded as a preliminary result warranting further and more detailed studies. Despite El Niño, the cooling simulated in the ensemble studies is not significantly reduced enough to explain the difference with the real observed signal after Krakatau. In a second approach, the aerosol size distribution was changed following suggestions of a significant large particle mode that was responsible for observations of 'green suns'. When the median of the aerosol was trippled to a value close to the early El Chichón aerosol, the climate signal disapeared. While this experiment violates both the total sulfate mass erupted by Krakatau and the decay rates for such large particles, it clearly points to a possibility

of significantly altering the climate impact of some events. A possible change in composition of the aerosol, for example by the presence of significant amounts of ash or black carbon inside the aerosol droplets (either would have to be in a higher concentration than 5% inside the droplet according to *Chylek et al.*, 1995), would also help to mediate the signal. Both mechanisms are not included in the general assumption that the sulfate flux measured in polar ice cores is a straightforward proxy for optical depth, since size distribution and composition significantly alter the spectral optical properties. In conclusion, the large Krakatau signal simulated by CSM could be expected if the visible optical depth were to be described with the stratospheric sulfate alone. While such an assumption seems to work for the eruptions during the 20th-Century, it fails for Krakatau. Other large events in previous centuries might also be affected by this and climate model simulations of these events have to be performed with care. Finally, a critical evaluation of the 'observations' should also be performed, particularly for the decades before 1900. Large corrections to the sea surface temperatures might have caused a dampend signal as land based observational series exhibit a much larger signal (0.4 *Budyko*, 1969; *Hansen et al.*, 1999). A more detailed study of Krakatau will be presented elsewhere.

6.4 North Atlantic response to volcanic forcing

This section focuses on one particular mode of climate variability, the North Atlantic Oscillation (NAO), and how it is impacted by the volcanic eruptions. As it has been discussed for El Niño in Chapter 4, the NAO is another example where eruptions could excite, suppress or influence the pacing of an important internal mode of the climate system, which, through teleconnections, would then determine the spatial imprint of the eruptions on climate. The more internal modes are modified in one particular way, the more coherent should the climate impact signal of individual events appear in the paleo records. This would make the identification of the volcanic forcing on climate more easy to detect.

Climatically, the North Atlantic area is of significance for several reasons. First, it is the location where centers of action guide a significant part of the annual to decadal climate variability of the high northern latitudes through the North Atlantic Oscillation (*van Loon and Rogers*, 1978; *Hurrell*, 1995; *Hurrell et al.*, 2001), or, when looking over the Arctic as a whole, and in particular in the upper troposphere and lower stratosphere, the Arctic Oscillation (*Thompson and Wallace*, 1998; *Wallace*, 2000; *Thompson and Wallace*, 2001). Second, it is the location where the interaction between atmosphere and ocean is driving and modulating the thermohaline circulation in the ocean (e.g. *Broecker*, 1997), a crucial component for low- to high-latitude energy exchange. Finally, more in the context of this study, the superposed epoch studies of volcanically perturbed years using the long climate reconstruction of *Mann et al.* (1998) presented in Chapter 1, exhibited the largest amplitudes of climate response in the vicinity of the North Atlantic basin. Fortunately, Western Europe and the eastern part of North America offer some of the longest high resolution climate records, instrumental and proxies alike (e.g. *D'Arrigo et al.*, 1993; *Appenzeller et al.*, 1998; *Luterbacher et al.*, 1999).

During the instrumental time period, the climatic signals reported after large volcanic eruptions seem to be quite strong around the North Atlantic (see Chapter 4). But several events suggest strong regional differences (*Harington*, 1992; *Jacoby et al.*, 1999; *D'Arrigo and Jacoby*, 1999), and a seasonally varying response was identified by *Groisman* (1994) and *Kelly et al.* (1996). They find a very distinct pattern across the North Atlantic, particularly in the first winter season after a number of large explosive events in the tropics. These years seem to exhibit warmer than normal temperatures in Northern Europe, cooler than normal conditions in the vicinity of Greenland, and also warmer than normal conditions over central North America. This pattern basically matches conditions during years with a high NAO index, i.e. when both the Icelandic Low and the Azores High pressure system are enhanced (*Hurrell*, 1995). This rises the question to what degree the direct cooling effect from the volcanic aerosol could be responsible for a shift in this dominating mode of climate variability. Interestingly, it has already been sug-

gested by *Defant* (1924) that while in the year of volcanic eruption the zonal pressure gradient over the North Atlantic was reduced. a year later it would be enhanced due to strong cooling in the polar areas. *Lamb* (1970), using an extended climate record and dividing the eruptions into high- and low-latitude groups. confirmed *Defant's* (1924) findings for low-latitude eruptions. For high latitude eruptions. on the other hand. rather the opposite seemed to be the case. an immediate enhancement in the flow.

Here. we re-evaluate these results with the help of observations and the simulated responses in the coupled climate experiments. To follow the suggestions of *Lamb* (1970), the eruptions of the low and high-latitudes are discussed separately. Mid-latitude eruptions are not discussed separately since they behave either like tropical or more like high-latitude events in terms of their radiative effect. First. the ensemble simulations of the largest high-latitude eruption of the 20th-Century. Katmai-Novarupta (1912). are presented. Using the superposed epoch technique. the ensemble simulations and observations of both tropical and high-latitude eruptions are then analyzed and compared for their impact on the NAO.

6.4.1 Climate response to high-latitude eruptions in CSM

Before discussing the impact on the NAO. a brief presentation of the simulated climate perturbations in ensemble events is added. Similar as for the tropical eruptions. the same forcing was applied in each experiment but with varying starting conditions (choosing another year to branch off from the long transient experiment).

The only event of significant magnitude within the instrumental time period is the sumultaneous 1912 eruption of neighbouring Katmai and Novarupta volcanoes. Alaska. which formed *The Valley of the Ten Thousand Smokes*. It was shown in Table 6.1 that the high-latude ensemble experiments of this event clearly show a different impact on global temperatures than from tropical eruptions. Although the signal is smaller and shorter lived due to the limited area of aerosol perturbation of the radiative budget. it is much more immediate as compared to tropical events.

211

This is also illustrated in Figure 6.19. This Figure presents the zonally averaged reference height temperatures for the three ensemble runs using Katmai-Novarupta (1912) aerosol. Additionally, the superposed composite is included. Large scale cooling is visible in the first winter over much of the northern high latitudes. This fits with the observations of very cold conditions after the eruption of Laki in 1783 (*Franklin*, 1785), at least in the zonally averaged case.

6.4.2 Volcanic eruptions and the NAO

The sets of large tropical and high-latitude eruptions of the past centuries both in the real world and ensemble experiments of CSM can be used to compare trends in the North Atlantic climate following the eruptions. Figure 6.20 shows the temporal evolution of the NAO index calculated after *Hurrell* (1995) in the 20th-Century simulation with volcanic forcing. Figure 6.21 maps the surface air pressure differences between years of high versus years with low NAO (threshold used: standardized NAO larger than 1 for positive and smaller than -1 for negative years). The classical behavior of strong interannual variations with superposed decadal to multi-decadal trends is well reproduced in the model. The simulation also reflects the spatial pattern of the NAO with high pressure over the Azores and low pressure over Iceland and the polar areas. This pattern not only compares favorably with recent maps of NAO correlations (e.g. *Hurrell*, 1995) but also with the old maps shown in *Defant* (1924, p. 18-19). This allows for an intercomparison of the independent results concerning the influence of volcanic eruptions on this important mode of climate variability.

6.4.2.1 NAO evolution after volcanic eruptions in CSM

To study the influence of the explosive eruptions on the NAO index, the results from the individual events in the transient experiment and the Krakatau ensemble simulations can be combined. Figure 6.22 shows the evolution of the NAO over the 130-year experiment with volcanic aerosol. The NAO evolution of the ensemble members are added at their position of branching off from
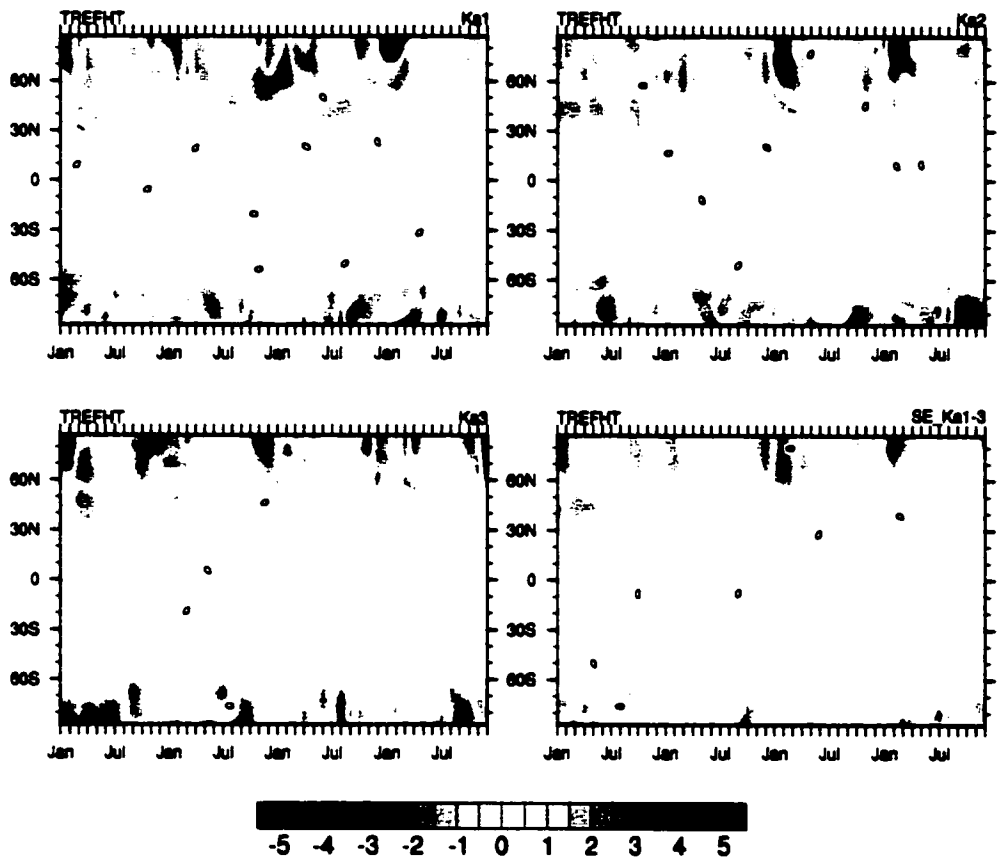
Figure 6.19: Reference Height temperatures zonally averaged for ensemble ka1-ka3 as well as for the superposed ensemble. Note the immediate cooling in the northern hemisphere in July of the first year. Already in the second winter after the eruption, the signal disappears in the noise of high-latitude interannual variability.

NAO DJFM
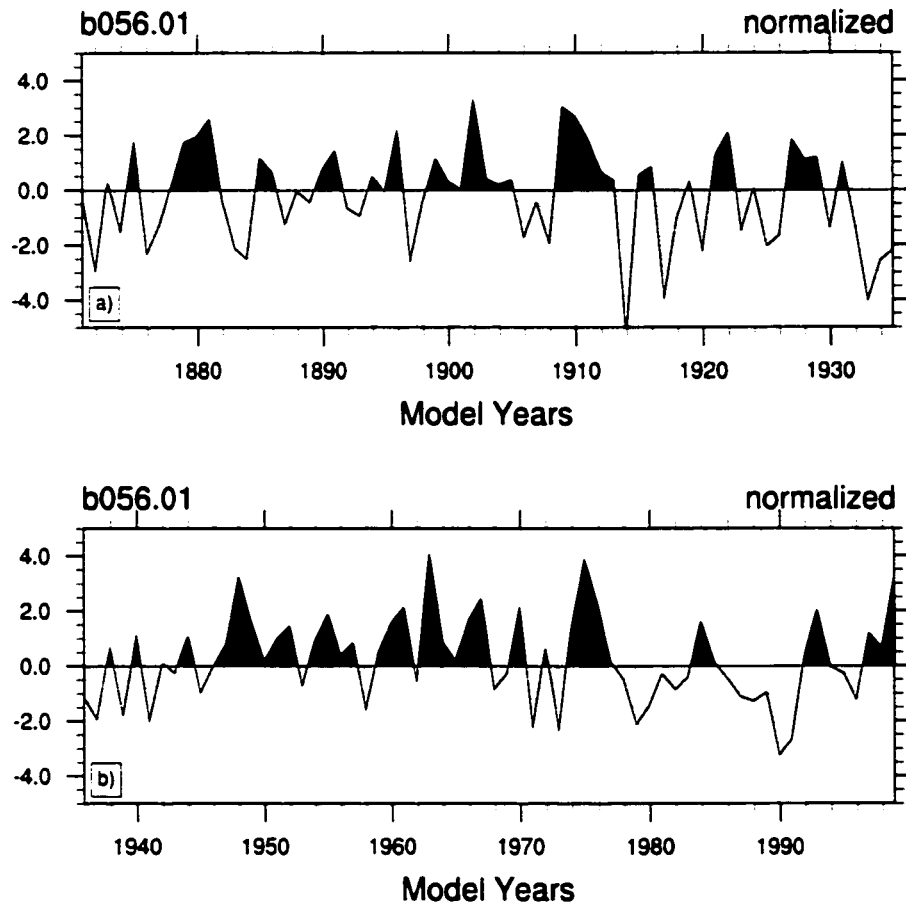
Figure 6.20: North Atlantic Oscillation Index after *Hurrell* (1995) in the coupled CSM run with volcanic forcing.

214

NAO DJFM

b056.01 PSL Diffs (NaoHigh - NaoLow)
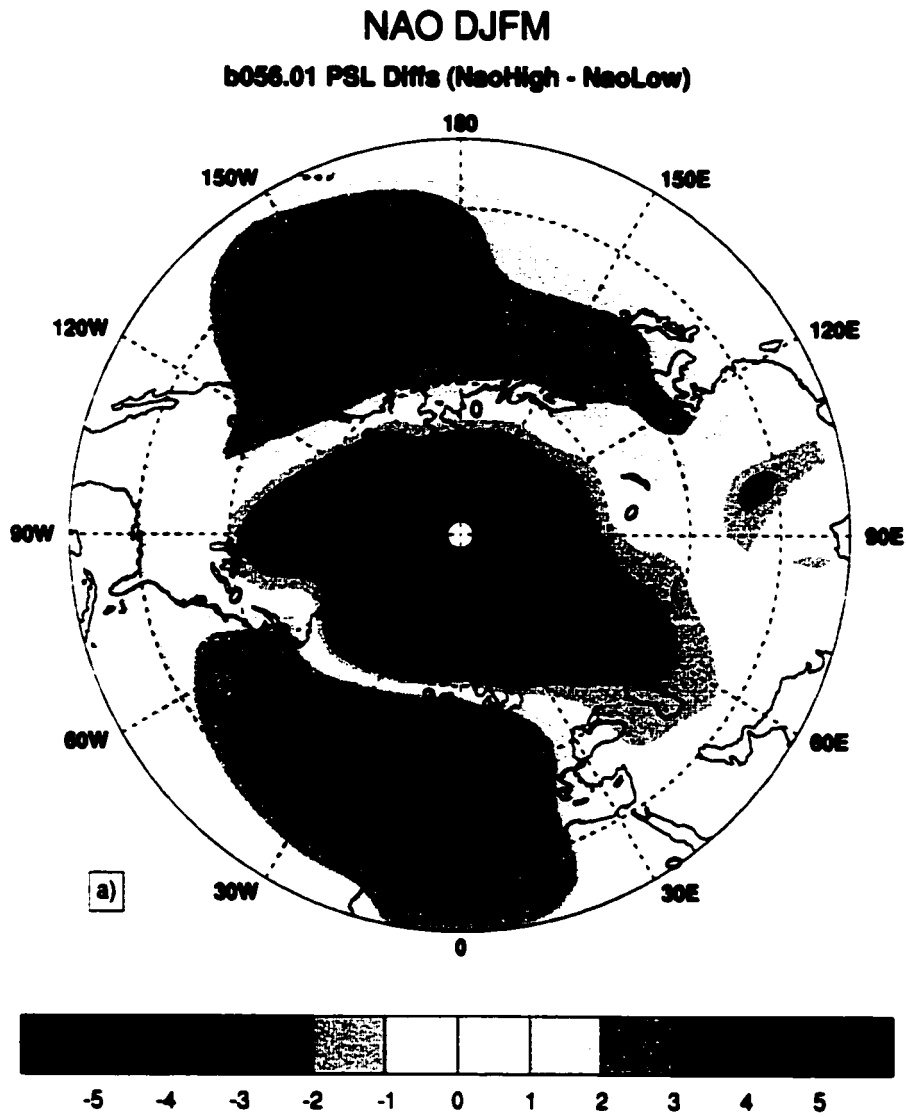
Figure 6.21: North Atlantic Oscillation pattern for difference between high versus low index years. Only the winter month December through March are included.

the long run with tropical events shown in red and high-latitude eruptions shown in blue. With the exception of the *large aerosol* experiment of Krakatau (ensemble member branching off in 1883), some common aspects are clearly present. The first winter immediately after the eruption sees a rising index relative to the control run (4 out of 5 tropical, and 3 out of 3 high-latitude events), while for the second winter the NAO commonly is reduced compared to the unforced (again 4 out of 5 tropical and 3 out of 3 high-latitude). The ones that stay in the positive area usually drop below the prior years value, following a decreasing trend which persists for the tropical events, but is reversed for the high-latitude eruptions.

These visual results are summarized in absolute indices in Tables 6.5 and 6.6. They show the winter NAO (December through March) evolution from the year of the eruption to three years after the events. In the year of the eruption, the spread of NAO indices is large and the average value is strongly dependent on a few events. The years following the eruptions usually show a more coherent picture, although not all eruptions follow the exact same pattern. Nevertheless, several tendencies can be recognized:

For tropical events, the number of negative NAO winters is reduced for up to two years. The average NAO reaches clear positive values. In the third year after the eruptions, the NAO tends to turn negative with large positive values being absent. This tendency is the same for the average of seven major tropical eruptions in the transient experiment and for the Krakatau ensemble (b056.kr1-b056.kr4) shown in Table 6.5.

High-latitude eruptions show a similar behavior, but the positive deviations after the eruptions only remain for one year, although for some events they don't even show up. Thereafter, the NAO drops sharply, reaching some of the lowest values during the experiments. The third year also shows a return to more normal conditions. See Table 6.6.

NAO DJFM
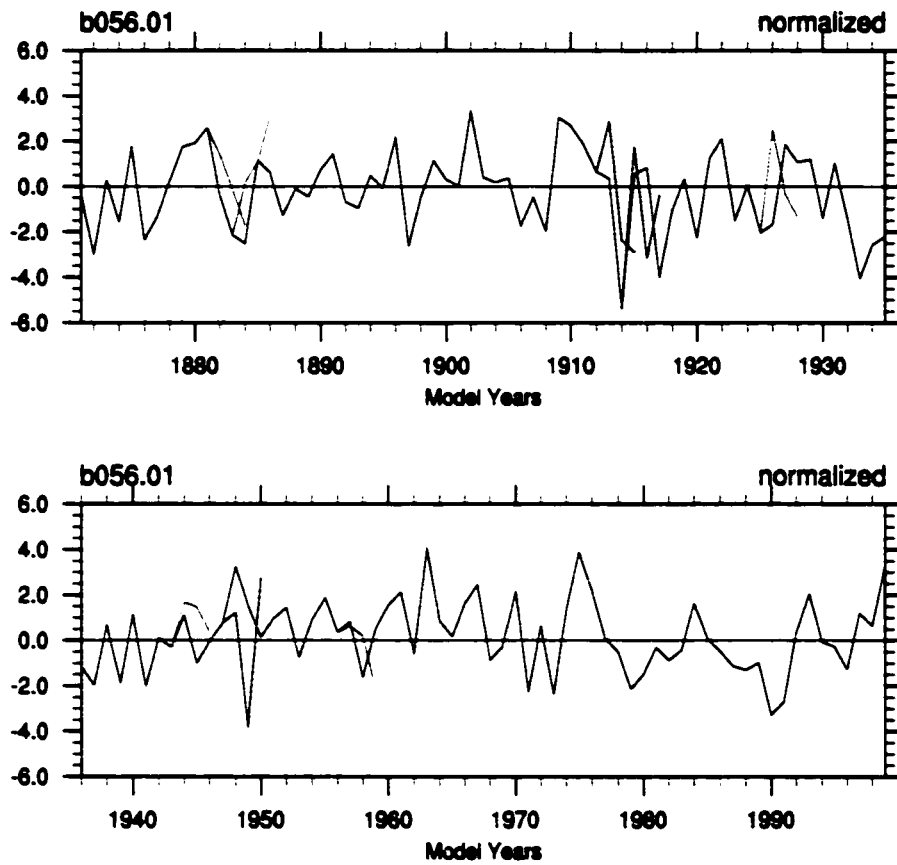
Figure 6.22: North Atlantic Oscillation time series from the coupled CSM run over 130 years. In color the trends from the ensemble simulations, red for the tropical, and blue for the high latitude eruptions.

Volcano, Year	Type	NAO 0	NAO +1	NAO +2	NAO +3	NAO +4	NAO +5
Krakatau, 1883	T	-1.16	-1.38	0.76	0.45	-0.65	0.04
Colima(?), 1890	T	0.52	0.91	-0.32	-0.48	0.36	0.03
Santa Maria, 1902	T	2.00	0.28	0.16	0.27	-0.96	-0.22
Agung, 1963	T	2.33	0.44	0.05	0.91	1.38	-0.56
Fuego, 1974	T	0.71	2.20	1.21	0.00	-0.37	-1.32
El Chichon, 1982	T	-0.58	-0.32	0.86	-0.02	-0.36	-0.75
Pinatubo, 1991	T	-1.65	0.12	1.10	-0.13	-0.26	-0.84
Average		*0.31*	*0.32*	*0.55*	*0.14*	*-0.12*	*-0.52*
b056.kr1	T	1.65	0.94	-0.07	-1.10		
b056.kr2	T	-0.17	1.07	0.93	0.25		
b056.kr3	T	0.24	0.40	0.13	-1.3		
b056.kr4	T	-1.30	1.60	-0.21	-0.85		
b056.krL	*T*	*-1.27*	*0.18*	*1.11*	*3.12*		
Average		*0.11*	*1.00*	*0.20*	*-0.75*		
Average (all tropical)		**0.24**	**0.57**	**0.42**	**-0.18**	**-0.12**	**-0.52**

Table 6.5: NAO after tropical eruptions in CSM : NAO index calculated and standardized after *Hurrell* (1995) following the largest volcanic eruptions in the tropics since 1870 in the coupled simulation and for ensemble simulations of Krakatau. Ensemble experiments (here using the Krakatau aerosol evolution) were limited to four years in length. The experiment *b056.krL* using the large aerosol size distribution, which did not cause a large surface disturbance, is only added for illustration and was not used in the averages.

Volcano, Year	Type	NAO 0	NAO +1	NAO +2	NAO +3	NAO +4	NAO +5
Ksudach, 1907	H	-0.22	-1.10	1.82	1.61	1.21	0.42
Katmai-Novarupta, 1912	H	0.42	0.24	-3.10	0.34	0.53	-2.29
Spurr, 1953	H	-0.47	0.51	1.06	0.18	0.45	-0.98
b056.ka1	H	0.44	0.70	-2.27	1.58		
b056.ka2	H	-3.10	1.05	-1.80	-0.19		
b056.ka3	H	0.42	1.72	-1.33	-1.64		
Average (Kat-Nova)		-0.45	0.93	-2.13	0.02		
Average (high-lat)		-0.42	0.52	-0.94	0.31	0.73	-0.95

Table 6.6: NAO after high-latitude eruptions in CSM : as Table 6.5. but for high-latitude eruptions. The four year long ensemble experiments were using the Katmai- Novarupta aerosol. The separate average (Kat-Nova) includes the three ensemble simulations and the Katmai-Novarupta event in the transient run.

6.4.2.2   NAO evolution in observational data

These simulated NAO trends can be compared with observations. The data from *Hurrell* (1995) (updated) are compiled in Table 6.7. While the NAO in winters prior to the tropical eruptions are quite evenly distributed between positive and negative indices, the first winter following the events shows a clear positive trend. This situation, on average of the standardized indices, is followed by two years of continuously decreasing values. While the NAO of the second winter is in all cases lower than in the first after the eruption but still positive compared to the years prior to the eruptions, the third winter, although even lower on average, already contains an equal number of rising indices, and the change is not significant.

Large high-latitude events are only porely documented by observations and proxy data. Table 6.7 also lists three of these events for which NAO data is available. To recognize a trend from these few events is not easy. The only palable conclusion could include the observation that the NAO in the first winter after the eruption is relatively higher than in the second, which shows a consistent drop of about two index points. The NAO remains low in the third winter. But

Volcano, Year	Type	NAO 0	NAO +1	NAO +2	NAO +3	NAO +4	NAO +5
Krakatau, 1883	T	-0.23	1.41	-0.89	-1.12	0.45	-2.75
Colima(?), 1890	T	1.78	-0.82	-2.02	-1.07	2.68	-3.97
Santa Maria, 1902	T	-1.41	3.89	0.23	1.98	2.06	2.06
Agung, 1963	T	-3.6	-2.86	-2.88	-1.69	1.28	-1.04
Fuego, 1974	T	1.23	1.63	1.37	-2.14	0.17	-2.25
El Chichon, 1982	T	0.80	3.42	1.60	-0.63	0.50	-0.75
Pinatubo, 1991	T	1.03	3.28	2.67	3.03	3.96	-3.78
Average tropical		**-0.06**	**1.42**	**0.01**	**-0.23**	**1.59**	**-1.78**
Ksudach, 1907	H	2.06	1.44	0.0	2.1	0.29	0.24
Katmai-Novarupta, 1912	H	0.24	2.69	1.48	-0.20	-0.69	-3.80
Spurr, 1953	H	0.18	0.13	-2.52	-1.73	1.52	-1.02
Average high-lat		**0.83**	**1.42**	**-0.35**	**0.06**	**0.37**	**-1.53**

Table 6.7: NAO - Observations : NAO indices from *Hurrell* (1995) (updated) following the largest tropical (Type T) eruptions since 1870 showing a clear positive excursion in the first winter after the volcanic eruption (**NAO +1**) with subsequent two winters (**NAO +2. NAO +3**) showing a decreasing trend. High-latitude eruptions are indicated by Type H.

due to the very small number of events covered by the observations, this tendency cannot really reveal its significance.

6.4.2.3 Comparison and conclusion

Both tropical and high-latitude eruptions show a similar evolution of the NAO in years following the events: The NAO index clearly increases during the first winter after eruptions, in some cases to very strong positive values. In subsequent years, the index representing the strength of the Westerlies through the relative difference in pressure systems changes decreases and soon reaches negative values. This drop is faster and more pronounced for high-latitude events than for the tropical eruptions. On the other hand, tropical events cause the NAO to decrease more or less continuously over a longer time. Despite the small number of events studied up to this point, the similarity between the NAO trends in the model and in observations is remarkable. Model and observations exhibit basically the same evolution. Additionally, the strong negative values after high-latitude events reached in the second winter in the model and the second or third winter after the eruptions in observations hint to a significant response of the atmospheric circulation to the volcanic dust veils in high-latitudes. While the global temperature response to high-latitude eruptions was shown to be rather small and insignificant, the regional effects through the influence on the NAO can be quite large.

How do these results compare to the previous studies of *Defant* (1924) and *Lamb* (1970)? While only looking at the years from 1881 to 1905, *Defant* (1924) identified two significant trends in the pressure patterns over the North Atlantic (see Figure 6.23). In the year of the eruptions themselves, he found a strongly reduced meridional pressure gradient (equivalent to a negative NAO). He interpreted this reduced gradient as a result of low latitude cooling due to the volcanic dust. The subsequent increase, especially after the large eruptions, he thought to occur due to high latitude cooling after a year of reduced heat transport into the high latitudes. The results from CSM and the observations of *Hurrell* (1995) overall are quite similar. But other

221
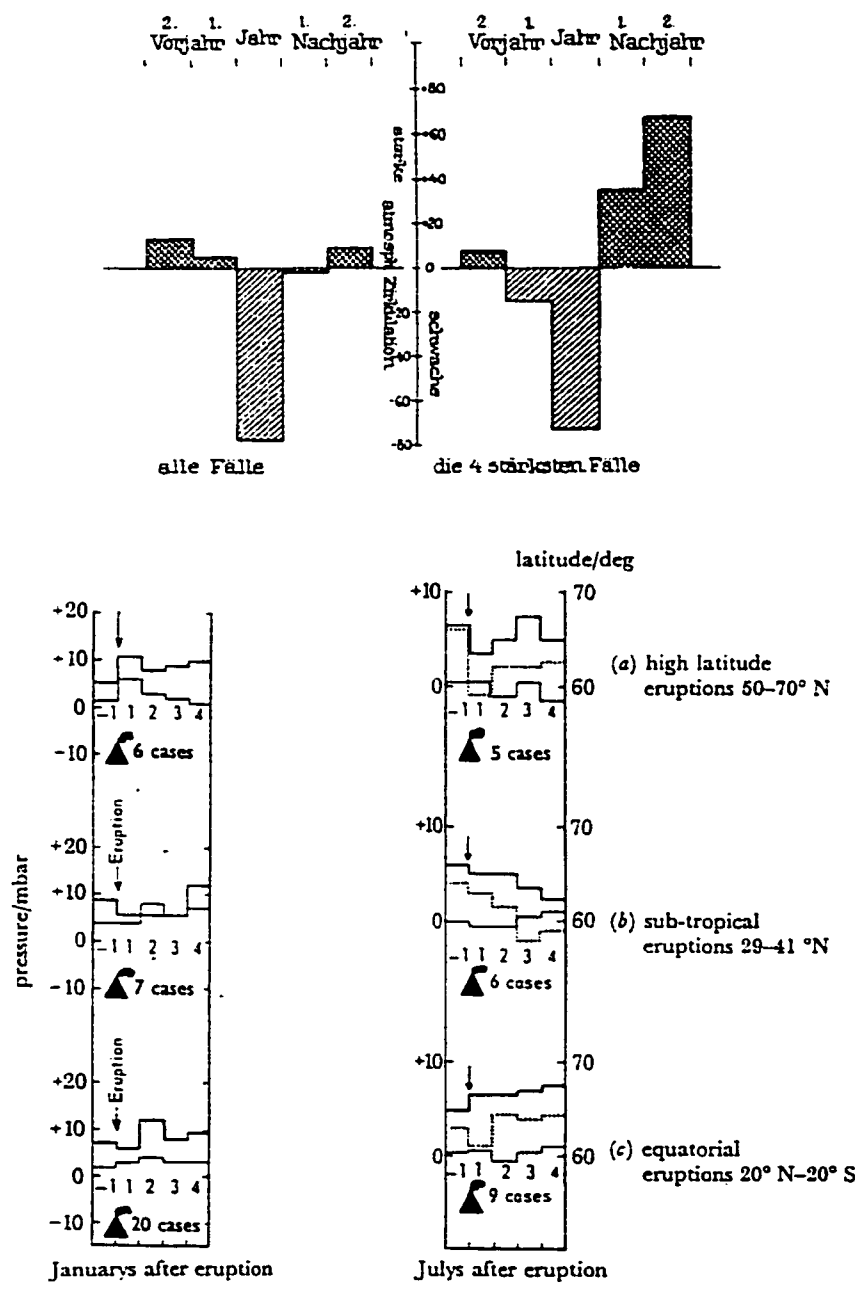
Figure 6.23: Average meridional pressure gradient in the North Atlantic after volcanic eruptions from *Defant* (1924) (top) and *Lamb* (1970) (bottom).

than in the results of *Defant* (1924), the year of the eruption was not found to be particularly low. This difference results from different temporal coverage of the indices. While commenting on the fact that the signals are stonger in winter, the values used by *Defant* (1924) (and shown in the upper panel of Figure 6.23) are annual averages. The results presented above contained NAO indices specifically for the winter season from December through March (*Hurrell*, 1995; *Hurrell et al.*, 2001). Since the large eruptions did not influence the previous winter (but could very well have influenced the latter part of the year), a slow down in the circulation and a reduced NAO cannot be detected in the winter data. But when looking at the individual monthly values of the simulated pressure difference between the Azores and Iceland after the eruptions (not shown), a reduction can be detected in 5 out of 7 events in the ensemble simulation of Krakatau and Katmai, and in X events in the transient experiemnt.

Lamb (1970) extended the record back in time (1750 and 1680 for which he used preliminary data) and separated the volcanic events by their latitude (tropical, mid-latitude and high-latitude events). He used two indices, one for the strength of the westerly flow and one for the meridional component, both of which would vary in synchrony with the NAO. Additionally, he distinguished between January and July conditions finding more signal in the northern hemisphere winter season. For the summer (see Figure 6.23, right side of lower panel) he mostly recognized a strong southward displacement of the mid-latitude trough in the first year after the eruption, which could add to the generally cooler conditions from reduced irradiation.

For the winter time, *Lamb* (1970) confirmed the results of *Defant* (1924) for tropical eruptions with decreasing westerlies during the year of the eruption followed by an increase thereafter. This trend could also be seen in the southerly component with a significant increase in the second winter after the eruption (at 1% level). This behavior is very similar to the simulated cases with CSM, which also show a two year increase in the NAO, later followed by a continuous decrease over the next couple years (see Table 6.5). Additionally, an increase in the NAO after tropical

eruptions is also consistent with increased temperatures over the higher latitudes during winter

(*Bradley*, 1988: *Graf et al.*, 1993: *Robock and Mao*, 1995). The spatial distribution of temperature

anomalies found by *Groisman* (1992) and *Parker et al.* (1996) also mirrors the positive mode of

the NAO. This phenomenon has been discussed before in Chapter 5.3.

For high-latitude events, on the other hand, *Lamb* (1970) could not find a decrease of westerlies

but instead an immediate increase of the circulation with a strong southerly component. This is

equivalent to an increase in the NAO. This same evolution was seen in the data of *Hurrell* (1995)

in Table 6.7 as well as in the CSM simulations (Table 6.6). In the second winter, the circulation

was already significantly weaker, similar to the few events covered by *Hurrell* (1995) and the

CSM simulations. However, the observational data does not exhibit the same dramatic decrease

as the simulations of the large Katmai-Novarupta event shown in Table 6.6. But when looking at

the two smaller high-latitude eruptions in CSM (Ksudach 1907, Spurr 1953), no such dramatic

collapse is visible, suggesting that smaller events could reduce the strength of the potential signal

in the compilation of *Lamb* (1970).

Finally, Lamb pointed out the fact that the North Atlantic area undergoes substantial varia-

tions without volcanic perturbations and that the signal from the volcanoes could be somewhat

diminished by individual temporal evolution where "effects take more or less time to mature",

depending on the conditions prior to the event. Some support for this possible delay can be

found in Tables 6.5 and 6.6, although, especially for weak events, the internal variations in the

system might be hard to separate from the signal. Nevertheless, the temporal consistency of the

signals throughout the events is remarkable with the NAO in the year +4 not being significant

less consistent than the year +3 or +2. This suggests that an orchestrated influence of volcanic

eruptions could extend over a longer time than would be expected from the atmospheric life time

of the aerosol alone. The volcanoes could therefore not only cause a spatially coherent signal in

areas influenced by modes like the NAO, but they might also build a certain memory by reset-

ting an internal mode in its oscillation. Since most internal modes exhibit typical time scales

for oscillations (*Defant,* 1924; *Mitchell,* 1976; *Mann and Park,* 1994, 1996), a resetting could therefore influence the climate beyond the initial perturbation. This 'mechanism' could be used to study the influence of single eruptions (as well as small and closely spaced groups of them) on the decadal climate variability. In fact, using the 25-year cumulative DVI anomaly, *Lamb* (1970) showed that the correlation with the decadal circulation indices over the North Atlantic is significant at the 1% level (note, this is ignoring the odd 1830s, see *Lamb* (1970) for explanation).

In conclusion, the response of the atmospheric circulation to the radiative perturbations from volcanoes is generally consistent between observations and the coupled model simulations. Thus, the results suggest that the NAO can orchestrate the spatial and, to some degree, the temporal evolution of the impact from volcanic perturbations, especially during the winter season. Yet, similar to the discussion of El Niño, the number of ensemble events used in this study is still small and the results should be taken with some caution. Further experiments are needed to evaluate this conclusion on the model side, and longer proxy series for the NAO should be evaluated

Chapter 7

SUMMARY AND

CONCLUSIONS

Stratospheric aerosol from explosive eruptions is an important player in natural climate variability. Although its forcing on the global, regional or local energy budget is relatively short lived, it can be large enough to cause a clearly identifiable effect on climate. Nevertheless, detailed studies of the impact of explosive volcanism on climate still face a host of complications and problems, even for the most recent times. Uncertainties in particle composition and sizes, the injection altitudes and regional stratospheric circulation, the speed of the removal process and interactions with upper tropospheric cirrus cloud formation or atmospheric chemical balances, are all components that need to be included at some level. Pessimistically, one might conclude that each eruption could be regarded as different. In this thesis, I have tried to find a level of generalization in the description of the volcanic forcing that offers a successful way for capturing the essentials of the volcanic forcing as well as its impact on climate. The following sections summarize the main conclusions from the proxy- and the model based approaches presented above. Instead of keeping the two lines separated, they are merged to highlight the current understand-

ing regarding the problem. It will be shown that by doing so, both approaches substantially contribute to gain further insight into the problem of identification of the level of generalization that might still be useful in paleoclimatic research. A summary of the remaining deficiencies and an outlook on possible pathways for their resolution is presented.

7.1 The volcanic record

Before looking at impacts of single events, we need to ask the question: Given the observational and indirect proxy records at hand, can we indeed build a useful time series of volcanic perturbations covering the recent past? Do we know when to search for an impact signal? Do we know which are the largest and climatically most important eruptions in the recent past? The answer to this question is not necessarily a confident yes, but rather a 'probably'. In general, our record of volcanic eruptions in the past few centuries is quite remarkable, with thousands of events recorded in the Smithsonian Catalogue. More recently, instead of focusing on the magnitude of an eruption as categorized in the catalogue, erupted sulfate has been identified as a better indicator for the eruption's potential climate impacts. This has put sulfate measurements in polar ice cores into the cross-hair for reconstructing climatically relevant past volcanic activity. The major problem to overcome here is that single ice cores suffer from noise in local depositional processes, and therefore cannot reliably record every single event. Compiling of data from many ice cores is currently the way to go, as averaging of the sulfate signal is more successful in representing past atmospheric loadings. Strong anthropogenic contamination in recent decades makes the detection and calibration of recent eruption signals difficult.

Despite significant improvements in recent years, several examples can be brought up to underline remaining uncertainty. We have strong evidence for the existence of a number of very large eruptions for which we still don't know the volcano of origin. This is especially the case for an enormous event in 1258 and the famous 'pre-Tambora' eruption in 1808. Additionally,

there is evidence for very large eruptions of volcanoes such as Long Island or Billy Mitchell, yet their date is still open and even rough associations are not clear. One has to conclude from this that we probably know about most, but not necessarily all large events. Symptomatic of this statement is the relatively recent recognition of Huaynaputina event of 1600 as one of the largest in the second millennium A.D. It is interesting to note that the primary hint for a reevaluation of this eruption (which was known to have happened before, but was classified as much smaller) came from studies of climate proxy data from tree rings. This symbolizes the way in which volcanologic, climatic and sometimes anthropologic proxies (plague, crop failures) can contribute to the study of volcanic influences on climate. It also points out that a host of fully independent data is available the can be used for cross-verification. The only danger that has to be omitted is not to introduce circulatory chains of argumentation. Although *Lamb* (1970) has received some criticism for including temperature information into his Dust Veil Index, if the proxy data is used in an *indicative* rather than a *quantitative* way, the above example underlines the value and importance of a multi-proxy approach to both the identification and analysis of past volcanic eruptions.

7.2   Radiative forcing

Injection and formation of particles in the lower stratosphere is the primary driver of the direct volcanic forcing. The impact on climate strongly depends on the magnitude and spectral distribution of the radiative forcing imposed by these particles. For simplicity, it can be broken down into two components: First, an increase in reflectance of the solar radiation by the volcanic particles results in a decrease in the direct solar beam hitting the ground. This effect is somewhat compensated for by an increase in the diffuse radiation. Second, the aerosol particles change the vertical absorption profile (SW and LW), which impacts the heating rates and therefore temperature. Since the increase in shortwave reflection is larger for most of the long lived (i.e. small)

particles than their capability to retain upwelling heat, the total climate system generally looses energy. A cooling will result.

7.2.1 Indications of atmospheric perturbations

Historically, strange atmospheric hazes and unusual optical phenomena have been documented. Observations of obscured sunlight or general haze that persists even after rainfall is often used to indicate that the location of the haze is above the tropopause. These perturbations can last for days, months or even years. The duration and spatial extent of these perturbations is important in order to make a case for a large volcanic eruption. A relatively small number of cases during the last 1000 years are documented extensively, but more isolated data exist for other cases. The largest events include the years 1258/9, 1452/3, 1600, 1783, 1815/6 and 1883/4. All of these years can easily be associated with very big volcanic eruptions, all of which have also left clear marks in form of sulfate deposits on the polar ice sheets. Additionally, all can be readily recognized in tree-ring datasets of the Northern Hemisphere (*Briffa et al.*, 1998).

From the identification of an event to the calculation of its forcing on climate, more information about the atmospheric cloud is needed. Sometimes, some information can be gained from observations directly, such as in cases when sunspots can be seen with bare eyes or if peculiar coloring of the moon is observed. Usually, a number of assumptions have to be accepted through which independent data can be evaluated. This often iterative procedure, in fact, is applied today in aerosol research. As the most promising continuous data, ice core recovered sulfate can offer a good way to estimate the volcanic cloud. Under the assumption of first order consistency in spread and deposition of the aerosols after formation in the stratosphere, the sulfate flux at the surface can be used to estimate the total sulfate mass of the aerosol cloud. Subsequently, assumptions about the particle sizes allow the computation of the resulting forcing. Again, intercomparison of independent estimates of particle mass as well as the magnitude and duration of optical perturbations are very helpful to bracket the volcanic cloud properties. At least for

the last 500 years, this seems possible.

7.2.2 Aerosol distribution in space and time

From the indication of an eruption and using mass estimates of the volcanic cloud, the spatial extent and its temporal evolution needs to be determined. While this is no problem in EBMs, where buildup and decay can be described easily, for GCMs a more sophisticated solution has to be found that reflects physical and dynamical characteristics of the atmospheric flow. Here, a simple parameterization has been proposed that fulfills these requirements. The aerosol cloud is given as the distribution of aerosol optical depth in the mid-visible ($\tau_{0.5}$ or τ_{vis}) which makes direct comparison with visually observed perturbations of atmospheric transmission possible. Note, this is equivalent to a description in terms of aerosol mass loading. Due to its simplicity of solely requiring a maximum aerosol optical depth (of mass) and the month in the year of eruption (if lacking, an intermediate month can be selected) to estimate the spatial evolution of the aerosol spread, the parameterization is well fitted to paleo applications. In this sense, paleo can be regarded as any time prior to the satellite time period starting in 1979. Using this simple approach, the construction of a homogeneous forcing dataset was presented. These data lack the dramatic changes in quality between different events and periods which are present in some commonly used datasets. Although some individual characteristics might be suppressed, this is a more consistent way of comparing the impact of eruptions through time.

7.2.3 Forcing evaluation

Based on the aerosol distribution and assuming a form and composition of the particles, the radiative forcing can be computed. *Lacis et al.* (1992) and *Hansen et al.* (1997) offered a simple estimate of the forcing (ΔF) given the optical depth in the mid-visible ($\tau_{0.5}$):

$$\Delta F[W m^{-2}] = 30 \times \tau_{0.5}$$

This or similar constant relationships have been used to estimate the volcanic forcing for experiments with EBMs (e.g.. *Andronova et al.*, 1999; *Crowley*, 2000). In GCMs, with full representation of radiative processes, the forcing can be computed in all spectral components allowing a much better spatial representation. Since forcing represents a change in the radiative balance at a specific location (IPCC uses the tropopause), it has to be separated from the daily noise of radiative changes which mostly arises from clouds. Since the cloud formation is not independent from the aerosol loading above (e.g.. suppression of convective activity below thick stratospheric layers), the computation of the aerosol forcing is not just spatially uniform but strongly varying. Additionally, full radiative transfer is the only way to vertically separate changes in SW and LW absorption and therefore its influence on the vertical heating profile. This effect is critical for the simulation of the strength of the polar vortex, which in turn drives a dynamic response leading to winter warming in high latitudes. EBMs cannot reproduce this effect. As shown by the influence of volcanic aerosol on the North Atlantic Oscillation, the impact from explosive volcanism is no longer purely radiative but contains a dynamic component as well. This fact makes GCMs a required tool if looking at spatial imprints of volcanic eruptions. This is also true for the separation of different forcings that have similar radiative but very different spatial imprints (*Pollack et al.*, 1993). On the global average level and given no low frequency effects from a single or series of large eruptions (for some hints suggesting otherwise see Chapter 4.6), the first order influence from aerosols, indeed, seems to be dominated by the radiation. Thus, EBMs are quite successful in estimating volcanic cooling on the globally averaged scale.

Due to all the above mentioned uncertainties, differences in the forcing result from radiative transfer calculations following an eruption can be substantial. Fortunately, the duration of the perturbations is usually short, so that the decadally averaged forcing estimates might be better (*Rind*, 1996). Probably the single largest remaining hurdle in order to better capture the impact of explosive eruptions is the evolving size distribution (see Chapter 6.3.3.

7.3 Climate impact

Due to a generally negative radiative balance imposed by the aerosol, the climate impact of volcanic aerosol clouds is expected to result in a cooling. The spatial extent, the magnitude and duration of this cooling is more difficult to capture. Even for some of the largest eruptions, such as Tambora in 1815, the detection of a signal is not without problems. Clearly, some areas and especially during some parts of the year, the impact seems to be readily recognizable. But this does not imply that each and every climatic time series therefore must exhibit a uniform signal. Large regional variations exist and dynamical effects in response to the radiative forcing can have opposite effects. In a climate model, the separation of a signal from noise is generally easier. The reason for this shows both the advantages and problems in the models. Accurate climate information is available at every grid cell, each number with quite homogeneous accuracy and stationarity in time. This is not necessarily the case in observations. Also, in models, one can run ensemble studies to increase the signal to noise ratio, a peculiar advantage of models over the single realization in the real world. But one also needs to critically look at the internal variability present in the models as compared to reality. It still seems that the models lack the range of variations and therefore possibly the full extent of feedbacks than enhance or suppress a signal. Prior to the instrumental record, the accuracy of the historical climate data might not match present day expectations, but careful reconstructions can nevertheless be used to describe past climatic evolutions. Despite open questions about the representation of certain frequencies, namely the low frequency component, they are often good enough to help evaluate model simulations. This is particularly the case for some regions of the globe, where high density and independently calibrated information is available. Again, a collaborative effort between proxy and model based studies, will be able to understand reality much better than isolated actions.

232

7.3.1 Global and hemispheric imprints

The most common studies on the effects of volcanism on climate focus on the impact of individual eruptions on the global average quantities of climate, mostly temperature. Since even today information from the southern hemisphere is scarce, most studies focus on the Northern Hemisphere or selected parts of it. Important is the temporal resolution, i.e. monthly, seasonal or annual averages. Warm season records are the best to recognize the volcanic cooling because winter temperatures, especially over the Northern Hemisphere continents, often show strong dynamical warming instead of radiative cooling. Therefore, compared to annual average temperatures, summer season indices of climate show a better correlation with the volcanic perturbations. Particularly well suited proxies are tree-rings, which might be sensitive to both average climate changes from direct radiative forcing as well as episodic disruptions of the otherwise relatively normal conditions.

This fact reveals itself in large differences in apparent sensitivity to volcanic eruptions through a quick inspection of changes in temperature reconstructions of the Northern Hemisphere by *Mann et al.* (1998), *Jones et al.* (1998), *Crowley* (2000) and *Briffa et al.* (1998) (or *Briffa et al.*, 2001). While the summer reconstructions from tree-rings contain a remarkable 'hit-list' of large eruptions, a clear identification of even some of the largest events is more difficult in the annual reconstruction of *Mann et al.* (1998). One reason for this effect could be the balancing winter warmings over the continents, or the representation of tropical and subtropical climates in *Mann et al.* (1998). Additionally, it should be tested if the spatial representation of large volcanic signals can be adequately sampled by the available proxy records in the reconstruction or if the lack of large volcanic signals in the calibration period neglects a separate response pattern which is then missing in the reconstruction based on primary modes of variability. Climate model output provides a chance to investigate this possibility.

The presented simulations capture a volcanic cooling. The insert in Figure 7.1 shows the clear
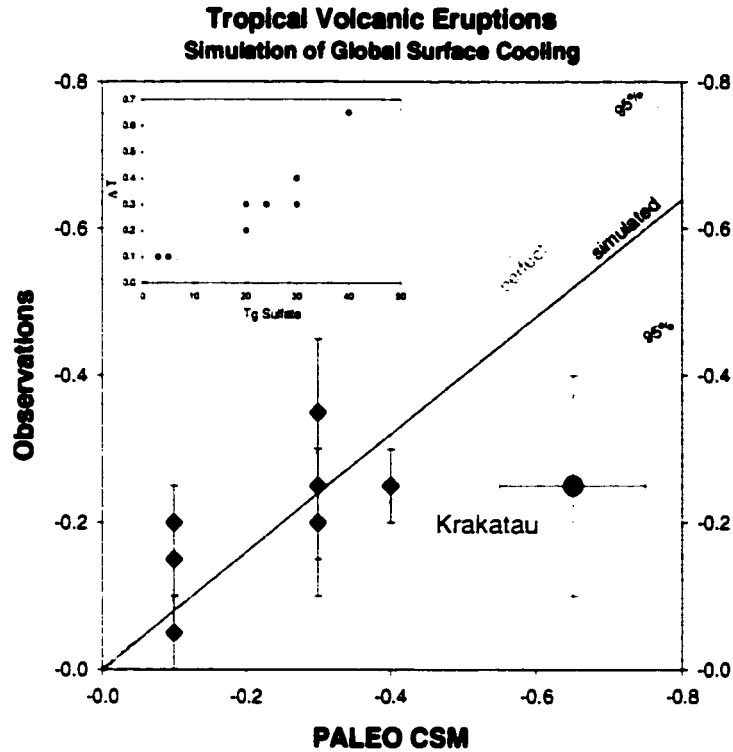
Figure 7.1: Comparison of temperature response to total sulfate loading for eruptions since 1870 in CSM simulation.

relationship between the sulfate loading and the temperature response under the assumption of a constant aerosol size distribution for the events in the 130-year simulation as compared with observations. The large Figure 7.1 plots the simulated temperature perturbation versus the observations for these eruptions. Error bars indicate roughly the uncertainty given by differences in observational datasets and the detection uncertainty of the signal out of the interannual noise. For the model, ensemble simulations are at this point only available for Krakatau.

The results agree well, if Krakatau is not included (see blue regression line). Only a slight over-prediction seems to occur. Krakatau, while clearly larger in every aspect than even Pinatubo, is not matched by a dramatic temperature signal in the observations. Only land temperatures do show a response (roughly 0.3-0.5), but ocean temperatures remain basically unchanged. In the

ensemble simulations. the forcing was implemented both when the model was heading into an El Niño or into a La Niña event. The difference in the global response is relatively small. and does not explain the difference with the observations. Given the restricted number of very large events in the simulated time period. this leads to a possible interpretation that with increasing sulfate loading the actual temperature perturbation falls. This could be explained through more efficient removal (e.g.. *Pinto et al.*. 1989) or. as shown in a sensitivity study. through further growth of the aerosol above one micron. The problem with this interpretation is that this contradicts the observations of atmospheric perturbations after Krakatau. Independent indications point to an almost persistent aerosol presence in the stratosphere for at least two years. A faster removal would not support this long duration. Additionally. not all Krakatau-sized eruptions lack a clear signal. Huaynaputina in 1600 and Parker in 1641 probably belong into the same group but both caused large temperature deviations as reconstructed by *Jones et al.* (1998) or *Briffa et al.* (1998). In fact. the reconstructed imprint is almost identical with the simulated signal of Krakatau. So what could it be that makes the signal of Krakatau look so different? *Rose et al.* (1995) suggested that caldera collapses at sea level would inject very large amounts of water vapor which could remove the sulfate more efficiently. Because of the long duration. again. the removal change does not seem to lead to a solution. But perhaps the concentration of the sulfuric acid was different (here the general assumption of 75% H_2SO_4 in 25% H_2O is used)? Could this large amount of water have caused the aerosol to freeze. which would significantly change the radiative properties and the response would very much look like the simulation with the large aerosol. The very first observation of noctilucent clouds follows the eruption of Krakatau by only two years. roughly the time needed for substances to get transported into the upper Mesosphere. Although a pure speculation at this point. this possibility should be investigated with appropriate middle atmosphere models. Overall. this eruption highlights where the problems remain for simulations of some of the eruptions. Other than that. the simulations are remarkably on target.

7.3.2 Regional patterns

The volcanic cooling is not spatially uniform. Already the radiative forcing is variable in space because of the local albedo, be it through surface characteristics or the presence of clouds. While the climate signal in some areas can be a direct response to the radiative perturbations, others see the largest change from dynamic responses. One such response is the general increase in Westerlies during the following winter time, causing warming at higher latitudes. While proxy data might suggest that several of the large natural modes of climate could be influenced, the North Atlantic Oscillation shows the strongest tendency following volcanic eruptions since 1870. This response can only be found in GCMs that can capture the dynamics and spatial structure of the NAO. The model agrees well with early works by *Defant* (1924) and *Lamb* (1970).

7.3.3 Meridional gradients

It has been suggested that reductions in the meridional temperature gradient are responsible for the dynamic effects on climate (*Pollack et al.*, 1993). The argument was that the tropics would cool immediately after the eruption while the high-latitudes would not yet see a signal. This decreases the temperature gradient and therefore the Westerlies. In the simulations, and supported by observations since 1870, this indeed can be seen, although for a very short time span of a few months after the eruptions. Already in the first winter following the eruption, the aerosol transport to the higher latitudes causes the lower stratospheric temperatures to rise enough to increase the temperature gradient at these altitudes. This in return causes a stronger polar vortex which reduces heat transport into the polar areas and deflects vertically propagating waves southward. Both effects cause further cooling over the poles which is only interrupted by some sudden stratospheric warmings. Thus, the concept of a reduced temperature gradient causing weaker Westerlies only holds for the early phase after the eruption, later dynamical effects higher up in the lower stratosphere guide a strengthened atmospheric flow. While in winter this causes

warming in high-latitudes where the temperature depends mostly on the advective component. in summer this enhanced flow could suppress the radiative heating normally taking place and some strong waves could be responsible for some of the cold air outbreaks (see below, Figure 7.2).

7.3.4 Vertical structure

Recent satellite observations, confirmed in the simulations, showed not only a seasonal structure in the climate response over large spatial scales, but the critical vertical differences mentioned above. In addition to the warming above and the cooling below the aerosol layer, a separation was found between the lower and the upper troposphere. The strongest cooling was found at 300-400 hPa, not at the surface. The reason for this is probably twofold. First, the large heat capacity of the ocean helps buffer the episodic radiative cooling at the surface. Second, the impact on the hydrologic cycle, which was shown to slow down very quickly, causes less water vapor and with it less latent heat to be transported into the mid to upper troposphere, enhancing the cooling. The combined effect results in a almost 50% larger signal at 300 hPa than at the surface, particularly in the tropics.

7.3.5 Single versus sequences of events

Based on a compilation of ice core sulfate data, and assuming stationarity in the depositional processes of stratospheric sulfate, a variation in the frequency of large volcanic events was presented. Interestingly, the periods with a higher frequency of events mostly correspond to cooler time intervals. A link between closely spaced eruptions and temperature has been suggested before, but not with the presented regularity. Whatever this is, an artefact or not, an improved volcanic record has to be established that will also include the magnitude of the events. We also need to independently evaluate the climate indices of these decades to determine if they indeed contain the right low frequency trends. Recently, a new temperature reconstruction based on

tree-rings by *Briffa et al.* (2001), which now conserves the low frequency component of climate better than before, suggests clear correlations with volcanic episodes. Should this variation in explosive volcanism indeed hold up, the implications would be quite dramatic for current estimates of the solar irradiance changes (see below).

The modeling results confirm that periods with higher volcanic loading do indeed see a general cooling. This was the case early in the 20th-Century and again since the mid 1960s, where the temperatures remain almost 0.2 $^\circ$C colder than normal.

7.4 Problems and future directions

Similar to the conclusions by *Lacis et al.* (1992), the sulfate mass, and (assuming a intermediate size distribution) the visible optical depth, very effectively describe the radiative forcing of a volcanic aerosol cloud. For a small number of events, namely Krakatau during the investigation period, this approach seems to fail. Particularly for these big events it would be important to have a better understanding of the evolution of sulfuric acid droplets in terms of their size and composition. Other such events have to be identified and their characteristics have to be compared. *Kondratyev* (1999) summarized it nicely:

> "Also, it is necessary to develop both theoretical and empirical models of the processes
>
> of formation, evolution, and removal from the atmosphere of aerosol particles, as well
>
> as various models of their size distribution and optical characteristics."

What are the directions in both the proxy and modeling approaches that would shed further light on the problem?

7.4.1 Further improvements in observational and proxy records

As repeatedly pointed out, tree rings seem to be the most sensitive climate proxy for identifying large volcanic eruptions. But how exactly is the tree ring response generated? Which component
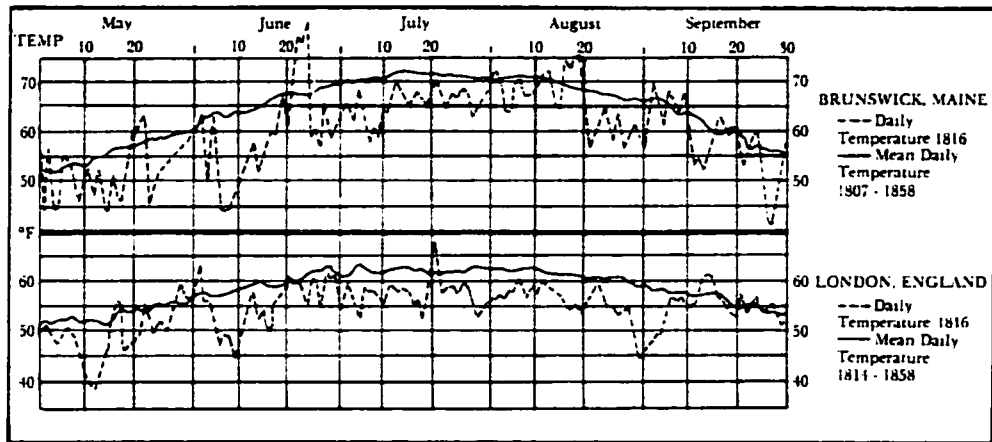
Daily and mean daily temperatures in Brunswick, Maine, and London, England, in 1816 and in the early 19th century.

Figure 7.2: Temperature evolution in New England during the summer 1816. which is commonly referred to as the 'Year without a Summer' (source: *Stommel and Stommel,* 1983).

of the climatic signal causes most of the tree ring signatures? Clearly, frost rings suggest rapid temperature drops during the warm season. But can monthly average temperatures from model simulations capture this signal or are daily data fields required? One such example is shown in Figure 7.2. Three episodes of unusual coldness occurred during the 'Year without a Summer' in New-England, each documented with frost events at the height of summer. Other weeks were rather normal and warm.

More generally, we need more quantitative ways to extract a volcanic signal from the proxy data. How can we separate the signal from local or interannual noise? *Naveau et al.* (in prep.) use a statistical technique for identifying pulse like perturbations in temperature series. Interestingly, their conclusions agree well with the simulation results: only large eruptions have a distinguishable impact on climate. But what is the contribution of the small events for which an individual signal is not that easy to detect? Are they responsible for helping drag out the signal?

Comparative studies between different proxy reconstructions should be undertaken to evaluate if the spatial or temporal estimation techniques are robust against the unusual perturbations from

volcanic eruptions that are more binary in nature rather than continuous.

On the event detection side, clearly, most promising efforts focus on ice cores. Could we identify all large volcanic eruptions during the last 500 years using chemical fingerprinting technique? This would increase our confidence in the separation between tropical events which impact the climate much more strongly than high latitude eruptions.

7.4.2 Limitations in current model approach

The current approach of prescribing the atmospheric loading using a simple seasonality parameterization seems to work reasonably well. The exception is Krakatau. Because it is the largest event in the investigated period, the simple concept of a fixed size distribution needs to be revisited. Could it be that with increasing sulfate mass also the particle growth is enhanced? A study using a model with full atmospheric chemistry would clearly help to find what the range in size distribution and composition could be that still would fit with observations.

A feedback not included in the model concerns the possible indirect effect on clouds. It has been proposed that settling volcanic aerosol could influence the Cirrus cloud cover (*Jensen and Toon*, 1992; *Sassen*, 1992; *Minnis et al.*, 1993). The net-radiative effect of Cirrus could reach as much as 8 Wm^{-2}! Additionally to the radiative influence, *Humphreys* (1940) and *Wexler* (1951a, 1956) suggested that the aerosol would also change the cloud efficiency to produce precipitation. *Portman and Gutzler* (1996) expect the large scale dynamic responses to change precipitation more than the aerosols themselves.

Also neglected in the model are any chemical feedbacks. How does volcanic aerosol impact the ozone concentrations and distribution? At least for Pinatubo, large reductions were found. Again, a coupling to an atmospheric chemistry model would be helpful.

A further deficit in the simulations presented is the limited vertical resolution in the model stratosphere. *Shindell et al.* (1999) showed that a high resolution is important for simulating ozone perturbations. Though it is currently unclear to what degree a resolution of the QBO

could impact the results, given that our aerosol spread is currently prescribed and not directly dynamically affected by zonal and meridional flow in the stratosphere.

In comparison to observations, the volcanic signal can be seen quite easily in models. As mentioned above, this points to a remaining deficiency in climate models: too small internal variability. The NCAR CSM has strongly improved its internal variability, but might still not capture the full natural spectrum. The statistical method proposed by *Naveau et al.* (in prep.) might help to quantify the difference for signal to noise ratio of volcanic eruptions.

Finally, another question not studied here is whether the signal changes if the same forcing is imposed on a different background climate. This would help in understanding if we can directly compare volcanic signals during a period such as the Maunder Minimum with the recent Pinatubo eruption.

7.5 Current potential of capturing the external forcing from explosive volcanism

The study of the effects of volcanic eruptions on climate has come a long way since the early works of *Humphreys* (1913) and *Lamb* (1970). Despite remaining issues, evidence accumulates that volcanoes contribute significantly to natural climate variability. The impact of Pinatubo (0.5 °C, although only for a short time) is comparable with the overall warming in most of the 20th-Century. No internal mechanism can cause such dramatic perturbations on such short time periods, at least not during the last Millennium.

Using a simple approach for the description of the spatial distribution and evolution of the volcanic aerosol together with a simple estimate of the particle size distribution, the description of forcing as well as the resulting climate impact look very reasonable. On a global average, the problem is to the first order a radiative balance question. Spatial effects and seasonal variations, maybe down to the daily scale, can only be done in the most sophisticated models. If one can make

use of the variety of proxy information and cross-evaluate them with the dynamic understanding gained from the climate system response in the model, a clearer picture emerges. Conversely, the critical evaluation of the models is not only valuable but crucial, particularly because these models are used for future forcasting of global warming. This thesis was an attempt to introduce such a collaborative effort.

Bibliography

Abbot, C., 1902: The relation of the sun-spot cycle to meteorology. *Monthly Weather Review,* *30,* 178–181.

Abbot, C., 1903: Recent studies on the solar constant of radiation. *Monthly Weather Review,* *31,* 587–592.

Abbot, C., F. Fowle, and L. Aldrich, 1922: *Solar constant and atmospheric transmission at Mount Wilson, 1912 to 1920.* Smithsonian Institution, Washington D.C., vol. 4 of *Annals of the Astrophysical Observatory of the Smithsonian Institution,* pp. 129–145. .

Abbot, C., L. Aldrich, and F. Fowle, 1932: *Annals of the Astrophysical Observatory of the Smithsonian Institution.* Smithsonian Institution, Washington D.C., vol. 5, p. 295. .

Agresti, A., 1990: *Categorical Data Analysis.* Wiley series in probability and mathematical statistics, John Wiley and Sons, Inc. New-York.

Allan, R. J., J. Lindesay, and D. E. Parker, 1996: *El Niño Southern Oscillation and climatic variability.* CSIRO, Australia.

Ammann, C., and P. Naveau, 2001: Multi-decadal periodicity in tropical explosive volcanism and its influence on climate. *submitted.*

Andreae, M., and P. Crutzen, 1997: Atmospheric aerosols: Biogeochemical sources and role in atmospheric chemistry. *Science,* *276,* 1052–1058.

Andronova. X.. and M. Schlesinger. 2000: Causes of global temperature changes during the 19th and 20th century. *Geophysical Research Letters*, 27(14), 2137–2140.

Andronova. X. G., E. V. Rozanov. F. Yang, M. E. Schlesinger, and G. L. Stenchikov, 1999: Radiative forcing by volcanic aerosols from 1850 to 1994. *Journal of Geophysical Research*, 104(D14), 16807–16826.

Angell. J. K., 1997a: Estimated impact of Agung, El Chichón and Pinatubo volcanic eruptions on global and regional total ozone after adjustment for the QBO. *Geophysical Research Letters*, 24(6), 647–650.

Angell. J. K., 1997b: Stratospheric warming due to Agung, El Chichón, and Pinatubo taking into account the Quasi-Biennial Oscillation. *Journal of Geophysical Research*, 102(D8), 9479–9485.

Appenzeller. C., T. F. Stocker, and M. Anklin. 1998: North Atlantic Oscillation dynamics recorded in Greenland ice cores. *Science*, 282, 446–449.

Baillie. M. G. L., 1994: Dendrochronology raises question about the nature of the AD 536 dust-veil event. *The Holocene*, 4, 212–217.

Baker. B., W. R. Kuhn, and E. Ryznar, 1984: Effects of the El Chichón volcanic cloud on direct and diffuse solar irradiances. *Journal of Climate and Applied Meteorology*, 23, 449–452.

Baldwin. B., J. B. Pollack, A. Summers, O. B. Toon, C. Sagan, and W. van Camp, 1976: Stratospheric aerosol and climatic change. *Nature*, 263, 551–555.

Barnett. T., B. Santer, P. Jones, R. Bradley, and K. Briffa, 1996: Estimates of low frequency natural variability in near-surface air temperature. *The Holocene*, 6, 255–263.

Barth. C., R. Sanders, R. Thomas, G. Thomas, B. Jakosky, and R. West, 1983: Formation of the El Chichón aerosol cloud. *Geophysical Research Letters*, 10(11), 993–996.

Barth. M. C.. P. J. Rasch. J. T. Kiehl. C. M. Benkovitz. and S. E. Schwartz. 2000: Sulfur chemistry in the National Center for Atmospheric Research Community Climate Model: Description. evaluation. features. and sensitivities to aqueous chemistry. *Journal of Geophysical Research. 105*(D1). 1387-1415.

Bertrand. C.. J.-P. van Ypersele. and A. Berger. 1999: Volcanic and solar impacts on climate since 1700. *Climate Dynamics. 15.* 355-367.

Bishop. S.. 1884: The remarkable sunsets. *Nature. 29.* 259-260.

Blong. R. J.. 1982: *The time of darkness. Local legends and volcanic reality in Papua New Guinea.* University of Washington Press. Seattle and London.

Bluth. G. J. S.. S. D. Doiron. C. C. Schnetzler. A. J. Krueger. and L. S. Walter. 1992: Global tracking of the SO_2 clouds from the June. 1991 Mount Pinatubo eruptions. *Geophysical Research Letters. 19.* 151-154.

Bluth. G. J. S.. C. C. Schnetzler. A. J. Krueger. and L. S. Walter. 1993: The contribution of explosive volcanism to global atmospheric sulphur dioxide concentrations. *Nature. 366.* 327-329.

Bluth. G. J. S.. W. I. Rose. I. E. Sprod. and A. J. Krueger. 1997: Stratospheric loading of sulfur from explosive volcanic eruptions. *The Journal of Geology. 105.* 671-683.

Bohren. C. F.. and D. R. Huffman. 1983: *Absorption and scattering of light by small particles.* John Wiley and Sons.

Bonan. G.. 1998: The land surface climatology of the NCAR land surface model coupled to the NCAR Community Climate Model. *Journal of Climate. 11*(6). 1307-1326.

Boutron, C., 1980: Respective influence of global pollution and volcanic eruptions on the past variations of the trace metals content of Antarctic snows since 1880's. *Journal of Geophysical Research*, *85*(C12), 7426-7432.

Boville, B., and P. Gent, 1998: The NCAR Climate System Model, version one. *Journal of Climate*, *11*(6), 1115-1130.

Boville, B., J. Kiehl, P. Rasch, and F. Bryan, 2001: Improvements to the NCAR CSM-1 for transient climate simulations. *Journal of Climate*, *14*, 164-179.

Boville, B. A., J. R. Holton, and P. W. Mote, 1991. Simulation of the Pinatubo aerosol cloud in general circulation model. *Geophysical Research Letters*, *18*, 2281-2284.

Bradley, R., 2000: 1000 years of climate change. *Science*, *288*, 1353-1355.

Bradley, R., and P. Jones, 1993: 'Little Ice Age' summer temperature variations: Their nature and relevance to recent global warming trends. *The Holocene*, *3*, 367-376.

Bradley, R., and P. Jones (eds.), 1995a: *Climate since A.D. 1500*. Routledge, London and New York, 2. edn.

Bradley, R., and P. Jones, 1995b: Records of explosive volcanic eruptions over the last 500 years, pp. 606-622, in: *Bradley and Jones* (1995a).

Bradley, R. S., 1988: The explosive volcanic eruption signal in Northern Hemisphere continental temperature records. *Climatic Change*, *12*, 221-243.

Bradley, R. S., and J. England, 1978a: Influence of volcanic dust on glacier mass balance at high latitudes. *Nature*, *271*, 736-738.

Bradley, R. S., and J. England, 1978b: Recent climatic fluctuations of the Canadian High Arctic and their significance for glaciology. *Arctic and Alpine Research*, *10*, 715-731.

Braitseva. O. A., I. V. Melekestsev. V. V. Ponomareva, and V. Y. Kirianov, 1996: The caldera-forming eruption of Ksudach volcano about cal. A.D. 240: the greatest explosive event of our era in Kamchatka. Russia. *Journal of Volcanology and Geothermal Research, 70*, 49-65.

Bray. J. R., 1976: Volcanic triggering of glaciation. *Nature, 260*, 414-415.

Briegleb. B., and D. Bromwich. 1998a: Polar climate simulation of the NCAR CCM3. *Journal of Climate, 11*(6), 1270-1286.

Briegleb. B., and D. Bromwich. 1998b: Polar radiation budgets of the NCAR CCM3. *Journal of Climate, 11*(6), 1246-1269.

Briegleb. B. P., 1992: Delta-Eddington approximation for solar radiation in the NCAR Community Climate Model. *Journal of Geophysical Research, 97*(D7), 7603-7612.

Briffa. K., T. J. Osborn. F. Schweingruber. I. C. Harris. P. Jones. S. G. Shiyatov, and E. A. Vaganov. 2001: Low-frequency temperature variations from a northern tree ring density network. *Journal of Geophysical Research, 106*(D3), 2929-2941.

Briffa. K. R., P. D. Jones. F. H. Schweingruber, and T. J. Osborn. 1998: Influence of volcanic eruptions on Northern Hemisphere summer temperature over the past 600 years. *Nature, 393*, 450-455.

Brock. C. A., et al., 1993: Relationship between optical extinction. backscatter and aerosol surface and volume in the stratosphere following the eruption of Mt. Pinatubo. *Geophysical Research Letters, 20*, 2555-2558.

Broecker. W. S., 1997: Thermohaline circulation. the achilles heel of our climate system: Will man-made CO_2 upset the current balance?. *Science, 278*, 1582-1588.

Bryan. F., 1998: Climate drift in a multicentury integration of the NCAR Climate System Model. *Journal of Climate, 11*(6), 1455-1471.

Bryan. F.. B. Kauffman. W. Large. and P. Gent. 1997: *The NCAR CSM Flux Coupler*. NCAR. NCAR/TN-424+STR.

Bryan. K.. 1984: Accelerating the convergence to equilibrium of ocean climate models. *Journal of Physical Oceanography. 14.* 666-673.

Budyko. M.. 1969: The effect of solar radiation variations on the climate of the earth. *Tellus. 21.* 611-619.

Budyko. M.. and Z. Pivovarova. 1967: Effect of volcanic eruptions on solar radiation arriving on the earth's surface. *Meteorologya y Gidrologiya. 10.* 3-7.

Bullard. F. M.. 1976: *Volcanoes of the Earth*. University of Texas Press. Austin and London.

Cadle. R. D.. C. S. Kiang. and J.-F. Louis. 1976: The global scale dispersion of eruption clouds from major volcanic eruptions. *Journal of Geophysical Research. 81(18).* 3125-3132.

Capone. L. A.. O. B. Toon. R. C. Whitten. R. P. Turco. C. A. Riegel. and K. Santhanam. 1983: A two-dimensional model simulation of the El Chichón volcanic eruption cloud. *Geophysical Research Letters. 10.* 1053-1056.

Capotondi. A.. and W. R. Holland. 1998: *Thermohaline circulation variability in the NCAR Climate System Model (CSM)*. National Center for Atmospheric Research. p. 58pp.. NCAR/TN-445-STR.

Castleman. A. W.. H. R. Munkelwitz. and B. Manowitz. 1974: Isotopic studies of the sulfur component of the stratospheric aerosol layer. *Tellus. 26.* 222-234.

Cess. R.. et al.. 1995: Absorption of solar radiation by clouds: Observations versus models. *Science. 267.* 496-499.

Charlson. R.. J. Lovelock. M. Andreae. and S. Warren. 1987: Oceanic phytoplankton. atmospheric sulphur. cloud albedo and climate. *Nature. 326.* 655-661.

Charlson. R.. S. Schwartz. J. Hales. R. Cess. J. Coakley. J. Hansen. and D. Hofmann. 1992: Climate forcing by anthropogenic aerosols. *Science*. *255*. 423–430.

Chenoweth. M.. 1996: Ships' logbooks and "the year without a summer". *Bulletin of the American Meteorological Society*. *77*. 2077–2093.

Chou. M.-D.. and M. J. Suarez. 1994: *An efficient thermal infrared radiation parametrization for use in general circulation models*. NASA. vol. 3. p. 85pp.. 104606 - [NTIS N-95-15745].

Chou. M.-D.. K.-T. Lee. S.-C. Tsay. and Q. Fu. 1999: Parametrization for cloud longwave scattering for use in atmospheric models. *Journal of Climate*. *12*. 159–169.

Chylek. P.. G. Videen. D. Ngo. R. Pinnick. and J. Klett. 1995: Effect of black carbon on the optical properties and climate forcing of sulfate aerosol. *Journal of Geophysical Research*. *100*(D8). 16325–16332.

Clausen. H. B.. and C. U. Hammer. 1988: The Laki and Tambora eruptions as revealed in Greenland ice cores from 11 locations. *Annals of Glaciology*. *10*. 16–22.

Clausen. H. B.. C. U. Hammer. C. S. Hvidberg. D. Dahl-Jensen. J. P. Steffensen. J. Kipfstuhl. and M. Legrand. 1997: A comparison of volcanic records over the past 4000 years from the Greenland Ice Core Project and Dye 3 Greenland ice cores. *Journal of Geophysical Research*. *102*(C12). 26707–26723.

Clemesha. B.. and D. Simonich. 1984: Lidar observations of the El Chichón aerosol at a southern latitude station. *Geofísica Internacional*. *23*(2). 289–297.

Coakley. J.. and R. Cess. 1985: Response of the NCAR Community Climate Model to the radiative forcing by the naturally occurring tropospheric aerosol. *Journal of the Atmospheric Sciences*. *42*(16). 1677–1692.

Coakley. J., R. Cess. and F. Yurevich. 1983: The effect of tropospheric aerosol on the Earth's radiation budget: A parameterization for climate models. *Journal of the Atmospheric Sciences*. *40*, 116–138.

Cole. J. E., R. G. Fairbanks. and G. T. Shen. 1993: Recent variability in the Southern Oscillation: Isotopic results from a Tarawa Atoll coral. *Science*. *260*, 1790–1793.

Cole-Dai. J., and E. Mosley-Thompson. 1999: The Pinatubo eruption in South Pole snow and its potential value to ice-core paleovolcanic records. *Annales of Glaciology*. *29*(99-105).

Cole-Dai. J., E. Mosley-Thompson. and L. G. Thompson. 1997a: Annually resolved southern hemisphere volcanic history from two Antarctic ice cores. *Journal of Geophysical Research*. *102*(D14), 16761–16771.

Cole-Dai. J., E. Mosley-Thompson. and L. G. Thompson. 1997b: Quantifying the Pinatubo volcanic signal in south polar snow. *Geophysical Research Letters*. *24*, 2679–2682.

Cole-Dai. J., E. Mosley-Thompson. S. Wight. and L. Thompson. 2000: A 4100-year record of explosive volcanism from an East Antarctica ice core. *Journal of Geophysical Research*. *105*(D19), 24431–24441.

Collins. W., 2001: Effects of enhanced shortwave absorption on coupled simulations of the tropical climate system. *Journal of Climate*. *14*, 1147–1165.

Cook. E., and L. Kairiukstis (eds.). 1990: *Methods of Dendrochronology: Applications in the Environmental Sciences*. Kluwer. Dordrecht.

Cornu. A., 1885: Observations relatives à la couronne visible actuaellement autour du soleiel. *J. Phys. Theor. Appl.*, *4*, 53–59.

Crowley. T. J., 2000: Causes of climate change over the past 1000 years. *Science*. *289*, 270–277.

Crowley, T. J., and K.-Y. Kim. 1999: Modeling the temperature response to forced climate change over the last six centuries. *Geophysical Research Letters, 26,* 1901–1904.

Crowley, T. J., T. Quinn, F. Taylor, C. Henin, and P. Joannot. 1997: Evidence for a volcanic cooling signal in a 335-year coral record from New Caledonia. *Paleoceanography, 12,* 633–639.

Crutzen, P. J., 1976: The possible importance of cso for the sulfate layer of the stratosphere. *Geophysical Research Letters, 3*(2), 73–76.

Currie, R. G., 1994: Luni-solar 18.6 and 10-11-year solar cycle signals in H.H. Lamb's Dust Veil Index. *International Journal of Climatology, 14,* 215–226.

Dai, A., I. Fung, and A. Del Genio. 1997: Surface observed global land precipitation variations during 1900-88. *Journal of Climate, 10,* 2943–2962.

Dai, J., E. Mosley-Thompson, and L. G. Thompson. 1991: Ice core evidence for an explosive tropical volcanic eruption 6 years preceding Tambora. *Journal of Geophysical Research, 96,* 17361–17366.

D'Arrigo, R. D., and G. C. Jacoby. 1999: Northern North American tree-ring evidence for regional temperature changes after major volcanic events. *Climatic Change, 41,* 1–15.

D'Arrigo, R. D., E. R. Cook, G. C. Jacoby, and K. R. Briffa. 1993: NAO and sea surface temperature signatures in tree-ring records from the North Atlantic sector. *Quaternary Science Reviews, 12,* 431–440.

De Angelis, M., and M. Legrand. 1994: Origins and variations of fluoride in Greenland precipitation. *Journal of Geophysical Research, 99*(D1), 1157–1172.

De Angelis, M., L. Fehrenbach, C. Jhanno, and M. Maurette. 1985: Micrometre-sized volcanic glasses in polar ices and snows. *Nature, 317,* 52–54.

de Silva. S. L.. and G. A. Zielinski. 1998: Global influence of the AD 1600 eruption of Huayna-
putina. Peru. *Nature. 393*, 455–458.

Decker, R.. and B. Decker. 1991: *Mountains of fire: The nature of volcanoes*. Cambridge Uni-
versity Press. Cambridge. USA.

Defant. A.. 1924: Die Schwankungen der atmosphärischen Zirkulation über dem nordatlantischen
Ozean im 25-jährigen Zeitraum 1881-1905. *Geografiska Annaler. 6*, 13–41.

Deirmendjian. D.. 1069: *Electromagnetic scattering on spherical polydispersions*. Elsevier. New
York.

Deirmendjian. D.. 1973: On volcanic and other particulate turbidity anomalies. *Advances in
Geophysics. 16*, 267–296.

Delfin. Francisco G.. J.. C. G. Newhall. M. L. Martinez. N. D. Salonga. F. E. B. Bayon. D. Trim-
ble. and R. Solidum. 1997: Geological. ^{14}C. and historical evidence for a 17th-Century eruption
of Parker Volcano. Mindanao. Philippines. *Journal of the Geologic Society of the Philippines.
LII*(1). 25–42.

Delmas. R. J.. M. Legrand. A. J. Aristarain. and F. Zanolini. 1985: Volcanic deposits in Antarctic
snow and ice. *Journal of Geophysical Research. 90*(D7). 12901–12920.

Delmas. R. J.. S. Kirchner. J. M. Palais. and J.-R. Petit. 1992: 1000 years of explosive volcanism
recorded at the South Pole. *Tellus. 44B*. 335–350.

DeLuisi. J. J.. E. Dutton. K. Coulson. T. DeFoor. and B. Mendonca. 1983: On some features of
the El Chichón volcanic stratospheric dust cloud and a cloud of unknown origin observed at
Mauna Loa. *Journal of Geophysical Research. 88*(C11). 6769–6772.

Delworth. T. L.. and M. E. Mann. 2000: Observed and simulated multidecadal variability in the
North Atlantic. *Climate Dynamics. 16*. 661–676.

Deshler. T.. J. Liley. G. Bodeker. W. Matthews. and D. Hofmann. 1997: Stratospheric aerosol following Pinatubo. comparison of the north and south mid latitudes using in situ measurements. *Advances in Space Research. 20*(11). 2089–2095.

Devine. J. D.. H. Sigurdsson. A. N. Davis. and S. Self. 1984: Estimates of sulfur and chlorine yield to the atmosphere from volcanic eruptions and potential climatic effects. *Journal of Geophysical Research. 89*(B7). 6309–6325.

Di Donfrancesco. G.. A. Adriani. G. P. Gobbi. and F. Cairo. 2000: Lidar observations of the stratospheric aerosol during 1993 above McMurdo Station. Antarctica. *Journal of Atmospheric and Solar-Terrestrial Physics. 62.* 713–723.

Diaz. H.. and V. Markgraf (eds.). 2000: *El Niño and the Southern Oscillation. Multiscale variability and global and regional impacts.* Cambridge University Press.

Dibb. J. E.. and S. I. Whitlow. 1996: Recent climate anomalies and their impact on snow chemistry at South Pole. 1987 - 1994. *Geophysical Research Letters. 23.* 1115–1118.

Donabasoglu. G.. 1998: On the wind-driven circulation of the uncoupled and coupled NCAR Climate System Ocean Model. *Journal of Climate. 11.* 1442–1454.

Doney. S.. W. Large. and F. Bryan. 1998: Surface ocean fluxes and water-mass transformation rates in the coupled NCAR Climate System Model. *Journal of Climate. 11*(6). 1420–1441.

Dunbar. R.. G. Wellington. M. Colgan. and P. Glynn. 1994: Eastern Pacific sea surface temperature since 1600 A.D.: The δ^{18}O record of climate variability in Galapagos corals. *Paleoceanography. 9*(2). 291–315.

Dutton. E.. P. Reddy. S. Ryan. and J. DeLuisi. 1994: Features and effects of aerosol optical depth observed at Mauna Loa. Hawaii: 1982-1992. *Journal of Geophysical Research. 99*(D4). 8295–8306.

Dutton, E. G., and B. Bodhaine, 2001: Solar irradiance anomalies caused by clear-sky transmission variations above Mauna Loa: 1958-99. *Journal of Climate, 14*, 3255-3262.

Dutton, E. G., and J. R. Christy, 1992: Solar radiative forcing at selected locations and evidence for global lower tropospheric cooling following the eruptions of El Chichón and Pinatubo. *Geophysical Research Letters, 19*(23), 2313-2316.

Dutton, E. G., and J. J. DeLuisi, 1983: Spectral extinction of direct solar radiation by the El Chichón cloud during December 1982. *Geophysical Research Letters, 10*, 1013-1016.

Dyer, A., 1974: The effect of volcanic eruptions on global turbidity, and an attempt to detect long-term trends due to man. *Quart. J. R. Met. Soc., 100*, 563-571.

Dyer, A. J., and B. B. Hicks, 1965: Stratospheric transport of volcanic dust inferred from solar radiation measurements. *Nature, 208*, 131-133.

Dyer, A. J., and B. B. Hicks, 1968: Global spread of volcanic dust from the Bali eruption of 1963. *Quart.J.R.Met.Soc., 94*, 545-554.

Enger, I., and S. Fritz, 1956: Opacity of the sky after July 1953. *Monthly Weather Review*, (Aug.), 301-304.

Eparvier, F. G., D. W. Rusch, R. T. Clancy, and G. E. Thomas, 1994: Solar Mesosphere Explorer satellite measurements of El Chichón stratospheric aerosols. 2. Aerosol mass and size parameters. *Journal of Geophysical Research, 99*(D10), 20533-20544.

Espindola, J. M., J. L. Macas, R. I. Tilling, and M. F. Sheridan, 2000: Volcanic history of El Chichón Volcano (Chiapas, Mexico) during the Holocene, and its impact on human activity. *Bulletin of Volcanology, 62*, 90-104.

Evans, W. F. J., and J. B. Kerr. 1983: Estimates of the amount of sulphur dioxide injected into the stratosphere by the explosive volcanic eruptions: El Chichón. Mystery Volcano. Mt. St. Helens. *Geophysical Research Letters*. *10*. 1049-1051.

Fagan, B. M.. 1999: *Floods. Famines, and Emperors : El Niño and the Fate of Civilizations*. Basic Books, New York.

Fahey, D. W., et al., 1993: In situ measurements constraining the role of sulphate aerosols in mid-latitude ozone depletion. *Nature*. *363*. 509-514.

Fiacco, R. Joseph, J., T. Thordarson, M. S. Germani, S. Self. J. M. Palais, S. Whitlow, and P. M. Grootes. 1994: Atmospheric aerosol loading and transport due to the 1783-84 Laki eruption in Iceland, interpreted from ash particles and acidity in the GISP2 ice core. *Quaternary Research*, *42*. 231-240.

Fiocco, G., D. Fuà, and G. Visconti (eds.). 1996: *The Mount Pinatubo Eruption. Effects on the atmosphere and climate*. vol. I 42 of *NATO ASI*. Springer Verlag, Berlin Heidelberg.

Fisher, D., and R. Koerner. 1994: Signal and noise in four ice-core records from the Agassiz ice cap, Ellesmere Island, Canada. Details of the last Millennium for stable isotopes, melt and solid conductivity. *The Holocene*, *4*. 113-120.

Fisher, W. J., 1924: The brightness of lunar eclipses 1860-1922. *Smithsonian Miscellaneous Collections*, *76(9)*, 1-61.

Flammarion, C., 1884: L'éclipse totale de lune du 4 Octobre. *L'Astronomie*, *3*, 401-408.

Flowers, E. C., and H. J. Vierbrock. 1965: Solar radiation: An anomalous decrease of direct solar radiation. *Science*, *148*, 493-494.

Franklin, B., 1785: Meteorological imaginations and conjectures. *Mem. Lit. Phil. Soc. Manchester*, *2*, 357-361.

Friis-Christensen. E.. and K. Lassen. 1991: Length of the solar cycle: An indicator of solar activity closely associated with climate. *Science.* *254.* 698–700.

Fröhlich. C.. and J. Eddy. 1984: Observed relation between solar luminosity and radius. *Advances in Space Research.* *4*(8). 121–124.

Gagan. M.. and A. Chivas. 1995: Oxygen isotopes in western Australian coral reveal Pinatubo aerosol-induced cooling in the Western Pacific warm pool. *Geophysical Research Letters.* *22*(9). 1069–1072.

Genin. A.. B. Lazar. and S. Brenner. 1995: Vertical mixing and coral death in the Red Sea following the eruption of Mount Pinatubo. *Nature.* *377.* 507–510.

Gent. P.. F. Bryan. G. Danabasoglu. S. Doney. W. Holland. W. Large. and J. McWilliams. 1998: The NCAR Climate System Model global ocean component. *Journal of Climate.* *11*(6). 1287–1306.

George. E. I.. 2000: The variable selection problem. *Journal of the American Statistical Association.* *95.* 1304–1308.

Gerlach. D. C.. F. A. Frey. H. Moreno-Roa. and L. Lopez-Escobar. 1988: Recent volcanism in the Puyehue-Cordon Caulle region. Southern Andes. Chile (40.5°S): Petrogenesis of evolved lavas. *Journal of Petrology.* *29.* 333–382.

Gerlach. M.. 1993: A magmatic vapor saturation and accumulation model for the 20-megaton SO$_2$ cloud from June 15. 1991. climactic eruption of Mount Pinatubo. in: *AGU FALL Meeting.* Fall Meeting Abstracts. pp. 104–105. AGU.

Gerlach. T. M.. H. R. Westrich. T. J. Casadevall. and D. L. Finnegan. 1994: Vapor saturation and accumulation in magmas of the 1989-1990 eruption of Redoubt Volcano. Alaska. *Journal of Volcanology and Geothermal Research.* *62.* 317–337.

Gilliland, R. L., 1981: Solar radius variations over the past 265 years. *The Astrophysical Journal,* *248,* 1144-1155.

Gilliland, R. L., and S. H. Schneider. 1984: Volcanic, CO$_2$, and solar forcing of Northern and Southern Hemisphere surface air temperatures. *Nature,* *310,* 38-41.

Glantz, M., R. Katz, and N. Nicholls, 1991: *Teleconnections linking worldwide climate anomalies.* Cambridge University Press.

Gleissberg, W., 1965: The eighty-year solar cycle in auroral frequency numbers. *Journal of the British Astronomical Association,* 75(4), 227-231.

Gooding, J. L., U. S. Clanton, E. M. Gabel, and J. L. Warren, 1983: El Chichón volcanic ash in the stratosphere: Particle abundances and size distribution after the 1982 eruption. *Geophysical Research Letters,* 10(11), 1033-1036.

Goodman, B. M., 1984: The climatic impact of volcanic activity. Ph.D. thesis, University of Wisconsin, Department of Meteorology.

Goodman, J., K. G. Snetsinger, R. F. Pueschel, G. V. Ferry, and S. Verma, 1994: Evolution of Pinatubo aerosol near 19 km altitude over western North America. *Geophysical Research Letters,* 21, 1129-1132.

Goto-Azuma, K., and R. Koerner, 2001: Ice core studies of anthropogenic sulfate and nitrate trends in the Arctic. *Journal of Geophysical Research,* 106(D5), 4959-4969.

Graf, H.-F., I. Kirchner, A. Robock, and I. Schult, 1993: Pinatubo eruption winter climate effects: model versus observations. *Climate Dynamics,* 9, 81-93.

Grainger, R., A. Lambert, C. Rodgers, F. Taylor, and T. Deshler, 1995: Stratospheric aerosol effective radius, surface area and volume estimated from infrared measurements. *Journal of Geophysical Research,* 100(D8), 16507-16513.

Grant. W. B.. E. V. Browell. C. S. Long. L. L. Stowe. R. G. Grainger. and A. Lambert. 1996: Use of volcanic aerosols to study the tropical stratospheric reservoir. *Journal of Geophysical Research. 101*(D2). 3973-3988.

Gras. J. L.. and J. E. Laby. 1979: Southern Hemisphere stratospheric aerosol measurements. 2. Time variations and the 1974-1975 aerosol events. *Journal of Geophysical Research. 84*(C1). 303-307.

Groisman. P. Y.. 1992: Possible regional climate consequences of the Pinatubo eruption: An empirical approach. *Geophysical Research Letters. 19*. 1603-1606.

Groisman. P. Y.. 1994: Unusual weather conditions in central and northern Europe after volcanic eruptions. *Publications of the Academy of Finland.*

Hack. J.. J. Kiehl. and J. Hurrell. 1998: The hydrologic and thermodynamic characteristics of the NCAR CCM3. *Journal of Climate. 11*(6). 1179-1206.

Halpert. M.. and C. Ropelewski. 1992: Surface temperature patterns associated with the Southern Oscillation. *Journal of Climate. 5*. 577-593.

Hammer. C. U.. 1977: Past volcanism revealed by Greenland Ice Sheet impurities. *Nature. 270*. 182-186.

Hammer. C. U.. H. B. Clausen. and W. Dansgaard. 1980: Greenland ice sheet evidence of post-glacial volcanism and its climatic impact. *Nature. 288*. 230-235.

Hand. I.. 1939: Variation in solar radiation intensities at the surface of the earth in the United States. *Monthly Weather Review. 67*. 338-340.

Hand. I. F.. 1937: Review of United States Weather Bureau solar radiation investigations. *Monthly Weather Review. 65*. 415-441.

Handler. P.. 1984: Possible association of stratospheric aerosols and El Niño type events. *Geophysical Research Letters.* *11*(11). 1121–1124.

Handler. P.. 1986: Possible association between the climatic effects of stratospheric aerosols and sea surface temperatures in the eastern tropical Pacific Ocean. *Journal of Climatology. 6.* 31–41.

Handler. P.. and K. Andsager. 1990: Volcanic aerosols. El Nino and the Southern Oscillation. *International Journal of Climatology. 10.* 413–424.

Hansen. J.. and L. Travis. 1974: Light scattering in planetary atmospheres. *Space Science Reviews. 16.* 527–610.

Hansen. J. E.. and A. E. Lacis. 1990: Sun and dust versus greenhouse gases: an assessment of their relative roles in global climate change. *Nature. 346.* 713–719.

Hansen. J. E.. W.-C. Wang. and A. E. Lacis. 1978: Mount Agung eruption provides test of a global climatic perturbation. *Science. 199.* 1065–1068.

Hansen. J. E.. R. Ruedy. M. Sato. and R. Reynolds. 1996a: Global surface air temperature in 1995: Return to pre-Pinatubo level. *Geophysical Research Letters. 23.* 1665–1668.

Hansen. J. E.. et al.. 1996b: A pinatubo climate modeling investigation. pp. 233–272. vol. I 42 of *Fiocco et al.* (1996).

Hansen. J. E.. M. Sato. and R. Ruedy. 1997: Radiative forcing and climate response. *Journal of Geophysical Research. 102*(D6). 6831–6864.

Hansen. J. E.. M. Sato. A. A. Lacis. R. Ruedy. I. Tegen. and E. Matthews. 1998: Climate forcings in the industrial era. *Proceedings of the National Academy of Sciences. 95.* 12753–12758.

Hansen. J. E.. R. Ruedy. J. Glascoe. and M. Sato. 1999: GISS analysis of surface temperature change. *Journal of Geophysical Research. 104*(D24). 30997–31022.

259

Hansen, J. E., M. Sato, R. Ruedy, A. A. Lacis, and V. Oinas, 2000: Global warming in the twenty-first century: An alternative scenario. *Proceedings of the National Academy of Sciences, 97,* 9875–9880.

Harington, C. (ed.), 1992: *The Year without a Summer?* Canadian Museum of Nature, Ottawa, Canada.

Harries, J., 1995: *Earthwatch. The climate from space,* Wiley-Praxis Series in Remote Sensing. John Wiley and Sons, Chichester.

Hartman, D. L., 1994: *Global physical climatology,* vol. 56 of *International Geophysics Series.* Academic Press, San Diego.

Hazen, H., 1884: Sun glows. *Science, 27,* 201–212.

Hedervari, P., 1980: Great volcanic eruptions and the luminosity of the moon during total eclipses. *Journal of the Association of Lunar and Planet Observers, 28,* 158–165.

Herber, A., L. W. Thomason, V. F. Radionov, and U. Leiterer, 1993: Comparison of trends in the tropospheric and stratospheric aerosol optical depth in the Antarctic. *Journal of Geophysical Research, 98*(D10), 18441–18447.

Herron, M. M., 1982: Impurity sources of F-, Cl-, NO_3- and SO_4^{2-} in Greenland Antarctic precipitation. *Journal of Geophysical Research, 87*(C4), 3052–3060.

Hildreth, W., and J. Fierstein, 2000: Katmai volcanic cluster and the great eruption of 1912. *GSA Bulletin, 112,* 1594–1620.

Hirono, M., 1988: On the trigger of El Niño Southern Oscillation by the forcing of early El Chichón volcanic aerosols. *Journal of Geophysical Research, 93*(D5), 5365–5384.

Hirschboeck, K. K., 1980: A new worldwide chronology of volcanic eruptions (with a summary of historical ash-producing activity and some implications for climatic trends of the last one hundred years). *Palaeogeography, Palaeoclimatology, Palaeoecology, 29*, 223–241.

Hitchman, M. H., M. McKay, and C. R. Trepte, 1994: A climatology of stratospheric aerosol. *Journal of Geophysical Research, 99*(D10), 20689–20700.

Hofmann, D., and J. Rosen, 1984a: Balloonborne particle counter observations of the El Chichón aerosol layers in the 0.01 – 1.3μm radius range. *Geofísica Internacional, 23*(2), 155.

Hofmann, D., and J. Rosen, 1984b: Measurement of the sulfuric acid weight percent in the stratospheric aerosol from the El Chichón eruption. *Geofísica Internacional, 23*(3), 309–320.

Hofmann, D. J., 1987: Perturbations to the global atmosphere associated with the El Chichón volcanic eruption of 1982. *Reviews of Geophysics, 25*, 743–759.

Hofmann, D. J., 1989: Ozone destruction through heterogenous chemistry following the eruption of El Chichón. *Journal of Geophysical Research, 94*(D4), 5029–5041.

Hofmann, D. J., and J. M. Rosen, 1977: Balloon observations of the time development of the stratospheric aerosol event of 1974-1975. *Journal of Geophysical Research, 82*(9), 1435–1440.

Hofmann, D. J., and J. M. Rosen, 1980: Stratospheric sulfuric acid layer: Evidence for an anthropogenic component. *Science, 208*, 1368–1370.

Hofmann, D. J., and J. M. Rosen, 1981: On the background stratospheric aerosol layer. *Journal of the Atmospheric Sciences, 38*, 168–181.

Hofmann, D. J., and J. M. Rosen, 1982: Balloon-borne observations of stratospheric aerosol and condensation nuclei during the year following the Mt. St. Helens eruption. *Journal of Geophysical Research, 87*(C12), 11039–11061.

261

Hofmann, D. J., and J. M. Rosen, 1983: Sulfuric acid droplet formation and growth in the stratosphere after the 1982 eruption of El Chichón. *Science*, *222*, 325-327.

Hofmann, D. J., and J. M. Rosen, 1984c: On the temporal variation of stratospheric aerosol size and mass during the first 18 months following the 1982 eruptions of El Chichón. *Journal of Geophysical Research*, *89*(D3), 4883-4890.

Hofmann, D. J., J. M. Rosen, R. Reiter, and H. Jger, 1983: Lidar- and balloon-borne particle counter comparisons following recent volcanic eruptions. *Journal of Geophysical Research*, *88*(C6), 3777-3782.

Holasek, R., 1995: Volcanic eruption plumes: Satellite remote sensing observations and laboratory experiments. Ph.D. thesis, University of Hawaii at Manoa, Hawaii.

Holland, W., J. Chow, and F. Bryan, 1998: Application of a third-order upwind scheme in the NCAR Ocean Model. *Journal of Climate*, *11*(6), 1487-1493.

Holm, N., 1992: *Marine Hydrothermal systems and the origin of life*. Kluwer Academic Publ., Dordrecht.

Hoyt, D. V., 1978: An explosive volcanic eruption in the Southern Hemisphere in 1928. *Nature*, *275*, 630-632.

Hoyt, D. V., 1979: Atmospheric transmission from the Smithsonian Astrophysical Observatory pyrheliometric measurements from 1923-1957. *Journal of Geophysical Research*, *84*(C8), 5018-5028.

Hoyt, D. V., and K. H. Schatten, 1993: A discussion of plausible solar irradiance variations, 1700-1992. *Journal of Geophysical Research*, *98*(A11), 18,895-18,906.

Hoyt, D. V., and K. H. Schatten, 1998: Group sunspot numbers: A new solar activity reconstruction. *Solar Physics*, *181*, 491-512.

Hummel, J. R., E. P. Shettle, and D. R. Longtin, 1988: *A new background stratospheric aerosol model for use in atmospheric radiation models*, AFGL-TR80-0166.

Humphreys, W., 1913: Volcanic dust and other factors in the production of climatic changes, and their possible relation to ice ages. *Bulletin of the Mount Weather Observatory, 6*, 1-34, +1 plate.

Humphreys, W., 1937: The greenhouse effect of volcanic dust. *Monthly Weather Review, 65(7)*, 261-262.

Humphreys, W. J., 1940: *Physics of the air*. McGraw-Hill, New York and London.

Hurrell, J., J. Hack, B. Boville, D. Williamson, and J. Kiehl, 1998: The dynamical simulation of the NCAR Community Climate Model Version 3 (CCM3). *Journal of Climate, 11(6)*, 1207-1236.

Hurrell, J., Y. Kushnir, and M. Visbeck, 2001: The North Atlantic Oscillation. *Science, 291*, 603-605.

Hurrell, J. W., 1995: Decadal trends in the North Atlantic Oscillation: Regional temperatures and precipitation. *Science, 269*, 676-679.

Jacoby, G. C., K. W. Workman, and R. D. D'Arrigo, 1999: Laki eruption of 1783, tree rings, and disaster for northwest Alaska Inuit. *Quaternary Science Reviews, 18*, 1365-1371.

Jäger, H., R. Reiter, W. Carnuth, and W. Funk, 1984: El Chichón cloud over Central Europe. *Geofisica Internacional, 23(2)*, 243.

Jäger, H., O. Uchino, T. Nagai, T. Fujimoto, V. Freudenthaler, and F. Homburg, 1991: Ground-based remote sensing of the decay of the Pinatubo eruption cloud at three Northern Hemisphere sites. *Geophysical Research Letters, 22(5)*, 607-610.

263

Jensen. E. J.. and O. B. Toon. 1992: The potential effects of volcanic aerosols on Cirrus cloud microphysics. *Geophysical Research Letters. 19.* 1759–1762.

Jones. P.. 1994: Hemispheric surface air temperature variations: a reanalysis and an update to 1993. *Journal of Climate. 7.* 1794–1802.

Jones. P. D.. K. R. Briffa. and F. H. Schweingruber. 1995: Tree-ring evidence of widespread effects of explosive volcanic eruptions. *Geophysical Research Letters. 22.* 1333–1336.

Jones. P. D.. R. S. Bradley. and J. Jouzel (eds.). 1996: *Climatic variations and forcing mechanisms of the last 2000 years.* vol. I 41 of *NATO ASI Series.* Springer. Berlin. Heidelberg.

Jones. P. D.. K. R. Briffa. T. P. Barnett. and S. F. B. Tett. 1998: High-resolution paleoclimatic records for the last millennium: interpretation. integration and comparison with General Circulation Model control-run temperatures. *The Holocene. 8.* 455–471.

Joseph. J.. W. Wiscombe. and J. Weinman. 1976: The delta-Eddington approximation for radiative flux transfer. *Journal of the Atmospheric Sciences. 33.* 2452–2459.

Junge. C. E.. C. W. Chagnon. and J. E. Manson. 1961: Stratospheric aerosols. *Journal of Meteorology. 18.* 81–108.

Kalitin. N. N.. 1926: Die Durchsichtigkeit der Erdatmosphäre nach Beobachtungen in Pawlowsk. *Gerlands Beitrge zur Geophysik. 15.* 376–400.

Kalitin. N. N.. 1938: Volcanic eruptions and atmospheric transmissivity. *Prıvoda (russ: Nature). 11-12.* 17–21.

Kalnay. E.. et al.. 1996: The NCEP/NCAR 40-year reanalysis project. *Bulletin of the American Meteorological Society. 77.* 437–471.

Kasten. F.. 1968: Falling speed of aerosol particles. *Journal of Applied Meteorology. 7.* 944–947.

Keen. R. A.. 1983: Volcanic aerosols and lunar eclipses. *Science. 222.* 1011–1013.

Keen. R. A.. 1997: Amospheric effects. *Bulletin of the Global Volcanism Network. 22*(11). 15–.

Kelly. P.. 1977: Volcanic dust veils and North Atlantic climatic change. *Nature. 268.* 616–617.

Kelly. P. M.. and C. B. Sear. 1984: Climatic impact of explosive volcanic eruptions. *Nature. 311.* 740–743.

Kelly. P. M.. P. D. Jones. and P. Jia. 1996: The spatial response of the climate system to explosive volcanic eruptions. *Journal of Climatology. 16.* 537–550.

Kelly. P. M.. P. D. Jones. A. Robock. and K. R. Briffa. 1998: The contribution of Hubert H. Lamb to the study of volcanic effects on climate. *Weather. 53.* 209–222.

Kepler. J.. 1604: *Astronomiae Pars Optica.* Marnium and Aubrii. Frankfurt.

Keppler. H.. 1999: Experimental evidence for the source of excess sulfur in explosive volcanic eruptions. *Science. 284.* 1652–1654.

Keys. D.. 1999: *Catastrophe. An investigation into the origins of the modern world.* Ballantine Books. New York.

Kidder. S.. and T. Vonder Haar. 1995: *Satellite Meteorology. An Introduction.* Academic Press.

Kiehl. J.. J. Hack. G. Bonan. B. Boville. B. Briegleb. D. Williamson. and P. Rasch. 1996: *Description of the NCAR Community Climate Model (CCM3).* National Center for Atmospheric Research. Boulder. Colorado. NCAR/TN-420+STR.

Kiehl. J.. J. Hack. and J. Hurrell. 1998a: The energy budget of the NCAR Community Climate Model: CCM3. *Journal of Climate. 11*(6). 1151–1178.

Kiehl. J.. J. Hack. G. Bonan. B. Boville. D. Williamson. and P. Rasch. 1998b: The National Center for Atmospheric Research Cummunity Climate Model: CCM3. *Journal of Climate. 11*(6). 1131–1149.

Kiehl, J. T., and B. P. Briegleb, 1991: A new parametrization of the absorptance due to the 15-mm band system of carbon dioxide. *Journal of Geophysical Research*, *96*(D5), 9013–9019.

Kiehl, J. T., and B. P. Briegleb, 1993: The relative roles of sulfate aerosol and greenhouse gases in climate forcing. *Science*, *260*, 311–314.

Kiehl, J. T., and S. Solomon, 1986: On the radiative balance of the Stratosphere. *Journal of the Atmospheric Sciences*, *43*, 1525–1534.

Kiehl, J. T., T. Schneider, P. Rasch, M. Barth, and J. Wong, 2000: Radiative forcing due to sulfate aerosols from simulations with the National Center for Atmospheric Research Community Climate Model, Version 3. *Journal of Geophysical Research*, *105*(D1), 1441–1457.

Kimball, H., 1912: The dense haze of june 10-11, 1912. *Bulletin of the Mount Weather Observatory*, *5*, 161–165.

Kimball, H., 1913: The effect upon atmospheric transparency of the eruption of Katmai Volcano. *Monthly Weather Review*, *41*, 153–159.

Kimball, H. H., 1924: Variation in solar radiation intensities measured at the surface of the earth. *Monthly Weather Review*, *52*, 527–529.

Kinnison, D. E., K. E. Grant, P. S. Connell, D. A. Rotman, and D. J. Wuebbles, 1994: The chemical and radiative effects of the Mount Pinatubo eruption. *Journal of Geophysical Research*, *99*(D12), 25705–25731.

Kirchner, I., G. L. Stenchikov, H.-F. Graf, A. Robock, and J. C. Antua, 1998: *Climate model simulation of winter warming and summer cooling following the 1991 Mount Pinatubo volcanic eruption*. Max-Plank-Institut fr Meteorologie, p. 35pp., 261.

Kistler, R., et al., 2001: The NCEP-NCAR 50-Year Reanalysis: Monthly Means CD-ROM and Documentation. *Bulletin of the American Meteorological Society*, *82*(2), 247–268.

Kondratyev. K.. and I. Galindo. 1997: *Volcanic Activity and Climate*. Studies in Geophysical Optics and Remote Sensing. A. Deepak Publishing.

Kondratyev. K. Y.. 1999: *Climatic effects of aerosols and clouds*. Springer Verlag. Berlin. Heidelberg and New York.

Können. G.. P. D. Jones. M. H. Kaltofen. and R. J. Allan. 1998: Pre-1866 extentions of the Southern Oscillation index using early Indonesian and Tahitian meteorological readings. *Journal of Climate*. *11*. 2325-2339.

Kreutz. K. J.. P. A. Mayewski. M. S. Twickler. S. I. Whitlow. J. W. C. White. C. A. Shuman. C. F. Raymond. H. Conway. and J. R. McConnell. 1999: Seasonal variations of glaciochemical. isotopic and stratigraphic properties in Siple Dome (Antarctica) surface snow. *Annals of Glaciology*. *29*. 38-44.

Krueger. A. J.. L. S. Walter. P. K. Bhartia. C. C. Schnetzler. N. A. Krotkov. I. E. Sprod. and G. J. S. Bluth. 1995: Volcanic sulfur dioxide measurements from the total ozone mapping spectrometer instrument. *Journal of Geophysical Research*. *100*(D7). 14057-14076.

Kump. L.. J. Kasting. and M. Barley. 2001: Rise of atmospheric oxygen and the "upside-down" Archean mantle. *G3 - Geochemistry. Geophysics. Geosystems*. *2*(2000GC00114). 10pp.

Kushnir. Y.. 1994: Interdecadal variations in North Atlantic sea surface temperature and associated atmospheric conditions. *Journal of Climate*. *7*. 141-157.

Labitzke. K.. and H. van Loon. 1996: The effect on the stratosphere of three tropical volcanic eruptions. pp. 113-125. vol. I 42 of *Fiocco et al*. (1996).

Labitzke. K.. B. Naujokat. and M. P. McCormick. 1983: Temperature effects on the stratosphere of the April 4. 1982 eruption of El Chichón. Mexico. *Geophysical Research Letters*. *10*. 24-26.

Lacis, A. E., J. E. Hansen, and M. Sato, 1992: Climate forcing by stratospheric aerosol. *Geophysical Research Letters*, *19*(15), 1607–1610.

LaMarche, V. C., and K. K. Hirschboeck, 1984: Frost rings in trees as records of major volcanic eruptions. *Nature*, *307*, 121–126.

Lamb, H. H., 1967: The problem of "Thompson Island": Volcanic eruptions and meteorological evidence. *British Antarctic Survey Bulletin*, *13*, 85–88.

Lamb, H. H., 1970: Volcanic dust in the atmosphere: with a chronology and assessment of its meteorological significance. *Transactions of the Royal Philosophical Society of London*, *A266*, 125–533.

Lamb, H. H., 1977: Supplementary volcanic dust veil assessments. *Climate Monitor*, *6*, 57–67.

Lamb, H. H., 1983: Update of the chronology of assessments of the volcanic dust veil index. *Climate Monitor*, *12*(3), 79–90.

Langway, C. C., J., H. B. Clausen, and C. U. Hammer, 1988: An inter-hemispheric volcanic time-marker in ice cores from Greenland Antarctica. *Annals of Glaciology*, *10*, 102–108.

Langway, C. C., J., K. Osada, H. B. Clausen, C. U. Hammer, and H. Shoji, 1995: A 10-century comparison of prominent bipolar volcanic events in ice cores. *Journal of Geophysical Research*, *100*(D8), 16241–16247.

Lassen, K., and E. Friis-Christensen, 1995: Variability of the solar cycle length during the past five centuries and the apparent association with terrestrial climate. *Journal of Atmospheric and Terrestrial Physics*, *57*(8), 835–845.

Lean, J., and D. Rind, 1994: Solar variability: Implications for global change. *EOS, Transactions, American Geophysical Union*, *75*(01), 1–5–7.

Lean. J.. J. Beer. and R. S. Bradley. 1995: Reconstruction of solar irradiance since 1610: Implications for climate change. *Geophysical Research Letters.* 22(23). 3195–3198.

Lean. J. L.. and D. Rind. 1999: Evaluating sun-climate relationships since the Little Ice Age. *Journal of Atmospheric and Solar-Terrestrial Physics. 61.* 25–36.

Legrand. M.. 1987: Chemistry of Antarctic snow and ice. *J. Phys.. Paris. 48(C1).* 77–86.

Legrand. M.. and R. J. Delmas. 1987: A 220-year continuous record of volcanic H_2SO_4 in the Antarctic ice sheet. *Nature. 327.* 671–676.

Legrand. M.. and C. Feniet-Saigne. 1991: Methanesulfonic acid in South Polar snow layers: A record of strong El Niño?. *Geophysical Research Letters. 18.* 187–190.

Link. F.. 1961: L'activite volcanique et les eclipses de lune. *Studia Geophysica et Geodaetica. 5.* 64–74.

Lockwood. G. W.. and D. T. Thompson. 1986: Atmospheric extinction: the ordinary and volcanically induced variations. 1972-1985. *The Astronomical Journal. 92.* 976–985.

Long. C. S.. and L. L. Stowe. 1994: Using the NOAA/AVHRR to study stratospheric aerosol optical thicknesses following the Mt. Pinatubo eruption. *Geophysical Research Letters. 21(20).* 2215–2218.

Lough. J. M.. and H. C. Fritts. 1987: An assessment of the possible effects of volcanic eruptions on North American climate using tree-ring data. 1602 to 1900 AD. *Climatic Change. 10.* 219–239.

Luterbacher. J.. C. Schmutz. D. Gyalistras. E. Xoplaki. and H. Wanner. 1999: Reconstruction of monthly NAO and EU indices back to AD 1675. *Geophysical Research Letters. 26.* 2745–2748.

Macias. J. L.. 1994: Violent short-lived eruptions from small-size volcanoes: El Chichón. Mexico (1982) and Shtyubel. Russia (1907). Ph.D. thesis. SUNY at Buffalo. Buffalo. NY.

Macias. J. L.. and M. F. Sheridan. 1995: Products of the 1907 eruption of Shtyubel' Volcano. Ksudach caldera. Kamchatka. Russia. *Geological Society of America Bulletin. 107.* 969–986.

Mandeville. C.. S. Carey. and H. Sigurdsson. 1996a: Magma mixing. fractional crystallization and volatile degassing during the 1883 eruption of Krakatau Volcano. Indonesia. *Journal of Volcanology and Geothermal Research. 74.* 243–274.

Mandeville. C.. S. Carey. and H. Sigurdsson. 1996b: Sedimentology of the Krakatau 1883 submarine pyroclastic deposits. *Bulletin of Volcanology. 57.* 512–529.

Mankin. W. G.. and M. T. Coffey. 1984: Increased stratospheric hydrogen chloride in the El Chichón cloud. *Science. 226.* 170–172.

Mankin. W. G.. M. T. Coffey. and A. Goldman. 1992: Airborne observations of SO_2. HCl. and O_3 in the stratospheric plume of the Pinatubo volcano in July 1991. *Geophysical Research Letters. 19.* 179–182.

Mann. M. E.. and J. Park. 1994: Global-scale modes of surface temperature variability on inter-annual to century timescales. *Journal of Geophysical Research. 99(*D12). 25819–25833.

Mann. M. E.. and J. Park. 1996: Joint spatiotemporal modes of surface temperature and sea level pressure variability in the Northern Hemisphere during the last century. *Journal of Climate. 9.* 2137–2162.

Mann. M. E.. R. S. Bradley. and M. K. Hughes. 1998: Global-scale temperature patterns and climate forcing over the past six centuries. *Nature. 392.* 779–787.

Mann. M. E.. R. S. Bradley. and M. K. Hughes. 2000: Long-term variability in the El Niño-Southern Oscillation and associated teleconnections. pp. 357–412. in: *Diaz and Markgraf* (2000).

Mao. J.. and A. Robock. 1998: Surface air temperature simulations by AMIP general circulation models: Volcanic and ENSO signals and systematic errors. *Journal of Climate*, *11*, 1538–1552.

Matsushima. S.. J. Zink. and J. Hansen. 1966: Atmospheric extinction by dust particles as determined from three-color photometry of the lunar eclipse of 19 december 1964. *The Astronomical Journal*, *71*(2). 103–110.

Mayewski. P.. W. Lyons. M. Spencer. M. Twickler. C. Buck. and S. Whitlow. 1990: An ice core record of atmospheric response to anthropogenic sulphate and nitrate. *Nature*, *346*, 554–556.

Mayewski. P.. G. Holdsworth. M. Spencer. S. Whitlow. M. Twicker. M. Morrison. K. Ferland. and L. Meeker. 1993: Ice-core sulfate from three northern hemisphere sites: source and temperature forcing implications. *Atmospheric Environment*, *27A*, 2915–1919.

Mayewski. P.. L. Meeker. M. Twickler. S. Whitlow. Q. Yang. W. Lyons. and M. Prentice. 1997: Major features and forcing of high-latitude northern hemisphere atmospheric circulation using a 110.000-year-long glaciochemical series. *Journal of Geophysical Research*, *102*, 26345–26366.

McCormick. M.. and T. Swissler. 1983: Stratospheric aerosol mass and latitudinal distribution of the El Chichón eruption cloud for october 1982. *Geophysical Research Letters*, *10*(9), 877–880.

McCormick. M.. C. Trepte. and G. Kent. 1983: Spatial changes in the stratospheric aerosol associated with the North Polar Vortex. *Geophysical Research Letters*, *10*(10), 941–944.

McCormick. M.. P.-H. Wang. and L. Poole. 1993: Stratospheric aerosols and clouds. In: Hobbs. P. (ed.): *Stratospheric aerosols and clouds*. vol. 54 of *International Geophysics Series*. chap. 8. pp. 205–222. Academic Press. San Diego.

McCormick. M. P.. and R. E. Veiga. 1992: SAGE II measurements of early Pinatubo aerosols. *Geophysical Research Letters*, *19*, 155–158.

McCormick, M. P., P. Hamill, T. J. Pepin, W. P. Chu, T. J. Swissler, and L. R. McMaster, 1979: Satellite studies of the stratospheric aerosol. *Bulletin of the American Meteorological Society, 60,* 1038–1046.

McCormick, M. P., W. Chu, G. Grams, P. Hamill, B. Herman, L. McMaster, T. Pepin, H. Steele, and T. Swissler, 1981: High-latitude stratospheric aerosol measured by the SAM II satellite system in 1978 and 1979. *Science, 214,* 328–331.

McCormick, M. P., L. Thomason, and C. R. Trepte, 1995: Atmospheric effects of the Mount Pinatubo eruption. *Nature, 373,* 399–404.

McCormick, R., and J. Ludwig, 1967: Climate modification by atmospheric aerosol. *Science, 156,* 1358–1359.

Meehl, G., 1997: The South Asian Monsoon and the Tropospheric Biennial Oscillation. *Journal of Climate, 10*(8), 1921–1943.

Meehl, G., and J. Arblaster, 1998: The Asian-Australian Monsoon and El Niño-Southern Oscillation in the NCAR Climate System Model. *Journal of Climate, 11*(6), 1356–1385.

Meehl, G., and G. Branstator, 1992: Coupled climate model simulation of El Niño/Southern Oscillation: Implications for paleoclimate. In: Diaz, H., and V. Markgraf (eds.): *Coupled climate model simulation of El Niño/Southern Oscillation: Implications for paleoclimate,* pp. 69–91. Cambridge University Press, Cambridge.

Meehl, G., P. Gent, J. Arblaster, B. Otto-Bliener, E. Brady, and A. Craig, 2001: Factors that affect the amplitude of El Niño in global coupled climate models. *Climate Dynamics, 17,* 515–526.

Meinel, A., and M. Meinel, 1983: *Sunsets, Twilights, and Evening Skies.* Cambridge University Press.

Meinel, A. B., and M. P. Meinel, 1964: Height of the glow stratum from the eruption of Agung on Bali. *Nature, 201,* 657–658.

Meinel, A. B., and M. P. Meinel, 1975: Stratospheric dust-aerosol event of November 1974. *Science, 188,* 477–478.

Mendonca, B. G., K. J. Hanson, and J. J. DeLuisi, 1978: Volcanically related secular trends in atmospheric transmission at Mauna Loa Observatory, Hawaii. *Science, 202,* 513–515.

Mergenthaler, J. L., J. B. Kumer, and A. E. Roche, 1995: CLAES observation of Mt. Pinatubo stratospheric aerosl. *Geophysical Research Letters, 22*(24), 3497–3500.

Minnis, P., E. F. Harrison, L. L. Stowe, G. G. Gibson, F. M. Denn, D. R. Doelling, and J. W. L. Smith, 1993: Radiative climate forcing by the Mount Pinatubo eruption. *Science, 259,* 1411–1415.

Mitchell, J. Murray, J., 1961: Recent secular changes of global temperature. *Annals New York Academy of Sciences, 235-250.*

Mitchell, J. Murray, J., 1970: A preliminary evaluation of atmospheric pollution as a cause of the global temperature fluctuation of the past century. In: Singer, S. (ed.): *A preliminary evaluation of atmospheric pollution as a cause of the global temperature fluctuation of the past century,* pp. 139–155. Springer Verlag, Reidel Publishing Company, Dordrecht.

Mitchell, J. Murray, J., 1976: An overview of climate variability and its causal mechanisms. *Quaternary Research, 6,* 481–493.

Moore, J. C., H. Narita, and N. Maeno, 1991: A continuous 770-year record of volcanic activity from East Antarctica. *Journal of Geophysical Research, 96*(D9), 17353–17359.

Moreno, H., N. Sanduleak, and J. Stock, 1965: Photometry at Cerro Tololo, Chile: Effects of Mount Agung Eruption. *Science, 148,* 364–366.

Mossop, S. C., 1963: Stratospheric particles at 20 km. *Nature, 199,* 325–326.

Mossop, S. C., 1964: Volcanic dust collected at an altitude of 20 km. *Nature, 203,* 824–827.

Mukherjee, B. K., 1990: Middle atmosphere dynamics and monsoon variability. *Mausam, 41,* 203–208.

Mukherjee, B. K., K. Indira, and K. K. Dani, 1987: Low-latitude volcanic eruptions and their effects on Sri Lankan rainfall during the North-East Monsoon. *Journal of Climatology, 7,* 145–155.

Murrow, P. J., W. I. Rose, and S. Self, 1980: Determination of the total grain size distribution in a vulcanian eruption column, and its implications to stratospheric aerosol perturbation. *Geophysical Research Letters, 7*(11), 893–896.

Neftel, A., J. Beer, H. Oeschger, F. Zrcher, and R. C. Finkel, 1985: Sulphate and nitrate concentrations in snow from South Greenland 1895-1978. *Nature, 314,* 611–613.

Newhall, C., and R. Punongbayan (eds.), 1997: *Fire and mud: Eruptions and lahars of Mount Pinatubo, Philippines.* Philippine Institute of Volcanology and Seismology and University of Washington Press, Quezon City, Seattle and London.

Newhall, C. G., and S. Self, 1982: The volcanic explosivity index (VEI): An estimate of explosive magnitude for historical volcanism. *Journal of Geophysical Research, 87*(C2), 1231–1238.

Nicholls, N., 1988: Low latitude volcanic eruptions and the El Niño-Southern Oscillation. *Journal of Climatology, 8,* 91–95.

Nicholls, N., 1990: Low-latitude volcanic eruptions and the El Niño/Southern Oscillation: A reply. *International Journal of Climatology, 10,* 425–429.

Niedziela, R. F., M. L. Norman, R. E. Miller, and D. R. Worsnop, 1998: Temperature- and composition-dependent infrared optical constants for sulfuric acid. *Geophysical Research Letters*, *25*, 4477–4480.

Oberbeck, V. R., E. F. Danielsen, K. G. Snetsinger, and G. V. Ferry, 1983: Effect of the eruption of El Chichón on stratospheric aerosol size and composition. *Geophysical Research Letters*, *10*(11), 1021–1024.

Oliver, R. C., 1976: On the response of hemispheric mean temperature to stratospheric dust: An empirical approach. *Journal of Applied Meteorology*, *15*, 933–950.

Oppenheimer, C., P. Francis, and J. Stix, 1998: Depletion rates of sulfur dioxide in tropospheric volcanic plumes. *Geophysical Research Letters*, *25*, 2671–2674.

Ortlieb, L., 1994: Las mayores precipitationes históricas en Chile central y la cronologia de eventos ENOS en los siglos XVI-XIX. *Revista Chilena de Historia Natural, 67*, 463–485.

Ortlieb, L., 2000: The documented historical record of El Niño events in Peru: An update of the Quinn record (sixteenth through nineteenth centuries), chap. 7, pp. 207–295, in: *Diaz and Markgraf* (2000).

Otto-Bliesner, B., and E. Brady, 2001: Tropical Pacific variability in the NCAR Climate System Model. *Journal of Climate*, *14*, 3587–3607.

Palais, J. M., and H. Sigurdsson, 1989: Petrologic evidence of volatile emissions from major historic and pre-historic volcanic eruptions. In: Berger, A., R. Dickinson, and J. Kidson (eds.): *Petrologic evidence of volatile emissions from major historic and pre-historic volcanic eruptions*, vol. 7 of *Geophysical Monographs 52*, pp. 31–53. American Geophysical Union, International Union of Geodesy and Geophysics.

Palais, J. M., S. Kirchner, and R. J. Delmas, 1990: Identification of some global volcanic horizons by major element analysis of fine ash in Antarctic ice. *Annals of Glaciology*, *14*, 216–220.

Palmer, K. F., and D. Williams, 1975: Optical constants of sulfuric acid: Application to the clouds of Venus?. *Applied Optics*, *14*(1), 208–219.

Pang, K. D., 1993: Climatic impact of the mid-fifteenth century Kuwae Caldera formation, as reconstructed from historical and proxy data. *EOS*, *74 (suppl.)*, 106.

Panofsky, H., and G. Brier, 1965: *Some applications of statistics to meteorology*. Penn. State University, University Park, Pennsylvania.

Parker, D., C. Folland, and M. Jackson, 1995: Marine surface temperature: observed variations and data requirements. *Climatic Change*, *31*, 559–600.

Parker, D., E. Horton, and L. Alexander, 2000: Global and regional climate in 1999. *Weather*, *55*, 188–199.

Parker, D. E., 1988: Stratospheric aerosols and sea-surface temperatures. *Journal of Climatology*, *8*, 87–90.

Parker, D. E., H. Wilson, P. D. Jones, J. R. Christy, and C. K. Folland, 1996: The impact of Mount Pinatubo on world-wide temperatures. *International Journal of Climatology*, *16*, 487–497.

Patrick, M. M., and P.-H. Wang, 1987: Background stratospheric aerosol reference model. *Advances in Space Research*, *7*(9), 73–80.

Patris, N., R. Delmas, and J. Jouzel, 2000: Isotopic signatures of sulfur in shallow Antarctic ice cores. *Journal of Geophysical Research*, *105*(D6), 7071–7078.

Paul, W., and R. V. Jones, 1951: Blue sun and moon. *Nature*, *168*, 554.

Petrov, B., and F. Csaki (eds.), 1973: *Information Theory and an Extension of the Maximum Likelihood Principle*. Budapest: Akademia Kiado. 2nd International Symposium on Information Theory.

Pfister. C.. 1999: *Wetternachhersage. 500 Jahre Klimavariationen und Naturkatastrophen.* Haupt Verlag. Bern.

Philander. S.. 1990: *El Niño. La Niña and the Southern Oscillation.* Academic Press. New York.

Pilewskie. P.. and F. Valero. 1995: Direct observations of excess solar absorption by clouds. *Science. 267.* 1626–1629.

Pinto. J. P.. R. P. Turco. and O. B. Toon. 1989: Self-limiting physical and chemical effects in volcanic eruption clouds. *Journal of Geophysical Research. 94.* 11165–11174.

Pivovarova. Z.. 1975: Secular variations in direct solar radiation. *Trudy GGO (in Russian). 338.* 39–60.

Pollack. J. B.. O. B. Toon. C. Sagan. A. Summer. B. Baldwin. and W. van Camp. 1976: Volcanic explosions and climatic change: a theoretical assessment. *Journal of Geophysical Research. 81.* 1071–1083.

Pollack. J. B.. D. Rind. A. Lacis. J. Hansen. M. Sato. and R. Ruedy. 1993: GCM simulations of volcanic aerosol forcing. Part I: Climate changes induced by steady-state perturbations. *Journal of Climate. 6.* 1719–1742.

Porter. S. C.. 1986: Pattern and forcing of Northern Hemisphere glacier variations during the last Millennium. *Quaternary Research. 26.* 27–48.

Portman. D. A.. and D. S. Gutzler. 1996: Explosive volcanic eruptions. the El Niño-Southern Oscillation. and U.S. climate variability. *Journal of Climate. 9.* 17–33.

Post. J.. 1977: *The Last Great Subsistence Crisis in the Western World.* The Johns Hopkins University Press.

Post. M. J., C. J. Grund, A. M. Weickmann, K. R. Healy, and R. J. Willis, 1996: Comparison of Mount Pinatubo and El Chichón volcanic events: Lidar observations at 10.6 and 0.69mm. *Journal of Geophysical Research*, *101*(D2), 3929–3940.

Pourchet, M., et al., 2000: Distribution and fall-out of ^{137}Cs and other radionuclides over Antarctica. *Journal of Glaciology*, pp. 435–445.

Pueschel, R. F., and S. A. Kinne, 1995: Physical and radiative properties of Arctic atmospheric aerosols. *The Science of the Total Environment*, *160/161*, 811–824.

Pueschel, R. F., L. Machta, G. F. Cotton, E. C. Flowers, and J. T. Peterson, 1972: Normal incidence radiation trends on Mauna Loa, Hawaii. *Nature*, *240*, 545–547.

Quinn, W., and V. Neal, 1995: The historical record of El Niño events, chap. 32, pp. 623–648, in: *Bradley and Jones* (1995a).

Quinn, W., V. Neal, and S. Antunez de Mayolo, 1987: El Niño occurrences over the past four and a half centuries. *Journal of Geophysical Research*, *92*(C13), 14449–14461.

Ramachandran, S., V. Ramaswamy, G. Stenchikov, and A. Robock, 2000: Radiative impact of the Mount Pinatubo volcanic eruption: Lower stratospheric response. *Journal of Geophysical Research*, *105*(D19), 24409–24429.

Ramanathan, V., and P. Downey, 1986: A nonisothermal emissivity and absorptivity formulation for water vapor. *Journal of Geophysical Research*, *91*(D8), 8649–8666.

Ramanathan, V., B. Subasilar, G. Zhang, W. Conant, R. Cess, J. Kiehl, H. Grassl, and L. Shi, 1995: Warm pool heat budget and shortwave cloud forcing: A missing physics?. *Science*, *267*, 499–503.

Rampino, M. R., and S. Self, 1982: Historic eruptions of Tambora (1815), Krakatau (1883), and Agung (1963), their stratospheric aerosols, and climatic impact. *Quaternary Research, 18*, 127-143.

Rampino, M. R., and S. Self, 1984: Sulphur-rich volcanic eruptions and stratospheric aerosols. *Nature, 310*, 677-679.

Rampino, M. R., and S. Self, 1992: Volcanic winter and accelerated glaciation following the Toba super-eruption. *Nature, 359*, 50-52.

Rampino, M. R., and S. Self, 1993: Climate-volcanism feedback and the Toba eruption of 74,000 years ago. *Quaternary Research, 40*, 269-280.

Rampino, M. R., S. Self, and R. B. Stothers, 1988: Volcanic winters. *Ann Rev Earth Planet Sci, 16*, 73-99.

Rasch, P. J., M. C. Barth, J. T. Kiehl, S. E. Schwartz, and C. M. Benkovitz, 2000: A description of the global sulfur cycle and its controlling processes in the National Center for Atmospheric Research Community Climate Model, Version 3. *Journal of Geophysical Research, 105*(D1), 1367-1385.

Rayner, N., E. Horton, D. Parker, F. C.K., and R. Hackett, 1996: *Version 2.2 of the global sea-ice and sea surface temperature dataset, 1903-94*. Hadley Center, U.K. Meteorological Office, Climate Researchy Technical Note 74.

Read, W., L. Froidevaux, and J. Waters, 1993: Microwave limb sounder measurement of stratospheric SO_2 from the Mt. Pinatubo Volcano. *Geophysical Research Letters, 20*(12), 1299-1302.

Reiter, R., H. Jaeger, W. Carnuth, and W. Funk, 1983: The El Chichón cloud cover over central europe, observed by lidar at Garmisch-Partenkirchen during 1982. *Geophysical Research Letters, 10*(11), 1001-1004.

Rind. D.. 1996: The potential for modeling the effects of different forcing factors on climate during the past 2000 years. pp. 563–581. vol. I 41 of *Jones et al.* (1996).

Rind. D.. and X. Liao. 1997: SAGE II. Stratospheric Aerosol and Gas Experiment II. CD-ROM. Langley distributed active archive center. NASA.

Rind. D.. and J. Overpeck. 1993: Hypothesized causes of decade-to-century-scale climate variability: Climate model results. *Quaternary Science Reviews. 12.* 357–374.

Robock. A.. 1978: Internally and externally caused climate change. *Journal of the Atmospheric Sciences. 35.* 1111–1122.

Robock. A.. 1979: The "Little Ice Age": Northern Hemisphere average observations and model calculations. *Science. 206.* 1402–1404.

Robock. A.. 1981: A latitudinally dependent volcanic dust veil index. and its effects on climate simulations. *Journal of Volcanology and Geothermal Research. 11.* 67–80.

Robock. A.. 2000: Volcanic eruptions and climate. *Reviews of Geophysics. 38.* 191–219.

Robock. A.. and M. P. Free. 1995: Ice cores as an index of global volcanism from 1850 to the present. *Journal of Geophysical Research. 100*(D6). 11549–11567.

Robock. A.. and M. P. Free. 1996: The volcanic record in ice cores for the past 2000 years. pp. 533–546. vol. I 41 of *Jones et al.* (1996).

Robock. A.. and J. Mao. 1992: Winter warming from large volcanic eruptions. *Geophysical Research Letters. 19.* 2405–2408.

Robock. A.. and J. Mao. 1995: The volcanic signal in surface temperature observations. *Journal of Climate. 8.* 1086–1103.

Robock, A., K. E. Taylor, G. L. Stenchikov, and Y. Liu, 1995: GCM evaluation of a mechanism for El Niño triggering by the El Chichón ash cloud. *Geophysical Research Letters, 22*(17), 2369–2372.

Roche, A., J. Kumer, J. Mergenthaler, G. Ely, W. Upliner, J. Potter, T. James, and L. Sterrit, 1993: The cryogenic limb array etalon spectrometer (CLAES) on UARS: Experiment description and performance. *Journal of Geophysical Research, 98*, 10763–10775.

Roosen, R., and R. J. Angione, 1984: Atmospheric transmission and climate: results from Smithsonian measurements. *Bulletin of the American Meteorological Society, 65*(9), 950–957.

Rose, W. I., 1977: Scavenging of volcanic aerosol by ash: Atmospheric and volcanologic implications. *Geology, 5*, 621–624.

Rose, W. I., and C. A. Chesner, 1990: Worldwide dispersal of ash and gases from earth's largest known eruption: Toba, Sumatra, 75ka. *Palaeogeography, Palaeoclimatology, Palaeoecology, 89*, 269–275.

Rose, W. I., D. J. Delene, D. J. Schneider, G. J. S. Bluth, A. J. Krueger, I. E. Sprod, C. McKee, H. L. Davies, and G. G. J. Ernst, 1995: Ice in the 1994 Rabaul erption cloud: implications for volcano hazard and atmospheric effects. *Nature, 375*, 477–479.

Rosen, J. M., 1971: The boiling point of stratospheric aerosols. *Journal of Applied Meteorology, 10*, 1044–1046.

Russell, Philip B., J. M. L., et al., 1996: Global to microscale evolution of the Pinatubo volcanic aerosol derived from diverse measurements and analyses. *Journal of Geophysical Research, 101*(D13), 18745–18763.

Russell, P. B., et al., 1993: Pinatubo and pre-Pinatubo optical-depth spectra: Mauna Loa measurements, comparisons, inferred particle size distributions, radiative effects, and relationship to Lidar data. *Journal of Geophysical Research, 98*, 22969–22985.

Rye. R. O.. J. F. Luhr. and M. D. Wasserman. 1984: Sulfur and oxygen isotopic systematics of the 1982 eruptions of El Chichón volcano. Chiapas. Mexico. *Journal of Volcanology and Geothermal Research. 23.* 109-123.

Sapper. K.. 1927: *Vulkankunde.* Bibliothek Geographischer Handbücher. J. Engelhorns Nachf.. Stuttgart. A. Penck. Herausgeber.

Saravanan. R.. 1998: Atmospheric low-frequency variability and its relationship to midlatitude SST variability: Studies using the NCAR Climate System Model. *Journal of Climate. 11*(6). 1386-1404.

Sassen. K.. 1992: Evidence for liquid-phase cirrus cloud formation from volcanic aerosols: Climatic implications. *Science. 257.* 516-519.

Sassen. K.. T. Peter. B. P. Luo. and P. J. Crutzen. 1994: Volcanic Bishop's ring: evidence for a sulfuric acid tetrahydrate particle aureole. *Applied Optics. 33*(21). 4602-4606.

Satheesh. S. K.. and V. Ramanathan. 2000: Large differences in tropical aerosol forcing at the top of the atmosphere and Earth's surface. *Nature. 405.* 60-63.

Sato. M.. J. E. Hansen. M. P. McCormick. and J. B. Pollack. 1993: Stratospheric aerosol optical depth. 1850-1990. *Journal of Geophysical Research. 98*(D12). 22987-22994.

Schimel. D.. et al.. 1996: Radiative forcing of Climate Change. In: Houghton. J.. L. Meira Filho. B. Callander. N. Harris. A. Kattenberg. and K. Maskell (eds.): *Radiative forcing of Climate Change.* chap. 2. pp. 65-131. Contribution of WG I to the Second Assessment Report of the Intergovernmental Panel on Climate Change. Cambridge University Press. Cambridge. UK.

Schlesinger. M. E.. and N. Ramankutty. 1994: An oscillation in the global climate system of period 65-70 years. *Nature. 367.* 722-726.

Schneider. S. H.. and C. Mass. 1975: Volcanic dust. sunspots. and temperature trends. *Science.* *190.* 741-746.

Schönwiese. C.-D.. and A. Cress. 1988: An improved northern hemisphere volcanic activity parameter based on the Smithsonian chronology. *Meteorologische Rundschau.* *41*(Heft 3). 89-92.

Schweingruber. F.. 1996: *Tree Rings and Environment Dendroecology.* Paul Haupt Verlag. Bern.

Scott. W.. R. Hoblitt. R. Torres. S. Self. M. Martin. and N. T.. 1997: Pyroclastic flows of the June 15. 1991. climactic eruption of Mount Pinatubo. in: *Newhall and Punongbayan* (1997).

Sedlacek. W. A.. E. J. Mroz. A. L. Lazrus. and B. W. Gandrud. 1983: A decade of stratospheric sulfate measurements compared with observations of volcanic eruptions. *Journal of Geophysical Research.* *88*(C6). 3741-3776.

Self. S.. 1992: Krakatau revisited: The course of events and interpretation of the 1883 eruption. *GeoJournal.* *28.* 109-121.

Self. S.. and A. King. 1996: Petrology and sulfur and chlorine emissions of the 1963 eruption of Gunung Agung. Bali. Indonesia. *Bulletin of Volcanology.* *58.* 263-285.

Self. S.. and M. R. Rampino. 1981: The 1883 eruption of Krakatau. *Nature.* *294.* 699-704.

Self. S.. and M. R. Rampino. 1988: The relationship between volcanic eruptions and Climate Change: still a conundrum? *EOS. Transactions. American Geophysical Union.* *69*(6). 74-75. 85-86.

Self. S.. M. R. Rampino. and J. J. Barbera. 1981: The possible effects of large 19th and 20th century volcanic eruptions on zonal and hemispheric surface temperatures. *Journal of Volcanology and Geothermal Research.* *11.* 41-60.

Self. S.. M. R. Rampino. and M. J. Carr. 1989: A reappraisal of the 1835 eruption of Coseguina and its atmospheric impact. *Bulletin of Volcanology. 52.* 57–65.

Self. S.. J.-X. Zhao. R. E. Holasek. R. C. Torres. and A. J. King. 1997a: The atmospheric impact of the 1991 Mount Pinatubo eruption. in: *Newhall and Punongbayan* (1997).

Self. S.. M. R. Rampino. J. Zhao. and M. G. Katz. 1997b: Volcanic aerosol perturbations and strong El Niño events: No general correlation. *Geophysical Research Letters. 24.* 1247–1250.

Shabaloba. M. V.. and S. L. Weber. 1998: Seasonality of low-frequency variability in early-instrumental European temperatures. *Geophysical Research Letters. 25.* 3859–3862.

Shaw. N.. 1936: *Manual of Meteorology.* vol. II: Comparative Meteorology. Cambridge University Press.

Shindell. D.. D. Rind. N. Balachandran. J. Lean. and P. Lonergan. 1999: Solar cycle variability. ozone. and climate. *Science. 284.* 305–308.

Sigurdsson. H.. 1990: Evidence of volcanic loading of the atmosphere and climate response. *Palaeogeography. Palaeoclimatology. Palaeoecology. 89.* 277–289.

Sigurdsson. H.. and P. Laj. 1992: Atmospheric effects of volcanic eruptions: *Atmospheric effects of volcanic eruptions.* pp. 183–199.

Sigurdsson. H.. S. Carey. C. Mandeville. and B. S.. 1991: Pyroclastic flows of the 1883 Krakatau eruption. *EOS. Transactions. AGU. 72*(36). 377. 380–381.

Simkin. T.. and R. Fiske. 1983: *Krakatau 1883 - The volcanic eruption and its effects.* Smithsonian Institution Press. Washington. D.C.

Simkin. T.. and K. A. Howard. 1970: Caldera collapse in the Galapagos Islands. 1968. *Science. 169.* 429–437.

Simkin. T.. and L. Siebert. 1994: *Volcanoes of the World.* Geoscience Press. Inc. and Smithsonian Institution. Tucson. AR. 2 edn.

Simkin. T.. L. Siebert. L. McClelland. D. Bridge. C. G. Newhall. and J. H. Latter. 1981: *Volcanoes of the World.* Hutchinson Ross. Stroudsberg. Penn.

Simkin. T.. L. Siebert. and B. Russell. 2001: Volcano fatalities - Lessons from the historical record. *Science. 291.* 255.

Solomon. S.. 1999: Stratospheric ozone depletion: A review of concepts and history. *Reviews of Geophysics. 37.* 275–316.

Solomon. S.. R. Portman. R. Garcia. L. Thomason. L. Poole. and M. McCormick. 1996: The role of aerosol variations in anthropogenic ozone depletion at northern midlatitudes. *Journal of Geophysical Research. 101*(D3). 6713–6727.

Spellman. G.. 1999: Wine. weather and climate. *Weather. 54.* 230–239.

Spencer. R.. and J. Christy. 1993: Precision lower stratospheric temperature monitoring with the MSU: technique. validation and results 1979-1991. *Journal of Climate. 6.* 1194–1204.

Spencer. R. W.. F. J. LaFontaine. T. DeFelice. and F. J. Wentz. 1998: Tropical oceanic precipitation changes after the 1991 Pinatubo eruption. *Journal of the Atmospheric Sciences. 55.* 1707-1713.

Stahle. D. W.. et al.. 1998: Experimental dendroclimatic reconstruction of the Southern Oscillation. *Bulletin of the American Meteorological Society. 79.* 2137–2152.

Stenchikov. G. L.. I. Kirchner. A. Robock. H.-F. Graf. J. C. Antua. R. G. Grainger. A. Lambert. and L. W. Thomason. 1998: Radiative forcing from the 1991 Mount Pinatubo volcanic eruption. *Journal of Geophysical Research. 103*(D12). 13837–13857.

Stenni, B., R. Caprioli, L. Cimino, C. Cremisini, O. Flora, R. Gragnani, A. Longinelli, V. Maggi, and S. Torcini, 1999: 200 years of isotope and chemical records in a firn core from Hercules Névé, northern Victoria Land, Antarctica. *Annals of Glaciology, 29,* 106–112.

Stolarski, R., and D. Butler, 1978: Possible effects of volcanic eruptions on stratospheric minor constituent chemistry. *Pure and applied Geophysics, 117,* 486–497.

Stolarski, R., and R. Cicerone, 1974: Stratospheric chlorine: a possible sink for ozone. *Canadian Journal of Chemistry, 52,* 1610–1615.

Stommel, H., and E. Stommel, 1983: *Volcano Weather.* Seven Seas Press, Newport, R.I.

Stone, M., 1977: An Asymptotic Equivalence of Choice of Model by Cross-Validation and Akaike's Criterion. *Journal of the Royal Statistical Society, Ser. B 41,* 276–278.

Stothers, R., 2001: Major optical depth perturbations to the stratosphere form volcanic eruptions: Stellar extinction period, 1961-1978. *Journal of Geophysical Research, 106*(D3), 2993-3003.

Stothers, R. B., 1984a: The great Tambora eruption in 1815 and its aftermath. *Science, 224,* 1191–1198.

Stothers, R. B., 1984b: Mystery cloud of AD 536. *Nature, 307,* 344–345.

Stothers, R. B., 1989: Volcanic eruptions and solar activity. *Journal of Geophysical Research, 94*(B12), 17371-17381.

Stothers, R. B., 1996a: The great dry fog of 1783. *Climatic Change, 32,* 79–89.

Stothers, R. B., 1996b: Major optical depth perturbations to the stratosphere from volcanic eruptions: Pyrheliometric period, 1881-1960. *Journal of Geophysical Research, 101*(D2), 3901-3920.

Stothers. R. B.. 1997: Stratospheric aerosol clouds due to very large volcanic eruptions of the early twentieth century: Effective particle sizes and conversion from pyrheliometric to visual optical depth. *Journal of Geophysical Research. 102*(D5). 6143-6151.

Stothers. R. B.. 1999: Volcanic dry fogs. climate cooling. and plague pandemics in Europe and the middle east. *Climatic Change. 42.* 713-723.

Stothers. R. B.. and M. R. Rampino. 1983: Volcanic eruptions in the Mediterranean before A.D. 630 from written and archaeological sources. *Journal of Geophysical Research. 88*(B8). 6357-6371.

Stott. P.. S. Tett. G. Jones. M. Allen. J. Mitchell. and G. Jenkins. 2000: External control of 20th-century temperature by natural and anthropogenic forcing. *Science. 290.* 2133-2137.

Stott. P. A.. S. F. B. Tett. G. S. Jones. M. R. Allen. W. J. Ingram. and J. F. B. Mitchell. 2001: Attribution of twentieth century temperature change to natural and anthropogenic causes. *Climate Dynamics. 17.* 1-21.

Svensmark. H.. and E. Friis-Christensen. 1997: Variation of cosmic ray flux and global cloud coverage - a missing link in solar-climate relationships. *Journal of Atmospheric and Solar-Terrestrial Physics. 59*(11). 1225-1232.

Symonds. R. B.. W. I. Rose. and M. H. Reed. 1988: Contribution of Cl- and F-bearing gases to the atmosphere by volcanoes. *Nature. 334.* 415-418.

Symons. G. (ed.). 1888: *The Eruption of Krakatoa and subsequent phenomena. Report of the Krakatoa Committee of the Royal Society.* Tübner and Co.. London.

Tabazadeh. A.. and R. P. Turco. 1993: Stratospheric chlorine injection by volcanic eruptions: HCl scavenging and implications for ozone. *Science. 260.* 1082-1086.

Tett. S. F. B.. P. Stott. M. Allen. W. Ingram. and J. Mitchell. 1999: Causes of twentieth-century temperature change near the Earth's surface. *Nature. 399*. 569–572.

Thomas. G. E.. B. M. Jakosky. R. A. West. and R. W. Sanders. 1983a: Satellite limb-scanning thermal infrared observations of the El Chichón stratospheric aerosol: First results. *Geophysical Research Letters. 10*. 997–1000.

Thomas. L.. D. B. Jenkings. D. P. Wareing. and M. Farrington. 1983b: Laser radar observations in mid-Wales of aerosols from the El Chichón eruption. *Nature. 304*. 248–250.

Thomason. L.. L. Poole. and T. Deshler. 1997: A global climatology of stratospheric aerosol surface area density deduced from Stratospheric Aerosol and Gas Experiment II measurements: 1984-1994. *Journal of Geophysical Research. 102*(D7). 8967–8976.

Thompson. D.. and J. Wallace. 2001: Regional climate impacts of the Northern Hemisphere Annular Mode. *Science. 293*. 85–89.

Thompson. D. W. J.. and J. M. Wallace. 1998: The Arctic Oscillation signature in the wintertime geopotential height and temperature fields. *Geophysical Research Letters. 25*. 1297–1300.

Thompson. L.. E. Mosley-Thompson. and B. Morales Arnao. 1984: Major El Niño/Southern Oscillation events recorded in stratigraphy of the tropical Quelccaya ice cap. *Science. 226*. 50–52.

Thompson. L.. K. Henderson. E. Mosley-Thompson. and P.-N. Lin. 2000: The tropical ice core record of ENSO. chap. 9. pp. 325–356. in: *Diaz and Markgraf* (2000).

Thordarson. T.. and S. Self. 1993: The Laki (Skaftar Fires) and Grimsvotn eruptions in 1783-1785. *Bulletin of Volcanology. 55*. 233–263.

Thordarson, T., S. Self, N. Oskarsson, and T. Hulsebosch, 1996: Sulfur, chlorine, and fluorine degassing and atmospheric loading by the 1783-1784 AD Laki (Skaftar Fires) eruption in Iceland. *Bulletin of Volcanology*, *58*, 205-225.

Thulasiraman, S., J. B. Nee, W. N. Chen, and J. H. Chen, 1999: Temporal characteristics of tropopause and lower stratosphere over Taiwan during 1990-1995. *Journal of Atmospheric and Solar-Terrestrial Physics*, *61*, 1299-1306.

Timmermans, J., 1960: *The physico-chemical constants of binary systems in concentrated solutions*, vol. 4. Interscience Publisher, Inc., New York.

Toon, O., and J. Pollack, 1973: Physical properties of the stratospheric aerosol. *Journal of Geophysical Research*, *78*, 7051-7056.

Trepte, C. R., and M. H. Hitchman, 1992: Tropical stratospheric circulation deduced from satellite aerosol data. *Nature*, *355*, 626-628.

Trepte, C. R., R. E. Veiga, and M. P. McCormick, 1993: The poleward dispersal of Mount Pinatubo volcanic aerosol. *Journal of Geophysical Research*, *98*(D10), 18563-18573.

Turco, R. P., K. Drdla, A. Tabazadeh, and P. Hamill, 1993: Heterogenous chemistry of polar stratospheric clouds and volcanic aerosols. In: Chanin, M.-L. (ed.): *Heterogenous chemistry of polar stratospheric clouds and volcanic aerosols*. pp. 65-134. Springer Verlag, Berlin und Heidelberg.

Valero, F. P. J., and P. Pilewskie, 1992: Latitudinal survey of spectral optical depth of the Pinatubo volcanic cloud - Derived particle sizes, columnar mass loadings, and effects on planetary albedo. *Geophysical Research Letters*, *19*, 163-166.

van Loon, H., and J. C. Rogers, 1978: The seesaw in winter temperatures between Greenland northern Europe. Part I: General description. *Monthly Weather Review*, *106*, 296-310.

Verbeek. R.. 1885: *Krakatau.* Landsrukkerij, Batavia.

Volz. F.. 1964: Twilight phenomena caused by the eruption of Agung Volcano. *Science. 144*, 1121–1122.

Volz. F.. 1969: Neutral points of sky polarization in spring and summer 1968. *Journal of Geophysical Research. 74*. 1920–1921.

Volz. F.. 1970: Atmospheric turbidity after the Agung eruption of 1963 and size distribution of the volcanic aerosol. *Journal of Geophysical Research. 75(27)*. 5185–5193.

Volz. F.. and R. Goody. 1962: The intensity of the twilight and upper atmospheric dust. *Journal of the Atmospheric Sciences. 19*. 385.

Volz. F. E.. 1968: *Twilights before and after the Agung eruption.* World Meteorological Organization. 248 TP. 136.

Volz. F. E.. 1975a: Distribution of turbidity after the 1912 Katmai eruption in Alaska. *Journal of Geophysical Research. 80(18)*. 2643–2648.

Volz. F. E.. 1975b: Volcanic twilights from the Fuego eruption. *Science. 189*. 48–50.

von Hann. J.. 1915: *Lehrbuch der Meteorologie.* Verlag Chr. Herm. Tauchnitz, Leipzig. 3rd edn.

Wallace. J. M.. 2000: North Atlantic Oscillation/annular mode: Two paradigms - one phenomenon. *Quart.J.R.Met.Soc.. 126*. 791–805.

Wallace. P. J.. and T. M. Gerlach. 1994: Magmatic vapor source for sulfur dioxide released during volcanic eruptions: Evidence from Mount Pinatubo. *Science. 265*. 497–499.

Wang. P.-H.. G. Kent. K. Powell. G. Yue. L. Poole. and M. McCormick. 2000: Properties of the 1979 SAM II Antarctic 1.0-μm extinction coefficients: Implications of dehydration and seasonal evolution of the Antarctic polar vortex. *Journal of Geophysical Research. 105(D7)*. 9407–9420.

Weatherly. J.. B. Briegleb. W. Large. and J. Maslanik. 1998: Sea ice and polar climate in the NCAR CSM. *Journal of Climate. 11*(6). 1472-1486.

Wexler. H.. 1951a: On the effects of volcanic dust on insolation and weather (I). *Bulletin of the American Meteorological Society. 32*(1). 10-15.

Wexler. H.. 1951b: Spread of the Krakatoa volcanic dust cloud as related to the high-level circulation. *Bulletin of the American Meteorological Society. 32*(2). 48-51.

Wexler. H.. 1956: Variations in insolation. general circulation and climate. *Tellus. VIII,* 480-494.

Whitworth. T.. 1983: Monitoring the transport of the Antarctic Circumpolar Current at Drake Passage. *Journal of Physical Oceanography. 13.* 2045-2057.

Wigley. T.. 1991: Climate variability on the 10-100-year time scale: Observations and possible causes. in: *Global Changes of the Past.* edited by R. Bradley. pp. 83-101. UCAR Office for Interdisciplinary Earth Studies. Boulder. CO.

Wigley. T.. 2000: ENSO. volcanoes and record-breaking temperatures. *Geophysical Research Letters. 27.* 4101-4104.

Williams. H.. 1952: *The great eruption of Coseguina. Nicaragua. in 1835.* University of California. Berkeley and Los Angeles. vol. 29 of *Publications in Geological Sciences.* pp. 21-46. 2.

Williams. S. N.. and S. Self. 1983: The October 1902 plinian eruption of Santa Maria volcano. Guatemala. *Journal of Volcanology and Geothermal Research. 16.* 33-56.

Woods. D.. R. Chuan. and W. Rose. 1985: Halite particles injected into the stratosphere by the 1982 El Chichón eruption. *Science. 230.* 170-172.

Woods. D. C.. and R. L. Chuan. 1983: Size-specific composition of aerosols in the El Chichón volcanic cloud. *Geophysical Research Letters. 10*(11). 1041-1044.

Yau. K.. and F. Stephenson. 1988: A revised catalogue of Far Eastern observations of sunspots (165 BC to AD 1918. *Quart. J. Roy. Astr. Soc.*, *29*, 175–197.

Zender. C. S.. B. Bush. S. K. Pope. A. Bucholtz. W. D. Collins. J. T. Kiehl. F. P. J. Valero. and J. John Vitko. 1997: Atmospheric absorption during the Atmospheric Radiation Measurement (ARM) enhanced shortwave experiment. *Journal of Geophysical Research*, *102*(D25). 29901–29915.

Zerefos. C. S.. K. Tourpali. and A. F. Bais. 1994: Further studies on possible volcanic signal to the ozone layer. *Journal of Geophysical Research*, *99*(D12). 25741–25746.

Zheng. J.. A. Kudo. D. A. Fisher. E. W. Blake. and M. Gerasimoff. 1998: Solid electrical conductivity (ECM) from four Agassiz ice cores. Ellesmere Island NWT. Canada: high-resolution signal and noise over the last millennium and low resolution over the Holocene. *The Holocene*, *8*. 413–421.

Zielinski. G. A.. 1995: Stratospheric loading and optical depth estimates of explosive volcanism over the last 2100 years derived from the Greenland Ice Sheet Project 2 ice core. *Journal of Geophysical Research*, *100*(D10). 20937–20955.

Zielinski. G. A.. P. A. Mayewski. L. D. Meeker. S. Whitlow. M. S. Twickler. M. Morrison. D. A. Meese. A. J. Gow. and R. B. Alley. 1994: Record of volcanism since 7000 B.C. from the GISP2 Greenland ice core and implications for the volcano-climate system. *Science*, *264*. 948–952.

Zielinski. G. A.. P. A. Mayewski. L. D. Meeker. S. Whitlow. and M. S. Twickler. 1996a: A 110.000-yr record of explosive volcanism from the GISP2 (Greenland) ice core. *Quaternary Research*, *45*. 109–118.

Zielinski. G. A.. P. A. Mayewski. L. D. Meeker. S. Whitlow. and M. S. Twickler. 1996b: Potential atmospheric impact of the Toba mega-eruption 71.000 years ago. *Geophysical Research Letters*, *23*. 837–840.

Zielinski. G. A.. J. E. Dibb. Q. Yang. P. A. Mayewski. S. Whitlow. and M. S. Twickler. 1997:

Assessment of the record of the 1982 El Chichón eruption as preserved in Greenland snow.

Journal of Geophysical Research. *102*(D25). 30031–30045.